An Integrated Approach to Understanding the Size-Dependent Properties of Atmospheric Aerosol Particles

Ryan Schmedding

Department of Atmospheric and Oceanic Sciences
McGill University
Montreal, Quebec, Canada

March 11, 2025

A thesis submitted to McGill University in partial fulfillment of the requirements of the degree of Doctor of Philosophy

"It is wrong to think that the task of physics is
to find out how Nature is.
Physics concerns what we say about Nature."

-Niels Bohr

Abstract

Atmospheric aerosols are colloidal suspensions of condensed particles and the air surrounding them. Aerosols are found in all environments and are a source of uncertainty in global climate models and a contributor to poor air quality. Aerosol particles range in size from tens of nanometers to several micrometers in diameter. Aerosol particles with spherical equivalent diameters below 100 nanometers are among the most numerous. Certain particles in this size range may also possess multiple distinct liquid phases within a single particle. As the diameter of atmospheric aerosol particles decreases below 100 nanometers the surface area-to-volume and interfacial area-to-volume ratios of these particles become increasingly large. Thus any unique phenomenon occurring at these two phase boundaries plays an increasingly important role.

The equilibrium surface composition of well-mixed particles under high relative humidity conditions is determined first, along with the corresponding bulk phase composition following the partitioning of species to and from the surface phase. This allows for a better understanding of the role of surface effects on cloud droplet activation of aerosol particles. It was found that aerosol particles will experience substantial enrichment of organic compounds and depletion of inorganic electrolytes at a three-dimensional surface phase. This leads to large reductions in the critical supersaturation necessary for cloud condensation nuclei activation in many systems.

Next, the role of interfacial tension under lower relative humidities was explored by comparing four approaches to modeling interfacial tension at a two-dimensional liquid–liquid or liquid–surface interface. The inclusion of in-

terfacial tensions at both interfaces had competing effects wherein the liquid-liquid interfacial tension suppressed phase separation and the liquid-surface interfacial tension encouraged it. For particles with spherical equivalent diameters less than approximately 30 nanometers, the effect of the liquid–liquid interface became stronger than the liquid–surface interface, and phase separation was suppressed. The degree of this suppression depended on the model for interfacial tension that was used.

Lastly, machine learning models were developed to predict the pure-component surface tensions of atmospherically relevant organic compounds. Three different types of inputs to characterize the molecular structure, namely simplified elemental ratios, Molecular ACCesS (MACCS) keys, and Morgan fingerprints, were used to train four different kinds of models, extreme gradient boosting, random forest, decision tree, and k-nearest neighbors. It was found that the extreme gradient boosting models performed the best, regardless of input types, and that MACCS key-based models had the best balance of input complexity and model performance.

Résumé

Les aérosols atmosphériques sont des suspensions colloïdales de particules condensés et de l'air qui les entoure. Les aérosols sont présents dans tous les environnements et constituent une source majeure d'incertitude dans les modèles climatiques mondiaux ainsi qu'un facteur important de mauvaise qualité de l'air. La taille des particules d'aérosols varie de quelques dizaines de nanomètres à plusieurs micromètres de diamètre. Les particules d'aérosol dont le diamètre équivalent sphérique est inférieur à 100 nanomètres sont parmi les plus nombreuses. Certaines particules de cette taille peuvent également présenter plusieurs phases liquides distinctes au sein d'une même particule. à mesure que le diamètre des particules d'aérosols atmosphériques diminue en dessous de 100 nanomètres, les rapports surface–volume et surface interfaciale–volume de ces particules deviennent de plus en plus importants. Par conséquent, tout phénomène unique se produisantà la limite de ces deux phases joue un rôle de plus en plus important.

La composition superficielle à l'équilibre de particules bien mélangées dans des conditions d'humidité relative élevée est déterminée en premier lieu, ainsi que la composition correspondante de la phase en vrac après le partage des espèces vers et à partir de la phase superficielle. Cela permet de mieux comprendre le rôle des effets de surface sur l'activation des gouttelettes de nuage des particules d'aérosol. Il a été constaté que les particules d'aérosol subissent un enrichissement substantiel en composés organiques et un appauvrissement en électrolytes inorganiques au niveau d'une phase de surface tridimensionnelle. Cela conduit à des réductions importantes de la

sursaturation critique nécessaireà l'activation des noyaux de condensation des nuages dans de nombreux systèmes.

Ensuite, le rôle de la tension interfaciale sous des humidités relatives plus faibles a été exploré en comparant quatre approches de modélisation de la tension interfacialeà une interface bidimensionnelle liquide–liquide ou liquide–surface. L'inclusion de tensions interfaciales aux deux interfaces a eu des effets concurrents, la tension interfaciale liquide–liquide supprimant la séparation des phases et la tension interfaciale liquide–surface l'encourageant. Pour les particules dont le diamètre sphérique équivalent est inférieurà environ 30 nanomètres, l'effet de l'interface liquide–liquide est devenu plus fort que celui de l'interface liquide–surface, et la séparation des phases a été supprimée.

Enfin, des modèles d'apprentissage automatique ont été développés pour prédire les tensions de surface des composants purs des composés organiques importants pour l'atmosphère. Trois types d'entrées différents, les rapports élémentaires simplifiés, les clés MACCS (Molecular ACCesS) et les empreintes digitales de Morgan, ont été utilisés pour entraîner quatre types de modèles différents : le renforcement du gradient extrême, la forêt aléatoire, l'arbre de décision et les voisins les plus proches. Il a été constaté que les modèles de renforcement du gradient extrême étaient les plus performants, quel que soit le type d'entrée, et que les modèles basés sur les clés MACCS présentaient le meilleur équilibre entre la complexité de l'entrée et la performance du modèle.

Author Contributions

The work outlined in this thesis is my own. In the sections indicated below, co-authors of journal articles from which the chapters were adapted are identified.

Chapter 2

Chapter 2 was reproduced from Schmedding and Zuend, "A Thermodynamic Framework for Bulk–Surface Partitioning in Finite-Volume Mixed Organic–Inorganic Aerosol Particles and Cloud Droplets," *Atmospheric Chemistry and Physics* (2023), 13, 7741–7765. I performed model development and simulations, visualized model outputs, and wrote the manuscript. Professor Zuend conceived the project, assisted with model development, co-wrote the manuscript, supervised the work, and secured funding.

Chapter 3

Chapter 3 was reproduced from SSchmedding and Zuend, "The Role of Interfacial Tension in the Size-Dependent Phase Separation of Atmospheric Aerosol Particles," *Atmospheric Chemistry and Physics* (2025), 25, 327–346. I performed model development and simulations, visualized model outputs, and wrote the manuscript. Professor Zuend conceived the project, assisted with model development and theory, co-wrote the manuscript, supervised the work, and secured funding.

Chapter 4

Chapter 4 was reproduced from RSchmedding, Franssen, and Zuend, "A Machine Learning Approach for Predicting the Pure Component Surface Tension of Atmospherically Relevant Organic Compounds," *In Press*. I conceived the project, performed model development, visualized figures, and wrote the manuscript. Mees Franssen performed model development and data collection for model training. Professor Zuend supervised the project, edited the manuscript, and secured funding.

Appendix A

Appendix A was reproduced from the supplementary information of Schmedding and Zuend, "A Thermodynamic Framework for Bulk–Surface Partitioning in Finite-Volume Mixed Organic–Inorganic Aerosol Particles and Cloud Droplets," *Atmospheric Chemistry and Physics* (2023), 13, 7741–7765. I performed model development and simulations, visualized model outputs, and wrote the manuscript. Professor Zuend conceived the project, assisted with model development, co-wrote the manuscript, supervised the work, and secured funding.

Appendix B

Appendix B was reproduced from the supplementary information of Schmedding and Zuend, "The Role of Interfacial Tension in the Size-Dependent Phase Separation of Atmospheric Aerosol Particles," *Atmospheric Chemistry and Physics* (2025), 25, 327–346. I performed model development and simulations, visualized model outputs, and wrote the manuscript. Professor Zuend conceived the project, assisted with model development and theory, co-wrote the manuscript, supervised the work, and secured funding.

Appendix C

Appendix C was reproduced from the supplementary information of Schmedding, Franssen, and Zuend, "A Machine Learning Approach for Predicting the Pure Component Surface Tension of Atmospherically Relevant Organic Compounds," *In Press*. I conceived the project, performed model development, visualized figures, and wrote the manuscript. Mees Franssen performed model development and data collection for model training. Professor Zuend supervised the project, edited the manuscript, and secured funding.

Acknowledgements

In many ways, writing this section of my dissertation was perhaps the most challenging part of my Ph.D., but also the part that I looked forward to the most. The experience of completing a Ph.D. is different for every person; however, we all must rely on numerous people to finish this journey. I would like to start by thanking my thesis defence committee. Reviewing doctoral dissertations is a laborious and often forgotten task that all professors must participate in.

I am grateful to the many current and past members of the Zuend group with whom I have shared this experience: Camilo Serrano Damha, with whom I shared an office during my time at McGill and bonded over our shared love of coffee; Joe Lilek, the first graduate student at McGill that I ever contacted, for his encouragement to join the Zuend group; Hang Yin and Xuehuan Hu, for their support during the long days of the COVID pandemic; Mees Franssen, for his patience as I gave him a half-finished project to work on for a summer; Dan Hassan-Barthaux, for his overwhelming positivity and dry sense of humor despite my best efforts to bring him down; Zixuan Shen, for her positivity and modeling expertise, which greatly helped in the development of Chapter 3 of this work; and Ben Bergen, for developing extensions of AIOMFAC which will make those laid out in this work more useful for others. Beyond the Zuend group, I would like to thank all of the graduate students in the Department of Atmospheric and Oceanic Sciences for their friendship and support.

My experience during my Ph.D. was also unique in that I spent multiple

extended periods away from McGill. As such, I would like to thank Professor Tom Peter, Dr. Claudia Marcolli, and Dr. Zamin Kanji for graciously hosting me at ETH Zurich for six months. I also would like to thank all of the students in the Peter group and the Institute for Atmosphere and Climate who welcomed a random Ph.D. student who showed up one July morning in 2022 and made me feel included. I also would like to thank my mentors and coworkers at NASA: Dr. Barry Lefer, Dr. Guanyu Huang, Stephanie Olaya, Rachel Wegener, Kelby Kramer, Marley Majetic, Mindy Priddy, and Riley McCue for their support and encouragement there.

Of course, none of this work would have been possible without the support of my supervisor, Professor Andreas Zuend. I appreciate the chance he gave me to develop as a scholar over the course of my Ph.D. There were many times when I faced a problem that felt insurmountable, and Prof. Zuend would calmly step in and correct my code. Prof. Zuend always encouraged me to seek out new opportunities to enrich my experience as a Ph.D. student, from traveling to Zurich, to working as an Air Quality Fellow for the U.S. State Department, to taking a summer to work at NASA. He also always provided valuable feedback on writing and presentations. Without his help, I doubt I would have completed my Ph.D..

Lastly, I would like to thank my family and loved ones. My parents, Beth and Bob, and my brothers, Thomas and Brent, always supported me and my decisions, regardless of whether they understood my research. My wonderful partner, Ros, whose love and encouragement helped me throughout the lowest lows and highest highs of this experience. And of course, I must thank Sam, without whom I would never know when the mail carrier was at the door and would surely oversleep my alarm countless times.

List of Publications

Peer-Reviewed Publications

Schmedding, R., Franssen, M., and Zuend, A.: "A machine learning approach for predicting the pure component surface tension of atmospherically relevant organic compounds", *In Press*, 2025.

Schmedding, R. and Zuend, A.: "The role of interfacial tension in the size-dependent phase separation of atmospheric aerosol particles", *Atmospheric Chemistry and Physics*, 2025.

Shahabadi, V., Vennes, B., Schmedding, R., Zuend, A., Mauzeroll, J., Schougaard, S., Preston, T.: "Quantifying Surface Tension of Metastable Aerosols", *Nature Communications*, 2024

Schmedding, R. and Zuend, A.: "A thermodynamic framework for bulk–surface partitioning in finite-volume mixed organic–inorganic aerosol particles and cloud droplets", *Atmospheric Chemistry and Physics*, 2023.

Schmedding, R., et al.: "Predicting secondary organic aerosol phase state and viscosity and its effect on multiphase chemistry in a regional scale air quality model", *Atmospheric Chemistry and Physics*, 2020.

Schmedding, R., et al.: "α-Pinene-derived organic coatings on acidic sulfate aerosol impacts secondary organic aerosol formation from isoprene in a box model", *Atmospheric Environment*, 2019.

Conference Presentations

Schmedding, R., Franssen, M., Zuend, A.: "A Machine Learning Approach

for Characterizing the Surface Tension of Atmospherically Relevant Organic Compounds" (Poster, AGU 2024, Washington, USA, December 9-13 2024)

Schmedding, R., Zuend, A.: "A Framework for Determining the Size-Dependent Morphology of Secondary Organic Aerosols", (Poster, AGU 2023, San Francisco, USA, December 11-15 2023)

Schmedding, R., Zuend, A.: "The Role of Interfacial Energy and Size-Dependent Morphology of Atmospheric Aerosol Particles", (Presentation, IAMA 2023, Davis, USA, December 6-8 2023)

Schmedding, R., Franssen, M., Zuend, A.: "A Machine Learning Approach for Determining the Pure Component Surface Tensions of Aerosol Particle Species", (Poster, IAMA 2023, Davis, USA, December 6-8 2023)

Schmedding, R., Zuend, A.: "A Thermodynamically Rigorous Treatment of Bulk-Surface Partitioning in Organic Aerosols and Cloud Condensation Nuclei", (Poster, IAC 2022, Athens, Greece, September 5-9 2022)

Schmedding, R., Zuend, A.: "Just Scratching the Surface – An Exploration of Bulk–Interface Partitioning in Atmospheric Aerosols" (Presentation, CCCE 2021, Online, August 13-19 2021)

Invited Talks

Schmedding, R., Zuend, A.: "A Framework for Determining the Size-Dependent Morphology of Secondary Organic Aerosols", (Stony Brook University, Stony Brook, USA, October 9, 2024)

Contributions to Original Knowledge

This work presents three novel frameworks for exploring the importance of surfaces and interfaces in atmospheric aerosol particles. Chapter 2 presents a framework for computing the composition of a coupled bulk and surface in aerosol particles with sizes ranging from the micrometer to tens of nanometers. The importance of bulk–surface partitioning for aerosol–cloud interactions is discussed, since such partitioning changes both the Kelvin and Raoult effect terms in the Köhler equation. The model developed in this chapter is compared to past measurement data and is in good agreement with past experiments. This is the first model that can simultaneously account for changes in the surface composition of an aerosol particle while maintaining mass balance and thermodynamic rigor.

Chapter 3 explores the role of interfacial tension in phase-separated aerosol particles. This chapter presents the first model that can account for the interfacial tension between two liquid phases and between the surface and bulk phases in an aerosol particle. It is the first model to rigorously examine the role of particle size in phase separation, an interaction that has been observed experimentally but not modeled from a theoretical basis.

Chapter 4 examines a key assumption made in Chapters 2 and 3, that of pure-component surface tensions. It develops three different machine learning-based models that can predict the pure-component surface tension of atmospherically relevant organic compounds with a high degree of accu-

racy. It is the first model of its kind to account for such a broad range of functional groups in its training data.

Thesis Outline

The work in this thesis aims to better understand the surface and interfacial properties of atmospheric aerosol particles. Chapter I introduces atmospheric aerosols and their importance to human health and the global climate system. Chapter I also introduces the thermodynamic principles and numerical models used to study the properties of atmospheric aerosol particles.

Chapter 2 introduces a theoretical framework for determining the composition of the surface phase of finite-volume aerosol particles and cloud droplets. It was found that bulk–surface partitioning can substantially modify the composition of the surface phase relative to the bulk phase below it, and that the inclusion of these properties may lead to large deviations from simplified models for the activation of cloud condensation nuclei.

Chapter 3 compares different treatments of interfacial tension at liquid-liquid phase boundaries in aerosol particles. This chapter also explores the role that interfacial tension plays in suppressing or encouraging liquid-liquid phase separation in aerosol particles as a function of particle size. It is shown that more extreme treatments of interfacial tension better reproduce measurements in highly immiscible systems, while less extreme treatments of interfacial tension better reproduce measurements in more miscible systems. The inclusion of interfacial tensions between bulk phases and between the bulk and surface phases leads to reductions in the onset relative humidity of liquid-liquid phase separation as a function of particle size.

Chapter 4 develops novel machine learning-based approaches for predicting the pure-component surface tension of individual compounds in an aerosol

particle. This directly addresses one of the key assumptions used in Chapters 2 and 3. It was found that the extreme gradient boosting approach provided the most accurate predictions of surface tension, and that MACCS keys provide the best balance of structural information about a molecule without requiring excessive input information. A simplified model that can be used with aerosol mass spectrometer data was also developed for comparison to more detailed models and for applications to field data with limited organic structure information.

Chapter 5 concludes the work presented in this thesis and describes future research that may be based on the findings included herein. Chapters A, B, and C contain supplementary information, figures, and tables that correspond to Chapters 2, 3, and 4, respectively.

Contents

I Introduction **1**

1 Background and Relevant Literature **2**
1.1 Atmospheric Aerosols 3
1.1.1 Aerosol Composition 5
1.1.2 Aerosol Morphologies and Mixing States 9
1.1.3 Aerosol-Cloud-Climate Interactions 12
1.2 Modeling Aerosol Thermodynamics 18
1.2.1 Activity Coefficients and Non-Ideal Mixing 18
1.2.2 The Aerosol Inorganic–Organic Mixtures Functional groups Activity Coefficients model 19
1.2.3 Surface Thermodynamics 23
1.3 Aerosol Surface Properties 25
1.4 Aerosol Interfacial Properties 30
1.5 Pure Component Surface Tensions 34

II Surface and Interfacial Energies **38**

2 A Thermodynamic Framework for Bulk–Surface Partitioning in Finite-volume Mixed Organic–Inorganic Aerosol Particles and Cloud Droplets **39**
2.1 Preface 40
2.2 Abstract 41
2.3 Introduction 43
2.3.1 Prior treatments of bulk–surface partitioning in aerosol systems 50

2.4 Theory and Methods 55
2.4.1 Calculation of Surface Composition 62
2.4.2 Initial guess generation 64
2.4.3 Model Assumptions 66
2.5 Results and discussion 69
2.5.1 Comparison of measured and predicted surface tension 69
2.5.2 Bulk phase depletion 73
2.5.3 Köhler curves 77
2.6 Theoretical and atmospheric implications 84
2.6.1 Theoretical implications 84
2.6.2 Atmospheric implications 89
2.7 Conclusion 92

3 The Role of Interfacial Tension in the Size-dependent Phase Separation of Atmospheric Aerosol Particles 106
3.1 Preface 107
3.2 Abstract 108
3.3 Introduction 109
3.4 Methods 115
3.4.1 Modeling interfacial tension between two liquid phases 115
3.4.2 Alternative models of interfacial tension 119
3.4.3 Coupled Vapor–liquid–liquid and bulk–surface equilibrium calculation 126
3.5 Results 129
3.5.1 Interfacial and surface tensions 129
3.5.2 Size-dependent phase separation in core–shell aerosols . 135
3.6 Discussion and atmospheric implications 142
3.7 Conclusions 149

4 A Machine Learning Approach for Predicting the Pure–Component Surface Tension of Atmospherically Relevant Organic Compounds 160
4.1 Preface 161
4.2 Abstract 162
4.3 Methods 174
4.3.1 Data Collection and Processing 174
4.3.2 Model Architecture 175
4.3.3 Model Testing 179

4.3.4 Model Applications 180
4.4 Results 181
4.5 Discussion 195
4.6 Conclusions 198
4.7 Code and Data Availability 199

III Discussion and Conclusions 212

5 Conclusions and Future Work 213
5.1 Conclusions 213
5.2 Future Work 216

A Supplement to Chapter 2 - A thermodynamic framework for bulk–surface partitioning in finite-volume mixed organic–inorganic aerosol particles and cloud droplets 238

B Supplement to Chapter 3 - The role of interfacial tension in the size-dependent phase separation of atmospheric aerosol particles 252

C Supplement to Chapter 4 - A Machine Learning Approach for Predicting the Pure Component Surface Tension of Atmospherically Relevant Organic Compounds 261

List of Figures

1.1 Aerosol Compositions at Different locations 8
1.2 Example of phase-separated aerosol morphologies 11
1.3 Example of a Köhler curve 15
1.4 Aerosol-Cloud-Climate Interactions 17

2.1 Schematic of bulk–surface partitioning in an aerosol particle. . 55
2.2 Comparisons of predicted surface tensions to contactless measurements of aerosol surface tensions. 71
2.3 The impact of particle diameter and surface thickness on predicted surface tension 74
2.4 Bulk–surface partitioning coefficients in a ternary aerosol system. 76
2.5 An alternative treatment of partial molar area and it's influence on surface tension. 78
2.6 Köhler curves for a ternary system for two different sized water-free aerosol particles. 82
2.7 The role of co-condensation of SVOCs on bulk–surface partitioning and cloud droplet activation. 85
2.8 The implications for CCN activation in different types of clouds as a function of particle size. 91

3.1 A cross-section of a phase-separated aerosol particle with the liquid-liquid interfaces and surfaces emphasized. 122
3.2 Values of interfacial and surface tensions for a μm-scale particle. 124
3.3 Predicted surface tensions based on simplified weighted averages of pure component values. 131
3.4 Comparison of predicted and measured interfacial tensions for four different systems. 133

3.5 The effect of varying ϕ in the Girifalco-Good equation (Eq. (3.2) on the predicted surface tension. 136
3.6 Relative amount of water in the aqueous and organic phases for phase-separated particles of different sizes. 138
3.7 Onset relative humidity of liquid-liquid phase separation as a function of particle size. 140
3.8 Interfacial tensions necessary to suppress phase separation in particles as a function of particle size. 143
3.9 The most energetically favorable surface thickness for a 250 nm particle. 148

4.1 A conceptual representation of the model inputs and outputs. 174
4.2 Distributions of reported surface tensions and temperatures used to train the models in chapter 4. 176
4.3 A comparison of the ML-based models to previous empirical treatments of pure–component surface tension 184
4.4 Feature importance for the three best performing models described in chapter 4. 187
4.5 Temperature dependence of two atmospherically relevant biogenic aerosol and biomass burning tracer compounds. 189
4.6 Köhler curves for the isoprene SOA system and the α-pinene SOA system. 193

A.1 Bulk–surface partitioning coefficients for different species in a particle as a function of bulk-phase water activity. 239
A.2 Bulk–surface partitioning coefficients for different species in a particle as a function of bulk-phase water mole fraction. 240
A.3 Predicted saturation ratio for a ternary water–malonic-acid–ammonium-sulfate system. 241
A.4 Predicted saturation ratio for a ternary water–glutaric-acid–ammonium-sulfate system. 242
A.5 Predicted saturation ratio for a ternary water–pimelic-acid–ammonium-sulfate system. 243
A.6 Predicted saturation ratio for a ternary water–succinic-acid–ammonium-sulfate system. 244
A.7 Model sensitivity to pure component surface tensions. 245
A.8 Comparison of the thermodynamic bulk–surface partitioning model to a statistical mechanics model. 246

B.1 The sensitivity of interfacial tension to pure component surface tensions. 256
B.2 The relative amount of PEG-400 in the aqueous phase of a phase-separated particle. 257
B.3 The relative amount of ammonium sulfate in the aqueous phase of a phase-separated particle. 258
B.4 The interfacial tension at the onset of phase-separation as a function of particle size. 259
B.5 The effect of ignoring the interfacial tension at the liquid–surface interface. 260

C.1 Two dimensional KDE for compound classes with 1 non-hydrocarbon functional group. 262
C.2 Two dimensional KDE for mixed compound classes. 263
C.3 Residuals from the XGBoost models for the highest erorr predictions. 264
C.4 Hierarchical similarities between compounds from the 100 most poorly performing MACCS keys based compounds. 266
C.5 Hierarchical similarities between compounds from the 100 most poorly performing Morgan fingerprints compounds. 267

List of Tables

2.1 Critical wet diameter and supersaturations for the Köhler curves shown in Figure 2.6. 83
2.2 Partial molar areas as a function of particle size and surface thickness. 87

3.1 A summary of the different interfacial tension treatments used in this chapter. 125

4.1 Performance metrics for different input types and model architectures. 182
4.2 Predicted surface tensions at room temperature for the isoprene SOA system. 194
4.3 Predicted pure–component surface tensions at room temperature for the α-pinene SOA system. 196

A.1 Composition of isoprene SOA system used in chapter 2. 247
A.2 List of abbreviations used in chapter 2. 248
A.3 list of mathematical symbols used in chapter 2. 249

B.1 List of abbreviations used in chapter 3 and their meanings. . . 253
B.2 List of mathematical symbols used in chapter 3 and their meanings. 254
B.3 Pure component surface tension values at room temperature used in chapter 3. 255

C.1 t-test results for the 100-worst performing values of the simplified model inputs. 265

List of Abbreviations

List of abbreviations used in this work and their meanings.

Abbreviation	**Meaning**
AI	Artificial Intelligence
AIOMFAC	Aerosol Inorganic–Organic Mixtures Functional groups Activity Coefficients
ANN	Artificial Neural Network
CCN	Cloud Condensation Nucleus
CSOA	Complex Secondary Organic Aerosol mixture
DFT	Density Functional Theory
DT	Decision Tree
ELVOC	Extremely Low-Volatility Organic Compounds
E-AIM	Extended Aerosol Inorganics Model
IFE	Interfacial Energy
INP	Ice Nucleating Particle
IVOC	Intermediate Volatility Organic Compound
KNN	K-Nearest Neighbors
LL	Liquid–Liquid
LLPS	Liquid–Liquid Phase Separation
LLE	Liquid–Liquid Equilibrium
LVOC	Low Volatility Organic Compound
MACCS	Molecular ACCess System
MAE	Mean Absolute Error
MAPE	Mean Absolute Percentage Error
MCM	Master Chemical Mechanism
MF	Morgan Fingerprints
MSE	Mean Squared Error

Abbreviation	**Meaning**
OIR	Organic-to-Inorganic dry mass Ratio
PFAS	Per- and polyFluoroAlkyl Substances
PM	Particulate Matter
POA	Primary Organic Aerosol
QSPR	Quantitative Structure–Property Relationship
RF	Random Forest
RH	Relative Humidity
RMSE	Root Mean Squared Error
Simp	Simplified Inputs
SMARTS	SMiles ARbitrary Target Specification
SMILES	Simplified Molecular Input Line Entry System
SOA	Secondary Organic Aerosol
SRH	Separation Relative Humidity
SVOC	Semi-Volatile Organic Compound
UNIFAC	Universal quasi-chemical Functional groups Activity Coefficients
VOC	Volatile Organic Compound
XGB	eXtreme Gradient Boosted descent
X-UNIFAC	Extended UNIFAC

List of mathematical symbols used in this work and their meanings.

Symbol	**Meaning**	**Units**
A	Area of the surface	m^2
$\mathscr{A}_i$	Partial molar area of i	$\mathrm{m}^2\,\mathrm{mol}^{-1}$
a_i	Chemical activity of i	[-]
A^{SL}	Szyszkowski–Langmuir fit parameter	$\mathrm{J}\,\mathrm{m}^{-2}$
B^{SL}	Szyszkowski–Langmuir fit parameter	$\mathrm{mol}\,\mathrm{m}^{-3}$
C^{SL}	Bulk concentration in Szyszkowski–Langmuir model	$[\mathrm{mol}\,\mathrm{m}^{-3}]$
D	Diameter of a particle or droplet	m
G	Gibbs energy	J
M	Molar mass of a compound	$\mathrm{kg}\,\mathrm{mol}^{-1}$
n_i	Number of moles of i	mol
P	Pressure	Pa
R	Universal gas constant	$\mathrm{J}\,\mathrm{mol}^{-1}\,\mathrm{K}^{-1}$
S	Entropy or saturation ratio	$\mathrm{J}\,\mathrm{K}^{-1}$ or [-]
SS	Supersaturation	%
T	Temperature	K
U	Internal energy	J
V	System volume	m^3
$\mathscr{V}_i$	Molar volume of i	$\mathrm{m}^3\,\mathrm{mol}^{-1}$
x_i	Mole fraction of i	[-]
Γ	Gibbs surface excess	$\mathrm{mol}\,\mathrm{m}^{-2}$
γ_i	Activity coefficient of i	[-]
δ	Thickness of Guggenheim surface phase	m
ε_i	Fraction of i in the surface phase	[-]
κ	Hygroscopicity parameter	[-]
μ_i	Chemical potential of i	$\mathrm{J}\,\mathrm{mol}^{-1}$
ρ_i	Density of i	$\mathrm{kg}\,\mathrm{m}^{-3}$
σ_i	Surface tension of i	$\mathrm{J}\,\mathrm{m}^{-2}$
τ	Line energy at a three-phase boundary	$\mathrm{J}\,\mathrm{m}^{-1}$

List of superscripts and subscripts used in this work and their meanings.

Symbol	**Meaning**
b	Bulk phase
c	Thermodynamic critical point
CF	Compressed film model
$calc$	Calculated value
$crit$	CCN critical activation property
dry	Dry particle (RH ¡ 1%)
el	Inorganic electrolyte species
G	Gas phase property
i	Chemical component or species index
max	Maximum
min	Minimum
np	Non-partitioning case
pm	Particle phase
SL	Szyszkowski–Langmuir model
s	Surface phase
tot	Total
w	Water
wet	Wet particle (RH 1%)
α	Inorganics-rich phase
β	Organics-rich phase
ϕ	Phase index
$\star$	Unnormalized
$\circ$	Standard or reference state

Part I

Introduction

1

Background and Relevant Literature

1.1 Atmospheric Aerosols

Aerosols are a type of colloidal system made up of condensed-phase particles or droplets and the gas that surrounds them. Atmospheric aerosols are aerosols in which the surrounding gas phase is the ambient air. Throughout this work, the term "aerosol" will be used to refer to atmospheric aerosol particles. Such atmospheric aerosols are found in all regions of the Earth, with variations both spatially and temporally (Kaufman et al., 2002). Although their concentrations are highest in the lower troposphere near emission sources, aerosols are also vertically distributed from ground level to the stratosphere (Gras, 1991; Gupta et al., 2021).

The size, composition, and location of aerosols can impact the interactions that a group of particles can have with the global climate system. The interactions between aerosols, clouds, and the climate are poorly constrained, as aerosols can exert both direct and indirect effects on the climate (Seinfeld et al., 2016; Boucher et al., 2013). Aerosols can both reflect and absorb light directly, as a function of their composition, altitude in the atmosphere, and structure (Andreae and Gelencsér, 2006; Quinn et al., 2008). In addition, atmospheric aerosols may act as cloud condensation nuclei (CCN) to form liquid cloud droplets or as ice nucleation particles (INP) to form solid ice crystals in the atmosphere. The number and size of cloud droplets and ice particles indirectly impact the climate system by increasing or decreasing cloud properties such as albedo, lifetime, and precipitation efficiency

(Twomey, 1974; Albrecht, 1989). Both the direct and indirect climate effects of atmospheric aerosols are governed by the microphysical properties of individual aerosol particles. There are a variety of ways by which aerosols are classified. The simplest method, often used by regulatory agencies, involves classifying particles by their size, where particles with spherical equivalent diameters less than 2.5 μm are classified as fine, and particles with spherical equivalent diameters greater than 2.5 μm as coarse. Coarse particles are typically formed through mechanical actions such as sea spray, dust storms, and pollen emissions. Such coarse particles have high inertia and short atmospheric lifetimes, making them less relevant for both human health and climate change. Fine aerosols can form through direct emission or through secondary processes, such as the photo-oxidation and subsequent condensation of gas-phase organic compounds, in the atmosphere.

Within the ultrafine regime of aerosols, there are distinct peaks in the log-normalized number concentration as a function of particle diameter. These peaks are also called "modes" by aerosol scientists. The mode corresponding to the smallest aerosols is the nucleation mode. Particles in this mode typically have spherical equivalent diameters of 1 nm to 20 nm. These particles form when molecules of a single compound, i, are saturated in an environment and begin to cluster. A new particle will form if a molecular cluster of i grows and overcomes the energetic penalty for growth, known as the nucleation barrier (Abraham and Zettlemoyer, 1974):

$$\Delta G = -\frac{4}{3} r_p^3 \frac{RT}{\mathscr{V}_i} \ln S + 4\pi r_p^2 \sigma_i^\circ \tag{1.1}$$

In the above equation, ΔG is the change in Gibbs energy, r_p is the radius of the molecular cluster or particle, R is the gas constant, T is temperature, $\mathscr{V}_i$ is the molar volume of i, S is the saturation ratio with respect to i, and σ_i° is the surface tension of i. If a system is supersaturated with respect to i, then the first term will always be less than 0; however, the second term cannot be neglected in cases of extremely small molecular clusters and may

lead to ΔG becoming greater than 0, despite $S > 1$. The particle radius at which the penalty of high surface energy is exceeded by the energy freed from gas-to-particle partitioning is known as the critical radius and is the location of the aforementioned nucleation barrier. Clusters of molecules that do not reach this critical size will eventually evaporate back into the gas phase, while those that grow to this critical radius will continue to grow into larger particles.

Aerosols with diameters between 20 nm and 100 nm fall into the Aitken mode. These particles grow in a similar manner to the previously mentioned nucleation mode particles. However, unlike nucleation mode particles, Aitken mode particles grow primarily through the heterogeneous condensation of many different gas-phase compounds onto an existing particle. This is in contrast to the homogeneous nucleation of one dominant gas-phase compound that drives the formation of nucleation mode particles. Particles in the Aitken mode have relatively short lifetimes, as once they reach sufficient sizes, collision and coagulation processes begin to quickly increase particle sizes while decreasing their number concentration (Hinds, 1982).

Should multiple Aitken mode particles collide and coagulate into a single particle, the new particle may enter the accumulation size mode. Aerosols in the accumulation mode typically have spherical equivalent diameters between 100 nm and 1000 nm. Accumulation mode particles can also be directly emitted through processes such as the release of soot particles from incomplete combustion (Andrew Gray and Cass, 1998). Particles that grow larger than the accumulation mode may activate into cloud droplets or be removed by gravitational settling. Because the rates of formation and removal are comparable for particles in this size mode, aerosols in the accumulation mode have high number concentrations (Guevara, 2016; Hinds, 1982).

1.1.1 Aerosol Composition

The composition of aerosol particles varies based on their location (Hallquist et al., 2009; Zhang et al., 2007; Kaufman et al., 2002) and formation mech-

anism (Jimenez et al., 2009; Hallquist et al., 2009). Broadly, aerosols are composed of inorganic and organic species. Inorganic compounds in aerosols include water, electrolyte species, and inorganic carbon. Water is ubiquitous in the atmosphere and may be found in aqueous aerosols from the condensation of water vapor or from direct emissions, such as sea spray (Thomas et al., 2022).

There are many inorganic electrolytes found in aerosols. Common inorganic cations include sodium (Na^+), ammonium ($NH_4{}^+$), calcium (Ca^{2+}), potassium (K^+), and magnesium (Mg^{2+}) (Seinfeld and Pandis, 2006; Johnston and Wexler, 1995). These cations may come from different sources. For example, sodium is typically emitted from sea spray, whereas ammonium forms from heterogeneous acid-base reactions when gas-phase ammonia (NH_3) emitted by agricultural activities partitions into aqueous particles (Nair and Yu, 2020). Calcium, potassium, and magnesium may all be emitted from mineral dust.

Inorganic anions of importance include sulfate ($SO_4{}^{2-}$), bisulfate ($HSO_4{}^-$), chloride (Cl^-), and nitrate ($NO_3{}^-$) (Seinfeld and Pandis, 2006). Sulfates and bisulfates can be emitted naturally through processes such as volcanic eruptions or form from photochemical oxidation of sulfur dioxide emitted from fossil fuel combustion or dimethyl sulfide emitted by the oceans (Andreae et al., 1985; Seinfeld and Pandis, 2006). Nitrates typically form through photochemical reactions that lead to the oxidation of reactive nitrogen oxides (NO_x) (Weng et al., 2020).

Inorganic carbon includes elemental carbon, carbonate ions ($CO_3{}^{2-}$), and methane sulfonic acid (CH_3SO_3H). Elemental carbon is primarily emitted from a variety of sources such as soot from combustion processes (Xu et al., 2021). Carbonate ions form from the partitioning of carbon dioxide into aqueous particles (Yin et al., 2022). Methane sulfonic acid is principally formed by the oxidation of dimethyl sulfide (Andreae et al., 1985). Other inorganic compounds found in aerosol particles include heavy metals such

as mercury (Hg), which can be emitted through volcanic eruption, mining, fossil fuel combustion, or other heavy industries (Ariya et al., 2015).

Much like their inorganic counterparts, organic aerosol (OA) compounds can be anthropogenic or naturally emitted. Anthropogenic sources of organic compounds include heavy industry and incomplete combustion (Lund et al., 2023). Natural sources of organic compounds include cellular respiration and photosynthesis (Weng et al., 2020). Many organic compounds that are found in aerosols are not directly emitted; rather, they undergo secondary photochemical reactions before partitioning into the particle phase. Organic particles that contain the products of secondary chemistry are known as secondary organic aerosol (SOA) particles, while those containing compounds that are directly emitted in the particle phase without undergoing additional chemical reactions are known as primary organic aerosol (POA) particles. It is important to note that an individual aerosol particle may contain a mixture of both POA compounds and SOA compounds (Mahrt et al., 2022).

The secondary atmospheric processes that lead to the formation of SOA can include processes such as photo-oxidation and subsequent reduction in volatility of gas-phase volatile organic compounds (VOCs). Reduced-volatility organic compounds include semi-volatile organic compounds, intermediate-volatility organic compounds, low-volatility organic compounds, and extremely low-volatility organic compounds (SVOCs, IVOCs, LVOCs, and ELVOCs respectively). ELVOCs can nucleate to form new particles as mentioned above, while SVOCs, IVOCs, and LVOCs can only condense onto pre-existing particles in the Aitken or accumulation modes. Because of the complexity of the chemical reactions in the atmosphere, up to 20% of SOA compounds in the particle phase have been characterized at the molecular structure level (Chen et al., 2020). Furthermore, both POA and SOA may be further mixed with the inorganic species mentioned above.

These mixtures may be external, where different particles in a population have different compositions, or internal, where a single particle contains

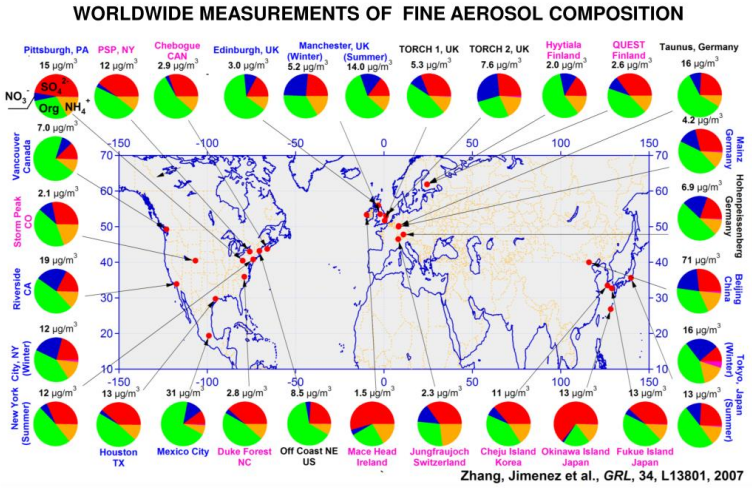

Figure 1.1: Pie charts show the average mass concentration and chemical composition of fine aerosol particles: organics (green), sulfate (red), nitrate (blue), ammonium (orange), and chloride (purple), as measured by an aerosol mass spectrometer. Figure reproduced with permission from Zhang et al. (2007).

a combination of inorganic and organic species. The interactions between water, secondary and primary organic species, and inorganic electrolytes lead to atmospheric aerosols becoming highly complex matrices of different compounds that may adopt complex morphologies and mixing states. Figure 1.1 (reproduced with permission from Zhang et al. (2007)) shows the relative contributions of organic species and specific inorganic species as measured by aerosol mass spectrometers at different monitoring sites around the world.

1.1.2 Aerosol Morphologies and Mixing States

In the previous section, the complexities of aerosol composition were discussed. Because organic compounds and inorganic compounds may not always have favorable energetic interactions, a single well-mixed aerosol containing organic and inorganic compounds may undergo a phenomenon known as liquid–liquid phase separation (LLPS). The result of LLPS is the formation of two or more distinct condensed phases coexisting inside a single particle.

Liquid–liquid phase separation in aerosol systems occurs through one of three mechanisms: nucleation and growth, spinodal decomposition, or growth of a new phase from the surface. Which mechanism occurs depends on where the system is (initially) located in the phase diagram. The first mechanism, nucleation and growth, occurs when a particle's composition state enters a region of its phase diagram in which a single homogeneous phase becomes thermodynamically metastable (Zuend et al., 2010). Small stable nuclei of a new phase may form which then grow over time as the surrounding material diffuses toward them. This process is typically observed when the system is in the metastable region. In order for phase separation to occur in this region, an energy barrier must be overcome. The second mechanism by which LLPS can take place, spinodal decomposition, occurs when a particle enters into a region where the homogeneous phase becomes unstable as the energy barrier to form a new phase vanishes completely, known as the spinodal region. In the spinodal region, there is no energy barrier for phase separation. Rather, small fluctuations in composition grow spontaneously throughout the system,

leading to the formation of different phases. The key difference between the mechanisms lies in the nature of the initial phase separation: nucleation and growth involve a discrete, localized initiation of phase separation, while spinodal decomposition involves a continuous, system-wide separation process. The final mechanism involves an increasingly distinct surface forming, which eventually overcomes the energetic penalty to form a complete phase leading to LLPS (Song et al., 2012).

Such phase-separated particles can exist in multiple geometric morphologies. The simplest phase-separated morphology is that of a particle with two distinct phases in a radially symmetric "core–shell" configuration. Typically, the inorganic-rich aqueous phase, α, is the "core" and the lower polarity organic-rich phase, β, forms the "shell" enveloping it (Reid et al., 2011). A slightly more complex configuration is known as partially-engulfing and occurs when the inner core of the particle is only partially covered by a lens of phase β (Kwamena et al., 2010; Reid et al., 2011; Ciobanu et al., 2009; Song et al., 2012, 2013; Shiraiwa et al., 2013). Such a configuration may occur even if there is sufficient material in phase β to completely cover phase α (Kwamena et al., 2010). Graphical depictions of core-shell and partially-engulfed particles are shown in Fig. 1.2 (reproduced with permission from Gorkowski et al. (2020)). More geometrically complex configurations of two-phase particles have also been identified (Kucinski et al., 2019). These three-dimensional configurations may be further complicated by the presence of additional phases. Particles with three or more liquid phases may display combinations of spherical core-shell configurations, partially-engulfed, or other configurations (Huang et al., 2021; Kucinski et al., 2019). Additionally, should the concentration of inorganic electrolytes be sufficiently high in an aerosol particle (reaching a critical ion activity product), they may crystallize out to form an additional solid phase.

The presence of LLPS has important implications for aerosols. Concentrations of species differ across different phases, which may lead to different

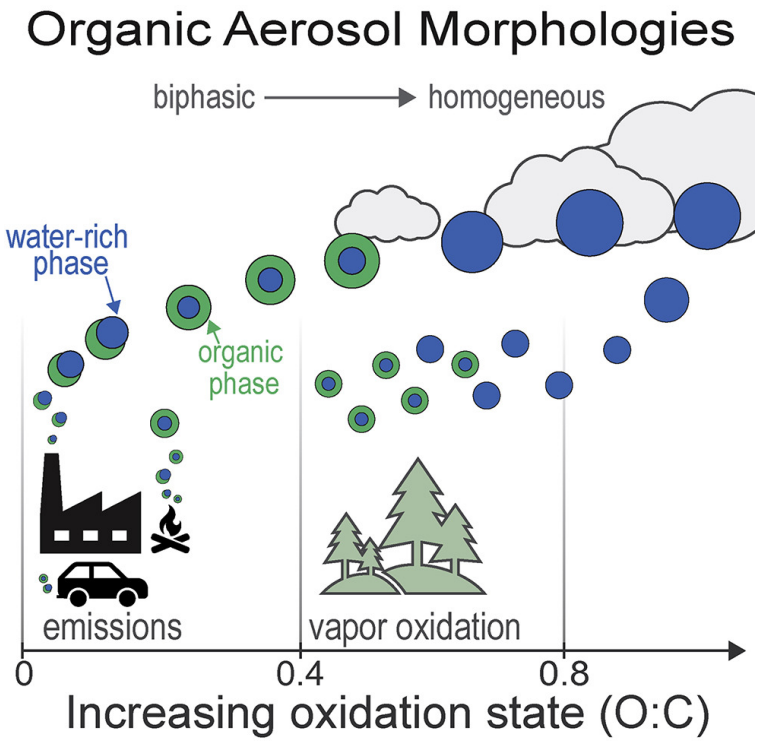

Figure 1.2: LLPS aerosols may exhibit "core-shell" structure where an organics-rich phase β completely encapsulates an aqueous phase α or "partially-engulfed" structure where phase β forms a semi-spherical lens on phase α. Figure reproduced with permission from Gorkowski et al. (2020).

heterogeneous chemistry occurring in phase α than in phase β. Likewise, the physical properties of individual phases may differ. One such example can be found in the viscosity of the different phases, where phase α may have substantially lower viscosity than phase β, which may exhibit a glass-like viscosity (Lilek and Zuend, 2022; Gervasi et al., 2020; Slade et al., 2019; Reid et al., 2018). Such differences in viscosity can lead to limitations in the reactive uptake of compounds, including isoprene epoxydiols (IEPOX) (Schmedding et al., 2019, 2020). Such glassy phases may also serve as effective ice nucleation sites under freezing conditions (Wagner et al., 2012; Wilson et al., 2012; Schill and Tolbert, 2013). Phase-separated aerosols may also have different interactions with incoming and outgoing radiation, thus impacting the Earth's energy balance. It is believed that under certain conditions, like a soot particle surrounded by an organic shell, a phase-separated aerosol may have a so-called lensing effect, which causes it to magnify radiation absorption (Lang-Yona et al., 2010). Likewise, the enrichment of elemental and organic carbon on the exterior of phase-separated compounds may impact the amount of radiation those particles absorb (Fard et al., 2018).

1.1.3 Aerosol-Cloud-Climate Interactions

In addition to absorbing sunlight, aerosols can also scatter incoming or outgoing radiation. This is known as the aerosol direct effect on the global climate system. The direct radiative effect of aerosols depends on their optical properties, which vary with their chemical composition and size. For example, aerosols containing primarily inorganic sulfate scatter incoming solar radiation, leading to an overall cooling effect (Quinn et al., 2008). In contrast, elemental carbon and many forms of organic carbon absorb solar radiation, contributing to a warming effect (Andreae and Gelencsér, 2006).

Beyond their direct effects on the climate system, aerosols can also indirectly impact the climate through their interactions with clouds. A subset of aerosols act as cloud condensation nuclei (CCN), around which water vapor condenses to form cloud droplets. The efficiency by which a particle acts

as a CCN is determined by its composition and size. These effects can be demonstrated by the Köhler equation (Köhler, 1936):

$$S = a_w \exp\left(\frac{4\sigma M_w}{RT\rho_w D_p}\right). \tag{1.2}$$

In the above equation, S is the droplet's equilibrium saturation ratio of water vapor, a_w is the chemical activity of water in a droplet, σ is the droplet surface tension, M_w is the molar mass of water, ρ_w is the density of water, and D_p is the particle diameter. Particles containing compounds that readily take up water vapor undergo hygroscopic growth and increase in diameter. Hygroscopic compounds are typically inorganic electrolytes and highly polar organic compounds such as dicarboxylic acids and sugars (Zhang et al., 2021; Pöhlker et al., 2023). However, dissolved inorganic ions typically raise the surface tension of the particle, which increases the influence of the exponential term in the above equation. Other compounds, which are usually more hydrophobic, may not readily take up water vapor, but instead have low pure-component tensions and thus reduce a CCN's effective surface tension, σ.

Much like Eq. (1.1), there is a maximum in S, S_{crit}, as determined by Eq. (1.2). Should the ambient saturation ratio be less than the maximum of S in Eq. (1.2) for a given particle, said particle will grow to the value of D_p corresponding to the ambient saturation ratio and will not become a cloud droplet. If the ambient saturation ratio is larger than S_{crit}, then the particle will continue to grow into a cloud droplet until it is removed by precipitation or evaporation due to entrainment of warmer or drier air in the cloud. As mentioned above, there are competing effects of aerosol composition on Eq. (1.2). Increases in hygroscopic compounds will increase water uptake and increase the water content of a particle at a given RH. Surface tension-reducing compounds will reduce the energetic penalty for expanding a highly curved surface, such as that of a CCN, despite reducing the amount of water that an individual particle will take up at a given RH

level. Figure 1.3 (reproduced from Davies et al. (2019) under a Creative Commons Attribution 4.0 License) shows an example of a Köhler curve for a 50 nm ammonium sulfate particle amnd the effects of reducing σ using various parameterizations on a Köhler curve.

To simplify calculations of aerosol water uptake and CCN activation, Petters and Kreidenweis (2007) introduced a single-parameter model of hygroscopic growth, known as κ-Köhler theory, in which a_w is related to the current volume of water in the particle, V_w, and the initial dry particle (solute) volume, V_{dry}, as follows:

$$\frac{1}{a_w} = 1 + \kappa \frac{V_{dry}}{V_w}. \tag{1.3}$$

The κ value for a multicomponent solution can be determined by a volume-fraction-based linear weighting of the κ values of the individual components. By combining Eqs. (1.2) and (1.3) with an assumption about σ, critical supersaturations of aerosol particles can be calculated given their composition and dry size (Petters and Kreidenweis, 2007). However, the applicability of κ-Köhler theory to ultrafine particles may be more limited (Topping et al., 2016). Indeed, κ in Eq. (1.3) assumes a constant σ in its calculation without any sort of surface effects on water uptake. Measurement derived κ values may assume $\sigma = \sigma_w$ even if that is not the case and thus may be inaccurate.

The availability of CCN influences cloud droplet number concentration (CDNC), which in turn affects cloud albedo and lifetime. High concentrations of aerosols generally lead to more numerous and on average smaller cloud droplets, assuming the total cloud liquid water content remains constant. This increases cloud albedo. This is known as the first aerosol indirect effect, or Twomey effect (Twomey, 1974). Smaller droplets are also less efficient at coalescing into larger drops and possibly drizzle or rain drops, typically leading to longer-lived clouds, which is referred to as the second indirect effect, or the Albrecht effect (Albrecht, 1989).

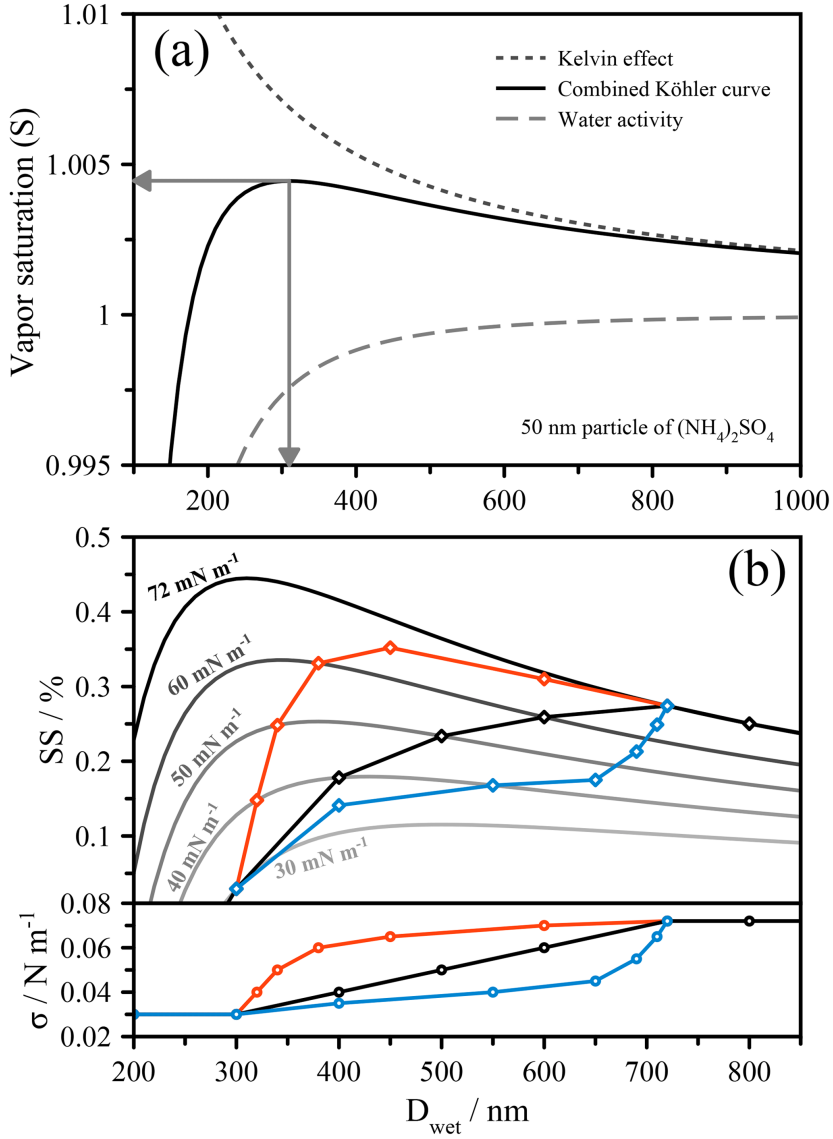

Figure 1.3: (A) an example of a Köhler curve for a 50 nm dry-diameter ammonium sulfate particle. (B) the impact of reducting surface tension on a Köhler curve. Figure reproduced from Davies et al. (2019) under a Creative Commons Attribution 4.0 License.

Aerosols may interact with clouds beyond forming liquid cloud droplets, as they may also serve as nucleation sites for ice crystal growth. However, an aerosol that serves as an efficient CCN may not be an efficient INP and vice versa (Kanji et al., 2017). Indeed, the mechanisms by which ice crystals form in the atmosphere are different from those by which cloud droplets form, as liquid water does not spontaneously freeze when the ambient temperature is below 273 K. Said spontaneous freezing only occurs when the ambient temperature is much lower (around 237 K (Matsumoto et al., 2002)). Thus, ice nucleating particles are necessary to initiate the formation of ice in supercooled droplets in the atmosphere. The following is a brief summary of the mechanisms by which an aerosol particle may serve as an INP. The primary mechanisms for ice nucleation are deposition nucleation, immersion freezing, contact freezing, and condensation freezing. In deposition nucleation, ice forms directly on the surface of an aerosol particle directly from the vapor phase. This occurs when humid air is supersaturated with respect to ice and the temperature is sufficiently low. Immersion freezing occurs when an aerosol particle is already immersed in a supercooled liquid droplet and induces ice formation within the droplet as the temperature drops below a particle-dependent threshold. Contact freezing involves an aerosol particle initiating ice formation upon contacting a supercooled droplet from the exterior. Condensation freezing is a process where water vapor first condenses onto an aerosol particle, forming a liquid droplet that then freezes as the temperature continues to decrease. Each of these mechanisms depends on the specific properties of the aerosol particle, such as its composition, surface characteristics, and size, as well as the environmental conditions, including temperature and supersaturation levels (Kanji et al., 2017).

As previously mentioned, the interactions between aerosols, clouds, and the climate are highly complex and warrant further study. Indeed, they are one of the largest sources of uncertainty in global climate models (Boucher et al., 2013; Seinfeld et al., 2016). Many of these impacts on cloud formation

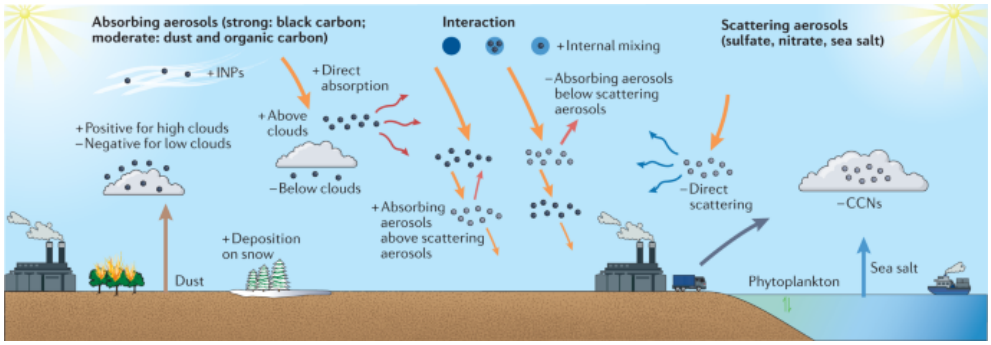

Figure 1.4: A summary of the direct and indirect effects of atmospheric aerosols and their interactions with the global climate system. Figure reproduced with permission from Li et al. (2022)

.

are governed by fundamental thermodynamic principles and thus require accurate models of aerosol thermodynamic properties to better understand them.

1.2 Modeling Aerosol Thermodynamics

1.2.1 Activity Coefficients and Non-Ideal Mixing

In classical thermodynamics, the Gibbs energy of a well-mixed aerosol system, including the gas phase, can be represented by the following equation:

$$G = TS + PV + \sum_i \mu_i n_i. \tag{1.4}$$

where T is temperature (K), S is entropy ($\mathrm{J\,K^{-1}}$), P is pressure ($\mathrm{J\,m^{-3}}$ or Pa), V is volume ($\mathrm{m^3}$), n_i is moles of component i, and μ_i is the chemical potential of species i ($\mathrm{J\,mol^{-1}}$). Many SOA particles are not simple mixtures of ideally behaved organic compounds; they may also contain species such as water and inorganic electrolytes. The inclusion of aqueous inorganic compounds mixed with organic species leads to stronger deviations from ideality in the mixing behavior of these SOA species. These deviations from ideality lead to modifications in the gas-particle partitioning of water and organic species through modified Raoult's Law:

$$\frac{P_i}{P_i^\circ} = x_i \gamma_i \tag{1.5}$$

where P_i is the partial pressure of species i in the gas phase, P_i° is the saturation vapor pressure of (pure) species i, x_i is the mole fraction of i in the condensed phase, and γ_i is the mole-fraction-based activity coefficient of i in the liquid phase. The energetic contributions of non-ideal mixing in a single homogeneously mixed particle can be expressed as a component of the chemical potential:

$$\mu_i = \mu_i^\circ + RT \ln(x_i \gamma_i) \tag{1.6}$$

where μ_i° is the reference state chemical potential R is the gas constant, and T is the temperature. The product of the mole fraction and the concentration-dependent activity coefficient is known as the chemical ac-

tivity and can be thought of as the effective concentration of i in a given phase. In more extreme cases, non-ideal mixing can lead a homogeneously mixed aerosol of organics and inorganics to split into an inorganic-rich phase (α) and an organics-rich phase (β). More than two distinct phases have also been observed, where phase β may split into higher and lower polarity-rich organic phases (Huang et al., 2021). In the event of phase separation, the Gibbs energy now becomes:

$$G = TS + PV + \sum_{\phi} \sum_{i} n_i^{\phi} \mu_i^{\phi} \tag{1.7}$$

where ϕ is the phase index. In the event of phase separation, the chemical activity or effective concentration for each species must be equal across distinct phases. For example the effective concentration of water must be the same across phases. The effective concentration of a solute must also be equal for that solute across all phases but it may differ from the effective concentration of water and so on.

1.2.2 The Aerosol Inorganic–Organic Mixtures Functional groups Activity Coefficients model

Accurate values of the activity coefficient for each species present in a particle are critical in order to fully represent the chemical mixing thermodynamics of a particle. There are past models that have been used for non-aerosol systems, including the UNIversal quasi-chemical Functional Groups Activity Coefficients (UNIFAC) model (Fredenslund et al., 1975; Hansen et al., 1991). The UNIFAC model predicts the activity coefficients of non-electrolyte compounds in a solution through a functional group contribution approach. Functional groups are individual components of a molecule, for example, a hydroxyl group (OH) or a methyl group (CH_3). Thus, instead of a solution of molecules, the UNIFAC method treats a system as a "solution of groups" (Fredenslund et al., 1975). The following is a brief summary of

the UNIFAC method for predicting activity coefficients. The activity coefficient of a species in a solution is assumed to be a combination of a residual contribution (γ_i^{R}) and a combinatorial contribution (γ_i^{C}).

Beginning with γ_i^{C},the combinatorial term is calculated by first computing the overall surface areas (q_i) and volumes (r_i) of each molecule present in a solution from the molecule's functional groups:

$$q_i = \sum_i Q_k n_i^{\mathrm{k}} \tag{1.8}$$

and

$$r_i = \sum_i R_k n_i^{\mathrm{k}} \tag{1.9}$$

From the absolute surface areas and volumes, the mole-fraction-weighted averages of both q_i and r_i are calculated:

$$\theta_i = \frac{x_i q_i}{\sum_j x_j q_j} \tag{1.10}$$

and

$$\phi_i = \frac{x_i r_i}{\sum_j x_j r_j}, \tag{1.11}$$

where θ_i is the mole-fraction-weighted average surface area of i and ϕ_i is the mole fraction weighted average of volume of i. The equation for the combinatorial term can then be defined as follows:

$$\ln \gamma_i^{\mathrm{C}} = \ln \frac{\phi_i}{x_i} + \frac{z}{2} q_i \ln \frac{\theta_i}{\phi_i} + L_i - \frac{\phi_i}{x_i} \sum_j x_j L_j. \tag{1.12}$$

Note that there are two additional variables in the above equation, z and L_i. z is the coordination number of i and is assumed to be 10. L_i is defined as follows below:

$$L_i = \frac{z}{2}(r_i - q_i) - (r_i - 1). \tag{1.13}$$

In order to calculate the residual contribution, the surface area of each functional group, k, (Q_k) present is calculated. Because the UNIFAC method relies on the so-called solution of groups approach, the fraction of each group k relative to the total number of functional groups across all species, j, must be calculated:

$$X_k = \frac{\sum_i x_i n_i^k}{\sum_m \sum_j x_j n_j^m}. \tag{1.14}$$

The normalized surface area of each functional group (Θ_k) relative to the total number of functional groups (summing over group index m) is then calculated as follows:

$$\Theta_k = \frac{X_k Q_k}{\sum_m X_m Q_m}. \tag{1.15}$$

The values of Q_k and Θ_k are used along with an additional term, $\Psi_{k,m}$. $\Psi_{k,m}$ is calculated as follows:

$$\Psi_{k,m} = \exp\left(\frac{-a_{k,m}}{T}\right) \tag{1.16}$$

where $a_{k,m}$ is the interaction energy between k and other functional groups (here m). The final equation for the residual term of a non-electrolyte activity coefficient thus becomes

$$\ln \gamma_i^{\mathrm{R}} = \sum_k n_i^{\mathrm{k}} \left(\ln \Gamma_k - \ln \Gamma_k^{(i)} \right), \tag{1.17}$$

where Γ_k is calculated as follows:

$$\ln \Gamma_k = Q_k \left(1 - \ln \sum_m \Theta_m \Psi_{m,k} - \sum_m \frac{\Theta_m \Psi_{k,m}}{\sum_n \Theta_n \Psi_{n,m}} \right). \tag{1.18}$$

$\Gamma_k^{(i)}$ is a reference value, calculated using Eq. (1.14) through Eq. (1.18) in the case of a pure solution of i where the mole fraction of i, x_i, is 1. It is important to emphasize that while the UNIFAC method is useful in many situations, it does have limitations. Indeed, because the UNIFAC method does not account for the presence of inorganic electrolyte interactions, it is not useful

in situations where said species may be present, such as aerosol particles. Past approaches to predicting the activities of compounds in aerosol systems have included extensions of the Brunauer–Emmett–Teller and and Guggenheim–Anderson–de Boer adsorption isotherms to higher solute concentrations (Dutcher et al., 2011). Others have included the Extended Aerosol Inorganics Model (E-AIM) Project (Wexler and Clegg, 2002), the extended UNIFAC (X-UNIFAC) model (Erdakos et al., 2006), and the LIFAC model (Yan et al., 1999). the UNIFAC approach in combination with the LIFAC model was extended to account for inorganic–organic interactions in the Aerosol Inorganic–Organic Mixtures Functional groups Activity Coefficients (AIOMFAC) model (Zuend et al., 2008, 2011).

The AIOMFAC model calculates activity coefficients as the combination of a short-range contribution (γ_i^{SR}), based on the UNIFAC method described in the preceding paragraphs; a medium-range contribution (γ_i^{MR}); and a long-range contribution (γ_i^{LR}); such that the AIOMFAC-predicted activity coefficient for neutral species is computed as

$$\ln \gamma_i = \ln \gamma_i^{\mathrm{SR}} + \ln \gamma_i^{\mathrm{MR}} + \ln \gamma_i^{\mathrm{LR}}. \tag{1.19}$$

γ_i^{LR} accounts for the ionic strength of inorganic electrolytes in the solvent, and γ_i^{MR} accounts for cation–anion interactions, ion–dipole interactions, and ion-induced dipole interactions. In the case of anion and cation electrolyte species, the AIOMFAC-predicted molality-based activity coefficient ($\gamma_i^{(\mathrm{m})}$) is calculated as follows:

$$\begin{aligned} \ln \gamma_i^{(\mathrm{m})} = &\left(\ln \gamma_i^{\mathrm{SR},(\mathrm{x}),\infty} + \ln \gamma_i^{\mathrm{MR},(\mathrm{x}),\infty} + \ln \gamma_i^{\mathrm{LR},(\mathrm{x}),\infty} \right) \\ &- \ln \left(\frac{M_w}{\sum_{s\prime} x'_s M_s} + M_w \sum_j m_j \right). \end{aligned} \tag{1.20}$$

In Eq. (1.20), $\gamma_i^{\mathrm{SR},(\mathrm{x}),\infty}$, $\gamma_i^{\mathrm{MR},(\mathrm{x}),\infty}$, and $\gamma_i^{\mathrm{LR},(\mathrm{x}),\infty}$ are the mole-fraction-based

short range, medium range and long range activity coefficient contributions with respect to an infinite dilution reference state in pure water for an ion. x'_s is the electrolyte-free mole fraction of each neutral solvent component in the solution and m_j is the molality of ion j. This final term on the right side converts the electrolyte activity coefficients from mole-fraction-based to molality-based. The specific derivations for the calculations of $\ln \gamma_i^{\mathrm{MR}}$, $\ln \gamma_i^{\mathrm{LR}}$, $\gamma_i^{\mathrm{SR,(x),\infty}}$, $\gamma_i^{\mathrm{MR,(x),\infty}}$, and $\gamma_i^{\mathrm{LR,(x),\infty}}$ in mixed inorganic–organic systems are too lengthy to fully describe here and can be found in Zuend et al. (2008).

The AIOMFAC model has been extended multiple times to account for atmospherically relevant organic functional groups and inorganic electrolytes (Zuend et al., 2011; Ganbavale et al., 2015; Yin et al., 2022). The AIOMFAC model can predict activity coefficients over an extremely high range of concentrations for species. This is a critical feature, as mixed inorganic-organic aerosol particles equilibrated to environmental conditions at low relative humidities may exhibit extremely high solute concentrations. Similarly, the AIOMFAC model is capable of predicting activity coefficients in the highly dilute, water-vapor-supersaturated regime of relative humidities, which is critical for modeling cloud droplet activation properties. The approach used by the AIOMFAC model is also thermodynamically consistent, such that it always obeys the Gibbs–Duhem relation. A consequence of this relation is that given the concentrations and activity coefficients of all species except for one, the activity coefficient of the remaining species can be calculated from the others without computing it directly (Matthews, 2000).

1.2.3 Surface Thermodynamics

It should be noted that Eq. (1.7) neglects an often forgotten additional term that is present in multi-phase systems. At the boundary between two distinct phases, there exists an energetic penalty, σ. In the case of a gas–liquid phase boundary, also referred to as a surface throughout this work, σ is commonly referred to as the surface tension. Correspondingly, at a liquid–liquid boundary, σ is commonly referred to as the interfacial tension. Note

that throughout the remainder of this work, surface will exclusively refer to a gas–liquid phase boundary and interface will refer to a liquid–liquid phase boundary. Thus, with the inclusion of surface and interfacial tensions, a more complete expression for G, which accounts for said penalties is as follows:

$$G = TS + PV + \sum_{\phi} \sum_{i} \mu_i^{\phi} n_i^{\phi} + \sum_{\iota} \sigma^{\iota} A^{\iota} + l\tau. \tag{1.21}$$

σ^{ι} represents the energetic penalty at interface ι ($\mathrm{J\,m^{-2}}$), A^{ι} is the area of interface iota ($\mathrm{m^2}$), l is the energetic penalty at a three-phase junction line ($\mathrm{J\,m^{-1}}$) and τ is the length of the three phase junction line (m). The net energetic contribution of $l\tau$, should a three phase line occur in a system, is thought to be several orders of magnitude lower than the contribution of $\sum_{\iota} \sigma^{\iota} A^{\iota}$ (Amirfazli and Neumann, 2004).

In macroscopic systems, the energetic contribution of $\sum_{\iota} \sigma^{\iota} A^{\iota}$ is assumed to be negligible; however, in systems with high surface (and interfacial) area to volume ratios, such a term warrants further exploration. The following sections will introduce and summarize existing research on the role of surface and interfacial tensions on atmospheric aerosols.

1.3 Aerosol Surface Properties

Given that the surface area of an individual spherical (aqueous) aerosol particle will always be larger than any interfacial areas present within the particle, the role of aerosol surface properties will be explored first. The surface area-to-volume ratio of a sphere scales inversely with its radius, making this ratio particularly significant for ultrafine particles. Assuming that the surface of a particle is represented by a monolayer of molecules in contact with the gas phase—an assumption that is further explored in this thesis—spherical particles with diameters smaller than 100 nm will have a substantial proportion of their molecules present at the surface. For instance, in a pure water droplet with a diameter of 50 nm, approximately 4% of the water molecules will be found in the surface monolayer, while in a droplet with a diameter of 3 nm, more than half of the water molecules will reside at the surface.

As mentioned in section 1.1, aerosol particles do not consist of single pure compounds; rather, they are complex mixtures of organic compounds, water, and inorganic species. Different species may exhibit different effects on the surface of a solution. Compounds that reduce the surface tension from the pure solvent (typically, although not always, water in the case of aerosol particles or cloud droplets) are often referred to as "surface-active" compounds or more commonly "surfactants." Likewise, compounds that raise the surface tension above that of the pure solvent are often called "tensoions." It is thought that surfactants may exhibit more favorable interactions in a surface monolayer than in the interior bulk phase of a solution. This is likely due to the fact that surfactants have both more and less polar regions in their molecular structure. In a surface monolayer, such non-polar regions may point towards the gas phase while polar regions of the molecule are oriented towards the solvent in the bulk phase. The inverse is likely true for tensoionic species, which are highly polar and thus prefer to remain completely solvated in the aqueous bulk of a droplet.

These differences in molecular properties lead to a phenomenon known as

bulk–surface partitioning, wherein the composition of the surface layer of a species is different from that of the underlying bulk as surfactants partition from the bulk to the surface and tensoions partition from the surface to the bulk. The exact size (or thickness) of the surface layer is a matter of ongoing debate (Davies et al., 2019; Ovadnevaite et al., 2017; Ruehl et al., 2016; Malila and Prisle, 2018). However, if one assumes that a single molecular monolayer is sufficient to describe the surface of a particle, then aerosol particles with spherical equivalent diameters less than 100 nm will have a non-negligible fraction of total particle-phase material present in their surface phase. Thus, the composition of the bulk and surface of an aerosol particle are inherently coupled.

Numerous models linking surface composition and surface tension have been developed in recent years (Sorjamaa et al., 2004; Nozière et al., 2014; Gérard et al., 2016; Petters and Petters, 2016; Ruehl et al., 2016; Ovadnevaite et al., 2017; Kroflič et al., 2018; Malila and Prisle, 2018; Gérard et al., 2019; Kleinheins et al., 2023, 2024). The redistribution of material between the bulk and surface can influence the equilibrium morphology of an aerosol particle depending on its size. Even in macroscopic systems, liquid–liquid phase-separated particles can adopt non-spherical, partially engulfed morphologies based on their surface properties (Binyaminov et al., 2021). The enrichment and depletion of surface-active species may, therefore, affect the conditions under which an aerosol particle undergoes LLPS as a function of its size and activates and grows into a cloud droplet.

The impact of surface tension modification by surfactants on cloud droplet activation has been studied extensively for decades (Facchini et al., 1999, 2000; Topping et al., 2007; Ovadnevaite et al., 2017; Prisle et al., 2010, 2008, 2011). The conditions under which a hygroscopically growing aerosol particle activates into a cloud droplet were first described by Köhler (1936), as previously mentioned in section 1.1.3. The importance of the global maximum of a particle's equilibrium saturation ratio, S_{crit}, as given by Eq. (1.2),

determines the conditions under which the particle activates into a cloud droplet.

Equation (1.2) contains two effects. The first effect, also known as the solute or Raoult effect, is contained in a_w. The exponential term of Eq. (1.2) represents the Kelvin (or surface) effect. These two effects compete: the Raoult effect reduces the supersaturation needed for an aerosol or cloud condensation nucleus (CCN) to activate into a cloud droplet, while the Kelvin effect increases the critical supersaturation. A common reason for considering these effects to be in competition is as follows: as surface-active species deplete from a droplet's interior "bulk" to populate the surface during hygroscopic droplet growth, their reduced concentration in the bulk typically raises a_w while simultaneously lowering σ. However, it is important to note that this competition is not always inevitable. In particular, for multicomponent organic–inorganic particles with substantial non-ideal mixing, such as those exhibiting LLPS, bulk–surface partitioning of low-polarity surfactants can lead to reductions in both surface tension and a_w (e.g. Ovadnevaite et al., 2017).

While the κ-Köhler theory previously described in section 1.1.3 may yield reasonable predictions for many systems, particularly for particles in the accumulation mode or larger sizes composed of highly soluble components, it neglects bulk–surface partitioning and the high surface area-to-volume ratios of ultrafine particles. This omission warrants further investigation. Various methods exist for determining the surface composition at a gas–liquid interface, each relying on different assumptions, such as the location and dimensionality of the interface and the inclusion of system-dependent fit parameters. One classical approach is the Gibbs two-dimensional (2D) dividing surface (or plane) theory, which relates changes in surface tension ($d\sigma$) to the surface excess concentration (Γ_i) and changes in the chemical potential ($d\mu_i$)

of component i in the bulk solution (Gibbs, 1874):

$$d\sigma = -\sum_i \Gamma_i d\mu_i. \tag{1.22}$$

In this context, the term surface excess concentration refers to the difference between the concentration of component i on the Gibbs dividing plane and its concentration in the interior bulk phase. Consequently, negative values of Γ_i are possible if the component preferentially partitions into the bulk solution, resulting in a lower surface concentration. The precise location of the Gibbs dividing plane is crucial in this approach, yet ambiguous based on an arbitrary definition applied. It is typically chosen such that the surface excess concentration of the primary solvent (usually water) is zero, making the plane's position a system-specific, composition- and size-dependent parameter. Determining the Gibbs dividing plane's location presents challenges since it is defined within the interfacial region between two phases but may not correspond exactly to the outer edge of the surface monolayer (which itself may not be well defined at the atomic level).

Building on Gibbs' theoretical framework, the semi-empirical Szyszkowski–Langmuir isotherm for bulk–surface partitioning was developed (Szyszkowski, 1908):

$$\sigma = \sigma_w(T) - A^{\mathrm{SL}} \ln\left(1 + \frac{B^{\mathrm{SL}}}{C_i^{\mathrm{SL}}}\right), \tag{1.23}$$

where σ_w is the surface tension of pure water at the temperature of interest, A^{SL} and B^{SL} are system-dependent fit parameters, and C_i^{SL} is the concentration of solute i in the bulk liquid. While simpler and often adequate for specific systems, such as interpreting laboratory studies, this equation's predictive power is limited due to the inclusion of two fit parameters for each chemical system.

A third approach to modeling bulk–surface partitioning, introduced by Jura and Harkins (1946), involves semi-empirical fitted models relating sur-

face concentrations to surface tension:

$$\sigma = \sigma_w(T) - (A_0^{\mathrm{CF}} - A_i^{\mathrm{CF}})\, m_\sigma, \tag{1.24}$$

which describes an insoluble compressed film (CF) at the liquid–gas interface using a 2D equation of state. Here, A_0^{CF} represents the maximum possible surface adsorption, A_i^{CF} is the current surface adsorption of component i, and m_σ is a term relating changes in surface tension to changes in surface concentration. When coupled with an isotherm relating bulk and surface concentrations, this equation provides a direct method to connect bulk solution concentrations to surface concentrations.

While Eqs. (1.22), (1.23), and (1.24) have primarily been developed and used to describe liquid–gas interfaces, they have also been employed to interpret macroscopic systems such as LLPS. Recent studies have generalized the concepts of LLPS for application in interpreting droplet microphysics (e.g., Nozière et al., 2014; Ruehl et al., 2016; Ovadnevaite et al., 2017). As previously discussed, LLPS systems can adopt different morphologies depending on their surface properties, with small and ultrafine particles often taking on core–shell or partially engulfed morphologies (Ciobanu et al., 2009; You et al., 2014; Malila and Prisle, 2018; Binyaminov et al., 2021; Gorkowski et al., 2020). LLPS systems are of particular interest due to their prevalence in the atmosphere. Most, if not all, SOA particles formed under atmospheric conditions will exhibit some degree of internal phase separation (Kroflič et al., 2018; Zhang et al., 2021). As such, the ability to accurately describe bulk–surface partitioning and interfacial behavior in LLPS systems is critical for accurately predicting their properties and behavior in the atmosphere. This is particularly true for ultrafine particles with high surface area-to-volume ratios and irregular, non-spherical morphologies. As previously mentioned, such particles have the potential to exhibit significant deviations from traditional Köhler theory, particularly in terms of cloud droplet activation and growth dynamics.

1.4 Aerosol Interfacial Properties

Turning now from the exterior surface of an aerosol particle to the interior, the liquid–liquid interface will be discussed. Similar to the boundary between a gas and a condensed phase, the interface between two condensed phases—especially two liquid phases—can exhibit analogous phenomena, such as the enrichment or depletion of certain compounds (Hua et al., 2016). There have been various efforts to measure the contribution of the liquid–liquid (LL) interface to the overall energy of a particle and to determine whether bulk phase depletion plays a role at this interface. Historically, it has been assumed that the energetic contributions from LL interfacial tension in typical aerosol particles are negligible for particles where the Kelvin effect is also minor (Russell and Ming, 2002; Zuend et al., 2010). However, recent studies suggest that the LL interface's contribution to the Gibbs energy of a particle may have a small but notable impact on the relative humidity (RH) at which the particle undergoes LLPS during dehydration (Ohno et al., 2023; Kucinski et al., 2019; Ott et al., 2021).

To gain a better understanding of the role of interfacial tension and its interaction with phase separation and particle morphologies, predictive models of interfacial tension and the associated changes in phase composition are required. Several approaches have been proposed for predicting liquid–liquid interfacial tension; a brief overview is provided in the following.

The simplest approximation for the interfacial tension between two liquid phases α and β, $\sigma^{\alpha\beta}$, is obtained by taking the absolute difference between the hypothetical gas–liquid surface tensions of the two phases (σ^{α} and σ^{β}) when each is considered in isolation:

$$\sigma^{\alpha\beta} = \left|\sigma^{\alpha} - \sigma^{\beta}\right|. \tag{1.25}$$

The above equation, known as Antonov's rule (Antonov, 1907), may provide a reasonable first-order approximation of interfacial tension for some systems.

However, it is ultimately an empirical method and lacks thermodynamic rigor (Makkonen and Kurkela, 2018; Winter, 1995). An alternative approach for determining the interfacial tension between two liquid phases was proposed by Girifalco and Good (1957), based on Antonov's rule, with additional considerations for the molecular interactions between the two phases:

$$\sigma^{\alpha\beta} = \sigma^{\alpha} + \sigma^{\beta} - 2\phi\sqrt{\sigma^{\alpha}\sigma^{\beta}}, \tag{1.26}$$

where ϕ is a system-specific interaction parameter. It has been shown that ϕ is constrained by the following inequality:

$$\phi \geq \left(1 - \frac{\sigma^{\alpha\beta}}{\sigma^{\alpha}}\right)^{\frac{1}{2}}. \tag{1.27}$$

In qualitative terms, ϕ tends to be lower in systems where the primary molecular interactions differ, such as dispersion forces in phase β and hydrogen bonding in phase α (Girifalco and Good, 1957). It is important to mention that any parameterization of interfacial tension must inherently reduce to 0 in a single well-mixed particle. For a single well-mixed phase where $\sigma^{\alpha\beta} = 0$, ϕ can only be equal to 1.

In the case of phase separation, there is a special case where $\phi = \left(1 - \frac{\sigma^{\alpha\beta}}{\sigma^{\alpha}}\right)^{\frac{1}{2}}$. In such a case, Eq. (1.26) reduces to Eq. (1.25). However, the applicability of this equation to systems with more than two components or with compounds that are soluble in both phases remains uncertain (Makkonen and Kurkela, 2018). Equation (1.26) was further refined by Fowkes (1962, 1963) to better account for dispersive and non-dispersive contributions to interfacial tension. Such an approach requires accurate estimates of the dispersive and non-dispersive contributions to the surface energies of both phases, which can limit its practical application in cases which systems are poorly characterized, such as those of atmospheric aerosol particles.

As mentioned earlier, certain atmospheric aerosol systems have been ob-

served to undergo LLPS for particles with large diameters, whereas particles with similar compositions but smaller diameters may not undergo LLPS (Kucinski et al., 2019; Freedman, 2020; Ott and Freedman, 2020; Ohno et al., 2023). It is believed that for sufficiently small diameters, the high surface-area-to-volume ratios of aerosol particles create an energetic barrier from the combined effects of surface and interfacial tensions, inhibiting the formation of additional phases (Ohno et al., 2023; Freedman, 2020). Additionally, the composition of aerosol particles, particularly the presence of different inorganic electrolytes, complicates the size-dependent LLPS behavior. For instance, Ott et al. (2021) report that particles containing sodium cations can phase-separate at smaller sizes than similar particles containing ammonium cations.

In summary, a similar energetic penalty to surface tension exists at the boundary between any two liquid phases, including a finite-depth surface and the bulk. The sum of this interfacial tension and the surface tension at the gas–liquid boundary forms the measurable surface tension that can be directly observed. Various methods have been proposed to determine the interfacial tension between two liquid phases, using thermodynamic theory, semi-empirical approaches, and system-specific fits to experimental data. The combined energetic contributions from these interfaces lead to differences in the total Gibbs energy between a well-mixed and a phase-separated particle. Greater differences in Gibbs energy occur in particles with higher surface/interfacial-area-to-volume ratios. Such differences in Gibbs energy may be large enough to reduce the onset a_w of LLPS or even completely suppress LLPS. While the onset a_w of LLPS may be reduced with the inclusion of interfacial tension treatments, the onset RH of LLPS is also a function of the Kelvin effect and thus may increase or decrease with the inclusion of both surface and interfacial tension treatments. Prior to this thesis research, no predictive model accounted for the coupled feedbacks of aerosol particle size and three-dimensional morphology on the conditions under which a par-

ticle will separate into two (or more) liquid phases or remain homogeneously mixed. The work described in Chapter 3 aims to close this gap while providing a thermodynamically consistent framework for solving such a complex problem in a single particle.

1.5 Pure Component Surface Tensions

A major source of uncertainty in both surface and interfacial tension estimates is the pure–component surface tension of each individual species, σ_i°. Accurate estimates of this value for each species are necessary for both bulk–surface partitioning calculations and estimates of interfacial tension. While some compounds, such as water and some simple organic compounds, have numerous measurements for their surface tensions at different temperatures, many other compounds do not have such data available. Further complicating this issue is the fact that the individual species inside an aerosol particle are poorly characterized, and thus finding measured surface tension values or proxy values from structurally similar compounds is challenging. Likewise, the reference state surface tension values for inorganic electrolyte compounds are also a matter of debate (Dutcher et al., 2010; Wexler and Dutcher, 2013).

One method used in fields beyond atmospheric science is known as quantitative structure–property relationships (QSPR) (Yee and Wei, 2012; Chen et al., 2020). The principle of QSPR is that molecules with similar structures will have similar properties. This approach is similar to functional group-based approaches, such as that of the AIOMFAC model, but with additional information about the relative positions of functional groups within a molecule. This additional structural information can be encoded through the use of molecular fingerprints. Molecular fingerprinting is a technique that translates a molecule's structure into a series of integer codes that represent atoms and functional groups, as well as their relative positions. There are many techniques for molecular fingerprinting, including Molecular ACCess System (MACCS) keys and Morgan fingerprints, which have been used for QSPR predictions for different molecular properties (Consonni et al., 2023).

Of the two fingerprinting methods described above, MACCS keys are slightly simpler. MACCS keys consist of 166 pre-defined molecular patterns and structures (Durant et al., 2002). Each MACCS key is associated with a SMARTS (SMiles ARbitrary Target Specification) code that matches a tar-

geted substructure. SMARTS are based on the Simplified Molecular Input Line Entry System (SMILES) notation, which is a method of representing molecules as a single string of characters. As an example the SMILES for D-Glucose ($C_6H_{12}O_6$) is "C([C@@H]1[C@H]([C@@H]([C@H](C(O1)O)O)O)O)O" where the "@" represents left-handed chirality and "@@" represents right handed chirality. From a SMILES, the corresponding MACCS keys can be generated. Since MACCS keys only describe 166 unique molecular features or patterns, they may not be able to represent more complex and nuanced patterns in a molecule. MACCS keys may also struggle to accurately describe larger molecules in fields such as biochemistry (Kuwahara and Gao, 2021). The more complex of the two fingerprinting methods is Morgan fingerprints. Morgan fingerprints encode more data about a molecule's structure; however, they are more abstract and thus less human-readable. They numerically encode each individual atom in a molecule and describe the atoms' neighboring atomic substructures in terms of a radius of adjacent atoms, which collectively encode the the whole molecular structure (Morgan, 1965).

Additionally, recent advances in the field of artificial intelligence and machine learning (ML) have led to the development of predictive QSPR models once a sufficiently large database of information is compiled to train a model (Chen et al., 2020). There have been past approaches attempting to use ML techniques to predict the surface tension of individual organic compounds (Sanjuán et al., 2020; Randová and Bartovská, 2016; Soori et al., 2021; Rafie et al., 2023; Ojaki et al., 2023; Mousavi et al., 2021; Lazzús et al., 2017; Lashkarbolooki and Bayat, 2018; Pierantozzi et al., 2021; G. R. Pazuki and Sahranavard, 2011; Tiejun Xu and Khanghah, 2019); however, many of these attempts have been on simplified datasets or confined to specific compound classes rather than on broad databases of highly functionalized organic compounds. For example, Sanjuán et al. (2020) used surface tension values of 87 different alcohols and compared models based on various combinations of temperature, molecular shape, and critical physicochemi-

cal properties. Models that depended on temperature, critical temperature, critical pressure, critical volume, molar volume, and acentric factor had the best correlations with the measurements in question (Sanjuán et al., 2020). Roosta et al. (2012) used an artificial neural network with a single hidden layer and 20 nodes and was able to accurately predict the surface tensions of organic compounds based on their critical and reduced properties, along with others, and their specific gravity at the compound's boiling temperature.

Lazzús et al. (2017) used 46 different functional groups, the molecular weight of the compound, and the absolute temperature to predict the surface tension of different ionic liquid compounds using an artificial neural network with one hidden layer of 30 neurons. Lashkarbolooki and Bayat (2018) specifically examined the surface tension of alkanes and alkenes using an artificial neural network and the simplified inputs of temperature, critical temperature, and number of carbons. Mousavi et al. (2021) also examined a functional-group-based approach for determining the surface tension of ionic liquids. Pierantozzi et al. (2021) used a neural network with a single hidden layer and 41 neurons, which took reduced, critical, and boiling point temperatures, along with the acentric factor from organic acids as inputs, to predict the surface tension of those acids.

While a combination of various ML techniques and functional group-based approaches may have a high degree of flexibility for many QSPR approaches, such approaches may not be able to adequately represent numerous compounds, spanning various compound classes of atmospheric relevance, to a high degree of accuracy. As an extreme example, cis–trans isomerism may lead to substantial differences in pure component surface tension (Ciccia-relli et al., 2007). Therefore, accurate descriptions of molecular structure are necessary to describe molecules for inputs into ML-based techniques to predict pure-component surface tensions. It is noted in Chapters 2 and 3 that accurate predictions of pure component surface tensions are necessary for more rigorous treatment of bulk–surface partitioning and its interactions with

LLPS. Thus chapter 4 compares four novel ML-based frameworks and three different sets of molecular descriptors for predicting pure-component surface tensions of highly-complex and atmospherically-relevant organic compounds.

Part II

Surface and Interfacial Energies

2

A Thermodynamic Framework for Bulk–Surface Partitioning in Finite-volume Mixed Organic–Inorganic Aerosol Particles and Cloud Droplets

2.1 Preface

In chapter I, the importance of atmospheric aerosol surface properties in relation to their interactions with clouds and past methods for modeling aerosol surface properties were discussed. Now, a method for modeling the equilibrium partitioning of species between the surface and bulk of an aerosol particle is described. The aim of chapter 2 is to determine the relative importance of the competing effects of surface tension depression and bulk-phase enrichment on cloud droplet activation. Chapter 2 was reproduced with modifications from Schmedding and Zuend (2023).

2.2 Abstract

Atmospheric aerosol particles and their interactions with clouds are among the largest sources of uncertainty in global climate modeling. Aerosol particles in the ultrafine size range with diameters less than 100 nm have very high surface area to volume ratios, with a substantial fraction of molecules occupying the air–droplet interface. The partitioning of surface-active species between the interior bulk of a droplet and the interface with the surrounding air plays a large role in the physicochemical properties of a particle and in the activation of ultrafine particles, especially those of less than 50 nm diameter, into cloud droplets. In this work, a novel and thermodynamically rigorous treatment of bulk–surface equilibrium partitioning is developed through the use of a framework based on the Aerosol Inorganic–Organic Mixtures Functional groups Activity Coefficients (AIOMFAC) model in combination with a finite-depth Guggenheim interface region on spherical, finite-volume droplets. We outline our numerical implementation of the resulting modified Butler equation, including accounting for challenging extreme cases when certain compounds have very limited solubility in either the surface or bulk phase. This model, which uses a single, physically constrained interface thickness parameter, is capable of predicting the size-dependent surface tension of complex multicomponent solutions containing organic and inorganic species. We explore the impacts of coupled surface tension changes and changes in bulk–surface partitioning coefficients for aerosol particles ranging in diameters from several μm to as small as 10 nm and across atmospherically relevant relative humidity ranges. The treatment of bulk–surface equilibrium leads to deviations from classical cloud droplet activation behavior as modeled by simplified treatments of the Köhler equation that do not account for bulk–surface partitioning. The treatments for bulk–surface partitioning laid out in this work, when applied to the Köhler equation, are in agreement with measured critical supersaturations of a range of different systems. However, we also find that challenges remain in accurately modeling the growth be-

havior of certain systems containing small dicarboxylic acids, especially in a predictive manner. Furthermore, it was determined that the thickness of the interfacial phase is a sensitive parameter in this treatment; however, constraining it to a meaningful range allows for predictive modeling of aerosol particle activation into cloud droplets, including cases with consideration of co-condensation of semivolatile organics.

2.3 Introduction

Atmospheric aerosols are suspensions of condensed particles and the gas which surrounds them. They can be a major contributor to poor indoor and outdoor air quality. Exposure to poor air quality is the leading environmental risk factor for premature mortality globally (Cohen et al., 2017; Burnett et al., 2018). Beyond their public health effects, the role of atmospheric aerosols and of aerosol–cloud interactions in the global climate system, remains one of the least understood processes in climate models (Boucher et al., 2013). Some light-absorbing aerosols exhibit a positive direct radiative forcing, while others mostly scatter solar radiation and exhibit negative direct radiative forcing. The magnitude and sign of the local or regional direct radiative forcing depends on numerous factors including an aerosol's composition, size distribution, geographic location, season, and altitude in the atmosphere (Bellouin et al., 2020). Furthermore, atmospheric aerosols interact with clouds and precipitation, thereby contributing to important indirect effects on Earth's climate that are poorly constrained (Seinfeld et al., 2016). Therefore, it is of the utmost importance to understand the physicochemical properties and microphysical processes of aerosol particles, including aerosol–cloud–radiation interactions, as these drive their impacts on the climate system.

Aerosol particles exist over a broad range of sizes. Differently sized particles frequently originate from distinct sources or form through unique processes. Particles in the nucleation mode are primarily formed via the spontaneous condensation of gaseous compounds to create or extend a tiny condensed phase. Similarly, Aitken mode particles may form by the continued growth of nucleation mode particles through condensation of gaseous species or coagulation of condensed particles. Particles in the nucleation mode or Aitken mode are collectively referred to as ultrafine particles. Accumulation mode particles form through coagulation and agglomeration of smaller Aitken mode particles in the air. The largest aerosols, such as mineral dust

and sea spray particles, are primarily composed of inorganic compounds and typically form via mechanical processes.

As aerosol particles decrease in size, they are more likely to originate from and grow through complex multiphase chemical reactions. Many fine and ultrafine aerosol particles are composed of organic compounds that form via oxidation reactions of volatile organic compounds (VOCs)or intermediate-volatility organic compounds (IVOCs) in the gas phase. Many of the products of these reactions are lower in volatility and partition into condensed particles. Semivolatile and low-volatility organic compounds (SVOCs and LVOCs) may also be emitted and partition into particles with minimal processing in the gas phase. Organic aerosol particles, or components thereof, formed through gas-phase or multiphase chemistry are known as Secondary Organic Aerosols (SOA) (Jimenez et al., 2009; Hallquist et al., 2009); for a complete list of abbreviations and symbols, please refer to Tables A.2 & A.3 in Appendix B. Within a condensed phase additional chemical reactions may proceed. This is particularly notable in low-viscosity aqueous aerosol particles and cloud droplets, those droplets provide aqueous media wherein numerous laboratory and field observations have observed the formation or transformation of SOA through chemical processing, e.g., Ervens et al. (2011). For certain species these reactions can further reduce their volatility, effectively "trapping" said species in the particle phase. For example, isoprene expoxydiols (IEPOX) are known to undergo acid-catalyzed reactions in aqueous $SO_4{}^{2-}$-containing particle phases (Surratt et al., 2010). The IVOCs and VOCs which lead to the formation of SOA can be biogenic (e.g. isoprene or monoterpenes) or anthropogenic (e.g. toluene, xylene, naphthalene) (Ng et al., 2007; Chan et al., 2009). Observational studies have concluded that the majority of SOA material is derived from biogenic precursors (Zhang et al., 2007).

The internal mixing state and geometries of aerosol particles are varied. Aerosol particles that are emitted by primary emission from biomass burning

often take the shape of long agglomerations of individual spherical particles (Pokhrel et al., 2021), while aqueous inorganic-rich particles and soluble SOA are thought to be approximately spherical. The frequent presence of liquid–liquid phase separation (LLPS) can complicate the shape aspect. LLPS particles may form radially symmetric structures with an organic-rich "shell" (phase β) covering an inorganic-rich "core" (phase α) or other, geometrically more complex structures, such as a partially engulfed morphology, wherein the particle is no longer radially symmetric nor perfectly spherical. In a partially engulfed particle, phase β does not spread completely over phase α and leaves a portion of phase α exposed (Song et al., 2013, 2012; Ciobanu et al., 2009; Shiraiwa et al., 2013). These particles are also called "russian dolls" or "janus particles" and interact with radiation differently than their core–shell counterparts (Lang-Yona et al., 2010). Furthermore, should phase β of core–shell phase-separated particles become a highly viscous liquid or even glassy, it can limit the reactive uptake of different species (Schmedding et al., 2020, 2019; Zhou et al., 2019; Kuwata and Martin, 2012).

Since the surface area to volume ratio of a sphere scales with the inverse of its radius, said ratio becomes of great importance for ultrafine particles. If the assumption is made that the surface of a particle is represented by a monolayer of molecules in contact with the gas phase, an assumption further explored in this study, then spherical particles with a diameter less than 100 nm will have a non-negligible quantity of molecules present at their surface. For example, in a pure water droplet with a diameter of 50 nm, $\sim$ 4 % of the water molecules will be present in the surface monolayer while more than half of the water molecules in a pure droplet with a diameter of 3 nm will be present in the surface monolayer.

Many ultrafine aerosol particles are complex multicomponent systems and contain numerous surfactant and tensoionic species in differing concentrations. These species modify the surface tension of a particle (Sorjamaa et al., 2004; Nozière et al., 2014; Gérard et al., 2016; Petters and Petters,

2016; Ruehl et al., 2016; Ovadnevaite et al., 2017; Kroflič et al., 2018; Malila and Prisle, 2018; Gérard et al., 2019). In finite-volume systems, surfactants may become depleted out of the particle interior, likewise tensoionic species may become increasingly concentrated in the particle interior. This may influence the equilibrium morphology of an aerosol particle for a given size. Even in macroscopic systems, it is possible for LLPS particles to adopt non-spherical partially engulfed morphologies based on their surface properties (Binyaminov et al., 2021). The surface enrichment and depletion of species may affect the conditions under which an aerosol particle will activate and quickly grow into a cloud droplet.

The impact of surface tension modification by surfactants on cloud droplet activation has been known and studied for decades (Facchini et al., 1999, 2000; Topping et al., 2007; Ovadnevaite et al., 2017). The conditions under which a hygroscopically growing aerosol particle will activate into a cloud droplet were first stated by Köhler (1936), recognizing the importance of the global maximum of a particle's equilibrium saturation ratio, S_{crit}, as expressed by the following equation:

$$S = a_w \exp\left(\frac{4\sigma M_w}{RT\rho_w D_p}\right). \tag{2.1}$$

Here, σ denotes the effective surface tension of the particle at the air–liquid interface. M_w and ρ_w are the molar mass and density of water, respectively. R is the gas constant, T is the temperature, and D_p is the diameter of the particle. The so-called solute or Raoult effect is captured by the water activity, a_w, whereas the exponential factor captures the Kelvin effect. These two effects are often considered to be in competition with one another since the Raoult effect decreases the supersaturation necessary for an aerosol (or cloud condensation nucleus, CCN) to reach activation into a cloud droplet while the Kelvin effect increases the critical supersaturation. Note that values of S are often reported as percentages, in which case the value of Eq. (2.1)

is multiplied by 100 %. A common reason for considering this a competition is the following: as surface-active species are depleted from a droplet's interior "bulk" to populate the surface during hygroscopic droplet growth, their lowered concentration in the bulk will typically raise the value of a_w while simultaneously decreasing the value of σ by lowering the effective surface tension. However, we note that there is not necessarily a competition. In particular, in multicomponent organic–inorganic particles with substantial nonideal mixing, such as in cases with LLPS, the bulk–surface partitioning of low-polarity surfactants can lead to both a relative lowering of surface tension as well as of a_w (e.g. Ovadnevaite et al., 2017).

In an effort to simplify calculations of aerosol water uptake and CCN activation, Petters and Kreidenweis (2007) developed a single-parameter model of hygroscopic growth, commonly known as κ-Köhler theory, wherein a_w can be related to the current volume of water in the particle V_w and the starting dry particle (solute) volume, V_{dry}, through the following equation:

$$\frac{1}{a_w} = 1 + \kappa \frac{V_{dry}}{V_w}. \tag{2.2}$$

The value of κ for a multicomponent solution can be found from a volume-fraction-based linear weighting of the κ values of individual components. The combination of Eqs. (2.1) and (2.2), along with an assumption about σ, allows for the calculation of critical supersaturations of aerosol particles given only their composition and dry sizes (Petters and Kreidenweis, 2007); however, the utility of κ-Köhler theory is thought to be more limited for ultrafine particles (Topping et al., 2016).

While κ-Köhler theory may provide reasonable predictions for many systems, including particles in the accumulation mode or of even larger sizes that are composed of highly soluble components, its neglect of bulk–surface partitioning treatments in combination with the high surface area-to-volume ratios of ultrafine particles is worth exploring in greater detail. There are

numerous methods for determining the surface composition at a gas–liquid interface, all of which rely on various assumptions, such as the location and dimensionality of said interface and the inclusion of various system-dependent fit parameters. One of the classical methods is the Gibbs 2-dimensional (2D) dividing surface (or plane) approach, which relates the change in surface tension of a solution ($d\sigma$) to the surface excess concentration (Γ_i) and change in chemical potential $d\mu_i$ of component i in the bulk solution via (Gibbs, 1874):

$$d\sigma = -\sum_i \Gamma_i d\mu_i. \tag{2.3}$$

The term surface excess concentration may be misleading in this case since it is defined as the difference between the concentration of i on the Gibbs dividing plane and that in the interior volume of a bulk phase adjacent to the plane. Thus negative values of Γ_i are possible if i partitions preferentially into the bulk of a solution and has consequently a lower concentration at the surface. The definition of the location of the Gibbs surface is of the utmost importance when utilizing this approach. Its location is typically selected such that the surface excess concentration of the first species (usually the main solvent, e.g. water) is precisely 0, thus making that 2D plane location a system-specific, composition- and size-dependent parameter. Determining the location of the Gibbs dividing plane presents additional challenges since the location of the surface is defined to be located within the interfacial region between 2 phases, but may not necessarily be found at the same radial position as that of the "outside" edge of the monolayer of molecules found at the boundary of a phase.

From the theoretical framework laid out by Gibbs, the semi-empirical Szyszkowski–Langmuir isotherm for bulk–surface partitioning was developed (Szyszkowski, 1908):

$$\sigma = \sigma_w(T) - A^{\mathrm{SL}} \ln\left(1 + \frac{B^{\mathrm{SL}}}{C_i^{\mathrm{SL}}}\right). \tag{2.4}$$

Here, σ_w is the surface tension of pure water at the temperature of interest, A^{SL} and B^{SL} are system-dependent fit parameters, and C_i^{SL} is the concentration of solute i in the bulk liquid of the system. While simpler as an approach and adequate in many system-specific cases (such as the interpretation of laboratory studies), the predictive power of this equation is limited due to the inclusion of two fit parameters for each chemical system.

A third treatment for modeling bulk–surface partitioning of different species was introduced by Jura and Harkins (1946). It combined semi-empirical fitted models relating surface concentrations to surface tension as follows:

$$\sigma = \sigma_w(T) - (A_0^{CF} - A_i^{CF})\, m_\sigma. \tag{2.5}$$

This equation describes an insoluble compressed film (CF) at the interface between a liquid and a gas with a 2D equation-of-state for bulk–surface partitioning. $A_0^{CF}$is the maximum surface adsorption possible, A_i^{CF} is the current surface adsorption of i, and m_σ is a term relating the change in surface tension to the change in surface concentration. This equation, when coupled with an isotherm relating bulk and surface concentrations, is capable of describing the surface tension as aerosol particles grow hygroscopically when exposed to increasing RH (Ruehl et al., 2016). In macroscopic systems, the approaches of (Szyszkowski, 1908) and (Jura and Harkins, 1946) assume that the enrichment or depletion of species at the particle surface has a negligible effect on the bulk particle composition; however, in ultrafine particles, depletion of surface active species from the bulk phase may become important. This bulk depletion effect has recently come under scrutiny (Prisle et al., 2010; Bzdek et al., 2020; Lin et al., 2020) and has already been considered previously by Sorjamaa et al. (2004), who considered binary systems of water and the surfactant sodium dodecyl sulfate (SDS). They noted that Köhler curve calculations should include the effect of bulk depletion since neglecting this effect led to unrealistically low critical supersaturation conditions. These results were supported by laboratory measurements of ternary

water–SDS–sodium chloride systems taken by (Prisle et al., 2008).

While many organic species present in the atmosphere are expected to be strongly surface-active, there are others classified as weak surfactants, including organosulfates (Hansen et al., 2015), certain components in mixtures of marine SOA and POA (Ovadnevaite et al., 2017), and aliphatic dicarboxylic acids (Ruehl et al., 2016). The surface enrichment of these compounds is difficult to predict, currently inaccessible experimentally (for airborne particles), and potentially showing complex interactions with particle size (Sorjamaa et al., 2004; Sorjamaa and Laaksonen, 2007; Davies et al., 2019; Ovadnevaite et al., 2017).

2.3.1 Prior treatments of bulk–surface partitioning in aerosol systems

There have been numerous methods developed for predicting the bulk–surface partitioning of aerosol chemical species, the following is a summary of recent works. Briefly, Sorjamaa et al. (2004) used an approach based on the 2D Gibbs dividing surface theory and found that the depletion of water-soluble surfactants may have a substantial impact on Köhler curves through both surface tension depression and modification of the Raoult effect as surfactants are depleted from the bulk. They report that failing to account for both surface and bulk effects in growing aerosol particles may lead to underpredictions of the critical supersaturation, particularly at higher organic mass fractions. Prisle et al. (2008) used the semi-empirical Szyskowski equation (Szyszkowski, 1908) to model the bulk–surface partitioning of various fatty acids with increasing carbon chain length. Importantly, they noted that using the surface tension of pure water while accounting for changes to the Raoult effect from bulk–surface partitioning, led to good agreement with experimental data and less costly calculations; however, the use of accurate values of a_w that accounted for bulk–surface partitioning were critical. These assumptions were more thoroughly explored by Prisle et al. (2010), wherein

they found that particles with at least 50 % of their mass composed of surfactant species required more accurate treatments of surface tension depression than considering σ to be the same as that of pure water. In systems with lower concentrations of surfactants it was noted that the surface tension may be similar to that of pure water at the point of CCN activation. Despite this, an evolving surface tension depression in growing aerosol particles that have not yet activated may play a role in their growth and activation behavior (Ovadnevaite et al., 2017; Davies et al., 2019). Further complicating the issue is a lack of measurements of surface tension on sub-500 nm diameter particles.

Romakkaniemi et al. (2011) included a Szyskowski–Langmuir treatment of bulk–surface partitioning to droplets containing methylglyoxal, a semivolatile species and moderate surfactant. They found that treating the surface as a hypothetical 2D plane that mixes ideally led to over one order of magnitude increase in the total particle-phase concentration of methylglyoxal, further confirming the importance of bulk–surface exchange treatments. Beyond Szyskowski–Langmuir isotherm-based treatments of bulk–surface partitioning, other equations of state have been employed, including 2D van der Waals models, compressed film models, and LLPS-based models of bulk–surface partitioning (Ruehl and Wilson, 2014; Ruehl et al., 2016; Ovadnevaite et al., 2017). The compressed film model of Jura and Harkins (1946); Ruehl et al. (2016) was also utilized by Forestieri et al. (2018) to examine long-chain fatty acid coatings on sodium chloride particles to mimic sea spray aerosols. It was found that different surfactant species may have large effects on CCN activation through both their impacts on σ and the effective hygroscopic growth parameter κ under high RH conditions. They note that compounds traditionally thought of as highly surface active, like the fatty acids in their study, may not have as large of an impact on CCN activation as others (Forestieri et al., 2018).

The treatment of bulk–surface partitioning was also studied using an

AIOMFAC-based coupled liquid–liquid equilibrium and gas–particle partitioning calculation (Ovadnevaite et al., 2017; Davies et al., 2019). The effective surface tension was estimated based on the predicted LLPS phase compositions and the surface coverage by an organic-rich shell phase, constrained to be of a defined minimum thickness $\delta_{\beta,min}$. This approach found that LLPS aerosols can be strongly affected by surface tension reductions, yet weakly by changes to the Raoult effect following bulk–surface partitioning (Ovadnevaite et al., 2017; Davies et al., 2019). The treatment of bulk–surface partitioning in the LLPS-based approach was primarily due to bulk equilibrium LLPS, organic surface coverage, and gas–particle partitioning, which directly account for substantial nonideal mixing. However, other more detailed effects, such as a size-dependent feedback from bulk–surface partitioning on LLPS phase compositions and liquid–liquid–interfacial-phase partitioning and energy effects were not accounted for. Furthermore, this approach did not depend on any assumptions about the maximum thickness of the interfacial region, only a prescribed minimum thickness (Ovadnevaite et al., 2017). Likewise, a subsequent study by Davies et al. (2019) compared a compressed-film model and three versions of AIOMFAC-based bulk–surface partitioning models. The first AIOMFAC-based approach involved using a full (unconstrained) liquid–liquid equilibrium calculation. This methodology assumed that the organic-rich phase β would form a spherical shell around phase α if there was sufficient material, otherwise phase β formed a partial spherical shell of thickness $\delta_{\beta,min}$ over phase α. An area-weighted mean of pure component surface tensions based on the areas of each phase exposed to the gas phase was used to determine the effective droplet surface tension. The second approach involved assuming a complete phase separation among organics and aqueous inorganic electrolytes, with only water allowed to partition between both phases and the assumption that the organic species formed a film, i.e. a partial monolayer or up to multiple molecular layers at the droplet surface. In case of insufficient organic material for forming a com-

plete monolayer over the droplet, the effective surface tension of the droplet is computed as the surface coverage area-weighted average of the pure organic species surface tension and the surface tension of water. These two treatments of surface tension provided a good and predictive estimate of the upper and lower bounds of the measured critical supersaturation of a CCN, given the initial dry composition of the particle.

Malila and Prisle (2018) developed a semi-empirical monolayer-based bulk–surface partitioning model based on an extension of an earlier method developed by Laaksonen and Kulmala (1991) wherein the surface tension of a droplet was related to a surface-composition-weighted average of pure-component surface tensions (σ_i°):

$$\sigma(x^b, T) = \frac{\sum_i \sigma_i^\circ \mathscr{V}_i x_i^s}{\sum_i \mathscr{V}_i x_i^s}. \tag{2.6}$$

Here, $\mathscr{V}_i$ and x_i^s are the molar volumes and surface mole fractions of i, respectively. Coupled with mass conservation, this equation must be solved iteratively from a given droplet size and overall composition. It is important to note that pseudo-binary approximations must be made for Eq. (2.6) for systems with three or more components and that the iterative solution must be optimized for each system tested, which somewhat limits the utility of this approach as a predictive tool.

Vepsäläinen et al. (2022) conducted a comparative study examining the differences between the 2D Gibbs adsorption model of Prisle et al. (2011), the simplified complete partitioning model of Prisle et al. (2011), the compressed film model of Ruehl et al. (2016), a partial monolayer model based on Ovadnevaite et al. (2017), the monolayer model of Malila and Prisle (2018), and a simple bulk-composition-based model that did not allow for bulk–surface partitioning. In their study, the hygroscopic growth of 50 nm particles of different, moderately surface-active dicarboxylic acid species were modeled. It was noted that the more complex models for bulk–surface partitioning,

those which allowed for the partial partitioning of species between the bulk and surface, had the best agreement with measured critical supersaturations. Despite the agreement between the more complex models with measured critical supersaturations as a function of dry particle size, they predicted varying degrees of bulk–surface partitioning for different species and, thus, different equilibrium compositions for the bulk and surface of the droplet. A related model comparison by Vepsäläinen et al. (2023) was also extended to systems including stronger surfactant species, such as myristic acid. In that recent work, it was also noted that the various bulk–surface partitioning treatments from Vepsäläinen et al. (2022) were in agreement at low surfactant mass fractions; however, there was disagreement at higher surfactant mass fractions.

Other recent work with thermodynamics-based models have attempted to predict the degree to which surfactants may cover an aerosol particle (surface) at equilibrium, with many surfactant species expected to have a surface coverage on the order of 60–85 %, while some surfactant remains dissolved in the particle bulk, both for compositions below and above the critical micelle concentration (McGraw and Wang, 2021).

While simplifying assumptions about bulk–surface partitioning are reasonable for macroscopic systems, in the case of ultrafine particles, the competing effects of interior bulk phase depletion and surface accumulation are complex and must be considered. Recent experimental findings have highlighted that even for larger droplets on the order of several micrometers which contain non-ionic surfactant species similar to those found in atmospheric aerosols, varying surface tensions may be exhibited across particle sizes (Bzdek et al., 2020). Thus, a rigorous framework for determining the equilibrium bulk–surface partitioning of a droplet is necessary to better understand the size-dependency of bulk–surface partitioning and related surface tension impacts in aerosol systems. Ideally, such a framework is predictive in design; i.e., it does not need to be fine-tuned or fitted specifically for every system or size range of interest. In the following, we introduce and evaluate

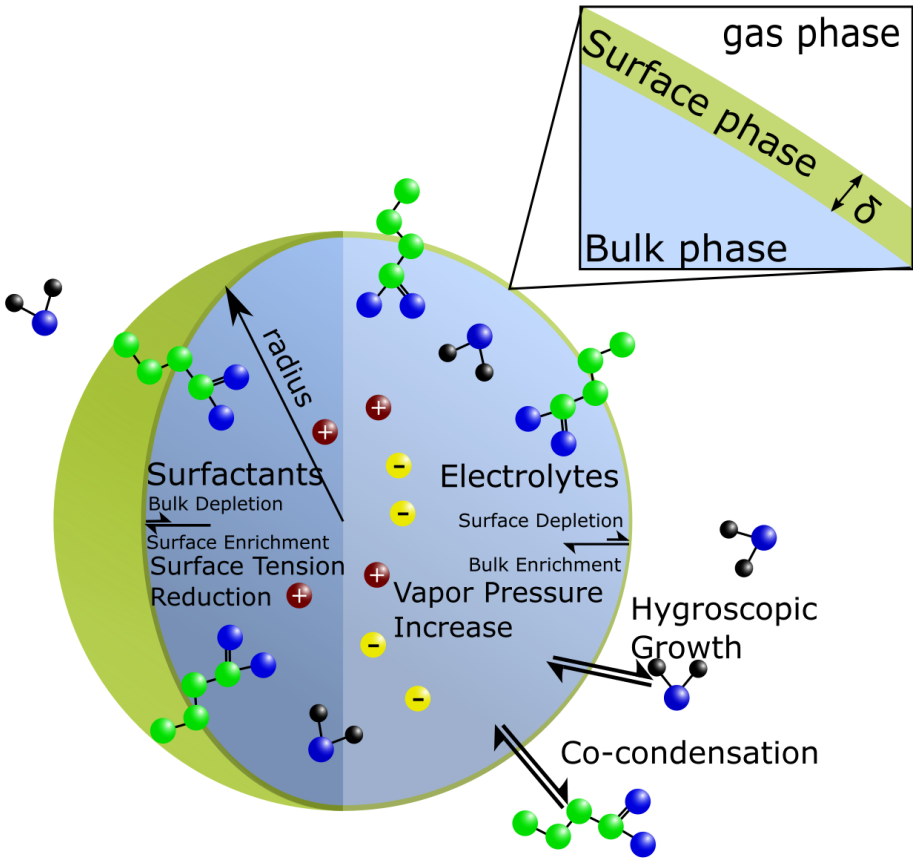

Figure 2.1: Conceptual diagram of bulk–surface partitioning in a single-bulk phase spherical aerosol particle or cloud droplet. The thickness of the finite-volume surface phase is represented by δ.

such a framework by extending the AIOMFAC-based gas–particle partitioning calculations to include a distinct surface phase present between aerosol particles and the surrounding gas phase; see Fig. 2.1.

2.4 Theory and Methods

In his seminal works, Gibbs (1874) defined the following equation capable of expressing the so-called "free" energy of a thermodynamic system (G) with

negligible energetic contributions from surfaces and interfaces as:

$$G = U - TS - PV. \tag{2.7}$$

Here, U is the internal energy of the system, T is temperature, S is entropy, P is pressure, and V is the volume of the system. Taking the derivative of Eq. (2.7) and then integrating with respect to the number of moles of i in the system (n_i) at constant T and P gives the following equation for a system with k components:

$$G = \sum_k \mu_k n_k. \tag{2.8}$$

Using the information given in Eq. (2.8), the equilibrium composition of a closed multiphase system can be found when its energy is at its global minimum. However, in order to accurately predict the chemical potential of each component in a system, physicochemical mixing models must be employed to account for non-ideal mixing effects on the chemical potential of i in a liquid-state bulk phase b as given by:

$$\mu_i^b = \mu_i^{\circ,b} + RT \ln(a_i^b), \tag{2.9}$$

where, $\mu_i^{\circ,b}$ is the standard chemical potential, R is the gas constant, and a_i^b is the (chemical) activity of i. The activity of a species is a unitless value which represents the "effective concentration" of component i on a chosen composition scale (e.g. mole fraction or molality) as determined by non-ideal mixing in a given phase of a system. Under equilibrium conditions, the chemical potentials of a component must be equivalent across all phases (e.g., Zuend et al., 2010). A useful choice, often employed when calculating μ_i for multiple phases of a system, is that μ_i° is defined to be identical for all phases. With that definition, also the activities of a species must be equal in all coexisting phases for a system at equilibrium. In order to accurately predict the various a_i^b over a wide range of solution compositions, complex

mixing models, such as the AIOMFAC model, must be employed to account for molecular interactions, shape and size differences.

The AIOMFAC model is a state-of-the-art thermodynamic mixing model capable of accurately predicting the chemical activity of species in atmospheric aerosol systems in a thermodynamically rigorous and consistent manner. AIOMFAC can be considered as a major extension of the UNIversal quasichemical Functional Groups Activity Coefficients (UNIFAC) model by Fredenslund et al. (1975), since AIOMFAC includes the treatment of aqueous electrolytes and interactions between ions and organic molecules. UNIFAC itself is a group-contribution model derived from the UNIversal QUAsi-Chemical (UNIQUAC) theory of liquid mixtures developed by Abrams and Prausnitz (1975). The UNIQUAC theory and model is a local composition model for mixtures of non-electrolyte components that generalizes the original quasi-chemical theory of Guggenheim (1952) to mixtures consisting of molecules of various shapes and sizes (while Guggenheim's quasi-chemical lattice model was restricted to spherical molecules of approximately equal sizes). The development of the UNIQUAC model, the UNIFAC group-contribution version, and subsequently extended variants like AIOMFAC, are therefore all deeply rooted in an advanced statistical mechanics treatment of mixing and interactions amongst different molecules in solution based on the local composition principle and are more rigorous than Guggenheim's two-component lattice gas model. AIOMFAC has been updated numerous times to include many atmospherically relevant inorganic cations, anions, and organic functional groups, so that this model can represent a large number of mixed organic–inorganic aerosol systems, including systems with tens to thousands of components (Zuend et al., 2008, 2011; Yin et al., 2022).

If two or more distinct phases (phases are here indexed by superscript ϕ) are present in a system at constant temperature and pressure, Eq. (2.8) may need to be expanded to account for the energy associated with the boundaries between the phases. This can be achieved via the addition of a

term accounting for the interfacial energy per unit area (σ) scaled by the area of the interface (A) (e.g., Aston and Herrington, 1991):

$$G = \sum_{\phi} \sum_{j} \mu_j^{\phi} N_j^{\phi} + \sigma A. \tag{2.10}$$

The interfacial Gibbs energy contribution can be important for microscopic systems, in which the contribution gains in magnitude relative to the collective energy content of the bulk volume of the phases. This interfacial Gibbs energy is therefore of interest in the context of small aerosol particles and cloud droplets. In the case of macroscopic systems, the interfacial energy term can usually be neglected due to its comparably tiny contribution.

Gibbs defined interfacial energy (or tension) as the excess energy attributed to the 2-dimensional boundary present between two phases. However, the choice to describe the boundary between two phases as a 2D surface and deciding its exact location presented several problems, because real systems may exhibit concentration gradients near an interface. To account for this, Guggenheim introduced the concept of a 3-dimensional (3D) interfacial phase, which includes the boundary between two distinct phases and the concentration gradients of species therein (Guggenheim, 1940). While often on the order of a molecular monolayer or bilayer in depth, such an interfacial compartment can be treated as a distinct phase and must abide by the thermodynamic equilibrium conditions. Given the above-mentioned challenges when using Gibbs' 2D surface treatment and in order to more easily connect geometrically confined interfacial and bulk phases in a mass-conserving finite-volume system, the approach of Guggenheim's 3D interface is adopted in our framework. Thus, for application to fine and ultrafine particles, we introduce an interface with a small but finite thickness (δ). We will focus in the following derivations on particles of spherical shape (droplets).

Following the approach of Cai and Griffin (2005), species adsorbed onto or absorbed into the surface of an aerosol particle contribute to the total

volume of the particle. Thus, the interface only extends from the limit of the particle's radius inward and the total number of condensed-phase molecules of i (n_i^{tot}) is defined as the sum of the number of molecules of i in the bulk (n_i^b) and in the surface (n_i^s):

$$n_i^s + n_i^b = n_i^{tot}. \tag{2.11}$$

If the surface of an aerosol is chemically distinct from the underlying bulk phase, then a particle with one condensed (here liquid) bulk phase, a distinct surface phase, and the surrounding gas phase, will satisfy the criterion of equivalency of chemical potentials at equilibrium, as mentioned previously. As described by Aston and Herrington (1991), the chemical potential of a surface can be defined by differentiating Eq. (2.10) for a surface phase with respect to the molar amount of component i in the surface n_i^s:

$$\left(\frac{\partial G^s}{\partial n_i^s}\right)_{T,P,n_j^s,A} = \left(\frac{\partial G^s}{\partial n_i^s}\right)_{T,P,n_j^s,\sigma} - \left(\frac{\partial G^s}{\partial A}\right)_{T,P,n_i^s} \times \left(\frac{\partial A}{\partial n_i^s}\right)_{T,P,n_j^s,\sigma}. \tag{2.12}$$

This leads to the following expression for the chemical potential of a surface phase:

$$\mu_i^s = \xi_i^s - \sigma \mathscr{A}_i, \tag{2.13}$$

where $\xi_i^s = \left(\frac{\partial G^s}{\partial n_i^s}\right)_{T,P,n_j^s,\sigma}$, σ is the surface energy per unit surface area of the solution (i.e. the interfacial energy per unit area of the gas–liquid interface), and $\mathscr{A}_i = \left(\frac{\partial A}{\partial n_i^s}\right)_{T,P,n_j^s,\sigma}$ is the partial molar area of i. $\mathscr{A}_i$ can be found for a finite-depth Guggenheim surface phase of a spherical particle as follows:

$$\left(\frac{\partial A}{\partial n_i^s}\right)_{T,P,n_i^s,\delta} = \frac{\left(\frac{\partial A}{\partial r}\right)_{T,P,n_i^s,\delta}}{\frac{\partial n_i^s}{\partial r}}. \tag{2.14}$$

Here, the change in surface area of a sphere with respect to its radius is:

$$\left(\frac{\partial A}{\partial r}\right)_{T,P,n_i^s,\delta} = 8\pi r \tag{2.15}$$

and the volume of the finite-depth surface phase on a spherical droplet is:

$$v^s = \frac{4}{3}\pi(r^3 - (r-\delta)^3). \tag{2.16}$$

Differentiating Eq. (2.16) with respect to the particle radius assuming a constant surface depth leads to

$$\left(\frac{\partial v^s}{\partial r}\right)_{\delta} = 4\pi(2\delta r - \delta^2). \tag{2.17}$$

Equation (2.17) can be converted into an expression for $\frac{\partial n_i^s}{\partial r}$ with the inclusion of the molar volume of i in the surface ($\mathscr{V}_i^s$). This value is assumed to be the same as the bulk molar volume of pure i, which can be calculated by dividing the molar mass (M_i) by the liquid-state density (ρ_i). This yields

$$\frac{\partial n_i^s}{\partial r} = \frac{4\pi(2\delta r - \delta^2)}{\mathscr{V}_i^s}. \tag{2.18}$$

Combining Eqs. (2.15) and (2.18) along with the assumption that the molar volumes are additive in order to determine n_i^s leads to Eq. (2.19) for the partial molar area $\mathscr{A}_i$:

$$\mathscr{A}_i = \left(\frac{\partial A}{\partial n_i^s}\right)_{T,P,n_j^s,\sigma} = \mathscr{V}_i^s \frac{2r}{2\delta r - \delta^2}. \tag{2.19}$$

In the extreme case of the depth of the interface approaching the value of a droplet's radius, $\lim_{\delta \to r}$ of Eq. (2.19) reduces to $\frac{2}{r}\mathscr{V}_i^s$. In the opposite limiting case of a macroscopic system, in which $\delta \ll r$ and $\delta^2 \approx 0$, the $\lim_{r\to\infty}$ of Eq. 2.19 is $\frac{1}{\delta} \times \mathscr{V}_i^s$. Integrating partial molar areas by Euler's theorem leads

to

$$A = \sum_j n_j^s \mathscr{A}_j \tag{2.20}$$

for a multicomponent system with $j = 1, \ldots, k$ different species present. Note that for cases in which the surface phase extends beyond monolayer thickness, Eq. (2.20) indicates that the $\mathscr{A}_i$ values will not necessarily correspond to the area per molecule located directly at the 2D gas–liquid surface.

Returning to Eq. (2.13), the intrinsic chemical potential, ξ_i^s, of components in the surface phase can be formulated analogously to that of a liquid phase (Aston and Herrington, 1991):

$$\xi_i^s = \xi_i^{\circ,s} + RT \ln(a_i^s). \tag{2.21}$$

Here, $\xi_i^{\circ,s}$ is the intrinsic standard chemical potential and a_i^s is the activity of i in the surface phase. In the case of pure component i, Eq. (2.13) yields:

$$\mu_i^{\circ,s} = \xi_i^{\circ,s} - \sigma_i^\circ \mathscr{A}_i^\circ \tag{2.22}$$

where σ_i° is the surface energy per unit area of pure component i. For a more general multicomponent surface phase, Eq. (2.13) becomes:

$$\mu_i^s = \mu_i^{\circ,s} + RT \ln(a_i^s) + \sigma_i^\circ \mathscr{A}_i^\circ - \sigma_i \mathscr{A}_i. \tag{2.23}$$

Assuming that $\mathscr{A}_i^\circ \approx \mathscr{A}_i$ under all conditions, defining $\mu_i^{\circ,s} = \mu_i^{\circ,b}$, and further requiring that at equilibrium the chemical potentials of species across phases are equal, the effective surface tension of a multicomponent solution can be isolated to form the following equation:

$$\sigma_i = \sigma_i^\circ + \frac{RT}{\mathscr{A}_i} \ln\left(\frac{a_i^s}{a_i^b}\right). \tag{2.24}$$

At equilibrium all σ_i values must be equivalent to a common value, the effec-

tive solution surface tension (σ) . In this case, Eq. (2.24) can be recognized as the Butler equation (Butler and Kendall, 1932; Sprow and Prausnitz, 1966). Employing Eq. (2.24) for each component in a system, along with Eq. (2.11), leads to a system of equations for the equilibrium composition of a 3D Guggenheim interface. These equations can be solved iteratively in a nested manner in combination with the AIOMFAC-based gas–particle partitioning and liquid–liquid phase separation algorithms laid out in Zuend et al. (2010) and Zuend and Seinfeld (2013).

2.4.1 Calculation of Surface Composition

In order to determine the composition of the surface phase in practice, a system of equations which allows maximum freedom of variable ranges, yet simultaneously satisfies the volume balance constraints of the 3D interface, is required. Furthermore those equations must not modify variables that should be held constant during the calculation of partial derivatives. For this purpose, we have developed a conforming implementation within the extended AIOMFAC equilibrium model. We begin by introducing a term representing the fractional amount of component i relative to the total amount of i in the particle phase:

$$\varepsilon_i = \frac{n_i^s}{n_i^{tot}}, \tag{2.25}$$

where n_i^s denotes the molar amount in the surface phase and n_i^{tot} is the total molar amount of i available for partitioning (a constant during partitioning calculations). From the values of r_p and δ, the total volume of the surface phase is calculated according to Eq. (2.16). Likewise n_i^s, ρ_i, and M_i can be used to determine the volume of i in the surface phase. The fraction of the total surface volume occupied by i is given by

$$f_i = \frac{v_i^s}{v^s} = \frac{v_i^s}{\sum_j v_j^s}. \tag{2.26}$$

We now define a new variable, ζ_i, expressing the fraction of i in the surface

relative to its assigned volume range such that

$$\zeta_i \, v_i^{rg} + v_i^{min} = v_i^{s\star}, \tag{2.27}$$

where $v_i^{rg} = v_i^{max} - v_i^{min}$ and v_i^{max} and v_i^{min} are the respective maximum and minimum possible surface volume contributions. $v_i^{s\star}$ is the unnormalized surface volume contribution of i. The values of ζ_i can vary in the range from 0.0 to 1.0; however, there can be non-zero v_i^{min} values for some components (e.g. for water at very high RH) in order to achieve volume closure between the targeted geometric surface shell volume and the (unnormalized) volume as calculated by summing up the surface quantities, such that $v_i^{min} \geq 0$ and $v_i^{max} \geq v_i^{min}$. For a given particle composition, r_p, and δ, both v_i^{min} and v_i^{max} are species-specific constants. As such, v_i^{min} can be determined depending on whether all other components $j \neq i$ can occupy all of the surface volume if they are at their maximum abundance in the surface. If this is the case, then $v_i^{min} = 0$. Otherwise, $v_i^{min} > 0$. This leads to

$$v_i^{min} = \max \left[v^s - \sum_{j,j\neq i} v_j^{max}, \;\; 0 \right]. \tag{2.28}$$

Here, v_i^{max} is the maximum possible volume in the surface phase, less than or equal to v^s, such that

$$v_i^{max} = \min \left[n_i^{tot} \times \mathscr{V}_i, \;\; v^s \right]. \tag{2.29}$$

Returning to ζ_i, Eq. (2.27) can be rearranged as

$$\zeta_i = \frac{v_i^{s\star} - v_i^{min}}{v_i^{max} - v_i^{min}}. \tag{2.30}$$

For a given value of ζ_i, $v_i^{s\star}$ can be computed and then normalized to find f_i

via

$$f_i = \frac{v_i^{s\star}}{\sum_j v_j^{s\star}} \tag{2.31}$$

and a value for v_i^s can be determined via

$$v_i^s = f_i \times v^s. \tag{2.32}$$

We note that such calculated f_i and v_i^s values may violate the condition that $v_i^s \leq v_i^{max}$. This issue is remedied by introducing the relative deviation of actual to targeted surface phase volume as an additional equation (constraint) to be solved alongside with the equations describing the partitioning of $k-1$ components. From v_i^s, variables n_i^s and ε_i can be computed via $n_i^s = \frac{v_i^s}{\mathscr{V}_i}$ and then applied in Eq. (2.25) to obtain ε_i.

2.4.2 Initial guess generation

An initial guess for the surface composition of a given particle can be derived from a first calculation for a non-partitioning (superscript np) case. In this trivial case, the relative compositions of the surface and bulk phases are set to be identical, such that $x_i^s = x_i^b$ and $f_i^s = f_i^b$. From this case, an estimation of ζ_i^{np} can be computed given that:

$$f_i^{np} = \frac{n_i^{tot}\mathscr{V}_i}{\sum_j n_j^{tot}\mathscr{V}_j} \tag{2.33}$$

and

$$v_i^{s\star,np} = \min\left(f_i^{np}\, v^s,\ \ v_i^{max}\right), \tag{2.34}$$

to yield

$$\zeta_i^{np} = \frac{v_i^{s\star,np} - v_i^{min}}{v_i^{max} - v_i^{min}}. \tag{2.35}$$

Given the definition that $a_i = x_i\gamma_i$ for neutral components (and $a_{\pm,i} = \frac{m_{\pm,i}}{m^\circ}\gamma_{\pm,i}$ for electrolytes), Eq. (2.24) can be rearranged to the following form:

$$\ln\left(\frac{x_i^s}{x_i^b}\right) = (\sigma - \sigma_i^\circ)\frac{\mathscr{A}_i}{RT} - \ln\left(\frac{\gamma_i^s}{\gamma_i^b}\right). \tag{2.36}$$

As long as the same nonideal mixing model is used for bulk and surface activity coefficients (in this case, AIOMFAC), the activity coefficient ratio on the right-hand side of Eq. (2.36) is equal to 1 (only in this non-partitioning case). For a spherical particle of known surface volume v^s as well as f_i^s, and $\mathscr{V}_i$ values, the non-partitioning assumption enables the calculation of the molar phase amounts and the surface-to-bulk molar ratios, $\frac{n_i^s}{n_i^b}$. Using a composition-weighted mean of the pure-component surface tensions for σ allows for the evaluation of Eq. (2.36), which yields $\frac{x_i^s}{x_i^b}$. For neutral components (mole fraction scale), the obtained mole fraction ratios can then be converted into a (new) guess for the set of ε_i values as follows:

$$\varepsilon_i^{guess} = \frac{n_i^s/n_i^b}{1 + (n_i^s/n_i^b)} = \frac{x_i^s}{x_i^b}\frac{\sum_j n_j^s}{\sum_j n_j^b}. \tag{2.37}$$

For electrolyte components with activities defined on molality scale, the corresponding bulk–surface partitioning guess is generated via scaling by the surface-to-bulk phase mass ratio:

$$\varepsilon_i^{guess} = \frac{x_i^s}{x_i^b}\frac{\sum_l n_l^s M_l}{\sum_j n_l^b M_l}, \tag{2.38}$$

where the summation index l covers non-electrolyte components (i.e. solvents) only. Using the determined set of ε_i^{guess} values, Eq. (2.24) can be evaluated to obtain updated activity coefficient ratios, $\frac{\gamma_i^s}{\gamma_i^b}$, as well as an updated weighted-mean estimate of the surface tension, which can then once more be evaluated with Eq. (2.36) and processed to obtain an updated ε^{guess} vector. If desired, one can expand on this approach by using the determined

activity coefficient ratios (in this case kept fixed) together with a set of distinct guesses for potential equilibrium σ values in Eq. (2.36), yielding a set of initial guesses for the ε_i values. Systematically generating more than one initial guess is useful when the subsequent numerical solution of the system of nonlinear equations, given by Eqs. (2.24) or (2.40), is unsuccessful in case of the first initial guess evaluated – or to further explore whether more than one solution may exist. In our modern Fortran implementation, the system of equations is solved by a modified, bound-constrained version of Powell's hybrid method (Moré et al., 1980, 1984). Our extensive numerical testing suggests that this approach results in a fast and robust method for finding the equilibrium bulk–surface partitioning state for a given overall particle composition, radius and interfacial thickness.

2.4.3 Model Assumptions

A key piece of information that is necessary to solve Eq. (2.24) is the liquid-state pure-component surface tension, σ_i°, at given temperature. In this work, σ_i° values of organic components were taken from published data (Hyvärinen et al., 2006; Riipinen et al., 2007; Booth et al., 2009) or, in the case of glutaric acid, extrapolated from high concentration data of a binary aqueous solutions (Booth et al., 2009). For inorganic electrolyte components, σ_i° was calculated using the approach for estimating pure molten salt surface tensions as described in Dutcher et al. (2010). Organic compounds with poorly constrained σ_i° values were assumed to have values of 35 $\mathrm{mJ\,m^{-2}}$. In addition, there are physical constraints applied to the surface phase thickness δ in this study. The lower limit of δ was selected to be 0.15 nm, or the approximate length of a single alkane C−C bond. The upper bound for δ was selected to be 1.0 nm for all systems tested, which is the approximate length of 3 water molecule diameters. An alternative assumption was also tested: a treatment where δ is a function of particle or surface phase composition; however, there is limited information on how exactly δ should change as a function of composition. Therefore, in this test case it was assumed that

a simple weighted average of molecular lengths based on the surface mole fraction in the particle phase could be used. These molecular lengths were computed based on $\mathscr{V}$ for each species and the assumption that the molecular length scale can be approximated by the side length of a volume-equivalent cube. Following the calculation of the surface composition, δ was updated and the surface composition was recalculated. This process was repeated iteratively until convergence (within a set tolerance) to a stable δ value. It is also important to note that Eqs. (2.24) and (2.40) cannot be solved directly for a species which is completely insoluble in either the surface or the bulk phase. As such, the relative surface tension deviations, to be solved for from these equations, are scaled by a smooth ($\sim$ rectangular step) weighting factor expressed by the following function:

$$\Delta\sigma_i = \frac{\sigma_i - \bar{\sigma}}{|\bar{\sigma}| + \tau_\sigma} \times \frac{\varepsilon_i(1-\varepsilon_i)}{\varepsilon_i(1-\varepsilon_i) + 100\sqrt{\epsilon}\cdot\exp\left[-\sqrt{\varepsilon_i(1-\varepsilon_i)}\right]}. \tag{2.39}$$

Here, ϵ is the floating point machine precision employed, $\bar{\sigma}$ the weighted mean surface tension and τ_σ a tolerance value, typically set to 0.1 $\mathrm{J\,m^{-2}}$. The weighting factor (expression after $\times$) on the right-hand side of Eq. (2.39) evaluates to near 1.0 in most cases and smoothly transitions to substantially smaller values only as i becomes very close to insoluble in either the surface phase or bulk phase, in which case ε_i approaches either 1 or 0. Therefore, in cases of extremely limited solubility of i in the surface or bulk, the contribution of i to the system of equations used to solve for bulk–surface equilibrium is diminished (a desired property, since the numerical uncertainty grows near the limits of solubility and numerical precision limitations become substantial). We note that the weighting factor is computed prior to (but not during) numerically solving the system of equations and is only updated if deemed necessary afterwards, such as when the solver was unsuccessful for set numerical tolerances and the equations solving needed to be repeated. Furthermore, a closely related weighting factor, which is normalized by the

sum of weightings such that the resulting fractional weights sum to 1.0, is used in the calculation of the weighted mean $\bar{\sigma}$ value during the process of iteratively solving the system of equations (i.e. solving simultaneously solving Eq. (2.39) via Eq. (2.24) for all components).

An additional assumption made in this study concerns the computation of activity coefficients. It is assumed that there are no modifications to the calculation (by AIOMFAC) of activity coefficients in the surface phase compared to the bulk phase. Lane (1983) introduced a common exponential correction factor, t, that is applied to the calculated activity coefficients of a surface phase, such that $\gamma_i^s = \left(\gamma_i^{s,calc}\right)^t$. The introduction of such an exponent is motivated by the idea that activity coefficients in a surface, affected by some limitations in the molecular packing options, may deviate slightly from those calculated for a bulk phase of identical composition and temperature. However, estimated values of t are system-dependent, yet often close to unity (Lane, 1983). Because the inclusion of additional semi-empirical terms limits the flexibility of the targeted predictive capability of the model developed in this work, it is assumed that $t = 1$ for all systems.

Returning to Eq. (2.24), if an alternate assumption is made about the partial molar areas, specifically that $\mathscr{A}_i^\circ \neq \mathscr{A}_i$, then the expressions previously leading to Eq. (2.24) result in:

$$\sigma_i = \sigma_i^\circ \frac{\mathscr{A}_i^\circ}{\mathscr{A}_i} + \frac{1}{\mathscr{A}_i} RT \ln\left(\frac{a_i^s}{a_i^b}\right). \tag{2.40}$$

and $\mathscr{A}_i^\circ$ can be found for a pure droplet of i analogous to Eq. (2.19), with the only modification being that the interfacial thickness used is that of the pure component, i.e. set $\delta = \delta_i^\circ$. If it is assumed that only a monolayer of molecules form the surface of a pure-component droplet then δ_i° can be estimated based on the molecular size of i. With this information, Eq. (2.40) can be employed with Eq. (2.11) and Eq. (2.39) in the same manner as Eq. (2.24) to form a system of equations for solving numerically the equilibrium bulk–surface

partitioning problem.

2.5 Results and discussion

2.5.1 Comparison of measured and predicted surface tension

In order to determine the validity of the described predictive model, comparisons were made to measurements for a selection of atmospherically relevant binary systems. Figure 2.2A shows the predicted surface tension (utilising AIOMFAC with Eq. 2.24) as a function of the total particle-phase concentration of glutaric acid in a binary water–glutaric acid droplet that was allowed to grow hygroscopically from a starting dry diameter of 5 μm to the point of cloud droplet activation, corresponding to a diameter of approximately 10 μm. This scenario allowed us to compare predicted surface tensions to the bulk tensiometry and optical tweezers measurements taken by (Bzdek et al., 2016). The three curves shown in Fig. 2.2A correspond to three different values of δ: 0.1 nm, which is the approximate length of a single carbon–carbon bond; 0.3 nm, which is the approximate length scale of a single water molecule (the same value was also used as a minimum thickness in models by Davies et al. (2019) and Ovadnevaite et al. (2017); and 1.0 nm, which corresponds to the approximate size of a single glutaric acid molecule along its longest axis.

It is shown that assuming a thinner interfacial thickness value leads to a surface tension curve which is highly sensitive to the overall concentration of glutaric acid in the droplet. Analogously, an interfacial thickness that is larger will require greater changes in the total particle-phase concentration of an organic species in order to observe a similar decrease in surface tension. In addition to the binary water–glutaric acid system, Bzdek et al. (2016) also analyzed a binary water–sodium chloride system of the same size using the bulk tensiometry and optical tweezers approaches. Shown along with these

data in Fig. 2.2B are bulk measurements by Ozdemir et al. (2009). While the surface tension increases with salt concentration in this case, a similar behavior can be seen in the surface tension vs. concentration curves for the inorganic electrolyte system, wherein the curve is sensitive to the selection of δ. However, for the system shown in Fig. 2.2B, the sensitivity of the modeled surface tension to the value of δ is opposite of that for surface-active organic species. This is likely due to the fact that electrolytes preferentially partition into the bulk phase; therefore, a thinner interface will contain a higher mole fraction of water (at a specific wet diameter) and requires greater concentrations of electrolytes to increase a droplet's surface tension.

Additional sensitivity comparisons were performed to determine the effect of modifying σ_i° by $\pm 10\%$. It was found that glutaric acid was more sensitive to modifications in the value of $\sigma_{glutaric}^\circ$ than NaCl, which was very weakly sensitive to increases in σ_{NaCl}° and somewhat sensitive to reductions in σ_{NaCl}°. Overall, using $\delta = 0.3$ nm leads to surface tension predictions in better agreement with the measurements shown for large droplets or macroscopic solutions. This suggests that a molecular monolayer assumption for representing the surface phase is a relatively good model, at least for the systems shown in Figs. 2.2A and 2.2B.

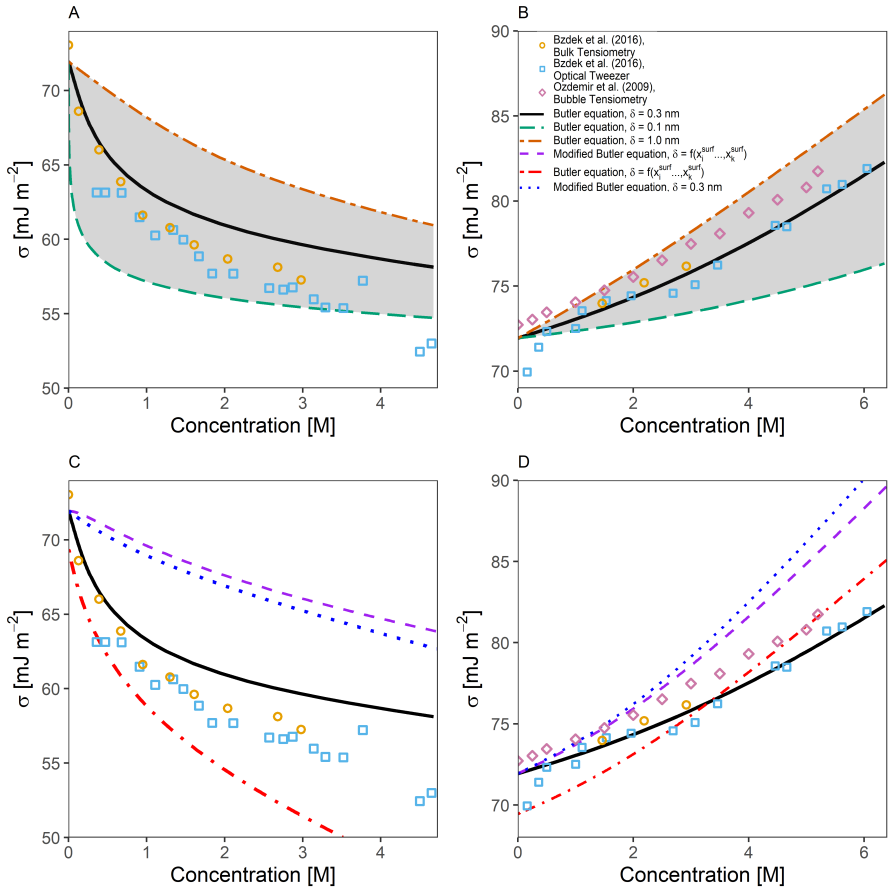

Figure 2.2: Predicted and measured surface tensions for (A) a binary water–glutaric acid system and (B) a binary water–sodium chloride system as a function of solute concentration in water at 298 K. The area shaded in grey represents the predicted surface tension bounded by the proposed limits for δ of 0.1 nm and 1.0 nm. The solid black line is the predicted surface tension for $\delta = 0.3$ nm. Also shown in (C) and (D) are the same systems as (A) and (B) respectively but with the assumption that $\mathscr{A}_i \neq \mathscr{A}_i^\circ$ leading to a modified form of the Butler Equation (Eq. 2.40) and the testing the surface composition based approach for determining δ.

Figures 2.2C and 2.2D show the effects of exploring different assumptions of Eq. (2.24) along with the same measurements from Figs. 2.2A and 2.2B. The modified Butler equation, which assumes that $\mathscr{A}_i^\circ \neq \mathscr{A}_i$ (Eq. 2.40 in this work) consistently overestimates the surface tension of the water–glutaric-acid-system and only agrees with the water–NaCl system at very low concentrations. Assuming that δ is surface composition-dependent also leads to poor agreement with experimental data at high concentrations for the water–glutaric-acid system and better agreement at low concentrations. For the water–NaCl system, it can be seen that the opposite is true; the composition-dependent δ leads to good agreement at higher concentrations than lower concentrations. The combination of Eq. (2.40) and a surface composition-dependent δ leads to poor agreement across all concentrations shown for the water–glutaric-acid system and only gives good agreement for the water–NaCl system at low concentrations.

It is important to note that the sizes of the droplets analyzed in Bzdek et al. (2016) are large relative to the more numerous but substantially smaller atmospheric aerosol particles of importance in cloud formation. However, there is a paucity of surface tension data available for droplets in the sub-500 nm size range, since it is extremely difficult to measure the surface tension of atmospherically relevant aerosol particles that are freely suspended while at sizes near or below the wavelengths of visible light. Recent developments in atomic force microscopy have allowed for surface tension measurements of sub-500 nm particles to be taken Lee et al. (2017) directly and are indeed promising as a source of measurement data at that size scale. In the present study, such measurements were not analyzed because placing the droplet on a glass substrate introduces a second interface, the substrate–droplet interface, which may modify the partitioning behavior of different species as well as affect the geometry of the droplet from spherical to approximately semi-spherical. At the moment, the framework laid out in this work is only capable of handling spherical geometries with a single gas–droplet surface;

the inclusion of interfaces between two condensed phases and the treatment of non-spherical geometries is the subject of future work.

2.5.2 Bulk phase depletion

While the measured particles associated with the data from Fig. 2.2 are large, the effects of bulk–phase depletion cannot be neglected entirely. Figures 2.3A, 2.3B, and 2.3C show surface tension as a function of particle size and δ for binary water–adipic acid systems of particles with dry diameters of 1.0 nm, 10 nm, 100 nm, 1 μm, 10 μm, 100 μm, 1 mm, and 1 cm (ranging over 8 orders of magnitude).

It is shown that even highly dilute particles with dry diameters below 100 μm have different surface tensions at the same total mole fraction of adipic acid in the condensed phase. If the value of δ decreases, the surface tension curves for larger dry diameters converge, and bulk phase depletion is only noticeable for the smallest particles. If δ is increased to be more similar to the molecular length scale of the solute species ($\sim$ 0.45 nm), there is better agreement between modeled and measured surface tension values in the larger sized droplets. Increases in δ also increase the minimum concentration of solute necessary to decrease the surface tension from that of pure water for all particle sizes; however, smaller particle sizes are more responsive to this change than larger ones. A method for determining this dependence is by taking the concentration of solute ($c_i^{\mathrm{d}\sigma}$) at which the change in surface tension with each additional molecule of solute added is the greatest; in other words, the global extrema (minimum for surfactant species and maximum for tensoionic species) of $\frac{\mathrm{d}\sigma}{\mathrm{d}X_i^{total}}$.

Figure 2.3D shows how $X_i^{\mathrm{d}\sigma}$ varies as a function of size for the binary water–adipic acid system. Droplets with initial dry diameters on the order of 1 μm may still experience mild bulk-depletion effects depending on the selection of the interfacial thickness value, with larger δ values leading to more pronounced bulk-phase depletion effects at larger sizes. Moreover, we note that the value of $X_i^{\mathrm{d}^2\sigma}$ is strongly dependent on δ at larger sizes compared

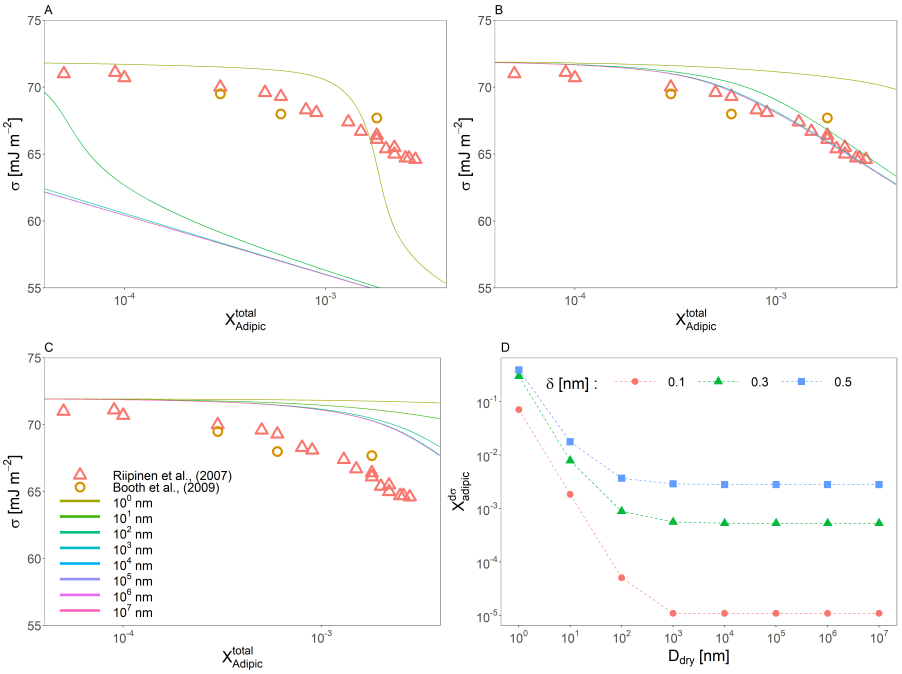

Figure 2.3: Predicted surface tensions of a binary water–adipic acid system across 8 orders of magnitude in dry particle diameter (see legend in panel C) for interfacial thickness values of (A) 0.1 nm, (B) 0.3 nm, and (C) 0.5 nm. (D) The specific concentrations of adipic acid for which the surface tension is the most sensitive to changes in the overall mole fraction of adipic acid as a function of dry diameter and δ. Also shown in (A), (B), and (C) are measurements taken by Riipinen et al. (2007) and Booth et al. (2009).

to smaller ones, with a doubling of the interfacial thickness from 0.15 nm to 0.3 nm leading to approximately 3 orders of magnitude increase in the value of $X_i^{\mathrm{d}\sigma}$ for particles with dry diameters larger than 1 μm. This same change in δ for particles with dry sizes below 100 nm leads to differences of about 2 orders of magnitude or less. Thus, we demonstrate that bulk-phase depletion may modify surface tension as a function of particle composition on particles up to the micrometer size scale.

The bulk–surface concentration ratio $\frac{x_i^{surf}}{x_i^{bulk}}$ is independent of the volume ratio and represents the physicochemical partitioning coefficient. Figure 2.4

shows these mole fraction ratios for each species in a ternary water–glutaric-acid–sodium-chloride system as a function of equilibrium saturation ratio (S). Monodisperse particles consisting of a 1:1 molar ratio of glutaric acid to sodium chloride, with dry diameter values ranging from 10 nm to 500 nm, were allowed to grow hygroscopically until the point of cloud droplet activation (while maintaining the same solute masses, i.e. no gas–particle partitioning of glutaric acid considered). In this test, a forced 1-phase calculation was performed (only allowing a single bulk liquid phase to exist), which prevented the particles from undergoing LLPS at compositions where that would be favorable. The value of δ was held constant at 0.3 nm and Eq. (2.24) was employed.

It can be seen that glutaric acid, while only a weakly surface-active compound compared to lower-polarity organics, is nevertheless strongly enriched in the surface of the particle across all particle sizes, especially at higher values of S. The predicted surface tension for each particle is also shown. The difference in σ of particles is largest at both very low and very high values of S with all of the σ values being most similar for saturation ratios between 0.675 and 0.725. However, particles with diameters below 25 nm exhibit greater deviations from the behavior of their larger counterparts. These smallest particles both achieve a slightly lower minimum surface tension and slightly higher surface tension values under low a_w conditions. This may be driven by the fact that under these conditions, more tensoionic species must be present in the surface due to limited amounts of both water and organic species. However, this effect is still quite weak even at such small particle sizes.

If Eq. (2.40) is employed for bulk–surface equilibrium predictions, the δ_i° values for water, glutaric acid, and sodium chloride are calculated based on their molecular sizes. This leads to modified bulk–surface partitioning behavior as shown in Figs. 2.5A and 2.5B. The assumption that $\mathscr{A}_i^\circ \neq \mathscr{A}_i$ effectively modifies the value of σ_i° by multiplying it by the ratio $\frac{\mathscr{A}_i^\circ}{\mathscr{A}_i}$. In

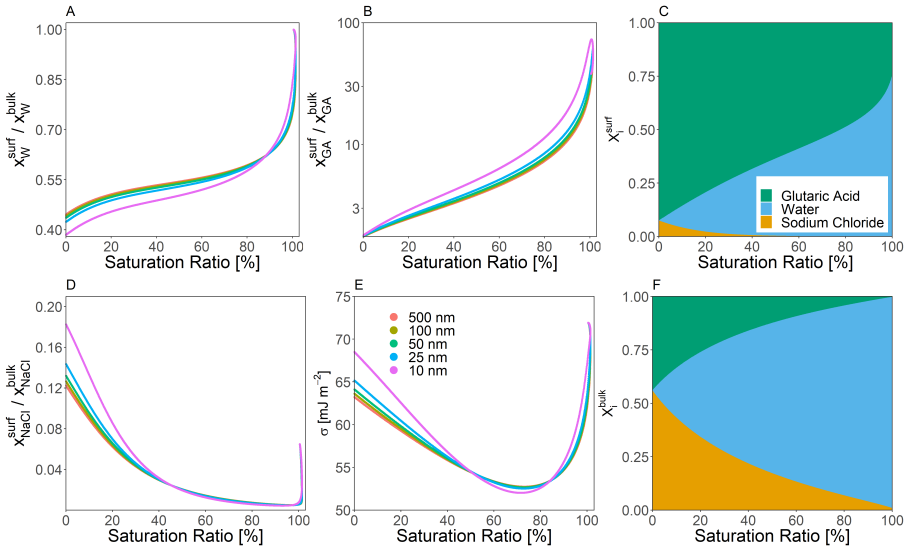

Figure 2.4: Predicted bulk–surface partitioning coefficient ($\frac{x_i^{\mathrm{surf}}}{x_i^{\mathrm{bulk}}}$) of (A) water, (B) glutaric acid, and (D) sodium chloride present in a forced single-bulk-phase particle at $T = 298$ K. A molar dry solute ratio of 1:1 was used in all cases. (E) Predicted effective surface tension for several particle dry diameters as indicated by color. Right column (composition bar graphs): shown are the mole fractions of each species in the surface and the bulk phase (α) for a particle of 25 nm dry diameter.

the macroscopic case, where $r \gg \delta$, then $\lim_{r\to\infty} \frac{\mathscr{A}_i^\circ}{\mathscr{A}_i} = \frac{\delta_i^\circ}{\delta}$, showing again an important effect of the calculated or assumed value of δ. In the case of species for which $\delta_i^\circ < \delta$, a stronger affinity for the surface results, while for $\delta_i^\circ > \delta$, it is expected that species i would have a weaker affinity for the surface phase. Notably, the feedbacks on the partitioning behavior of one species can still modify the bulk–surface partitioning of other species since modifications to the composition of the surface phase will modify the activity coefficients for all species in the phase.

In Fig. 2.5, it can be seen that the assumption that $\delta = \delta_{water}^\circ$ leads to decreased partitioning of water as both glutaric acid and sodium chloride show an increased affinity for the surface phase. This also modifies the effective solution surface tension. In the case where $\delta = \delta_{water}^\circ$, σ is consistently lower than the values predicted by Eq. (2.24). In the case where δ lies between all of the values of δ_i°, σ predicted by Eq. (2.40) is lower than the value predicted by Eq. (2.24) when the solution is highly concentrated in both organic and inorganic solutes (low a_w) and higher than the Eq. (2.24) in more dilute cases (high a_w). These findings suggest that it is best to assume that $\mathscr{A}_i^\circ \approx \mathscr{A}_i$ for most systems.

2.5.3 Köhler curves

Numerous different test systems have been used in laboratory experiments and modeling studies to better understand the role of bulk–surface partitioning on the behavior of CCN both before and after activation. One such system that will now be considered has been studied in experiments and theory by Ruehl et al. (2016). They generated 150 nm (dry diameter) mixed suberic acid–ammonium sulfate particles corresponding to a spherical 50 nm diameter ammonium sulfate core coated with a 50 nm layer of suberic acid. Figure 2.6A shows the Köhler curve calculated via Eq. (2.1) with the assumption that a_w in that equation is determined from the bulk phase composition of the particle. Figure 2.6B also shows a particle with the same organic volume fraction as Figure 2.6A, but of a water-free diameter of 40 nm instead

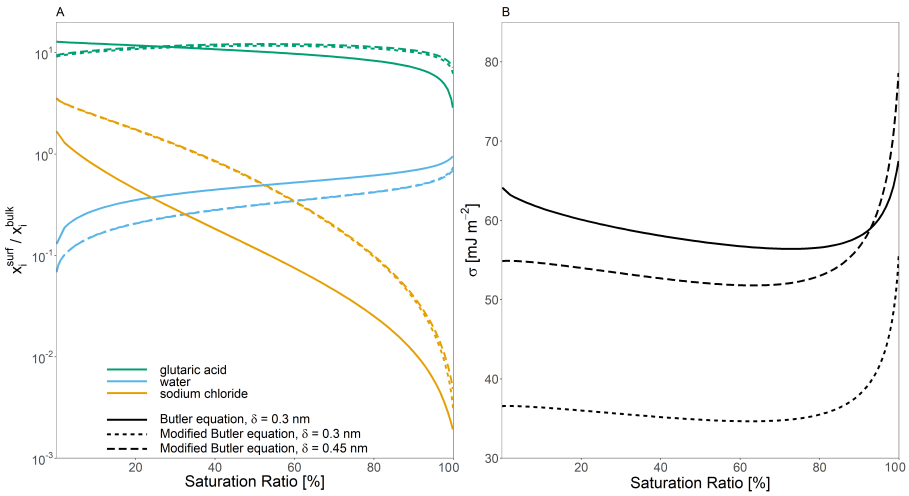

Figure 2.5: The effect of implementing a modified form of the Butler equation (Eq. 2.40) with the assumption that $\mathscr{A}_i^\circ \neq \mathscr{A}_i$ for a water–glutaric acid–sodium chloride system with a 1:1 water-free molar ratio of glutaric acid to sodium chloride on (A) the bulk–surface partitioning coefficient, $\frac{x_i^{\mathrm{surf}}}{x_i^{\mathrm{bulk}}}$, and (B) predicted surface tension, σ. All calculations were performed at a temperature of 298 K.

of 150 nm. Different interfacial thicknesses (δ) are shown including the values determined by the compressed film model used in (Ruehl et al., 2016). The resulting behavior of the Köhler curve is highly sensitive to the value of δ; particularly as δ approaches the lower limit of physically realistic values. The shape of these Köhler curves are determined by the point at which the surface tension of the particle becomes similar to that of pure suberic acid relative to a given saturation ratio. In systems with δ values that are smaller the surface remains is enriched in suberic acid at higher S values than systems with larger δ values. This lowered surface tension at high S values may lead to modifications of the shape of the Köhler curve, including the branch at sizes greater than the critical wet diameter for CCN activation. Such behavior can be seen in the blue curve of Fig. 2.6A .

Also shown in panels A and B of Fig. 2.6 are AIOMFAC-based predictive treatments of bulk–surface partitioning and CCN activation for such systems, as discussed in prior work (Ovadnevaite et al., 2017; Davies et al., 2019). These prior treatments both assume a surface with adjustable depth, consideration of LLPS and, in the presence or absence of bulk LLPS at higher a_w values, the calculation of an effective surface tension using a volume-fraction-weighted mixing rule of the pure-component surface tension values based on the bulk liquid phase compositions (and area fractions in case of LLPS) in contact with the droplet surface. In this case, both simulations used $\delta = 0.3$ nm and the same pure-component surface tension values as used in the more detailed approach developed in this work. Briefly, these are two thermodynamic model variants for the computation of droplet surface tension as a function of composition, size, and temperature, introduced by (Ovadnevaite et al., 2017) (see their supplementary information) and also discussed and applied by (Davies et al., 2019).

AIOMFAC-Equil is a full "bulk" equilibrium model, including gas–particle partitioning and liquid–liquid phase separation (LLPS), but without consideration of bulk–surface partitioning. In the context of surface tension

predictions, a procedure for the post-processing of model outputs has been introduced by (Ovadnevaite et al., 2017), which assumes a core–shell droplet morphology in the case of LLPS. The AIOMFAC-Equil model treats the droplet surface tension as the surface-area-fraction-weighted average of the surface tensions of the present liquid phases (when no complete shell is formed by an organic-rich phase). The initial surface tensions of those phases are computed based on a volume-fraction-weighted mean of the pure component surface tensions.

The "AIOMFAC-CLLPS with organic film" model variant assumes complete LLPS among organics and inorganics (except for water) at all RH levels. It further assumes that all organic species in the droplet are present in a water-free layer at the surface of the droplet, while all electrolytes are present in an (aqueous) core phase of the droplet. The surface tension of the droplet in this model is equal to the surface tension of the organic film (phase), assuming complete coverage by the organic phase, or the surface-area-fraction-weighted average of the organic phase and the electrolyte-rich aqueous phase, should there be insufficient organic material to completely cover the droplet (Davies et al., 2019). The AIOMFAC-Equil. prediction leads to substantially higher critical supersaturations than observed, because this model variant ignores bulk–surface partitioning in the case of a single bulk phase present at higher RH, as in the system of Fig. 2.6. In contrast, the AIOMFAC-CLLPS variant with an imposed organic film assumption agrees reasonably well with the measured critical supersaturations. Indeed, if δ is assumed to be 0.3 nm for both prior AIOMFAC-based treatments (in those cases setting the minimum thickness of the surface phase), then the calculation by the AIOMFAC-CLLPS variant with an organic film represents the measured data better than the approach laid out in this work. However, if the δ value is lowered, then the bulk–surface equilibrium approach from this study shows excellent agreement with the measured peak supersaturation and, importantly, does not rely on the same simplifying assumptions as the

organic-film-based calculation.

Figure 2.6B demonstrates the effect of particle size (dry diameter of 40 nm) and bulk–surface partitioning on CCN activation, since the deviations from classical Köhler curve behavior (using a fixed surface tension, that of pure water) are more pronounced in both the $\delta = 0.3$ nm and $\delta = 0.15$ nm cases. In the example of Fig. 2.6, the AIOMFAC-Equil. prediction is representative of a classical Köhler curve, since that model does not predict LLPS in the high-a_w range close to the CCN activation point for this system. Clearly, in the case of ultrafine particles, a more detailed treatment of bulk–surface partitioning and associated surface tension evolution leads to notable deviations from classical behavior. Indeed a more detailed and thermodynamically rigorous treatment of bulk–surface partitioning leads to better agreement of the activation conditions in comparison to laboratory studies of water–suberic-acid–ammonium-sulfate particles than previous AIOMFAC-based treatments.

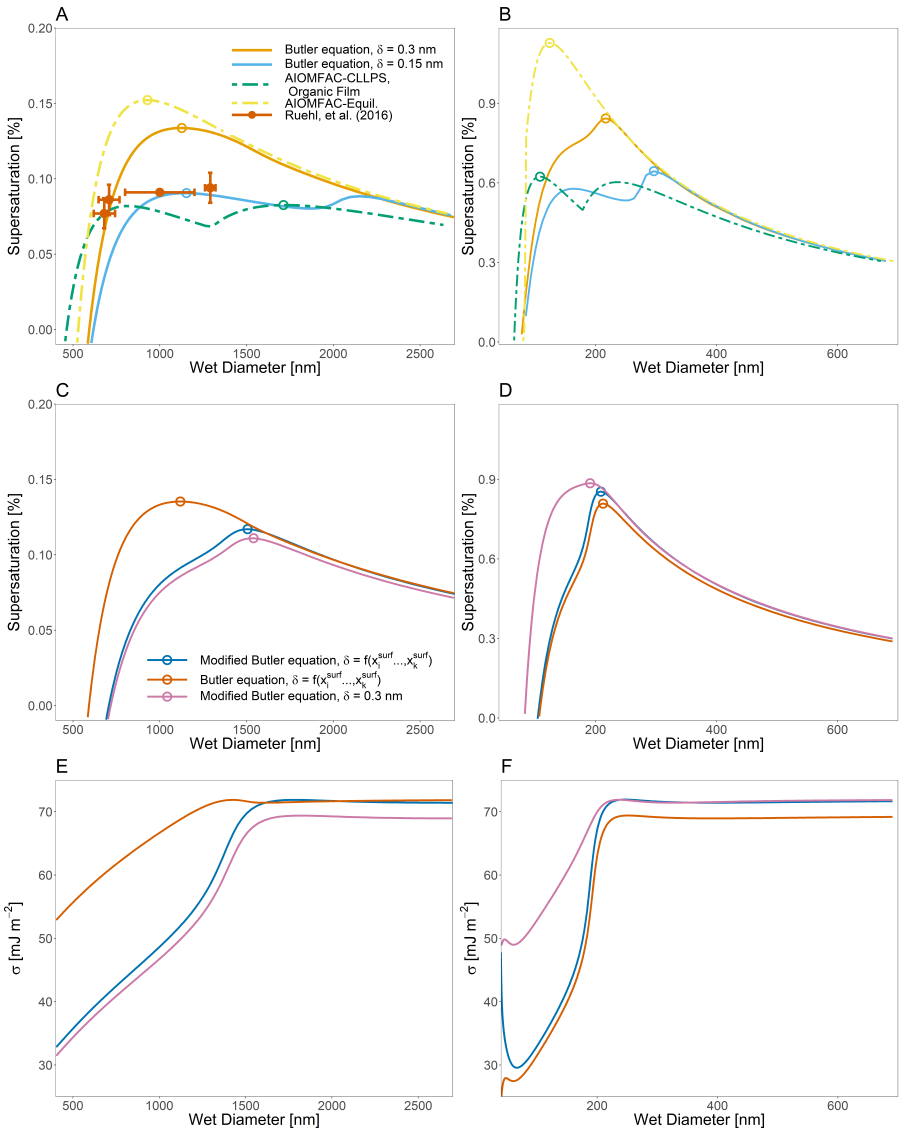

Figure 2.6: Köhler curves for ternary water-suberic acid-ammonium sulfate particles at 298 K at an organic volume fraction of 0.88 and with a water-free diameter of (A) 150 nm (B) 40 nm. Also shown in (A) are the measured SS_{crit} and the critical wet diameter measured by Ruehl et al. (2016). (C) and (D) show the calculated Köhler curves if the assumption is made that $\mathscr{A}_i^\circ \neq \mathscr{A}_i$ leading to the modified Butler equation (Eq. (2.40)), as well as the effect of modifying δ as a function of overall particle composition. (E) and (F) show the calculated σ values for the systems shown in (C) and (D).

Table 2.1: Critical wet diameter and supersaturations for the Köhler curves shown in Figure 2.6.

Model type	δ [nm]	$\mathscr{A}_i^\circ$	$D_{dry} = 150$ nm		$D_{dry} = 40$ nm	
			D_{crit} [nm]	SS_{crit} [%]	D_{crit} [nm]	SS_{crit} [%]
Eq. (2.24)	$\delta = 0.3$ nm	$\mathscr{A}_i^\circ = \mathscr{A}_i$	1127.0	0.13	216.8	0.84
Eq. (2.24)	$\delta = 0.15$ nm	$\mathscr{A}_i^\circ = \mathscr{A}_i$	1153.4	0.09	296.3	0.64
Eq. (2.40)	$\delta = f(x_i^{surf}, ..., x_k^{surf})$	$\mathscr{A}_i^\circ \neq \mathscr{A}_i$	1505.8	0.12	208.8	0.85
Eq. (2.24)	$\delta = f(x_i^{surf}, ..., x_k^{surf})$	$\mathscr{A}_i^\circ = \mathscr{A}_i$	1118.3	0.14	212.29	0.81
Eq. (2.40)	$\delta = 0.3$ nm	$\mathscr{A}_i^\circ \neq \mathscr{A}_i$	1540.4	0.11	190.9	0.89
AIOMFAC-Equil	$\delta = 0.3$ nm	–	929.2	0.15	124.1	1.1
AIOMFAC-CLLPS, organic film mode	$\delta = 0.3$ nm	–	1713.0	0.09	108.1	0.62

To further demonstrate the predictive power of the model developed in this work, an isoprene SOA system was considered as well. This system consists of water and 21 semivolatile isoprene photo-oxidation products, as proposed for a simplified isoprene-derived SOA representation in previous modeling work (Rastak et al., 2017; Gervasi et al., 2020). Because of the higher volatility of some of the isoprene SOA species, the effects of organic co-condensation (or more generally gas–particle partitioning) during hygroscopic growth should also be analyzed to better understand atmospheric implications of such aerosol systems. Concentrations simulated by the Master Chemical Mechanism (Jenkin et al., 2015, 1997, 2012) were used as inputs for the "co-condensation enabed" case (Rastak et al., 2017) (see table A.1 in Appendix B). A distinct case, in which the organic composition of the particle was fixed, termed the "co-condensation disabled" case, was also used for comparison. In that case, the equilibrium composition of the particle was taken from a bulk equilibrium gas–particle partitioning calculation at 0.1 % RH and then fixed for the organics (essentially rendering them nonvolatile), such that only water could partition between the gas and particle phases in subsequent computations. We note that for this isoprene SOA system, the values of the various σ_i° have not been measured. We therefore assumed

that $\sigma_i^\circ = 35\ \mathrm{mJ\,m^{-2}}$ for all species, which is in line with the assumptions made in Davies et al. (2019); Ovadnevaite et al. (2017) (see figure A.7 in Appendix B for an analysis of the framework sensitivity to σ_i° values). Based on experiments as well as AIOMFAC LLPS equilibrium computations for bulk solutions, this system is not expected to undergo LLPS at any RH (Rastak et al., 2017).

Figure 2.7A shows the Köhler curve for a particle of 25 nm in dry diameter with co-condensation enabled and disabled. Figure 2.7B shows the contribution of the Raoult effect for both systems shown in Fig. 2.7A. Likewise Fig. 2.7C shows the contribution of the Kelvin effect for the same system. The inclusion of co-condensation of organic species leads to substantial reductions in S_{crit} for this system through modifications to both the Raoult effect and the Kelvin effect.

2.6 Theoretical and atmospheric implications

2.6.1 Theoretical implications

One source of uncertainty in the approaches to bulk–surface partitioning described in Sect. 2.3 is determining the effective partial molar area of a given species, $\mathscr{A}_i$, in a mixed surface phase and how that value may differ from the molar area of pure i, $\mathscr{A}_i^\circ$. A common assumption is that the apparent molar area can be calculated from the molar volume ($\mathscr{V}_i$) of a species as $\mathscr{A}_i = \mathscr{V}_i^{\frac{2}{3}}$ and that the molar area of a species in solution is the same as its pure-component value $\mathscr{A}_i \approx \mathscr{A}_i^\circ$. Table 2.2 lists the partial molar areas of numerous organic species calculated using Eq. (2.19) for particles of three distinct diameters and $\delta = 0.15$ nm or $\delta = 1.0$ nm. Those diameter choices serve to demonstrate a size dependence in this parameter when calculated via Eq. (2.19). Also shown are the size-independent partial molar areas when computed under the $\mathscr{A}_i = n_A^{\frac{1}{3}} \mathscr{V}_{b,i}^{\frac{2}{3}}$ assumption or with the empirical approach

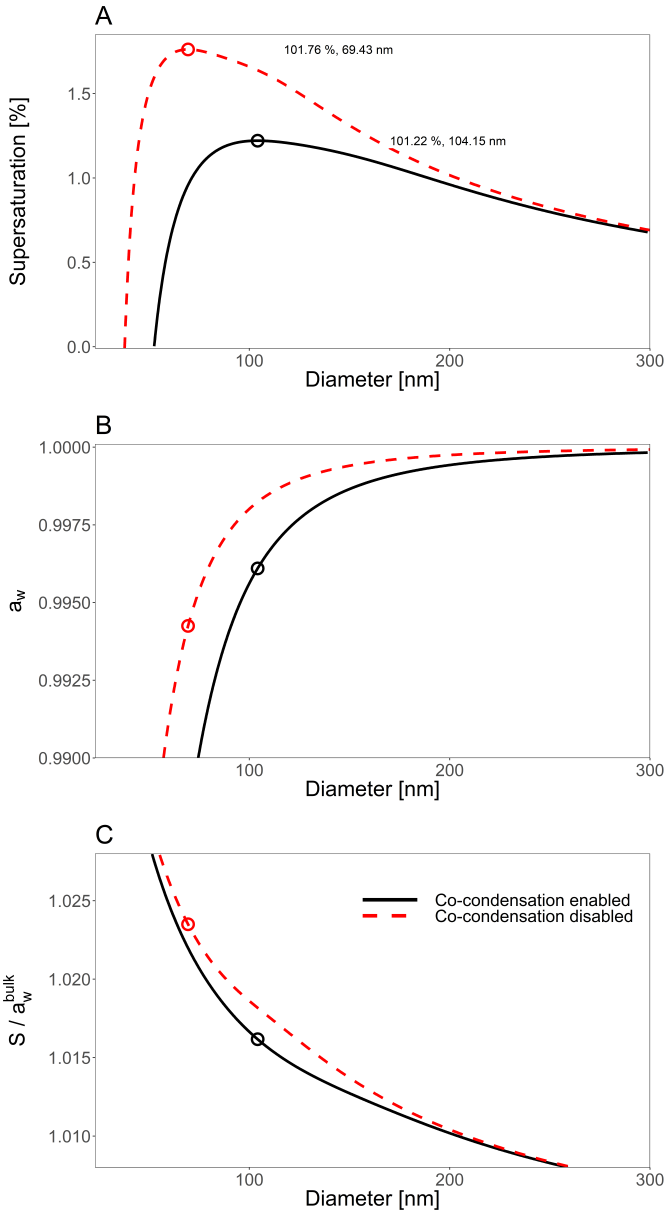

Figure 2.7: (A) The effect of including co-condensation of SVOC species for an aqueous 21-component system of isoprene-derived SOA (Rastak et al., 2017; Gervasi et al., 2020) with $D_{dry} = 23$ nm. (B) The bulk-phase water activity, corresponding to the contribution of the Raoult effect to the Köhler curves shown in (A). Panel (C) shows the Kelvin effect term's contribution to the curves in (A). For the co-condensation-disabled case, the particle's water-free composition was taken at RH = 0.1% and then only water was allowed to partition to and from particles with this dry composition. For a detailed description of the system components, see Table A.1 in Appendix A.

developed by Goldsack and White (1983):

$$\mathscr{A}_i = 1.021 \times 10^8 \times \mathscr{V}_{c,i}^{\frac{6}{15}} \mathscr{V}_{b,i}^{\frac{4}{15}}, \tag{2.41}$$

where $\mathscr{V}_{c,i}$ and $\mathscr{V}_{b,i}$ are the critical and bulk molar volumes. It should be noted that the scaling factor in Eq. (2.41) requires that the values of $\mathscr{V}_{c,i}$ and $\mathscr{V}_{b,i}$ are input in units of $\mathrm{cm}^3\,\mathrm{mol}^{-1}$; the equation then returns $\mathscr{A}_i$ in units of $\mathrm{cm}^2\,\mathrm{mol}^{-1}$. In the mathematically sound framework developed in this work, the values of $\mathscr{A}_i$ are weak functions of particle radius r_p; however, they are stronger functions of the value of δ, with smaller δ values leading to smaller $\mathscr{A}_i$ values.

Another important assumption made regarding the treatment of $\mathscr{A}_i$, is the assumption that the density of i in the surface phase (ρ_i^s) is equivalent to that of the pure component value of a (bulk) liquid state. Currently, all AIOMFAC-based bulk solution calculations make the assumption that the $\mathscr{V}$ and related ρ_i of a species do not change as a function of solution composition and that the total volume of a phase is a linearly additive function of the individual component molar volumes times their molar abundance. Other studies have noted that ρ_i^s may differ from ρ_i^b and that lower values of ρ_i^s may lead to better agreement between surface tension models and experimental data (Defay et al., 1966).

It should also be noted that deviations in activity coefficients are possible when comparing surface versus bulk phases of the same molar composition. As mentioned in Sect. 2.4.3, the introduction of a single exponential scaling factor (t) for all component activity coefficients in the surface phase has been used in the past as a fit parameter in order for binary solution surface tension curves to better match experimental data without violating the Gibbs–Duhem relation. This t value may be thought of as treating the surface phase nonideality as taking place at a different temperature than that of the bulk phase, since $RT \ln\left[(\gamma_i^s)^t\right] = R(tT) \ln\left[(\gamma_i^s)\right]$. Therefore, one may argue that the value of t should be constrained such that the temperature

Table 2.2: Partial molar areas ($m^2\,mol^{-1}$) of different organic species calculated using a simplified geometric approach based on the values given in Topping et al. (2007) and the model developed by Goldsack and White (1983), as well as by Eq. (2.19) of this study for particle diameters of 5, 50, and 5000 nm and two distinct δ values (0.15 nm or 1.0 nm).

Species	**Previous Treatments**		**This study**					
	Goldsack & White (1983)	Simplified Geometric Approach	$D =$ 5 nm		$D =$ 50 nm		$D =$ 5000 nm	
			$\delta = 0.15$ nm	$\delta = 1.0$ nm	$\delta = 0.15$ nm	$\delta = 1.0$ nm	$\delta = 0.15$ nm	$\delta = 1.0$ nm
Succinic Acid	3.43×10^6	1.76×10^5	5.12×10^5	8.41×10^4	5.05×10^5	7.65×10^4	5.05×10^5	5.05×10^5
Malonic Acid	4.98×10^6	1.51×10^5	4.35×10^5	7.14×10^4	4.29×10^5	6.49×10^4	4.28×10^5	4.28×10^5
Oxalic Acid	2.56×10^6	1.31×10^5	3.21×10^5	5.26×10^4	3.16×10^5	4.79×10^4	3.16×10^5	3.16×10^5
Glutaric Acid	3.78×10^6	1.93×10^5	6.28×10^5	1.03×10^5	6.19×10^5	9.37×10^4	6.19×10^5	6.19×10^5
Citric Acid	4.25×10^6	2.16×10^5	8.43×10^5	1.38×10^5	8.32×10^5	1.26×10^5	8.31×10^5	8.31×10^5
Malic Acid	3.59×10^6	1.88×10^5	5.67×10^5	9.31×10^4	5.59×10^5	8.46×10^4	5.58×10^5	5.58×10^5
Maleic Acid	3.34×10^6	1.69×10^5	4.94×10^5	8.11×10^4	4.87×10^5	7.37×10^4	4.87×10^5	4.87×10^5
Adipic Acid	4.25×10^6	2.29×10^4	7.27×10^5	1.19×10^5	7.17×10^5	1.09×10^5	7.16×10^5	7.16×10^5
Fulvic Acid	1.04×10^7	4.83×10^5	1.17×10^6	1.91×10^5	1.15×10^6	1.74×10^5	1.15×10^6	1.15×10^6
Levoglucosan	4.21×10^6	2.14×10^5	6.44×10^5	1.06×10^5	6.35×10^5	9.61×10^5	6.34×10^5	6.34×10^5
Pinic Acid	4.99×10^6	2.69×10^5	1.05×10^6	1.72×10^5	1.04×10^5	1.57×10^5	1.03×10^6	1.03×10^6

change remains physically realistic. Thus, a value of $t = 25$ is physically unrealistic for a system at 298 K which shows substantial nonideal mixing, since it would mean that the surface phase nonideality would be behaving as if it were at $7,450$ K. The inclusion of t also introduces an additional fit parameter that is likely unique for each system, thus limiting the predictive power of the model introduced in this work. Use of exponent t in combination with an unconstrained fit leads to better agreement with points below cloud droplet activation for some of the Köhler curves presented in Ruehl et al. (2016), such as a ternary water–succinic–acid–ammonium-sulfate, water–pimelic-acid-ammonium-sulfate, and water–glutaric-acid-ammonium-sulfate particles. However, those fitted t values must be combined with rather extreme values of δ and σ_{org} for good agreement with the experimental data at both the CCN activation point and at points below activation (see Appendix B Figs. A.3–A.5 for examples).

The framework laid out in this work is incapable of simultaneously matching the growth data points and critical supersaturation point reported by Ruehl et al. (2016) for water–malonic-acid-ammonium-sulfate particles (see Appendix B Figs. A.3). Further explorations of variations in the activity coefficients of species in the surface phase are warranted to better understand how these activity coefficients may differ in value from those of a bulk solution with the same molar composition.

The explicit treatment of the dissociation of organic acids under dilute aqueous conditions is not considered in regards to its role in bulk–surface partitioning in this study. Under highly dilute conditions, such as those found in activating CCN, many dicarboxylic acids may partially or fully dissociate. It is possible that consideration of such acid dissociation may lead to modifications of both the surface enrichment and bulk depletion of different species as well as enhancements of the solute effect via an increase in dissolved ionic species. Explicit treatments of organic acid dissociation and resulting interactions among various additional ions in an AIOMFAC-based

model framework are thus a direction to be explored in future work.

An alternative approach to using the framework laid out in this work is to use other statistical mechanics models to predict the surface tension as a function of bulk solution composition. A simplified statistical mechanics-based approach for surface tension predictions was developed by Wexler and Dutcher (2013), which relies on a single physically constrained fitted parameter, r, which represents the average number of water molecules displaced by a solute molecule at the surface. As shown in Figure A.8, this model had a root mean square error of 2.90 mJm^{-2} in comparison to measurements of surface tension for a (macroscopic) binary water–ethanol system (Ernst et al., 1935). In comparison, the model developed in this work has a root mean square error of 2.930 mJm^{-2}, when using our default assumption that the thickness of the interface is $\delta = 0.3$ nm. The fitted value of r as reported by Wexler and Dutcher (2013) is 3.00. If the number of water molecules displaced by an ethanol molecule at the surface of a droplet is assumed to be determined based on the respective values of $\mathscr{A}_{water}$ and $\mathscr{A}_{ethanol}$, then the number of water molecules displaced by an ethanol molecule in the surface phase is 3.02. Despite both models being in good agreement in the macroscopic case, it is important to note that their statistical mechanical model does not directly account for bulk-phase depletion in volume-constrained systems. For a comparison of various other frameworks for estimating the surface tension of liquid solutions and/or atmospheric aerosol particles, we refer the reader to the recent work by Kleinheins et al. (2023) and Vepsäläinen et al. (2022, 2023).

2.6.2 Atmospheric implications

The effect of bulk–surface partitioning on Köhler curve shapes is evident for submicron-sized aerosol particles. Even the use of relatively "thick", yet reasonable, δ values (> 0.5 nm) still exhibit substantial suppression of the critical supersaturation and modifications to the shape of the Köhler curve for the particle size range prior to reaching the CCN activation point under

growth conditions. The inclusion of the thermodynamic treatment of equilibrium bulk–surface partitioning outlined in this study leads to simulated droplets that will grow to larger diameters at lower relative humidities than classical Köhler theory would otherwise suggest. If the value of δ is lowered, Köhler curves may exhibit a second local maximum as the CCN surface tension approaches that of pure water after the point of droplet activation. This behavior suggests that particles with very thin surface phases are more likely to activate into cloud droplets (for a given dry diameter). Clouds which form from rising air parcels populated by surfactant-containing particles may exhibit substantially higher cloud droplet number concentrations than those forming from air parcels of comparable particle size distributions, but lack in aerosol particles of lowered (yet evolving) surface tensions.

Figure 2.8A shows the critical supersaturation for CCN activation of particles with the same condensed phase composition as those of Fig. 2.6, with D_{dry} values ranging from 25 nm to 130 nm. Similarly, Fig. 2.8B shows particles that grow under the same input parameters as used for Fig. 2.7, with dry sizes from 25 nm to 130 nm. The colored horizontal bands shown in Fig. 2.8 correspond to the typical supersaturation values experienced by aerosol particles in marine (blue), clean continental (green), background (orange), and urban polluted (brown) cloud base conditions, according to the classification by Pinsky et al. (2014).

If the AIOMFAC-Equil. model is used to determine the CCN activation conditions, particles with D_{dry} between approximately 60 nm and 75 nm would not be predicted to activate in continental clouds for both systems shown. For the isoprene-derived SOA system, in particular, the inclusion of both equilibrium co-condensation of SVOCs and bulk–surface partitioning leads to larger modifications in predicted S_{crit}, especially for $D_{dry} > 50$ nm. This can have important implications for both the radiative forcing effects of resulting clouds and for the precipitation formation microphysics in these clouds, since lowering the critical dry diameter for typical

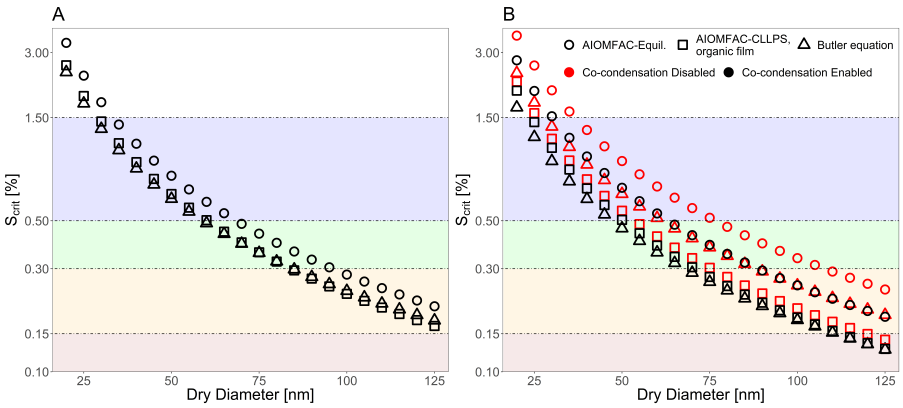

Figure 2.8: Critical supersaturations vs. dry diameter as predicted by the AIOMFAC-Equil. model, the AIOMFAC-CLLPS with organic film model, and a model from this work (Eq. 2.24) for (A) water–suberic acid–ammonium sulfate particles and (B) water–isoprene-SOA particles. The horizontal shaded bands represent distinct regimes of maximum supersaturations encountered by aerosols in either marine (blue), clean continental (green), background (orange-yellow), or urban polluted (brown) conditions at cloud base, as reported by Pinsky et al. (2014).

peak supersaturation experienced at cloud base conditions may lead to substantially increased cloud droplet number concentrations (depending on the present aerosol number–size distribution) (Ovadnevaite et al., 2017).

It is also important to note that the new framework introduced in this study to date only considers impacts of organic components on CCN activation, yet does not consider the role that bulk–surface partitioning may play (if any) for ice nucleating particles in cirrus clouds or mixed-phase clouds. Likewise, the interplay of bulk–surface partitioning and co-condensation with liquid–liquid equilibria is not yet considered in a fully coupled manner. For example, in the case of phase separation, such interactions may influence particle morphology and the RH range within which LLPS occurs. Consequently, coupled size and LLPS effects may also change the interactions between aerosol particles and light.

2.7 Conclusion

The surface area to volume ratio of atmospheric aerosol particles increases substantially as particle diameter decreases in the fine and ultrafine size ranges. Any unique properties of the exterior surface of an aerosol particle must be accounted for in order to accurately model the behavior of the smallest (sub-100 nm-sized) particles. This study builds on the finite-depth Guggenheim surface phase treatment in combination with variants of the Butler equation and AIOMFAC-based vapor–liquid equilibrium computations to create a thermodynamically rigorous treatment of bulk–surface partitioning in spherical aerosol particles with diameters as low as 10 nm. This model relies on one adjustable, loosely constrained parameter, the surface phase thickness δ, and applies consistently to any number of species in multicomponent organic–inorganic aerosol systems. The approach is capable of representing experimentally measured surface tension data for atmospherically relevant systems across a range of relative humidities. The inclusion of a thermodynamically sound treatment of interfacial regions leads to modified Köhler curve predictions that are in agreement with measured data, including for cases for which simpler approaches with fixed surface tension fail. For particles with diameters larger than $\sim$ 100 nm, the simpler AIOMFAC-CLLPS model variant with an organic film assumption agrees reasonably well with the more thermodynamically sound model in terms of predicted SS_{crit} values and may serve as a good approximation when computational efficiency is a key concern. For smaller particles, where bulk phase depletion may play a larger role, larger disagreement arises between the AIOMFAC-CLLPS model with organic film and the approaches laid out in this work.

While measurements of physicochemical properties of particles, such as surface tension and chemical composition, in the size range below 1 μm and especially below 100 nm are rare or nonexistent, there have been numerous measurements made on larger particles. Models trained on data from bulk measurements and large microscopic droplets have been used to study sub-

100 nm particles. Frequently, those measurements were done on droplets exhibiting a single liquid (bulk) phase and spherical shape when freely suspended, but phase separation and associated phase boundaries can affect the particle shape. Indeed, many systems have been modeled or observed to adopt more complex, non-spherical morphologies, in some cases involving multiple liquid phases (Huang et al., 2021; Kwamena et al., 2010; Reid et al., 2011). The basic thermodynamic theory introduced in Sect. 2.4 is generally applicable; however, we show that when applied to finite-volume droplets, geometric considerations introduce shape and mass-balance constraints which impact the bulk–surface partitioning, particularly in submicron-sized particles. In this study, we have outlined the detailed expressions for spherical single-bulk-phase particles, which were implemented in our AIOMFAC-based bulk–surface partitioning model. To date, this model does not account for non-spherical shape or feedback effects from energy stored in liquid–liquid interfaces. However, our model provides a basis for future extensions to account for size-dependent feedback between droplet size, liquid–liquid interfaces, non-sphericity, and size effects on LLPS onset. Furthermore, the use of Eq. (2.24) or Eq. (2.40) for gas–liquid interfaces requires accurate measurements or predictions of a reference state values of σ, usually pure-component surface tension, for many atmospherically relevant species. These data do not exist or, in the case of inorganic electrolytes, are disputed as to what the correct value should be. This may limit the systems for which our approach can be used – or requires assumptions to be made. Therefore, this study highlights the need for, and benefit of, reliable data for pure-component surface tension. A key goal for applications of thermodynamic multiphase aerosol models in atmospheric chemistry is achieving predictive capability, unrestricted by system- and size-dependent fit parameters. The model introduced here marks a major step toward this goal. It enables us to better quantify the role of interfacial properties in environmental systems on the nanometer and micrometer size scales. Models like those introduced in this

study can serve as a bridge between the measurable particle size range and the presently experimentally inaccessible ultrafine size range of interest for cloud formation.

Bibliography

Schmedding, R.; Zuend, A. A thermodynamic framework for bulk–surface partitioning in finite-volume mixed organic–inorganic aerosol particles and cloud droplets. Atmospheric Chemistry and Physics **2023**, 23, 7741–7765.

Cohen, A. J. et al. Estimates and 25-year trends of the global burden of disease attributable to ambient air pollution: an analysis of data from the Global Burden of Diseases Study 2015. The Lancet **2017**, 389, 1907–1918.

Burnett, R. et al. Global estimates of mortality associated with long-term exposure to outdoor fine particulate matter. Proceedings of the National Academy of Sciences **2018**, 115, 9592–9597.

Boucher, O.; Randall, D.; Artaxo, P.; Bretherton, C.; Feingold, G.; Forster, P.; Kerminen, V. M.; Kondo, Y.; Liao, H.; Lohmann, U.; Rasch, P.; Satheesh, S. K.; Sherwood, S.; Stevens, B.; Zhang, X. Y. Clouds and aerosols. Climate Change 2013: The Physical Science Basis. Contribution of Working Group I to the Fifth Assessment Report of the Intergovernmental Panel on Climate Change **2013**, 571–657.

Bellouin, N. et al. Bounding Global Aerosol Radiative Forcing of Climate Change. Reviews of Geophysics **2020**, 58, e2019RG000660, e2019RG000660 10.1029/2019RG000660.

Seinfeld, J. H. et al. Improving our fundamental understanding of the role of aerosol - cloud interactions in the climate system. Proceedings of the National Academy of Sciences **2016**, 113, 5781–5790.

Jimenez, J. L. et al. Evolution of Organic Aerosols in the Atmosphere. Science **2009**, 326, 1525–1529.

Hallquist, M. et al. The formation, properties and impact of secondary organic aerosol: current and emerging issues. Atmospheric Chemistry and Physics **2009**, 9, 5155–5236.

Ervens, B.; Turpin, B. J.; Weber, R. J. Secondary organic aerosol formation in cloud droplets and aqueous particles (aqSOA): a review of laboratory, field and model studies. Atmospheric Chemistry and Physics **2011**, 11, 11069–11102.

Surratt, J. D.; Chan, A. W. H.; Eddingsaas, N. C.; Chan, M.; Loza, C. L.; Kwan, A. J.; Hersey, S. P.; Flagan, R. C.; Wennberg, P. O.; Seinfeld, J. H. Reactive intermediates revealed in secondary organic aerosol formation from isoprene. Proceedings of the National Academy of Sciences **2010**, 107, 6640–6645.

Ng, N. L.; Kroll, J. H.; Chan, A. W. H.; Chhabra, P. S.; Flagan, R. C.; Seinfeld, J. H. Secondary organic aerosol formation from m-xylene, toluene, and benzene. Atmospheric Chemistry and Physics **2007**, 7, 3909–3922.

Chan, A. W. H.; Kautzman, K. E.; Chhabra, P. S.; Surratt, J. D.; Chan, M. N.; Crounse, J. D.; Kürten, A.; Wennberg, P. O.; Flagan, R. C.; Seinfeld, J. H. Secondary organic aerosol formation from photooxidation of naphthalene and alkylnaphthalenes: implications for oxidation of intermediate volatility organic compounds (IVOCs). Atmospheric Chemistry and Physics **2009**, 9, 3049–3060.

Zhang, Q. et al. Ubiquity and dominance of oxygenated species in organic aerosols in anthropogenically-influenced Northern Hemisphere midlatitudes. Geophysical Research Letters **2007**, 34.

Pokhrel, R. P.; Gordon, J.; Fiddler, M. N.; Bililign, S. Impact of combustion conditions on physical and morphological properties of biomass burning aerosol. Aerosol Science and Technology **2021**, 55, 80–91.

Song, M.; Marcolli, C.; Krieger, U. K.; Lienhard, D. M.; Peter, T. Morphologies of mixed organic/inorganic/aqueous aerosol droplets. Faraday Discuss. **2013**, 165, 289–316.

Song, M.; Marcolli, C.; Krieger, U. K.; Zuend, A.; Peter, T. Liquid-liquid phase separation and morphology of internally mixed dicarboxylic

acids/ammonium sulfate/water particles. Atmospheric Chemistry and Physics **2012**, 12, 2691–2712.

Ciobanu, V. G.; Marcolli, C.; Krieger, U. K.; Weers, U.; Peter, T. Liquidâ^'Liquid Phase Separation in Mixed Organic/Inorganic Aerosol Particles. The Journal of Physical Chemistry A **2009**, 113, 10966–10978, PMID: 19775109.

Shiraiwa, M.; Zuend, A.; Bertram, A. K.; Seinfeld, J. H. Gas-particle particle partitioning of atmospheric aerosols: interplay of physical state, non-ideal mixing and morphology. Phys. Chem. Chem. Phys. **2013**, 15, 11441–11453.

Lang-Yona, N.; Abo-Riziq, A.; Erlick, C.; Segre, E.; Trainic, M.; Rudich, Y. Interaction of internally mixed aerosols with light. Physical Chemistry Chemical Physics **2010**, 12, 21–31.

Schmedding, R.; Rasool, Q. Z.; Zhang, Y.; Pye, H. O. T.; Zhang, H.; Chen, Y.; Surratt, J. D.; Lopez-Hilfiker, F. D.; Thornton, J. A.; Goldstein, A. H.; Vizuete, W. Predicting secondary organic aerosol phase state and viscosity and its effect on multiphase chemistry in a regional-scale air quality model. Atmos. Chem. Phys. **2020**, 20, 8201–8225.

Schmedding, R.; Ma, M.; Zhang, Y.; Farrell, S.; Pye, H. O. T.; Chen, Y.; Wang, C.-t.; Rasool, Q. Z.; Budisulistiorini, S. H.; Ault, A. P.; Surratt, J. D.; Vizuete, W. alpha-Pinene-Derived organic coatings on acidic sulfate aerosol impacts secondary organic aerosol formation from isoprene in a box model. Atmospheric Environment **2019**, 213, 456–462.

Zhou, S.; Hwang, B. C. H.; Lakey, P. S. J.; Zuend, A.; Abbatt, J. P. D.; Shiraiwa, M. Multiphase reactivity of polycyclic aromatic hydrocarbons is driven by phase separation and diffusion limitations. Proceedings of the National Academy of Sciences **2019**, 116, 11658–11663.

Kuwata, M.; Martin, S. T. Phase of atmospheric secondary organic material affects its reactivity. Proceedings of the National Academy of Sciences **2012**, 109, 17354–17359.

Sorjamaa, R.; Svenningsson, B.; Raatikainen, T.; Henning, S.; Bilde, M.; Laaksonen, A. The role of surfactants in Köhler theory reconsidered. Atmos. Chem. Phys. **2004**, 4, 2107–2117.

Nozière, B.; Baduel, C.; Jaffrezo, J.-L. The dynamic surface tension of atmospheric aerosol surfactants reveals new aspects of cloud activation. Nature Communications **2014**, 5, 3335.

Gérard, V.; Nozière, B.; Baduel, C.; Fine, L.; Frossard, A. A.; Cohen, R. C. Anionic, Cationic, and Nonionic Surfactants in Atmospheric Aerosols from the Baltic Coast at Askö, Sweden: Implications for Cloud Droplet Activation. Environmental Science and Technology **2016**, 50, 2974–2982.

Petters, S. S.; Petters, M. D. Surfactant effect on cloud condensation nuclei for two-component internally mixed aerosols. Journal of Geophysical Research: Atmospheres **2016**, 121, 1878–1895.

Ruehl, C. R.; Davies, J. F.; Wilson, K. R. An interfacial mechanism for cloud droplet formation on organic aerosols. Science **2016**, 351, 1447–1450.

Ovadnevaite, J.; Zuend, A.; Laaksonen, A.; Sanchez, K. J.; Roberts, G.; Ceburnis, D.; Decesari, S.; Rinaldi, M.; Hodas, N.; Facchini, M. C.; Seinfeld, J. H.; O' Dowd, C. Surface tension prevails over solute effect in organic-influenced cloud droplet activation. Nature **2017**, 546, 637–641.

Kroflič, A.; Frka, S.; Simmel, M.; Wex, H.; Grgić, I. Size-Resolved Surface-Active Substances of Atmospheric Aerosol: Reconsideration of the Impact on Cloud Droplet Formation. Environmental Science and Technology **2018**, 52, 9179–9187.

Malila, J.; Prisle, N. L. A Monolayer Partitioning Scheme for Droplets of Surfactant Solutions. Journal of advances in modeling earth systems **2018**, 10, 3233–3251.

Gérard, V.; Noziere, B.; Fine, L.; Ferronato, C.; Singh, D. K.; Frossard, A. A.; Cohen, R. C.; Asmi, E.; Lihavainen, H.; Kivekäs, N.; Aurela, M.; Brus, D.; Frka, S.; Cvitešić Kušan, A. Concentrations and Adsorption Isotherms for Amphiphilic Surfactants in PM1 Aerosols from Different Regions of Europe. Environmental Science and Technology **2019**, 53, 12379–12388.

Binyaminov, H.; Abdullah, F.; Zargarzadeh, L.; Elliott, J. A. W. Thermodynamic Investigation of Droplet–Droplet and Bubble–Droplet Equilibrium in an Immiscible Medium. The Journal of Physical Chemistry B **2021**, 125, 8636–8651, PMID: 34310143.

Facchini, M. C.; Mircea, M.; Fuzzi, S.; Charlson, R. J. Cloud albedo enhancement by surface-active organic solutes in growing droplets. Nature **1999**, 401, 257–259.

Facchini, M. C.; Decesari, S.; Mircea, M.; Fuzzi, S.; Loglio, G. Surface tension of atmospheric wet aerosol and cloud/fog droplets in relation to their organic carbon content and chemical composition. Atmospheric Environment **2000**, 34, 4853–4857.

Topping, D. O.; McFiggans, G. B.; Kiss, G.; Varga, Z.; Facchini, M. C.; Decesari, S.; Mircea, M. Surface tensions of multi-component mixed inorganic/organic aqueous systems of atmospheric significance: measurements, model predictions and importance for cloud activation predictions. Atmospheric Chemistry and Physics **2007**, 7, 2371–2398.

Köhler, H. The nucleus in and the growth of hygroscopic droplets. Transactions of the Faraday Society **1936**, 32, 1152–1161.

Petters, M. D.; Kreidenweis, S. M. A single parameter representation of hygroscopic growth and cloud condensation nucleus activity. Atmospheric Chemistry and Physics **2007**, 7, 1961–1971.

Topping, D.; Barley, M.; Bane, M. K.; Higham, N.; Aumont, B.; Dingle, N.; McFiggans, G. UManSysProp v1.0: an online and open-source facility for molecular property prediction and atmospheric aerosol calculations. Geoscientific Model Development **2016**, 9, 899–914.

Gibbs, J. W. On the Equilibrium of Heterogeneous Substances. **1874**,

Szyszkowski, B. V. Experimentelle Studien über kapillare Eigenschaften der wässerigen Lösungen von Fettsäuren. **1908**,

Jura, G.; Harkins, W. D. Surfaces of Solids. XIV. A Unitary Thermodynamic Theory of the Adsorption of Vapors on Solids and of Insoluble Films on Liquid Subphases. Journal of the American Chemical Society **1946**, 68, 1941–1952.

Prisle, N. L.; Raatikainen, T.; Laaksonen, A.; Bilde, M. Surfactants in cloud droplet activation: mixed organic-inorganic particles. Atmos. Chem. Phys. **2010**, 10, 5663–5683.

Bzdek, B. R.; Reid, J. P.; Malila, J.; Prisle, N. L. The surface tension of surfactant-containing, finite volume droplets. Proceedings of the National Academy of Sciences **2020**, 117, 8335–8343.

Lin, J. J.; Kristensen, T. B.; Calderón, S. M.; Malila, J.; Prisle, N. L. Effects of surface tension time-evolution for CCN activation of a complex organic surfactant. Environmental Science: Processes and Impacts **2020**, 22, 271–284.

Prisle, N. L.; Raatikainen, T.; Sorjamaa, R.; Svenningsson, B.; Laaksonen, A.; Bilde, M. Surfactant partitioning in cloud droplet activation: a study of C8, C10, C12 and C14 normal fatty acid sodium salts. Tellus B **2008**, 60, 416–431.

Hansen, A. M. K.; Hong, J.; Raatikainen, T.; Kristensen, K.; Ylisirniö, A.; Virtanen, A.; Petäjä, T.; Glasius, M.; Prisle, N. L. Hygroscopic properties and cloud condensation nuclei activation of limonene-derived organosulfates and their mixtures with ammonium sulfate. Atmos. Chem. Phys. **2015**, 15, 14071–14089.

Sorjamaa, R.; Laaksonen, A. The effect of H¡sub¿2¡/sub¿O adsorption on cloud drop activation of insoluble particles: a theoretical framework. Atmos. Chem. Phys. **2007**, 7, 6175–6180.

Davies, J. F.; Zuend, A.; Wilson, K. R. Technical note: The role of evolving surface tension in the formation of cloud droplets. Atmos. Chem. Phys. **2019**, 19, 2933–2946.

Romakkaniemi, S.; Kokkola, H.; Smith, J. N.; Prisle, N. L.; Schwier, A. N.; McNeill, V. F.; Laaksonen, A. Partitioning of semivolatile surface-active compounds between bulk, surface and gas phase. Geophysical Research Letters **2011**, 38.

Ruehl, C. R.; Wilson, K. R. Surface Organic Monolayers Control the Hygroscopic Growth of Submicrometer Particles at High Relative Humidity. The Journal of Physical Chemistry A **2014**, 118, 3952–3966.

Forestieri, S. D.; Staudt, S. M.; Kuborn, T. M.; Faber, K.; Ruehl, C. R.; Bertram, T. H.; Cappa, C. D. Establishing the impact of model surfactants on cloud condensation nuclei activity of sea spray aerosol mimics. Atmos. Chem. Phys. **2018**, 18, 10985–11005.

Laaksonen, A.; Kulmala, M. An explicit cluster model for binary nuclei in water–alcohol systems. The Journal of Chemical Physics **1991**, 95, 6745–6748.

Vepsäläinen, S.; Calderón, S. M.; Malila, J.; Prisle, N. L. Comparison of six approaches to predicting droplet activation of surface active aerosol – Part 1: moderately surface active organics. Atmospheric Chemistry and Physics **2022**, 22, 2669–2687.

Prisle, N. L.; Dal Maso, M.; Kokkola, H. A simple representation of surface active organic aerosol in cloud droplet formation. Atmospheric Chemistry and Physics **2011**, 11, 4073–4083.

Vepsäläinen, S.; Calderón, S. M.; Prisle, N. L. Comparison of six approaches to predicting droplet activation of surface active aerosol – Part 2: strong surfactants. EGUsphere **2023**, 2023, 1–23.

McGraw, R.; Wang, J. Surfactants and cloud droplet activation: A systematic extension of Köhler theory based on analysis of droplet stability. The Journal of Chemical Physics **2021**, 154, 024707.

Zuend, A.; Marcolli, C.; Peter, T.; Seinfeld, J. H. Computation of liquid-liquid equilibria and phase stabilities: implications for RH-dependent gas/particle partitioning of organic-inorganic aerosols. Atmospheric Chemistry and Physics **2010**, 10, 7795–7820.

Fredenslund, A.; Jones, R. L.; Prausnitz, J. M. Group-contribution estimation of activity coefficients in nonideal liquid mixtures. AIChE Journal **1975**, 21, 1086–1099.

Abrams, D. S.; Prausnitz, J. M. Statistical thermodynamics of liquid mixtures: A new expression for the excess Gibbs energy of partly or completely miscible systems. AIChE Journal **1975**, 21, 116–128.

Guggenheim, .-., E. A. (Edward Armand) Mixtures; the theory of the equilibrium properties of some simple classes of mixtures, solutions and alloys.; The International series of monographs on physics; Clarendon Press: Oxford, 1952.

Zuend, A.; Marcolli, C.; Luo, B. P.; Peter, T. A thermodynamic model of mixed organic-inorganic aerosols to predict activity coefficients. Atmospheric Chemistry and Physics **2008**, 8, 4559–4593.

Zuend, A.; Marcolli, C.; Booth, A. M.; Lienhard, D. M.; Soonsin, V.; Krieger, U. K.; Topping, D. O.; McFiggans, G.; Peter, T.; Seinfeld, J. H. New and extended parameterization of the thermodynamic model AIOMFAC: calculation of activity coefficients for organic-inorganic mixtures containing carboxyl, hydroxyl, carbonyl, ether, ester, alkenyl, alkyl, and aromatic functional groups. Atmospheric Chemistry and Physics **2011**, 11, 9155–9206.

Yin, H.; Dou, J.; Klein, L.; Krieger, U. K.; Bain, A.; Wallace, B. J.; Preston, T. C.; Zuend, A. Extension of the AIOMFAC model by iodine and carbonate species: applications for aerosol acidity and cloud droplet activation. Atmospheric Chemistry and Physics **2022**, 22, 973–1013.

Aston, M. S.; Herrington, T. M. The effect of added electrolyte on surface pressure/area per molecule isotherms. Journal of Colloid and Interface Science **1991**, 141, 50–59.

Guggenheim, E. A. The thermodynamics of interfaces in systems of several components. Transactions of the Faraday Society **1940**, 35, 397–412.

Cai, X.; Griffin, R. J. Theoretical Modeling of the Size-Dependent Influence of Surface Tension on the Absorptive Partitioning of Semi-Volatile Organic Compounds. Journal of Atmospheric Chemistry **2005**, 50, 139–158.

Butler, J. A. V.; Kendall, J. P. The thermodynamics of the surfaces of solutions. Proceedings of the Royal Society of London. Series A, Containing Papers of a Mathematical and Physical Character **1932**, 135, 348–375.

Sprow, F. B.; Prausnitz, J. M. Surface tensions of simple liquid mixtures. Trans. Faraday Soc. **1966**, 62, 1105–1111.

Zuend, A.; Seinfeld, J. H. A practical method for the calculation of liquid–liquid equilibria in multicomponent organic–water–electrolyte systems using physicochemical constraints. Fluid Phase Equilibria **2013**, 337, 201–213.

Moré, J. J.; Garbow, B. S.; Hillstrom, K. E. User Guide for MINPACK-1; Argonne National Laboratory Report ANL-80-74, 1980.

Moré, J. J.; Sorensen, D. C.; Hillstrom, K. E.; Garbow, B. S. The MINPACK Project, in Sources and Development of Mathematical Software; Prentice-Hall, Inc.: Englewood Cliffs, New Jersey, United States, 1984; pp 88–111.

Hyvärinen, A.-P.; Lihavainen, H.; Gaman, A.; Vairila, L.; Ojala, H.; Kulmala, M.; Viisanen, Y. Surface Tensions and Densities of Oxalic, Malonic, Succinic, Maleic, Malic, and cis-Pinonic Acids. Journal of Chemical & Engineering Data **2006**, 51, 255–260.

Riipinen, I.; Koponen, I. K.; Frank, G. P.; Hyvärinen, A.-P.; Vanhanen, J.; Lihavainen, H.; Lehtinen, K. E. J.; Bilde, M.; Kulmala, M. Adipic and Malonic Acid Aqueous Solutions: Surface Tensions and Saturation Vapor Pressures. The Journal of Physical Chemistry A **2007**, 111, 12995–13002, PMID: 18044850.

Booth, A. M.; Topping, D. O.; McFiggans, G.; Percival, C. J. Surface tension of mixed inorganic and dicarboxylic acid aqueous solutions at 298.15 K and their importance for cloud activation predictions. Phys. Chem. Chem. Phys. **2009**, 11, 8021–8028.

Dutcher, C. S.; Wexler, A. S.; Clegg, S. L. Surface Tensions of Inorganic Multicomponent Aqueous Electrolyte Solutions and Melts. The Journal of Physical Chemistry A **2010**, 114, 12216–12230.

Lane, J. SURFACE ACTIVITY COEFFICIENTS. **1983**, 51–64.

Bzdek, B. R.; Power, R. M.; Simpson, S. H.; Reid, J. P.; Royall, C. P. Precise, contactless measurements of the surface tension of picolitre aerosol droplets. Chem. Sci. **2016**, 7, 274–285.

Ozdemir, O.; Karakashev, S. I.; Nguyen, A. V.; Miller, J. D. Adsorption and surface tension analysis of concentrated alkali halide brine solutions. Minerals Engineering **2009**, 22, 263–271.

Lee, H. D.; Estillore, A. D.; Morris, H. S.; Ray, K. K.; Alejandro, A.; Grassian, V. H.; Tivanski, A. V. Direct Surface Tension Measurements of Individual Sub-Micrometer Particles Using Atomic Force Microscopy. The Journal of Physical Chemistry A **2017**, 121, 8296–8305, PMID: 28981283.

Rastak, N. et al. Microphysical explanation of the RH-dependent water affinity of biogenic organic aerosol and its importance for climate. Geophysical Research Letters **2017**, 44, 5167–5177.

Gervasi, N. R.; Topping, D. O.; Zuend, A. A predictive group-contribution model for the viscosity of aqueous organic aerosol. Atmospheric Chemistry and Physics **2020**, 20, 2987–3008.

Jenkin, M. E.; Young, J. C.; Rickard, A. R. The MCM v3.3.1 degradation scheme for isoprene. Atmospheric Chemistry and Physics **2015**, 15, 11433–11459.

Jenkin, M. E.; Saunders, S. M.; Pilling, M. J. The tropospheric degradation of volatile organic compounds: a protocol for mechanism development. Atmospheric Environment **1997**, 31, 81–104.

Jenkin, M. E.; Wyche, K. P.; Evans, C. J.; Carr, T.; Monks, P. S.; Alfarra, M. R.; Barley, M. H.; McFiggans, G. B.; Young, J. C.; Rickard, A. R. Development and chamber evaluation of the MCM v3.2 degradation scheme for β-caryophyllene. Atmospheric Chemistry and Physics **2012**, 12, 5275–5308.

Goldsack, D. E.; White, B. R. An iterative technique for calculating surface tensions of -on-electrolyte solutions. Canadian Journal of Chemistry **1983**, 61, 1725–1729.

Defay, R.; Prigogine, I.; Bellemans, A. Surface tension and adsorption; Longmans, 1966.

Wexler, A. S.; Dutcher, C. S. Statistical Mechanics of Multilayer Sorption: Surface Tension. The Journal of Physical Chemistry Letters **2013**, 4, 1723–1726, PMID: 26282984.

Ernst, R. C.; Watkins, C. H.; Ruwe, H. The Physical Properties of the Ternary System Ethyl Alcohol–Glycerin–Water. The Journal of Physical Chemistry **1935**, 40, 627–635.

Kleinheins, J.; Shardt, N.; El Haber, M.; Ferronato, C.; Nozière, B.; Peter, T.; Marcolli, C. Surface tension models for binary aqueous solutions: a review and intercomparison. Phys. Chem. Chem. Phys. **2023**, 25, 11055–11074.

Pinsky, M.; Mazin, I. P.; Korolev, A.; Khain, A. Supersaturation and diffusional droplet growth in liquid clouds: Polydisperse spectra. Journal of Geophysical Research: Atmospheres **2014**, 119, 12,872–12,887.

Huang, Y.; Mahrt, F.; Xu, S.; Shiraiwa, M.; Zuend, A.; Bertram, A. K. Coexistence of three liquid phases in individual atmospheric aerosol particles. Proceedings of the National Academy of Sciences **2021**, 118, e2102512118.

Kwamena, N. O. A.; Buajarern, J.; Reid, J. P. Equilibrium Morphology of Mixed Organic/Inorganic/Aqueous Aerosol Droplets: Investigating the Effect of Relative Humidity and Surfactants. The Journal of Physical Chemistry A **2010**, 114, 5787–5795.

Reid, J. P.; Dennis-Smither, B. J.; Kwamena, N.-O. A.; Miles, R. E. H.; Hanford, K. L.; Homer, C. J. The morphology of aerosol particles consisting of hydrophobic and hydrophilic phases: hydrocarbons, alcohols and fatty acids as the hydrophobic component. Physical Chemistry Chemical Physics **2011**, 13, 15559–15572.

3

The Role of Interfacial Tension in the Size-dependent Phase Separation of Atmospheric Aerosol Particles

3.1 Preface

In chapter 2, it was found that partitioning between a 3-D surface phase and the underlying bulk phase led to substantial reductions in the surface tension and enrichment of tensoionic species under high relative humidity conditions. Under such conditions, many aerosol particles have a homogeneously mixed bulk phase. The following chapter discusses the role of liquid-liquid phase separation in aerosol particles under lower relative humidities and compares different models for the treatment of interfacial tension between two liquid phases. The aim of this chapter is to explore the size at which the energetic contributions from surface and interfacial tensions become so large that a liquid-liquid phase-separated particle with a surface phase is no longer favorable in comparison to a particle with a single well-mixed bulk phase and a surface phase. It was reproduced with modifications from Schmedding and Zuend (2024).

3.2 Abstract

Atmospheric aerosol particles span orders of magnitude in size. In ultrafine particles, the energetic contributions of surfaces and interfaces to the Gibbs energy become significant and increase in importance as particle diameter decreases. For these particles, the thermodynamic equilibrium state depends on size, composition, and temperature. Various aerosol systems have been observed to undergo liquid–liquid phase separation (LLPS), impacting equilibrium gas–particle partitioning, modifying physicochemical properties of the particle phases, and influencing cloud droplet activation. Numerous laboratory experiments have characterized the onset relative humidity of LLPS in larger aerosol particles and macroscopic bulk systems. However, in sufficiently small particles, the interfacial tension between two liquid phases constitutes an energetic barrier that may prevent the formation of an additional liquid phase. Determining said small-size limit is a key question.

We introduce a predictive droplet model based on the Aerosol Inorganic–Organic Mixtures Functional groups Activity Coefficients model. This model enables size-dependent computations of surface and interfacial tension effects on bulk–surface partitioning within phase-separated and single-phase particles. We evaluate four approaches for computing interfacial tension in multicomponent droplets, including a new method introduced in this work. Of the approaches tested, Antonov's rule best matches observed liquid–liquid interfacial tensions in highly immiscible mixtures, while a modified Butler equation fits well in more miscible systems. We find that two approaches substantially lower the onset relative humidity of LLPS for the studied systems.

3.3 Introduction

Atmospheric aerosols and their interactions with clouds and radiation are a major source of uncertainty in global climate models (Intergovernmental Panel on Climate, 2014). The condensed particle phase component of an aerosol, henceforth referred to as aerosol particles or "aerosols" varies in composition regionally and over time (Jimenez et al., 2009). Organic compounds contribute a substantial mass fraction to the total condensed material within ambient aerosols. Organic-rich particles can be emitted directly (primary organic aerosols) or formed from gas-phase reactions involving volatile organic compounds (VOCs). Aerosols which contain substantial amounts of secondary organic compounds are often referred to as secondary organic aerosols (SOA). For complete lists of abbreviations, symbols, and their meanings, please refer to tables B.1 and B.2 in the supplementary information. SOA mixed with inorganic species such as dissolved aqueous electrolytes form the majority of fine-mode aerosols in many regions of the world (Zhang et al., 2007). Therefore, understanding the properties of aerosol particles is important for better constraints on global air quality and climate models and related future climate projections.

The effects of a population of aerosol particles on weather and climate depend on the collective properties of the particles. Two properties which have been the focus of numerous studies are the number of condensed phases present in an aerosol particle and the morphology of the particle, whether said particle is of spherical or non-spherical shape, or consists of a combination of smaller three-dimensional structures (Kucinski et al., 2019; Ohno et al., 2023). Liquid–liquid phase separation (LLPS) has been observed in numerous laboratory-generated and atmospheric aerosols, with many particles of varying compositions splitting into two distinct phases in contact with one another (Marcolli and Krieger, 2006; You et al., 2012; Ciobanu et al., 2009; Bertram et al., 2011; Freedman, 2017). More recently, the presence of three liquid phases within single aerosol particles has been observed in laboratory

mimics of urban aerosols (Huang et al., 2021; Kucinski et al., 2019). The unique composition of each liquid phase present in a particle determines a range of the physicochemical properties of those phases and/or a particle overall. These properties include the hygroscopicity and related equilibrium water content, the surface tension, viscosity, acidity, and ionic strength, all of which may vary as a function of environmental (thermodynamic) conditions and phase-specific composition Lilek and Zuend (2022); Gervasi et al. (2020); Schmedding and Zuend (2023); Kleinheins et al. (2023). Organic-rich phases may exhibit atmospherically relevant physical properties similar to that of an aqueous electrolyte-containing phase or properties which are quite different than those of the aqueous ion-rich phase (Li et al., 2021; Chan et al., 2006). These properties may affect the growth and aging of aerosol particles by limiting the reactive uptake of species such as isoprene-derived epoxydiols, or N_2O_5 (Gaston et al., 2014; Schmedding et al., 2020). Aerosol–cloud interactions can also be affected by the presence of liquid–liquid phase separation in aerosol particles, especially so if LLPS persists to high relative humidities (RH) (Ovadnevaite et al., 2017; Malek et al., 2023). The reduction in droplet surface tension typically caused by an enrichment of organics at the gas–particle surface and the coupled simultaneous modification to the bulk phase composition due to bulk–surface partitioning, have competing effects on the water vapor saturation ratio and minimum dry particle size necessary for cloud droplet activation. This can ultimately lead to a substantial shift in the critical saturation ratio and diameter necessary for the activation of aerosol particles into cloud droplets (Ruehl et al., 2016; Ovadnevaite et al., 2017; Davies et al., 2019; Schmedding and Zuend, 2023).

Beyond changes to the physicochemical properties of aerosol particles stemming from the formation of distinct condensed phases within a particle, the three-dimensional (3-D) morphology of a particle may be modified. Homogeneously mixed particles assume a spherical shape under equilibrium conditions due to the impact of surface tension. In the case of a phase-

separated particle, deviations from sphericity are possible (Kwamena et al., 2010; Gorkowski et al., 2020). Some LLPS particles still form an overall spherical structure with an organic-rich shell (phase β) covering an inorganic-rich core (phase α). Other, more complex structures are possible, such as a partially engulfed morphology, wherein the particle is no longer radially symmetric nor perfectly spherical. In a partially engulfed particle, phase β does not spread completely over phase α and leaves a portion of phase α exposed (Kwamena et al., 2010; Reid et al., 2011; Ciobanu et al., 2009; Song et al., 2012, 2013; Shiraiwa et al., 2013). Such particle geometries interact with radiation differently than their core–shell counterparts (Lang-Yona et al., 2010).

It has also been observed that LLPS particles composed of 3-methylglutaric acid and ammonium sulfate, which have a core–shell morphology at higher RH, form partially engulfed particles at lower RH (Lam et al., 2021). Should additional condensed phases be present beyond the simplest two-phase case, various combinations of spherical shells and partially engulfing phases are possible (Huang et al., 2021), leading to geometric structures which may be highly complex. Under equilibrium conditions, the sequence of these phases in terms of the innermost to outermost phase of the particle is determined by the configuration which minimizes the overall Gibbs energy of the particle. Usually, this results in arrangements that favor placing the phases with higher hypothetical gas–liquid surface tensions closer to the center of the particle, while those with lower surface tensions are closer to or at the gas–particle boundary.

Analogous to the surface between a gas phase and a condensed phase, the interface between two condensed phases, particularly two liquid phases, might experience a similar phenomenon with respect to the enrichment and depletion of different compounds (Hua et al., 2016). Note that hereafter in this article, “surface” refers to a gas–liquid phase boundary and “interface” refers to the boundary between two condensed (liquid) phases. There have

been several attempts to quantify the relative contribution of the liquid–liquid (LL) interface between two condensed phases to the overall energy of a particle and whether bulk phase depletion plays a role at the LL interface. Until recently, it has been assumed that the energetic contributions from LL interfacial tension in typical aerosol particles are negligible for particles with diameters larger than approximately 100 nm, for which the Kelvin effect is also relatively minor (Russell and Ming, 2002; Zuend et al., 2010). Despite this, recent studies have found that the contribution of a LL interface to the Gibbs energy of a particle may have a small but not insignificant effect on the RH at which the particle will undergo LLPS upon dehydration (Ohno et al., 2023).

In order to better understand the role of interfacial tension and its interaction with phase separation and particle morphologies, predictive models of interfacial tension and associated phase composition changes are necessary. Different approaches have been considered for the prediction of liquid–liquid interfacial tension; a brief overview is presented in the following, with additional theory and methods discussed in Sect. 3.4.

The simplest approximation for the interfacial tension between two phases α and β, $\sigma^{\alpha\beta}$, is by taking the absolute difference of the hypothetical gas–liquid surface tensions of the two phases (σ^{α} and σ^{β}) when each is considered in isolation,

$$\sigma^{\alpha\beta} = \left|\sigma^{\alpha} - \sigma^{\beta}\right|. \tag{3.1}$$

Equation (3.1) is known as Antonov's rule (Antonov, 1907). While Eq. (3.1) may be a good first-order approximation of the interfacial tension for some systems, it is an empirical estimation method and not thermodynamically rigorous (Makkonen and Kurkela, 2018; Winter, 1995). A distinct approach for determining the interfacial tension between two liquid phases was proposed by Girifalco and Good (1957):

$$\sigma^{\alpha\beta} = \sigma^{\alpha} + \sigma^{\beta} - 2\phi\sqrt{\sigma^{\alpha}\sigma^{\beta}}, \tag{3.2}$$

where ϕ is a system-dependent interaction/correction parameter. It has been shown that ϕ may be constrained by the following inequality:

$$\phi \geq \left(1 - \frac{\sigma^{\alpha\beta}}{\sigma^{\alpha}}\right)^{\frac{1}{2}}. \tag{3.3}$$

The value of ϕ can be defined in the case of binary systems with molecules 1 and 2 of approximately equal size and spherical shape in a hexagonal arrangement as

$$\phi = \frac{d_{1,1}d_{2,2}}{d_{1,2}^2}, \tag{3.4}$$

where d is the equilibrium distance between the two molecules denoted in the subscript (Girifalco and Good, 1957). In the case of binary systems with molecules of unequal sizes or shapes, the value of ϕ could be approximated by the following equation:

$$\phi = \frac{4\mathscr{V}_1^{1/3}\mathscr{V}_2^{1/3}}{\left(\mathscr{V}_1^{1/3} + \mathscr{V}_2^{1/3}\right)^2}. \tag{3.5}$$

where $\mathscr{V}$ is the molar volume of 1 or 2 respectively (Girifalco and Good, 1957). Qualitatively, ϕ is described as being lower in systems where the the primary molecular interactions are different, for example dispersion forces in phase β and hydrogen bonding in phase α (Girifalco and Good, 1957).

Note that in the case of a single well-mixed phase, where $\sigma^{\alpha\beta} = 0$, $\phi = 1$. In the limiting case where $\phi = \left(1 - \frac{\sigma^{\alpha\beta}}{\sigma^{\alpha}}\right)^{\frac{1}{2}}$, Eq. (3.2) reduces to Eq. (3.1). However, the utility of this equation for systems with more than two components, or with compounds that are soluble in both phases, remains an open question (Makkonen and Kurkela, 2018). Equation. (3.2) was further refined to

$$\sigma^{\alpha\beta} = \sigma^{\alpha} + \sigma^{\beta} - 2\left(\sigma^{\alpha,\mathrm{disp}} \cdot \sigma^{\beta,\mathrm{disp}}\right)^{\frac{1}{2}}, \tag{3.6}$$

where $\sigma^{\alpha,\mathrm{disp}}$ and $\sigma^{\beta,\mathrm{disp}}$ are the contributions from dispersion forces to the

surface tensions of phases α and β, respectively (Fowkes, 1962, 1963). Of course, such a model relies on accurate constraints on the dispersive and non-dispersive contributions to the surface energies per unit area of both phases, thus limiting the utility of this approach.

As mentioned above, some atmospheric aerosol systems have been observed to undergo LLPS for particles with large diameters, yet particles of the same or similar composition may not undergo LLPS should their diameters be substantially smaller (Kucinski et al., 2019; Freedman, 2020; Ott and Freedman, 2020; Ohno et al., 2023). Indeed, it is thought that at sufficiently small diameters, the high surface area to volume ratios of atmospheric aerosol particles lead to a sufficient energetic barrier from the combined effects of surface and interfacial tensions that the formation of an additional phase is inhibited (Ohno et al., 2023; Freedman, 2020). It should be noted that the effect of aerosol composition, particularly the presence of different inorganic electrolytes, complicates size-dependent LLPS; for example, Ott et al. (2021) report that particles containing sodium cations are phase-separated down to smaller sizes than similar particles which contain ammonium cations.

In summary, at the boundary between two distinct phases there exists an energetic penalty. In the case of a gas–liquid boundary, this penalty is often referred to as the surface tension. A similar tension exists at the boundary between two liquid phases. If the gas–liquid interface can be thought of as a finite-depth region, with a distinct composition from the adjacent liquid phase beneath it, then there must exist an interfacial tension at this boundary as well. The sum of this interfacial tension and the surface tension at the gas–liquid boundary form the measurable surface tension that can be observed directly. Numerous methods have been proposed to determine the interfacial tension between two liquid phases using thermodynamic theory and semi-empirical approaches and system-specific fits. The sum of the three energetic interfacial contributions lead to differences in the total Gibbs energy for a well-mixed or phase-separated particle. Greater differences in Gibbs

energy occur in particles with higher surface/interfacial-area-to-volume ratios. Such differences in Gibbs energy may be sufficiently large that they lead to reductions in the onset RH of LLPS or even the complete suppression of LLPS. To our knowledge, no predictive model exists that accounts for the coupled feedbacks of aerosol particle size and three-dimensional morphology on the conditions under which a particle will separate into two (or more) liquid phases or remain homogeneously mixed. As such, we present a thermodynamic framework for exploring and quantifying the size-dependent LLPS in aerosol particles.

3.4 Methods

3.4.1 Modeling interfacial tension between two liquid phases

In the case of a closed thermodynamic system with two or more liquid phases, the Gibbs energy at constant temperature and pressure can be expressed as follows:

$$G = \sum_{\phi} \sum_{j} \mu_j^{\phi} n_j^{\phi} + \sum_{\iota} \sigma^{\iota} A^{\iota} + \tau l. \tag{3.7}$$

Here, μ_j^{ϕ} and n_j^{ϕ} are the chemical potential and molar amount of species j in phase ϕ. σ^{ι} is the surface or interfacial tension at phase boundary ι and A^{ι} is the area of phase boundary ι. τ represents the energetic contribution of a 3-phase boundary line, sometimes referred to as the line tension, and l is the length of the 3-phase boundary line. Note that a 3-phase boundary line will only exist in a particle with a partially engulfed morphology or when particles are deposited on a substrate for analysis in laboratory experiments. Furthermore, given that measured and predicted line energy contributions in complex systems are thought to be orders of magnitude lower than those from LL interface contributions, energetic contributions from the τl term is usually assumed to be negligible (Amirfazli and Neumann, 2004).

Schmedding and Zuend (2023) developed an approach for predicting the equilibrium surface tension of a single-liquid-phase droplet with a finite-depth Guggenheim interface of radial thickness δ^{s}. Guggenheim interfaces are an alternative approach to the classical Gibbsian treatment of interfaces, the latter treating them as infinitely thin two-dimensional surfaces located at the point where the excess concentration of some species in the system, typically the solvent, is zero (Gibbs, 1906). Guggenheim interfaces instead treat the surface of a solution as a thermodynamically distinct region from the bulk liquid phase beneath it and the gas phase above it (Guggenheim, 1940). Such a definition allows for more flexibility in defining the location of the interface, its extent and composition, as well as accounting for the feedback of bulk–surface partitioning on the bulk composition in small droplets. Their approach employed the Aerosol Inorganic–Organic Mixtures Functional groups Activity Coefficients (AIOMFAC) model (Zuend et al., 2008, 2011; Yin et al., 2022) to calculate activity coefficients in the surface and bulk phases of an aerosol particle for application in the Butler equation:

$$\sigma_i = \sigma_i^{\circ} + \frac{RT}{\mathscr{A}_i} \ln\left(\frac{a_i^{\mathrm{s}}}{a_i^{\mathrm{b}}}\right). \tag{3.8}$$

Here, σ_i is the surface tension of the droplet as predicted by the right-hand-side expression based on component i, σ_i° is the surface tension of i in the pure-component case at the same pressure and temperature, R is the universal gas constant, T is the temperature, $\mathscr{A}_i$ is the partial molar area of i, which depends on the surface phase geometry.

a_i^{s} is the mole-fraction-based activity of i in the surface phase and a_i^{b} is the mole fraction-based (or molality-based, in the case of inorganic electrolytes) activity of i in the liquid bulk phase. a_i^{b} can be calculated as the product of the concentration of species i, either in mole fraction or molality as previously mentioned, and the activity coefficient, γ_i, at a given temperature on the associated composition scale. For a surface phase represented by a concentric

shell on a spherical droplet core, $\mathscr{A}_i$ is defined as:

$$\mathscr{A}_i = \left(\frac{\partial A}{\partial n_i^{\mathrm{s}}}\right)_{T,P,n_j^{\mathrm{s}},\sigma} = \mathscr{V}_i^{\mathrm{s}} \frac{2r_{\mathrm{p}}}{2\delta^{\mathrm{s}} r_{\mathrm{p}} - \delta^{\mathrm{s}2}},$$

where A is the outer surface phase area, n_i^{s} and denote the molar amount and molar volume of i, respectively, in the finite-depth surface phase. r_p is the particle radius, i.e. the outer radius of the surface phase and δ^{s} is the radial thickness of the surface. For a derivation of Eq. (9), see Schmedding and Zuend (2023).

Under equilibrium conditions the surface tensions computed via Eq. (3.8) for all k components in solution must be equal, such that

$$\sigma_1 = \sigma_2 = ... = \sigma_k. \tag{3.9}$$

While the structure of a gas–liquid interface may be best represented by a thin, yet finite-depth surface phase to account for bulk–surface partitioning, the structure of a LL interface may be more easily represented by a two-dimensional (2-D) dividing surface. The latter is the case since the absolute material and density gradients across LL interfaces are much smaller than across a gas–liquid surface. Therefore, unlike the approach to bulk–surface partitioning described in Schmedding and Zuend (2023), there is no depletion from phase α nor phase β to the LL interface between them as the tightly coupled partitioning between phases α and β accounts for the depletion of either phase with respect to the LL interface. Note, however, that modifications to the equilibrium partitioning of components between the two liquid phases due to the presence of the interface can be accounted for. This 2-D LL interface treatment has the added benefit of simplifying the approach used to determine the interfacial tension as the interplay between partitioning and non-ideal mixing may be greatly simplified in the liquid–liquid interface.

Returning to the approach of Schmedding and Zuend (2023), which utilized Eq. (3.8) to predict surface tension, we now extend the same approach

to account for the boundary between two liquid phases. For a LL interface Eq. (3.8) must be modified, since the reference state surface tension values (σ_i°) are inherently different from those found at the gas–liquid surface. At a gas–liquid boundary, σ_i° is assumed to be surface tension of a droplet of pure component i. Analogously, for LL interfaces, σ_i° is assumed to be the interfacial tension that exists between two molecular layers of pure component i. Because the compositions of the two layers of i are identical in the LL reference state case – a hypothetical interface – any molecule present at this reference LL interface would not experience an additional energetic penalty. Therefore, in the case of a LL interface,

$$\sigma_1^{\alpha\beta,\circ} = \sigma_2^{\alpha\beta,\circ} = ... = \sigma_k^{\alpha\beta,\circ} = 0. \tag{3.10}$$

Consequently, in the case of a LL interface, Eq. (3.8) simplifies to (Bahramian and Danesh, 2005, 2004):

$$\sigma_i^{\alpha\beta} = \frac{RT}{\mathscr{A}_i^{\alpha\beta}} \ln\left(\frac{a_i^{\alpha\beta}}{a_i^{\mathrm{b}}}\right). \tag{3.11}$$

Note that for a 2-D LL interface $\mathscr{A}_i^{\alpha\beta} = 2\mathscr{V}_i^{\alpha}/r^{\alpha}$. Analogous to Eq. (3.9), the interfacial tension values determined via Eq. (3.11) for individual components must match at equilibrium, i.e.,

$$\sigma_1^{\alpha\beta} = \sigma_2^{\alpha\beta} = ... = \sigma_3^{\alpha\beta}. \tag{3.12}$$

An approach developed by Bahramian and Danesh (2004) utilized lattice theory and suggested that the activity coefficients present in a LL interface ($\gamma^{\alpha\beta}$) can be approximated by the geometric mean of the activity coefficients in the liquid phases α and β on either side of the interface:

$$\gamma_i^{\alpha\beta} = \sqrt{\gamma_i^{\alpha}\gamma_i^{\beta}}. \tag{3.13}$$

However, they note that the choice of $\frac{1}{2}$ for the exponent in this case is determined by the configuration of molecules present in the interfacial region. This approach was also later expanded by Wang and Anderko (2013) to account for the effect of electrolyte species in mixed organic–inorganic systems with good agreement to experimental data. Therefore, in this study, the geometric mean approach for activity coefficients was chosen as one option for multicomponent aerosol systems containing mixtures of water, organic species, and electrolytes.

If the assumption of Eq. (3.13) is used, and recalling that under equilibrium conditions $x_i^{\alpha}\gamma_i^{\alpha} = x_i^{\beta}\gamma_i^{\beta}$ and $\sum x_i^{\alpha\beta} = 1$, Eq. (3.11) can be rearranged to the following form (Bahramian and Danesh, 2004, 2005):

$$\sum_i \sqrt{x_i^{\beta} x_i^{\alpha}} \, \exp\left(\frac{\mathscr{A}_i^{\alpha\beta}\sigma^{\alpha\beta}}{RT}\right) = 1. \tag{3.14}$$

This leads to a single unknown variable, $\sigma^{\alpha\beta}$, which must be the same for all species such that the criteria given by Eq. (3.12) are satisfied. Thus, the interfacial tension value can be solved for numerically in a direct manner, rather than relying on a more complex bulk–interface partitioning algorithm (unlike the case for bulk–surface partitioning). It should be noted that the behavior of electrolyte species in solution may require more complex treatments of their impacts on interfacial tension (Wang and Anderko, 2013). However, many of these treatments rely on semi-empirical relationships fitted to experimental data, thus reducing their predictive power and flexibility. As such, in this approach we assume that electrolyte components (here as neutral cation–anion combinations) can be treated in the same manner as water and the organic components.

3.4.2 Alternative models of interfacial tension

In order to determine the importance of a rigorous treatment of interfacial energetic contributions in aerosol particles and the resulting geometric mor-

phologies, we introduce the following approaches, allowing for a quantitative comparison (see Sect. 3.5). A first option is a model which allows for LLPS and bulk–surface partitioning, but assumes that the LL interface is a 2-D dividing surface with an energetic contribution of 0 (labeled as "no IFE" approach).

A more thorough treatment includes assuming a 2-D LL interface with the interfacial tension value estimated by the difference in (hypothetical) gas–liquid surface tensions of the organic phase and the aqueous phase (Eq. 3.1) (Antonov's rule). One caveat of this treatment is that it renders determining whether a particle is of core–shell or partially engulfed morphology impossible. This is because of a known inconsistency of Antonov's rule with the constraints imposed by the triangle inequality necessary for calculating the contact angles among the phases (Binyaminov et al., 2021). As a similar option, Eq. (3.2) can be employed as a semi-empirical representation of the LL interfacial tension. This Girifalco–Good equation can be tuned with a single, system-specific parameter ϕ to improve agreement with pertinent experimental data.

A final semi-empirical approach for the LL interfacial tension is based on a modified version of the approach of Bahramian (2024), who stated that $x_i^{\alpha\beta} \geq \sqrt{x_i^{\alpha} x_i^{\beta}}$. In this case, we treat the composition of the interfacial layer as the weighted average of the compositions of a monolayer of phase α and β on either side of the 2-D dividing plane such that

$$v_i^{\alpha\beta} = \left(v_i^{\alpha} v_i^{\beta}\right)^{\eta}. \tag{3.15}$$

Here, v_i is the effective volume fraction of i in phase α, phase β, or the two (mono)layers of α and β immediately adjacent to the interfacial dividing plane (the hypothetical interfacial bilayer). η is defined as the value that satisfies the criteria that $\sum \left(v_i^{\alpha} v_i^{\beta}\right)^{\eta} = 1$ and $\eta > 0$ in order to satisfy the criteria of (Bahramian, 2024). A reference energetic contribution value for

this bilayer system can be estimated by

$$\sigma^{\alpha\beta,\circ} = \sum \left(v_i^{\alpha} v_i^{\beta} \right)^{\eta} \sigma_i^{\circ}. \tag{3.16}$$

Given $\sigma^{\alpha\beta,\circ}$, the energetic contributions from either phase at the liquid–liquid interface may be estimated by applying Antonov's rule separately to each monolayer adjacent to the interface, such that

$$\sigma^{\alpha,\star} = \left| \sigma^{\alpha,\mathrm{vf}} - \sigma^{\alpha\beta,\circ} \right| \qquad \text{and} \qquad \sigma^{\beta,\star} = \left| \sigma^{\beta,\mathrm{vf}} - \sigma^{\alpha\beta,\circ} \right|. \tag{3.17}$$

Note that the superscript vf refers to the volume-fraction-weighted mean of pure component values. The sum of these two energetic contributions ($\sigma^{\alpha,\star} + \sigma^{\beta,\star}$) yields the effective interfacial tension at the liquid–liquid interface:

$$\sigma^{\alpha\beta} = \left| \sigma^{\alpha,\mathrm{vf}} + \sigma^{\beta,\mathrm{vf}} - 2\ \sigma^{\alpha\beta,\circ} \right|. \tag{3.18}$$

It is important to note that an interface also exists between the exterior surface phase (which we treat as a 3-D Guggenheim interfacial phase) and the interior bulk of a particle (see Fig. 3.1 for details). This interface, henceforth referred to as the bulk–surface interface, can be treated in much the same way as the liquid–liquid interface between phases α and β using any of the approaches outlined in Table 3.1. This "ls" interface contributes an additional energetic term, which scales with σ^{ls}, to the overall Gibbs energy of the particle in addition to the interfacial tension contribution that scales with $\sigma^{\alpha\beta}$. While the energetic contribution from this boundary is likely small, it cannot be neglected categorically, since differences in composition between the surface phase and the adjacent bulk phase may become significant, especially at higher RH, at which the particle is well-mixed or phases α and β similar in composition. At intermediate and lower relative humidities in the presence of LLPS, the compositions of phases α and β tend to be more distinct from each other. Under those conditions it is likely that the α–β LL

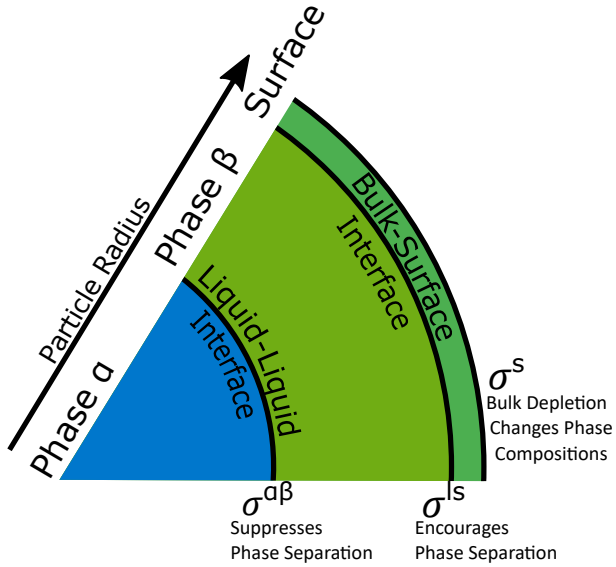

Figure 3.1: Schematic of phase and interface configurations considered in this study. In a liquid–liquid phase-separated aerosol particle with two liquid phases α and β, there exist two energetic penalties ($\sigma^{\alpha\beta}$ and σ^{ls}) due to interfaces between the condensed phases. There is also an energetic penalty at the gas–particle surface (σ^{s}). The interplay between these three energetic contributions has a feedback on the composition of particle phases and via gas–particle partitioning, the aerosol system overall.

interface plays a larger role than the bulk–surface interface (see Fig. 3.2). The area of the bulk–surface interface can be calculated as follows:

$$A^{\mathrm{ls}} = 4\pi \left(r_{\mathrm{p}} - \delta^{\mathrm{s}}\right)^2 . \tag{3.19}$$

The value of σ^{ls} can be calculated using the same approaches as for $\sigma^{\alpha\beta}$. For consistency, we always apply the same method to both interfaces for a given case. Refer to Table 3.1 for a summary of the various interfacial tension approaches applied in this work.

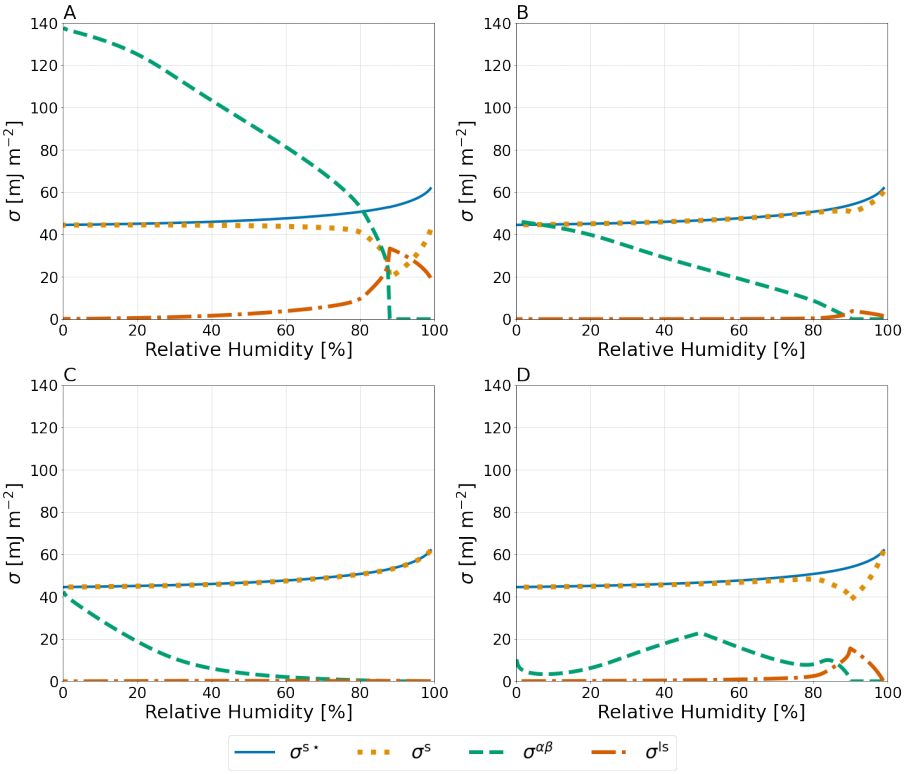

Figure 3.2: Predicted values of $\sigma^{s\star}$, which represent the measurable effect of expanding a finite depth surface phase as defined in Eq. (23); σ^{s}; $\sigma^{\alpha\beta}$; and σ^{ls} (see legend) for a particle of 1000 nm dry diameter composed of water–PEG-400–ammonium-sulfate at $T = 298$ K. $\sigma^{\alpha\beta}$ and σ^{ls} were calculated using (A) Antonov's rule (Eq. 3.1), (B) the Girifalco–Good equation (Eq. 3.2), (C) the Butler equation with geometric mean activity coefficients (Eq. 3.14), and (D) the weighted mean interfacial composition approach (Eq. 3.18).

Table 3.1: Summary of interfacial tension treatments used for the interfaces between phases α and β as well as between the surface phase and the liquid bulk phase just beneath it.

Name	**Equation**	**Reference**
No IFE	$\sigma^{\alpha\beta} = 0$	–
Antonov's rule	$\sigma^{\alpha\beta} = \left\lvert \sigma^{\alpha,\mathrm{vf}} - \sigma^{\beta,\mathrm{vf}} \right\rvert$	Antonov (1907)
Girifalco–Good equation	$\sigma^{\alpha\beta} = \sigma^{\alpha,\mathrm{vf}} + \sigma^{\beta,\mathrm{vf}} - 2\phi\sqrt{\sigma^{\alpha,\mathrm{vf}}\sigma^{\beta,\mathrm{vf}}}$	Girifalco and Good (1957)
Weighted mean approach	$\sigma^{\alpha\beta} = \left\lvert \sigma^{\alpha,\mathrm{vf}} + \sigma^{\beta,\mathrm{vf}} - 2\sum_i \left(\mathrm{vf}_i^{\alpha}\mathrm{vf}_i^{\beta}\right)^{\eta}\sigma_i^{\circ} \right\rvert$	This work
Geometric mean activity coefficients	$\sum_i \left[\sqrt{x_i^{\beta}x_i^{\alpha}}\exp\left(\frac{\mathscr{A}_i^{\alpha\beta}\sigma^{\alpha\beta}}{RT}\right)\right] = 1$	Bahramian and Danesh (2005)

An important feature of σ^{ls} is that it cannot be fully disentangled from σ^{s} as expanding the surface of a solution droplet will expand both the boundary at the gas–liquid interface as well as the boundary between the bulk phase and the surface phase. Therefore, the expression for the chemical potential of the surface phase as described in Schmedding and Zuend (2023) must be modified slightly when accounting for this additional interface. An exception is the case of a pure-component droplet, in which case $\sigma^{\mathrm{ls}} = 0$.

The following equations define the component-specific and interface-aware chemical potentials in the surface phase and an adjacent liquid bulk phase (Aston and Herrington, 1991):

$$\mu_i^{\mathrm{s}} = \mu_i^{\circ,\mathrm{s}} + RT\ln\left(a_i^{\mathrm{s}}\right) + \sigma_i^{\circ}\mathscr{A}_i^{\mathrm{s}} - \sigma^{\mathrm{s}}\mathscr{A}_i^{\mathrm{s}}\,; \tag{3.20}$$

$$\mu_i^{\mathrm{b}} = \mu_i^{\circ,\mathrm{b}} + RT\ln\left(a_i^{\mathrm{b}}\right) - \sigma^{\mathrm{ls}}\mathscr{A}_i^{\mathrm{ls}}. \tag{3.21}$$

Equation (3.21) describes the chemical potential of components (i) in a liquid bulk phase when additionally accounting for the contributions of i to the 2-D LL interfacial energy per unit amount of substance of the ls interface. Equations (3.20) and (3.21) may be combined under equilibrium conditions ($\mu_i^{\mathrm{b}} = \mu_i^{\mathrm{s}}$) while assuming (defining) that $\mu_i^{\circ,\mathrm{s}} = \mu_i^{\circ,\mathrm{b}}$. This leads to a coupled

expression for the surface tension at the gas–liquid interface:

$$\sigma_i^{\mathrm{s}\star} = \frac{RT}{\mathscr{A}_i^{\mathrm{s}}} \ln\left(\frac{a_i^{\mathrm{s}}}{a_i^{\mathrm{b}}}\right) + \sigma_i^{\circ} + \sigma^{\mathrm{ls}} \frac{\mathscr{A}_i^{\mathrm{ls}}}{\mathscr{A}_i^{\mathrm{s}}}. \tag{3.22}$$

Note that σ^{s} is now defined as $\sigma^{\mathrm{s}} = \sigma^{\mathrm{s}\star} - \sigma^{\mathrm{ls}}$; when σ^{ls} is negligible, $\sigma_i^{\mathrm{s}\star} = \sigma_i^{\mathrm{s}}$. An alternative, mathematically equivalent option is to fold the effect of an LL interface into adjusted bulk phase activities ($a_i^{\prime;\mathrm{b}}$), as described in Section 3.4.3.

3.4.3 Coupled Vapor–liquid–liquid and bulk–surface equilibrium calculation

Using the coupled vapor–liquid–liquid equilibrium modeling approach of Zuend et al. (2010); Zuend and Seinfeld (2012), for a given overall condensed-phase composition, a bulk liquid–liquid equilibrium (LLE) calculation is first performed while ignoring any adjustments due to bulk–surface equilibrium (BSE). This provides an initial guess in form of a condensed-phase equilibrium state for a given particle composition. Given the overall composition and particle size, an initial guess for the surface composition of the entire particle and the associated BSE problem can be generated using the initial guess algorithm of Schmedding and Zuend (2023). Rather than fully depleting species out of phase β or α, it is assumed that both phases contribute material proportionally to the total amount of surface molecules, n^{s}, such that

$$n_j^{\mathrm{s}} = q_j^{\alpha} \varepsilon_j n_j^{\mathrm{tot}} + (1 - q_j^{\alpha}) \varepsilon_j n_j^{\mathrm{tot}}, \tag{3.23}$$

where q_j^{α} is the fraction of neutral component j in phase α, $(1 - q_j^{\alpha})$ is the fraction of j in phase β, ε_j is the ratio of j in the surface phase to the total amount of j in the particle phase or $n_j^{\mathrm{s}}/n_j^{\mathrm{tot}}$, and n_j^{tot} is the total amount of species j in the liquid phases plus the surface phase while excluding any amount of species j in the gas phase. Similarly, for electrolyte component el,

the contributions from phases α and β can be written as follows:

$$n_{el}^{\mathrm{s}} = q_{el}^{\alpha}\varepsilon_{el}n_{el}^{\mathrm{tot}} + (q_{\mathrm{lim},el}^{\alpha} - q_{el}^{\alpha})\varepsilon_{el}n_{el}^{\mathrm{tot}}, \tag{3.24}$$

where $q_{\mathrm{lim},el}^{\alpha}$ is the maximum fraction of species el, which may partition into phase α. Returning to the uncoupled or "BSE-free" calculation, these initial guess values are used for a second liquid–liquid equilibrium calculation for the interior bulk of the particle. Once a value of $\sigma^{\alpha\beta}$ is obtained, the energetic impact of the interface can be represented as an additional contribution to each component's chemical potential. In practice, this is equivalent to expressing the interfacial tension effect as an adjustment factor to the activities of components of phase α in the following form:

$$a_i^{\prime,\alpha} = a_i^{\alpha}\,\exp\left(\frac{\sigma^{\alpha\beta}\,\mathscr{A}_i^{\alpha}}{RT}\right). \tag{3.25}$$

Likewise, in order to accurately capture the equilibrium partial pressures, p_i, of gas-phase species over the curved droplet surface and thus the equilibrium number concentration of gas phase molecules, n_i^G, the activities of each component in the particle must be scaled by the Kelvin effect as follows:

$$S_i = a_i^{\prime,\alpha}\,\exp\left(\frac{2\,\sigma^{\mathrm{s}}\mathscr{V}_i}{RT\,r_{\mathrm{p}}}\right). \tag{3.26}$$

Here, $S_i = p_i/p_i^{\circ,\mathrm{sat}}$ is the equilibrium saturation ratio and r_{p} is the overall particle or droplet radius. The droplet's equilibrium RH ($= S_w$) is calculated using a_w'. In the case where gas–particle partitioning of organic species is allowed, the gas-phase quantity of species i per m^3 of air, n_i^{G} is given by:

$$n_i^{\mathrm{G}} = \frac{a_i'\,\exp\left(\frac{2\,\sigma^{\mathrm{s}}\mathscr{V}_i}{RT\,r_{\mathrm{p}}}\right)}{p_i^{\circ,\mathrm{sat}}V^{\mathrm{G}}RT}, \tag{3.27}$$

where V^{G} denotes the unit gas-phase volume (1 m^3).

At this point, for a given overall droplet composition and temperature and with initial guesses established for both the liquid–liquid equilibrium phase compositions (if predicted to be present) as well as the bulk–surface equilibrium and associated surface tension and interfacial tensions, we can proceed to solve the fully coupled interior phase partitioning problem of a single droplet of given size. In our present proof-of-concept implementation, which is not optimized for best computational performance, we approach this as a nested interior problem to the overall gas–particle partitioning solution as qualitatively described in the following. We run a modified version of the BSE algorithm of Schmedding and Zuend (2023) to solve the Butler equation iteratively while updating the interfacial tensions and LLE state and phase compositions.

In practice, the modification is to embed the LLE refinement method by Zuend and Seinfeld (2013) to solve the LLE problem within each iteration of the parent BSE algorithm, while accounting for adjusted amounts available for phases α and β (due to changes in bulk–surface partitioning) and using interfacial-tension-adjusted activities for the components in phases α and β. This means that during each iteration within the LLE solver (and hence also within the BSE solver), the interfacial tensions are updated with the selected method (e.g. Antonov's rule or Girifalco–Good) and the normalized Gibbs energy of mixing of the droplet is updated as well. This procedure allows for a numerical solution of these coupled systems of equations within a single particle, and in conjunction with the vapor–liquid equilibrium solver (the outermost nesting level), the full equilibration of the gas phase with a population of (monodisperse) particles within a unit volume of air. It also allows for an initially assumed LLPS state (for the corresponding bulk system) to disappear if it becomes unfavorable due to bulk–surface partitioning and interfacial tension impacts on adjusted component activities.

In summary, a coupled system of nonlinear algebraic equations needs to be solved, the solution of which must fulfill the necessary condition that the

interface-corrected activities (a_i') are equivalent across all phases at equilibrium. These corrected activities can be employed along with the relative molar amounts in each phase to determine the change in Gibbs energy due to mixing and interfaces per mole of particulate matter (G^{PM}) for a given particle radius, r_{p}. The following expanded equation is employed:

$$G^{\mathrm{PM}} = \frac{1}{n^{\mathrm{PM}}}\left(\sum_j \left(n_j^{\alpha} RT \ln a_j'^{,\alpha}\right) + \sum_j \left(n_j^{\beta} RT \ln a_j'^{,\beta}\right) + \sum_j \left(n_j^{\mathrm{s}} RT \ln a_j'^{,\mathrm{s}}\right) + \sum_j \left(n_j^{\mathrm{PM}} \frac{2\sigma^{\mathrm{s}} \mathcal{V}_j}{r_{\mathrm{p}}}\right)\right) \tag{3.28}$$

where n_j^{PM} represents the moles of j in the particulate matter (any condensed phase) and $n^{\mathrm{PM}} = \sum_j n_j^{\mathrm{PM}}$. Note that this equation only applies to a monodisperse aerosol population.

3.5 Results

3.5.1 Interfacial and surface tensions

Throughout this study we presume that both $\sigma^{\alpha\beta}$ and σ^{ls} can be determined using one of the introduced methods. Several of those methods rely on the assumption that hypothetical gas–liquid surface tensions of the phases involved can be estimated based on a weighted average of the pure-component surface tensions, σ_i°. A complete list of all σ_i° for the components of the systems examined in this work can be found in Table B.3. Also reported in Table B.3 are the organic-to-inorganic dry mass ratio (OIR) for each system. In order to explore the validity of this assumption, volume-fraction-based and mole-fraction-based approaches for estimating the surface tension are compared to experimental surface tension data. Figure 3.3 shows the predicted surface tensions using the aforementioned weighted average approaches based on the composition of the surface and bulk phases as determined by the bulk–surface partitioning treatment of Schmedding and Zuend (2023) along with

the more thermodynamically rigorous treatment of surface tension from that same work. It is shown that all three approaches can reasonably approximate the measured surface tensions of the finite volume droplets, with the volume-fraction-based approach performing better than the mole-fraction-based approach for the water and glutaric acid system. Both weighted average approaches give similar results for the aqueous NaCl system.

To compare the relative magnitudes of the different approaches laid out in this work, a 1000 nm dry diameter water–PEG-400–ammonium-sulfate system was modeled with each of the four approaches described in Sections 3.4.1 and 3.4.2. The potential crystallization (efflorescence) of ammonium sulfate at lower RH was ignored in our model calculations, hence rendering predictions for RH $<\sim$ 35 % rather hypothetical, but allowing us to perform and interpret calculations over a wide range in electrolyte concentrations. Shown in Fig. 3.2 are the values of $\sigma^{\alpha\beta}$, σ^{ls}, σ^{s}, and $\sigma^{\mathrm{s}\star}$ for each of the aforementioned approaches. Antonov's rule (Eq. 3.1, panel A) leads to the largest predicted values of $\sigma^{\alpha\beta}$ and σ^{ls} along with the smallest σ^{s}. The other three approaches have minimal effects on σ^{s}, except near the onset of phase separation. In these panels of Fig. 3.2, when viewed from high to low RH, the onset of LLPS is the reason for the visible and related kinks in the σ^{ls} and σ^{s} curves, as well as the more obvious onset of nonzero $\sigma^{\alpha\beta}$ values. The weighted mean interfacial composition approach (Eq. 3.18) (panel D) exhibits unique behavior with a local maximum of $\sigma^{\alpha\beta}$ at $\sim$ 50 % RH and a local minimum at $\sim$ 10 % RH. Such behavior may be caused by the compositions of phases α and β becoming more similar as water is removed from the system and other organic species become dominant as solvents.

Given the lack of interfacial tension data for atmospherically relevant aerosol systems, it is difficult to compare any of the approaches laid out in this work to direct measurements for validation. However, Song et al. (2013) reported interfacial tension values near the onset of liquid–liquid phase separation for a bulk water–PEG-400–ammonium sulfate system. Shown in

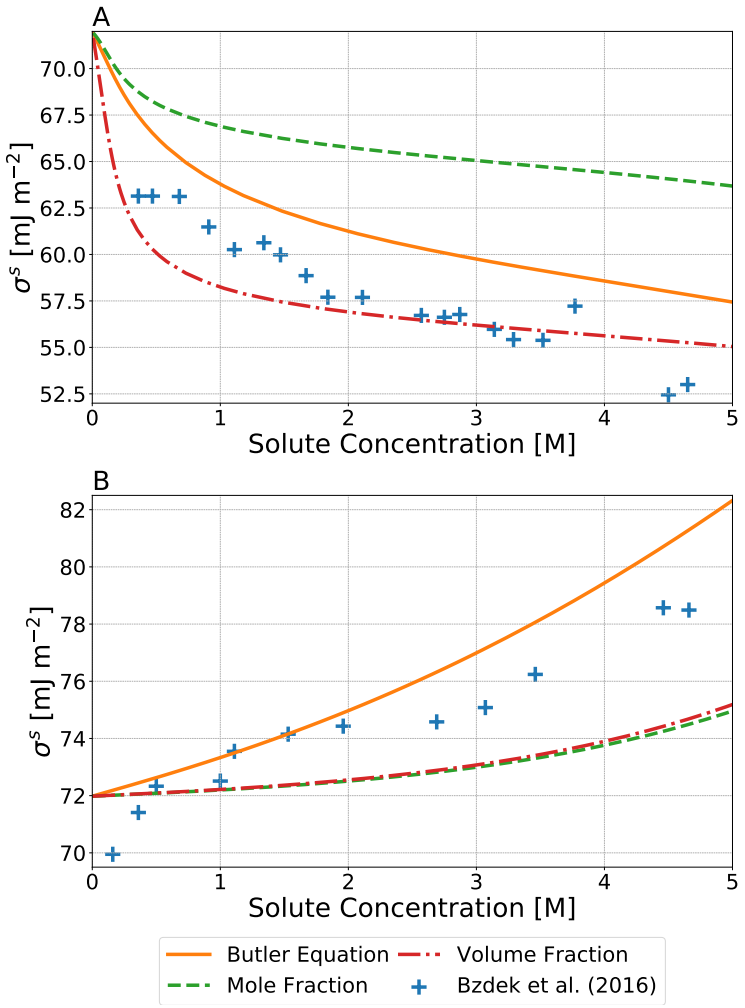

Figure 3.3: Predicted σ^{s} values using the Butler equation based approach of (Schmedding and Zuend, 2023), a surface phase volume-fraction-weighted mean of pure component surface tensions, and a surface phase mole-fraction-weighted mean of pure component surface tensions as a function of solute concentration for binary systems of (A) water and glutaric acid and (B) water and NaCl. The cross symbols show measurements based on the optical tweezer method by (Bzdek et al., 2016) at 298 K. Surface phase compositions were calculated using the Butler equation with the assumption that $\sigma^{ls} = 0$ mJ m^{-2}. Bulk–surface partitioning calculations were performed assuming a water-free particle diameter of 5000 nm.

Fig. 3.4A are these measurements in comparison to Antonov's rule (Eq. 3.1), the Girifalco–Good equation (Eq. 3.2), the Butler equation with geometric mean activity coefficients (Eqs. 3.11 and Eq. 3.13), and the weighted mean approach developed in this work (Eq. 3.18).

For this system, which only included measurements near the onset of phase separation, the Butler equation with geometric mean activity coefficients (Eq. 3.11) best matches the measured interfacial tension followed by the Girifalco–Good equation (Eq. 3.2), while Antonov's rule (Eq. 3.1) performs most poorly. It should be noted that adjusting the value of ϕ in the Girifalco–Good equation (Eq. 3.2) may lead to a better match with measured data; however, use of such adjusted parameters requires refitting of ϕ for each specific system and thus reduces the predictive power and application of the model. Figure 3.4B shows the predicted interfacial tensions from a water–benzene–sodium-chloride system along with bulk solution measurements as a function of sodium chloride concentration in the salt-rich aqueous phase. In this case, none of the models described in this work are capable of reasonably matching the measurements, with Antonov's rule (Eq. 3.1) performing the best and the other approaches yielding substantially lower interfacial tensions, including at zero NaCl content. Similarly, Fig. 3.4C, shows measured and predicted interfacial tensions for a water–dodecane–potassium-chloride system as a function of the aqueous phase electrolyte molality. In this case, Antonov's rule (Eq. 3.1) performs the best of the various approaches and is capable of closely matching the measured interfacial tension at high electrolyte concentrations, while all of the other approaches fail to capture the measured behaviour. Finally, measurements of an electrolyte free system of water–benzene–methanol is shown in Fig. 3.4D. At high methanol mole fractions, the measured interfacial tensions are most similar to those predicted by the weighted mean interfacial composition approach (Eq. 3.18), while the Butler equation with geometric mean activity coefficients (Eq. 3.11) approach underpredicts the interfacial tension, but performs the second best. At low

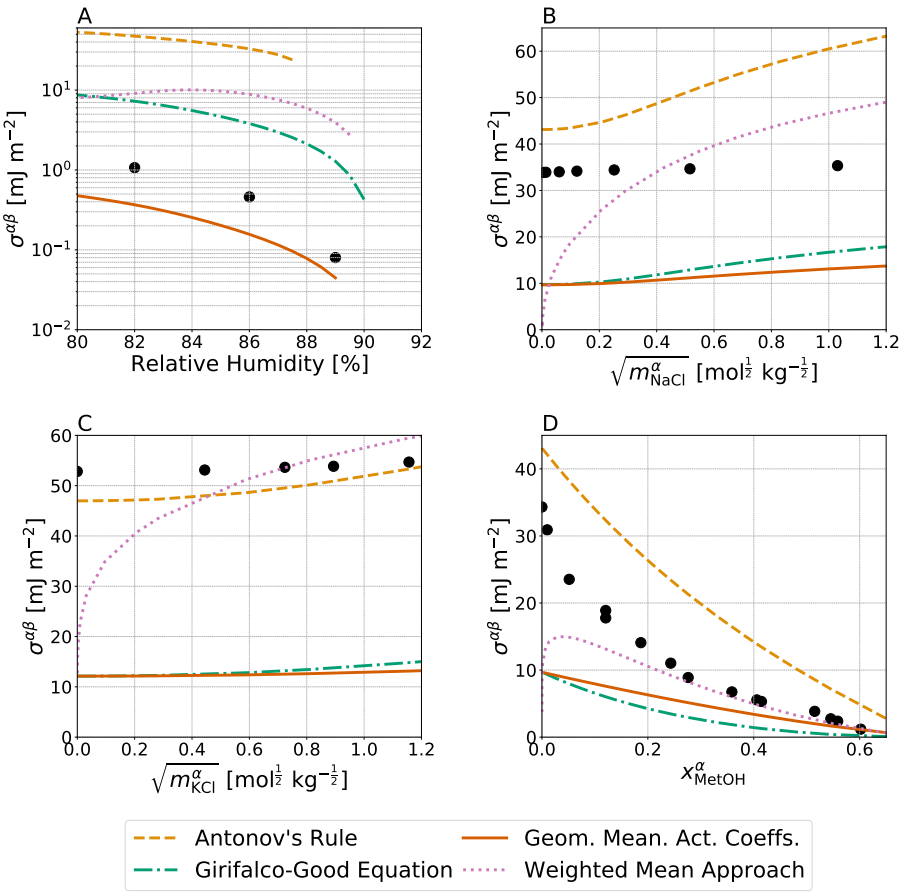

Figure 3.4: Predicted $\sigma^{\alpha\beta}$ values (curves) compared to measurements (solid circles). The x-axis scales correspond to those used in the experimental data references. Data and predictions for all systems are for $T = 298$ K. (A) A water–PEG-400–ammonium-sulfate system with experimental data by Song et al. (2013), (B) a water–benzene–sodium-chloride system (Harkins and Humphery, 1915), (C) a water–dodecane–potassium-chloride system (Aveyard and Saleem, 1976), and (D) a water–benzene–methanol system (Pliskin and Treybal, 1966; Paul and De Chazal, 1967). The four distinct parameterizations for interfacial tension from Table 3.1 are shown (except for the No IFE case). The pure-component surface tensions of organic components can be found in Table B.3

.

methanol content, Antonov's rule (Eq. 3.1) is again the best method for this nearly completely phase-separated system (as in Fig. 3.4B). In order to better understand the importance of σ_i° in determining the value of $\sigma^{\alpha\beta}$ and σ^{ls}, predictions corresponding to those shown in Fig. 3.4 were performed with adjustments to $\sigma_{\mathrm{org}}^\circ$ and $\sigma_{\mathrm{el}}^\circ = \sigma_{\mathrm{w}}^\circ$; those are shown in Fig. B.1.

Briefly, minor adjustments to σ_i° lead to better agreement between the Girifalco–Good equation (Eq. 3.2) and measured data fro the water–PEG-400–ammonium-sulfate system in panel A. In panels B and C, there is better agreement between Antonov's rule (Eq. 3.1) and the water–benzene–sodium-chloride system and the water–dodecane–potassium-chloride system with the adjustments to σ_i°. However, in panel D, Antonov's rule (Eq. 3.1) performs more poorly for the interfacial tension in comparison to measurements for the water–benzene–methanol, assuming the same values of benzene and methanol as those in panels B and C of Fig. S1.

The Girifalco–Good equation (Eq. 3.2) contains a single semi-empirical fit parameter, ϕ, which grants it some degree of flexibility at the expense of predictive power. Harris and Byers (1989) reported that fitted values of ϕ lie between approximately 0.55 and 1.15 for many systems. Note that, as previously in section 3.3, it is assumed that $\phi = 1$ when an interface-free LLE calculation predicts a homogeneously mixed particle. If this were not the case then non-zero interfacial tension values between two identical phases would be possible. Thus ϕ is allowed to deviate from its default value of 1.0 when the interface-free LLE calculation predicts phase separation. Shown in Fig. 3.5 are the values of the predicted LL interfacial tensions when ϕ is varied over the range of 0.55 to 1.15 for a water–suberic acid–ammonium-sulfate system. Values of ϕ greater than 1 can produce unrealistically small $\sigma^{\alpha\beta}$ values (including negative interfacial tensions), while $\phi < 1$ increases $\sigma^{\alpha\beta}$ values. Overall, the tested range in values of ϕ from 0.55 to 1 results in a relatively wide range of physically feasible outcomes for the shown system, e.g. spanning about 70 $\mathrm{mJ\,m^{-2}}$ in $\sigma^{\alpha\beta}$ at 80 % RH. Hence, optimizing this

parameter for a specific system could be a successful approach for achieving a close match to measurements, especially if a composition dependence is also considered. However, such a tuning approach is inconsistent with a typical goal in atmospheric aerosols modeling, namely that of developing generally predictive methods (here of interfacial tension) applicable to a wide range of multicomponent aerosol systems and independent of any experimental data required for specific tuning purposes.

3.5.2 Size-dependent phase separation in core–shell aerosols

Figure 3.6 shows the predicted and normalized mole fraction of water in the ammonium-sulfate-rich phase α ($x_w^{\alpha}/x_w^{\alpha,\text{no IFE}}$) for water–PEG-400–ammonium sulfate particles using the four treatments for interfacial tension laid out in this work. (see figures B.2 and B.3 in Appendix B for the plots corresponding to the normalized mole fractions of PEG-400 and ammonium sulfate in phase α). In order to better understand the role of interfacial energy in terms of its feedback on particle phase compositions, the shown mole fractions are normalized by those predicted by the no IFE treatment for the same conditions. Even at RH values above the onset of LLPS, where only σ^{ls} affects the composition of the single liquid phase (α) present, there is a reduction in the concentration of water relative to the no IFE case. That is, the values of $x_{\text{w}}^{\alpha}/x_{\text{w}}^{\alpha,\text{no IFE}}$ are consistently $\leq$ 1.0, indicating a reduction in the relative water content of phase α when $\sigma^{\alpha\beta}$ and σ^{ls} are accounted for. This indicates that interfacial tension effects in aerosols are not only of importance for shifting the onset in LLPS or for cloud droplet activation, but that they also impact the equilibrium compositions of the various particle phases, unlike in macroscopic bulk systems (for which the no IFE case is a better proxy). At lower RH values, the difference in composition is more pronounced, as all four approaches lead to differences of an order of magnitude from the interfacial energy-free treatment. With each approach there was also a noticeable dependence on particle dry diameter. For the 10 nm particles, these differences in composition are most substantial, while the 1000 nm

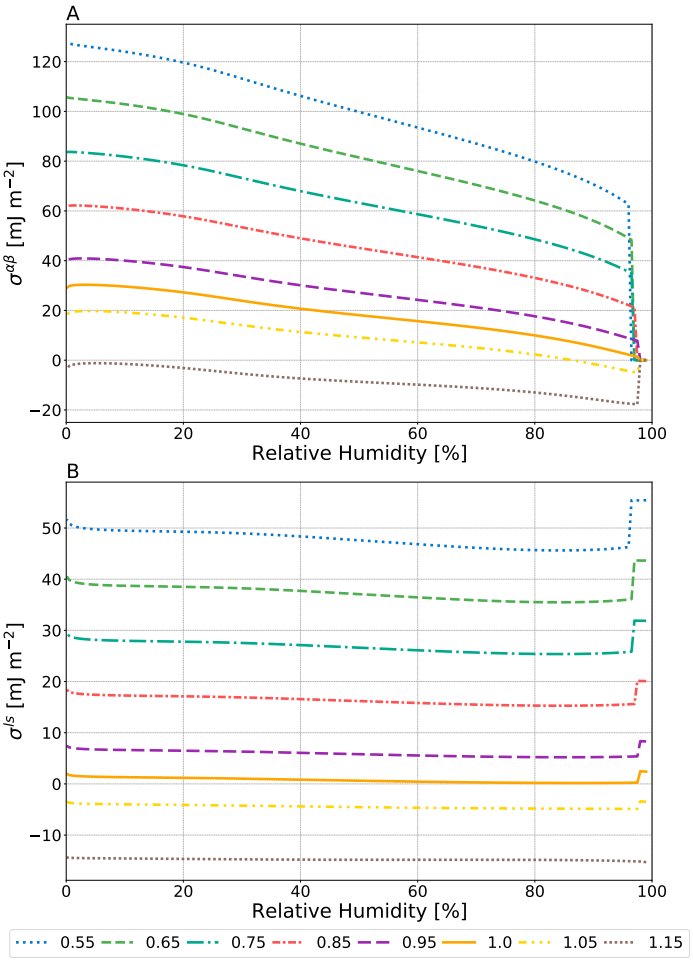

Figure 3.5: The effect of varying ϕ (see legend) on $\sigma^{\alpha\beta}$ of a water–suberic-acid–ammonium-sulfate particle with a water-free diameter of 1000 nm as predicted by the Girifalco–Good approach (Eq. 3.2). $\phi_{\min} = 0.55$ and $\phi_{\max} = 1.15$ as reported by Harris and Byers (1989).

particle and the 100 nm particle behaved more similarly to one another. In Fig. 3.6A, the 10 nm particle exhibits complete suppression of LLPS, across the entire RH range. However, all other interfacial tension treatments lead to LLPS in a certain RH range, as marked by the sudden change (kinks) in $x_{\mathrm{w}}^{\alpha}/x_{\mathrm{w}}^{\alpha,\mathrm{no\ IFE}}$ with decreasing RH.

Figure 3.7 shows the equilibrium water vapor saturation ratio (i.e. RH) corresponding to the onset of liquid–liquid phase separation (also denoted as SRH) for: (A) a water–PEG-300–ammonium-sulfate system and (B) a water–1,2,6-hexanetriol–ammonium-sulfate system, both corresponding to systems examined by Ohno et al. (2023); (C) a 12-component complex SOA surrogate mixture (CSOA) with succinic acid mixed with water and ammonium sulfate and (D) a water–α-pinene-SOA–ammonium sulfate system. (C) and (D) correspond to systems studied experimentally by Kucinski et al. (2019). The α-pinene SOA surrogate system used here for the model predictions is based on the components and relative compositions tabulated by Rastak et al. (2017). Shown for each system are the impacts of the four interfacial tension estimation approaches on the separation RH of LLPS: $\sigma^{\alpha\beta} = 0$, Eq. (3.1),the Girifalco–Good equation (Eq. 3.2), and Butler equation with geometric mean activity coefficients (Eq. 3.11). For all systems, applying Eq. (3.1) led to the most substantial reductions in the onset RH of LLPS, with noticeable decreases in the separation RH occurring in particles with wet diameters between approximately 100 nm and 250 nm. In the case where $\sigma^{\alpha\beta} = 0$, our model predicts an increase in the separation RH for small particle sizes, caused mostly by an increase in effective equilibrium RH at small particle diameters due to the Kelvin effect. It should also be noted that the consideration of nonzero σ^{ls} encourages the occurrence of LLPS and shifts the onset of LLPS in smaller particles to higher RH values as compared to particles with the same initial composition but a larger dry diameter. Indeed, relative to said larger particles, there is a slight increase in the separation RH values in the sub-100 nm (wet diameter) size range for the water–PEG-300–

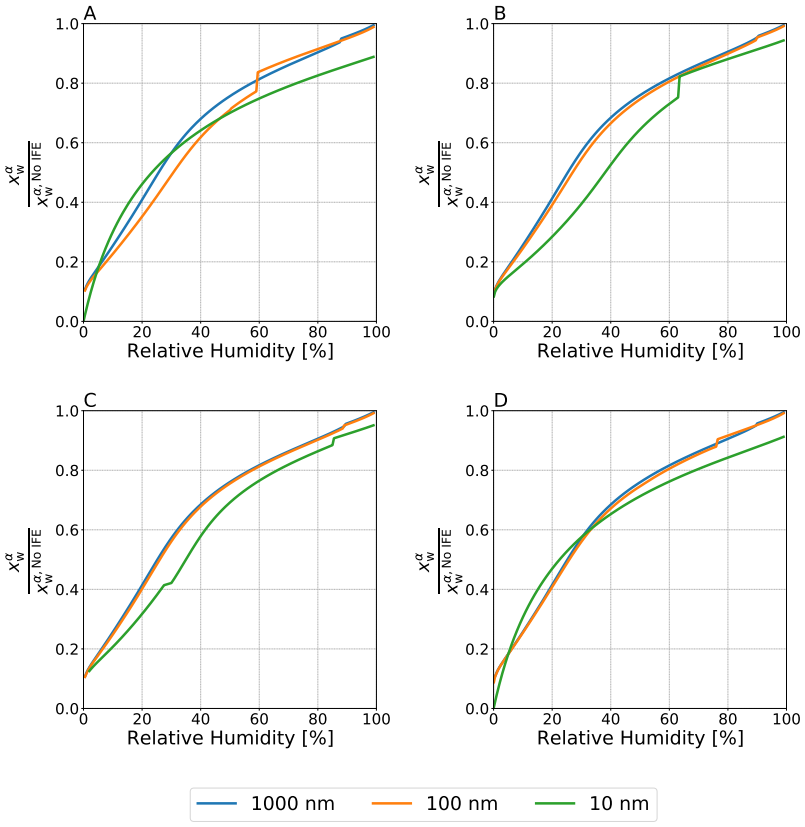

Figure 3.6: Normalized mole fraction of water in the aqueous phase α for water–PEG-400–ammonium sulfate particles with dry diameters ranging from 10 nm to 1000 nm at $T = 298$ K. (A) Antonov's rule (Eq. 3.1), (B) the Girifalco–Good equation (Eq. 3.2), (C) the Butler equation with geometric mean activity coefficients treatment (Eq. 3.11), and (D) the weighted mean interfacial composition approach (Eq. 3.18). Kinks in the curves are indicative of the onset of LLPS.

ammonium sulfate system, while a more noticeable decrease in separation RH is predicted for particles with diameters < 20 nm. In comparison to observations of size-dependent LLPS behavior, Antonov's rule (Eq. 3.1) is the only approach that is consistently capable of suppressing phase separation to below 20 % RH for small wet diameters (likely reported as complete suppression in measurements) for all of the systems shown. The application of Antonov's rule (Eq. 3.1) also leads to measurable decreases in the onset RH of LLPS even for relatively large particle wet diameters (> 200 nm), in agreement with the experimental data reported by Ohno et al. (2023) and Kucinski et al. (2019). Indeed, for the α-pinene SOA system shown in Fig. 3.7D, only Antonov's rule (Eq. 3.1) leads to a notable size dependence in the LLPS onset RH. The corresponding values of $\sigma^{\alpha\beta}$ at the onset of LLPS are shown in Fig. B.4 and the water-free OIRs are listed in Table B.3. For treatments which predict stronger size-dependencies on the separation RH, there is less agreement between $\sigma^{\alpha\beta}$ at the onset of LLPS for the weighted mean interfacial composition approach (Eq. 3.18). This is due to the fact that the predicted $\sigma^{\alpha\beta}$ exhibits a local minimum at low RH values (see fig. 3.2D). The location of such a local minimum is a function of particle size and thus smaller particles may undergo LLPS at RHs below the RH which minimizes $\sigma^{\alpha\beta}$.

Figure B.4 shows the value of $\sigma^{\alpha\beta}$ at the SRH for the systems shown in Fig. 3.7. For all systems, $\sigma^{\alpha\beta}$ at the SRH is lower for larger particles and begins to increase with decreasing particle size. This is due to the fact that these particles experience a decrease in the SRH and therefore the compositions of phases α and β become more distinct at the SRH. However, it should be noted that for very small particles the value of $\sigma^{\alpha\beta}$ at the SRH begins to decrease. Said trend is most clear when Antonov's rule (Eq. 3.1) is applied. This decreasing trend suggests that the compositional differences between liquid phases at very small sizes and low RH become less distinct as the overall water content of the particle is low. Such a trend may be responsible

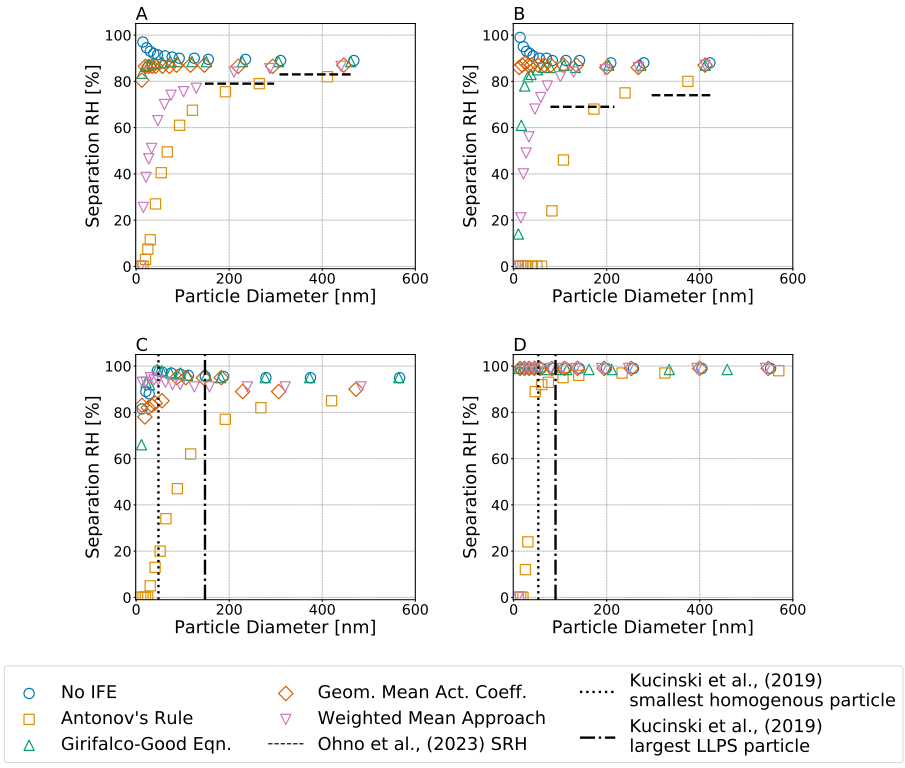

Figure 3.7: Predicted equilibrium separation RH versus particle wet diameter for particles of the same dry composition but different choices of interfacial tension treatment; see legend. Systems shown are: (A) water–PEG-300–ammonium-sulfate, (B) water–1,2,6-hexanetriol–ammonium-sulfate, (C) water–CSOA-with-succinic-acid—ammonium-sulfate, and (D) water–α-pinene-SOA–ammonium-sulfate. (A, B) Dashed horizontal lines indicate measured equilibrium separation RH values by Ohno et al. (2023). (C, D) Vertical lines show the observed largest homogeneous and the smallest phases-separated particles, respectively, as determined by Kucinski et al. (2019). All calculations were performed at 298 K.

for the behavior shown in Fig. 3.7B and C, wherein the smallest particles do not neatly decrease in SRH with respect to particle size; indeed, the competing effects among $\sigma^{\alpha\beta}$, σ^{ls}, and $\sigma^{s,\star}$ lead to weaker decreases in SRH and in the case of panel C and either the Girifalco–Good equation (Eq. 3.2) or the Butler equation with geometric mean activity coefficients treatment (Eq. 3.11), a plateauing effect with a local maximum and then a continued decrease in SRH. However, this effect is small relative to the overall decrease in SRH with decreasing particle size.

Figure B.5 shows the same systems as in Fig. 3.7, but with the assumption that $\sigma^{\mathrm{ls}} = 0$. For the more extreme treatments of $\sigma^{\alpha\beta}$, such as with Antonov's rule (Eq. 3.1) or the weighted mean interfacial composition approach (Eq. 3.18), the exclusion of σ^{ls} has a negligible impact on the size-dependent SRH. However, if $\sigma^{ls} = 0$ and a less extreme treatment of $\sigma^{\alpha\beta}$, such as the Girifalco–Good equation (Eq. 3.2) or the Butler equation with geometric mean activity coefficients treatment (Eq. 3.11) is used, then there is a positive increase in the SRH that is very similar to the No IFE case. It is also important to note that the local maximum behavior discussed in Figure 7 is still present and thus cannot be attributed to the presence or absence of σ^{ls}. Employing either the Girifalco–Good equation (Eq. 3.2) or the Butler equation with geometric mean activity coefficients treatment (Eq. 3.11) yield quantitatively similar LLPS behavior. This suggests that the Girifalco–Good equation (Eq. 3.2) may serve as a good approximation of a more thermodynamically rigorous treatment for the LL interface – at least for qualitatively similar systems to the ones studied in this work.

For particles of less than 100 nm in (wet) diameter, the hypothetical minimum LL interfacial tension necessary to fully suppress LLPS, $\sigma^{\alpha\beta}_{\mathrm{suppr}}$, was calculated based on the difference between the predicted molar Gibbs energy of the phase-separated solution and that of the homogeneous solution in the No IFE case. These values are shown in Fig. 3.8 for the systems from Fig. 3.7. Both the water–PEG-300–ammonium-sulfate and the water–

1,2,6-hexanetriol–ammonium-sulfate systems exhibited weaker size dependence for $\sigma^{\alpha\beta}_{\text{suppr}}$ than the water–CSOA-with-succinic-acid–ammonium-sulfate system, and the water–α-pinene-SOA–ammonium-sulfate system. At low RH ($< 30\%$), both of these SOA-proxy systems required large (> 100 mJ m^{-2}) $\sigma^{\alpha\beta}_{\text{suppr}}$ values to inhibit LLPS, even in the ultrafine size regime. As expected, at RH levels near the onset of phase separation, very small values of $\sigma^{\alpha\beta}$ already exceed $\sigma^{\alpha\beta}_{\text{suppr}}$ in case of all systems. However, the systems shown in Fig. 3.8 do not include any feedback from the inclusion of σ^{ls} treatments. The different treatments for σ^{ls} lead to differences in the composition of the particle before the onset of phase separation and as such, may lead to modifications to the value of $\sigma^{\alpha\beta}_{\text{suppr}}$ for the systems shown. The comparison and size effects shown in Fig. 3.8 mainly serve the purpose of demonstrating that a size dependence exists, yet that complete suppression of LLPS in the RH range from 40 % to 80 % is energetically rather difficult (at least when assuming that AIOMFAC reasonably represents the molecular interactions).

3.6 Discussion and atmospheric implications

The approaches for predicting LL interfacial tension described and tested in this work can produce a broad range of values for the a system under otherwise the same conditions. For mixtures in which there is a higher degree of mutual solubility among components preferring either phase α or β, e.g., the water–PEG-300–ammonium-sulfate, water–PEG-400–ammonium-sulfate, water–1,2,6-hexanetriol–ammonium-sulfate, and the water–benzene–methanol systems, the Girifalco–Good equation and the Butler equation with geometric mean activity coefficients (Eq. 3.14) agree well with previously reported experimental data. In the case of systems with more complete phase separation, such as the water–benzene–NaCl system and the water–dodecane–KCl system, Antonov's rule (Eq. 3.1) appears to be an appropriate method. It is important to note that such systems exhibiting nearly complete phase separation are not necessarily representative of atmospherically

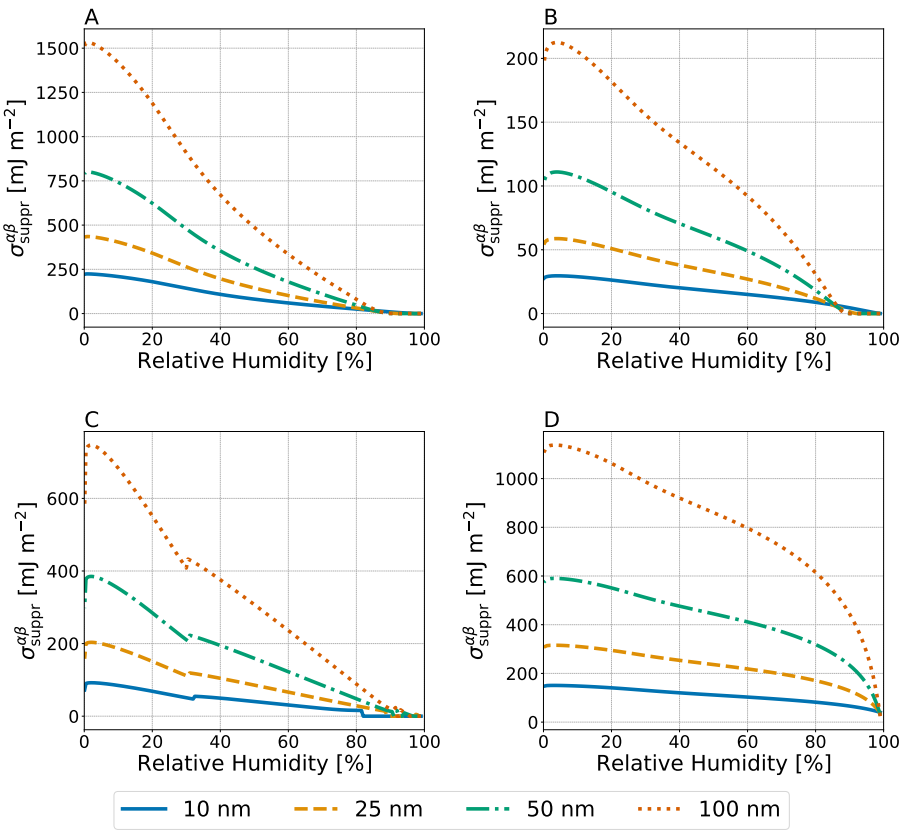

Figure 3.8: Predicted hypothetical $\sigma^{\alpha\beta}$ values necessary to completely suppress phase separation in the No IFE case ($\sigma^{\alpha\beta}_{\text{suppr}}$) as a function of RH for particles with dry diameters of 10, 25, 50, and 100 nm (see legend) at $T = 298$ K. Systems as in Fig. 3.7: (A) water–PEG-300–ammonium-sulfate, (B) water–1,2,6-hexanetriol–ammonium-sulfate, (C) water–CSOA-with-succinic-acid–ammonium-sulfate, and (D) water–α-pinene-SOA–ammonium sulfate.

relevant systems that may be found in ambient mixtures of water, SOA and inorganic ions (Zuend et al., 2011).

The inclusion of interfacial energy corrections mapped onto the chemical activities of components in affected particles can be important for the resulting equilibrium particle phase compositions, even of larger particles, as shown in Fig. 3.6. The effects are more pronounced for smaller particles; however, the magnitude of the change in composition in comparison to the No IFE case is approximately the same for the four approaches of interfacial energy prediction discussed in this work.

Despite better agreement with interfacial tension measurements, the application of the Girifalco–Good (Eq. 3.2) equation and the Butler equation with geometric mean activity coefficients treatment (Eq. 3.11) do not agree well with observed separation relative humidities as a function of particle size. Indeed, Antonov's rule (Eq. 3.1) is the only approach which consistently predicts size-limited phase separation for the systems examined in this work. Importantly, the application of Antonov's rule (Eq. 3.1) to the systems examined in Ohno et al. (2023) leads to relatively good agreement with the observed size-dependent reduction in separation RH for both the water–PEG-300–ammonium-sulfate and the water–1,2,6-hexanetriol–ammonium-sulfate systems. We note that the No IFE simulations lead to higher separation relative humidities for larger particles in both cases. However, in the case of the water–PEG-300–ammonium-sulfate system, Ohno et al. (2023) discuss limiting the upper bound of the explored RH range in their experiments to 83% to avoid issues with condensation in their setup.

For the complex SOA system with ammonium sulfate analyzed by Kucinski et al. (2019), the application of Antonov's rule (Eq. 3.1) leads to a predicted reduction in SRH; however, only particles with diameters below 20 nm exhibited complete suppression of phase separation. Likewise, the α-pinene SOA surrogate system only exhibited complete suppression of LLPS for particles with diameters below 15 nm. For this system, the components were

based on those generated by the Master Chemical Mechanism for a specific ozonolysis case study (Rastak et al., 2017); therefore, most of the used $\sigma^{\circ}_{\mathrm{org}}$ values were not available from measurements and we assumed a value of 35 $\mathrm{mJ\,m^{-2}}$ for those organic products. It is possible that better constraints on these values may lead to larger $\sigma^{\alpha\beta}$ values, which are capable of further suppressing LLPS at higher relative humidities. However, for this system the interfacial tension required to suppress LLPS becomes quite high as the RH decreases. It is therefore unlikely that realistic interfacial tensions of typically less than 100 $\mathrm{mJ\,m^{-2}}$ will completely inhibit LLPS across the full RH range for all but the smallest ultrafine particles.

The energetic contributions of the LL interface and the bulk–surface interface have competing effects on a particle's internal mixing state. If an energetic contribution from the LL interface is included and the bulk–surface interface is neglected then particles may exhibit decreases in SRH. However, if both contributions are included and assuming that the same treatment is used for both interfaces (e.g., the Girifalco–Good equation (Eq. 3.2)) then particles with smaller diameters phase-separate at the same or higher relative humidities than larger particles in all but the most extreme cases of interfacial tension. This is likely due to the fact that in a particle in which phase separation is suppressed (compared to the macroscopic bulk case), the composition of the surface will be more distinct from that of the interior bulk, leading to a larger energetic contribution at the bulk–surface interface. Given that the area of the bulk–surface interface must inherently always be larger than the $\alpha\beta$ LL interface, a comparable bulk–surface LL interface value would lead to a larger total energetic contribution per particle. Thus, in many cases it becomes favorable even for an ultrafine particle to form a LLPS and thereby substantially lower σ^{ls} while introducing a nonzero $\sigma^{\alpha\beta}$.

The inclusion of surface energy, liquid–liquid interface, and bulk–surface interface may also lead to a more complete picture regarding the structure of the surface phase. Thicker 3-D surface phases of larger corresponding δ^{s}

values typically imply higher surface energy contributions. However, surfaces with thicker δ^{s} values tend to be of compositions that are more similar to the interior bulk of the particle. This would reduce the energetic penalties from the bulk–surface interface and inhibit phase separation by increasing depletion of species out of the interior bulk of the particle to the surface phase. Likewise, the opposite effects likely would occur in a particle with a surface that has a small δ^{s} value. The particle would have a lower surface energy coupled with a higher bulk–surface LL interfacial tension and reduced inhibition of LLPS. To explore this trade-off quantitatively, we have run a range of predictions during which δ^{s} was allowed to vary from 0.1 to 17.5 nm in surface thickness and evaluated the resulting normalized Gibbs energy of the system. Simulations were not conducted above $\delta^{s} > 17.5$ nm as this would represent an extreme case wherein the volume of the surface could become substantially greater than the volume of phase β. Figure 3.9 shows the determined optimum values of δ^{s} for a water–1,2,6-Hexanetriol–ammonium sulfate particle with a water-free diameter of 250 nm as function of RH. For this system, the optimum δ^{s} value (δ^{s}_{best}) is calculated for the various interfacial tension options for $\sigma^{\alpha\beta}$ and σ^{ls} compared throughout this work: the No IFE case, Antonov's rule (Eq. 3.1), the Girifalco–Good equation (Eq. 3.2), the Butler equation with geometric mean activity coefficients (Eq. 3.14) and the weighted mean interfacial composition approach (Eq. 3.18). As the relative humidity is decreased, the thickness of δ^{s}_{best} increases near the onset of LLPS. Values of δ^{s}_{best} remain high and then decrease in all cases. In the case of the weighted mean interfacial composition approach (Eq. 3.18), the decrease in δ^{s}_{best} is more gradual at lower RH. The application of Antonov's rule (Eq. 3.1) leads to unique behavior among the different methods tested, due to it's suppression of LLPS when δ^{s} is large. This causes δ^{s}_{best} to return to large values at lower RHs which forces the particle to form a single bulk phase with a very thick surface phase. Such behaviour is due to the particle trying to minimize compositional differences across phases α, β, and the

surface by increasing the material present in the surface phase. The relative changes $\delta^{\mathrm{s}}_{\mathrm{best}}$ with decreasing RH near the onset of phase separation are similar in magnitude for the no IFE case, the Girifalco–Good equation, the Butler equation with geometric mean activity coefficients treatment (Eq. 3.11), and the weighted mean interfacial composition approach. Such behavior suggests that the inclusion of bulk–surface partitioning is more important for determining the structure of the surface phase than the inclusion of σ^{ls}. At RH values further below the onset of LLPS $\delta^{\mathrm{s}}_{\mathrm{best}}$ becomes much smaller again for the no IFE case, the Girifalco–Good equation, the the Butler equation with geometric mean activity coefficients treatment (Eq. 3.11), approaching the physical limit of a three-dimensional surface phase ($\delta^{\mathrm{s}}_{\mathrm{best}} = 0.1$ nm) in agreement with Schmedding and Zuend (2023). This is likely due to the fact that the energetic contributions of $\sigma^{\alpha\beta}$ are much larger than those of σ^{ls} and that lower values of δ^{s} correspond to lower values of $\sigma^{\mathrm{s}\star}$. The results reported by Schmedding and Zuend (2023), which did not account for the energetic penalty of the bulk–surface interface, found that thinner surfaces are more energetically favorable for well-mixed particles. The inclusion of this interfacial contribution suggests that the most favorable surface thickness is dynamic; typically favoring a thin surface phase in dilute aqueous droplets. Moreover, in some cases a thicker surface is preferred to a thinner one, especially close to the onset of LLPS. This could suggest a potential mechanism wherein LLPS may occur initially as a form of bulk–surface partitioning with a gradual thickening of the surface phase before an additional distinct bulk phase forms. It is possible that such behavior may be responsible for some of the observed size-limited phase separation behavior reported in previous studies since, with limited depth resolution in an experiment, it is difficult to distinguish between a thick surface phase that is enriched in organic species and a thin, organic-rich phase β in particles in which such a configuration for the surface may be favorable.

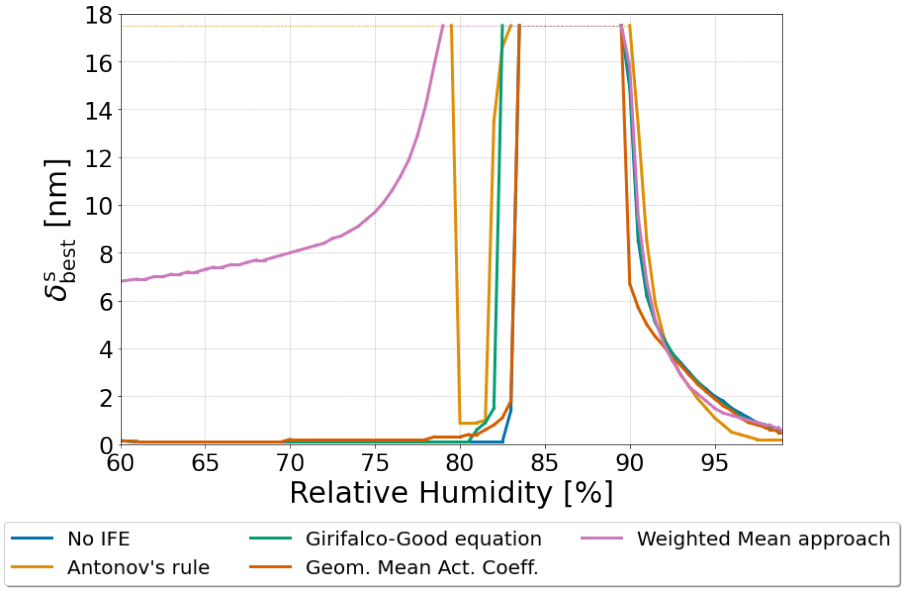

Figure 3.9: The δ^s value corresponding to the overall minimum in Gibbs energy of a 250 nm dry diameter particle for each interfacial tension treatment. The particle was composed of water, 1,2,6-hexanetriol, and ammonium sulfate with a 2:1 organic-to-inorganic dry mass ratio. δ^s values between 0.1–17.5 nm were tested.

3.7 Conclusions

Atmospheric aerosol particles may exhibit liquid-liquid phase separation (e.g., You et al., 2014; Huang et al., 2021). Recent observations have noted that some aerosol systems may exhibit size-dependent LLPS wherein smaller particles undergo LLPS under more extreme conditions (e.g. substantially lower RH), than large particles. This study aims to explore the interactions between phase separation, bulk–surface partitioning, and LL interfaces in aerosol particles through the extension of a previously developed bulk–surface partitioning model which now includes the coupling with a liquid–liquid phase separation model. Various treatments for the energetic contribution of LL interfaces are explored. For systems with greater miscibility among the solution components, the Girifalco–Good equation and the Butler equation more accurately reproduce measured interfacial tensions. For systems exhibiting increased immiscibility among components, Antonov's rule performs better than the other approaches. The inclusion of LL interfacial tension terms and bulk–surface partitioning leads to a predicted lowering of the separation RH of LLPS in many systems. This reduction in the separation RH was most pronounced for particles with wet diameters below 50–70 nm. The weighted mean composition approach and Antonov's rule led to the largest decreases in the predicted separation RH for all of the systems examined in this work. For the smallest particle sizes studied ($10 - 50$ nm in wet diameter), these two approaches lead to substantial suppression of LLPS to below 40 % RH ($\sim$ efflorescence RH of ammonium sulfate) or complete inhibition of LLPS. An energetic contribution from the LL boundary between the surface phase and its adjacent bulk phase was considered in this work. This interfacial tension contribution is shown to be at its maximum near the, where the difference in composition between the surface and bulk phases is greatest.

While numerous studies have examined LLPS in larger particles and macroscopic bulk solutions, studies on LLPS in submicron-sized particles are scarce (Kucinski et al., 2019; Ohno et al., 2023; Ott and Freedman, 2020;

Ott et al., 2021). For small particles, it can be difficult to experimentally distinguish between a surface phase of more than monolayer thickness phase and a thin bulk phase in a core–shell configuration, since the minimum required thickness to call a surface layer a "regular" liquid phase rather than a multilayer surface is a matter of perspective. The interplay of bulk–surface partitioning, interfacial tensions, and LLPS hint at the difficulties in conducting measurements on nanoparticles. Measurements of size-dependent particle properties in the submicron range should be contactless. Contact with the particle (surface) will change the surface area to volume ratio, may generate additional interfaces, induce bulk–surface partitioning feedbacks, and indirectly influence the targeted particle properties. The applicability of measurements performed on macroscopic systems for microscopic droplets needs to be considered carefully. Most LL interfacial tension measurements are made using bulk solution techniques; therefore, caution is warranted when extrapolating these data to sub-100 nm particles, for which deviations from bulk solution are pronounced. This study highlights the interest in additional measurements covering sub-100 nm particles to provide guidance for constraining model parameters. This work represents a step towards more physically realistic representations of aerosol particles accounting for LL interfaces and size-dependent LLPS behavior. While offering options for interfacial tension treatment, this model remains predictive and broadly applicable in its design. It will allow for a predictive treatment of particles in the ultrafine aerosol regime and aids in connecting measurements taken on larger particles to their smaller counterparts.

The interfacial tension at the $\alpha\beta$ interface, and the surface energies of phases α and β may be used to predict if a particle's equilibrium morphology is core–shell or partially engulfed. Because partially engulfed morphologies require additional considerations, these morphological questions are a direction for future studies.

Bibliography

Schmedding, R.; Zuend, A. The role of interfacial tension in the size-dependent phase separation of atmospheric aerosol particles. EGUsphere **2024**, 2024, 1–35.

Intergovernmental Panel on Climate, C., Ed. Climate Change 2013 – The Physical Science Basis: Working Group I Contribution to the Fifth Assessment Report of the Intergovernmental Panel on Climate Change; Cambridge University Press: Cambridge, 2014; pp 1–30.

Jimenez, J. L. et al. Evolution of Organic Aerosols in the Atmosphere. Science **2009**, 326, 1525–1529.

Zhang, Q. et al. Ubiquity and dominance of oxygenated species in organic aerosols in anthropogenically-influenced Northern Hemisphere midlatitudes. Geophysical Research Letters **2007**, 34.

Kucinski, T. M.; Dawson, J. N.; Freedman, M. A. Size-Dependent Liquid–Liquid Phase Separation in Atmospherically Relevant Complex Systems. The Journal of Physical Chemistry Letters **2019**, 10, 6915–6920.

Ohno, P. E.; Brandão, L.; Rainone, E. M.; Aruffo, E.; Wang, J.; Qin, Y.; Martin, S. T. Size Dependence of Liquid–Liquid Phase Separation by in Situ Study of Flowing Submicron Aerosol Particles. The Journal of Physical Chemistry A **2023**, 127, 2967–2974, PMID: 36947002.

Marcolli, C.; Krieger, U. K. Phase Changes during Hygroscopic Cycles of Mixed Organic/Inorganic Model Systems of Tropospheric Aerosols. The Journal of Physical Chemistry A **2006**, 110, 1881–1893, PMID: 16451021.

You, Y.; Renbaum-Wolff, L.; Carreras-Sospedra, M.; Hanna, S. J.; Hiranuma, N.; Kamal, S.; Smith, M. L.; Zhang, X.; Weber, R. J.; Shilling, J. E.; Dabdub, D.; Martin, S. T.; Bertram, A. K. Images reveal that atmospheric particles can undergo liquid–liquid phase separations. Proceedings of the National Academy of Sciences **2012**, 109, 13188–13193.

Ciobanu, V. G.; Marcolli, C.; Krieger, U. K.; Weers, U.; Peter, T. Liquidâ^'Liquid Phase Separation in Mixed Organic/Inorganic Aerosol Particles. The Journal of Physical Chemistry A **2009**, 113, 10966–10978, PMID: 19775109.

Bertram, A. K.; Martin, S. T.; Hanna, S. J.; Smith, M. L.; Bodsworth, A.; Chen, Q.; Kuwata, M.; Liu, A.; You, Y.; Zorn, S. R. Predicting the relative humidities of liquid-liquid phase separation, efflorescence, and deliquescence of mixed particles of ammonium sulfate, organic material, and water using the organic-to-sulfate mass ratio of the particle and the oxygen-to-carbon elemental ratio of the organic component. Atmospheric Chemistry and Physics **2011**, 11, 10995–11006.

Freedman, M. A. Phase separation in organic aerosol. Chem. Soc. Rev. **2017**, 46, 7694–7705.

Huang, Y.; Mahrt, F.; Xu, S.; Shiraiwa, M.; Zuend, A.; Bertram, A. K. Coexistence of three liquid phases in individual atmospheric aerosol particles. Proceedings of the National Academy of Sciences **2021**, 118, e2102512118.

Lilek, J.; Zuend, A. A predictive viscosity model for aqueous electrolytes and mixed organic–inorganic aerosol phases. Atmospheric Chemistry and Physics **2022**, 22, 3203–3233.

Gervasi, N. R.; Topping, D. O.; Zuend, A. A predictive group-contribution model for the viscosity of aqueous organic aerosol. Atmospheric Chemistry and Physics **2020**, 20, 2987–3008.

Schmedding, R.; Zuend, A. A thermodynamic framework for bulk–surface partitioning in finite-volume mixed organic–inorganic aerosol particles and cloud droplets. Atmospheric Chemistry and Physics **2023**, 23, 7741–7765.

Kleinheins, J.; Shardt, N.; El Haber, M.; Ferronato, C.; Nozière, B.; Peter, T.; Marcolli, C. Surface tension models for binary aqueous solutions: a review and intercomparison. Phys. Chem. Chem. Phys. **2023**, 25, 11055–11074.

Li, W.; Teng, X.; Chen, X.; Liu, L.; Xu, L.; Zhang, J.; Wang, Y.; Zhang, Y.; Shi, Z. Organic Coating Reduces Hygroscopic Growth of Phase-Separated Aerosol Particles. Environmental Science & Technology **2021**, 55, 16339–16346, PMID: 34894668.

Chan, M. N.; Lee, A. K. Y.; Chan, C. K. Responses of Ammonium Sulfate Particles Coated with Glutaric Acid to Cyclic Changes in Relative Humidity: Hygroscopicity and Raman Characterization. Environmental Science & Technology **2006**, 40, 6983–6989, PMID: 17154005.

Gaston, C. J.; Thornton, J. A.; Ng, N. L. Reactive uptake of N_2O_5 to internally mixed inorganic and organic particles: the role of organic carbon oxidation state and inferred organic phase separations. Atmospheric Chemistry and Physics **2014**, 14, 5693–5707.

Schmedding, R.; Rasool, Q. Z.; Zhang, Y.; Pye, H. O. T.; Zhang, H.; Chen, Y.; Surratt, J. D.; Lopez-Hilfiker, F. D.; Thornton, J. A.; Goldstein, A. H.; Vizuete, W. Predicting secondary organic aerosol phase state and viscosity and its effect on multiphase chemistry in a regional-scale air quality model. Atmos. Chem. Phys. **2020**, 20, 8201–8225.

Ovadnevaite, J.; Zuend, A.; Laaksonen, A.; Sanchez, K. J.; Roberts, G.; Ceburnis, D.; Decesari, S.; Rinaldi, M.; Hodas, N.; Facchini, M. C.; Seinfeld, J. H.; O' Dowd, C. Surface tension prevails over solute effect in organic-influenced cloud droplet activation. Nature **2017**, 546, 637–641.

Malek, K.; Gohil, K.; Olonimoyo, E. A.; Ferdousi-Rokib, N.; Huang, Q.; Pitta, K. R.; Nandy, L.; Voss, K. A.; Raymond, T. M.; Dutcher, D. D.; Freedman, M. A.; Asa-Awuku, A. Liquid–Liquid Phase Separation Can Drive Aerosol Droplet Growth in Supersaturated Regimes. ACS Environmental Au **2023**, 3, 348–360.

Ruehl, C. R.; Davies, J. F.; Wilson, K. R. An interfacial mechanism for cloud droplet formation on organic aerosols. Science **2016**, 351, 1447–1450.

Davies, J. F.; Zuend, A.; Wilson, K. R. Technical note: The role of evolving surface tension in the formation of cloud droplets. Atmos. Chem. Phys. **2019**, 19, 2933–2946.

Kwamena, N. O. A.; Buajarern, J.; Reid, J. P. Equilibrium Morphology of Mixed Organic/Inorganic/Aqueous Aerosol Droplets: Investigating the Effect of Relative Humidity and Surfactants. The Journal of Physical Chemistry A **2010**, 114, 5787–5795.

Gorkowski, K.; Donahue, N. M.; Sullivan, R. C. Aerosol Optical Tweezers Constrain the Morphology Evolution of Liquid-Liquid Phase-Separated Atmospheric Particles. Chem **2020**, 6, 204–220.

Reid, J. P.; Dennis-Smither, B. J.; Kwamena, N.-O. A.; Miles, R. E. H.; Hanford, K. L.; Homer, C. J. The morphology of aerosol particles consisting of hydrophobic and hydrophilic phases: hydrocarbons, alcohols and fatty acids as the hydrophobic component. Physical Chemistry Chemical Physics **2011**, 13, 15559–15572.

Song, M.; Marcolli, C.; Krieger, U. K.; Zuend, A.; Peter, T. Liquid-liquid phase separation and morphology of internally mixed dicarboxylic acids/ammonium sulfate/water particles. Atmospheric Chemistry and Physics **2012**, 12, 2691–2712.

Song, M.; Marcolli, C.; Krieger, U. K.; Lienhard, D. M.; Peter, T. Morphologies of mixed organic/inorganic/aqueous aerosol droplets. Faraday Discuss. **2013**, 165, 289–316.

Shiraiwa, M.; Zuend, A.; Bertram, A. K.; Seinfeld, J. H. Gas-particle particle partitioning of atmospheric aerosols: interplay of physical state, non-ideal mixing and morphology. Phys. Chem. Chem. Phys. **2013**, 15, 11441–11453.

Lang-Yona, N.; Abo-Riziq, A.; Erlick, C.; Segre, E.; Trainic, M.; Rudich, Y. Interaction of internally mixed aerosols with light. Physical Chemistry Chemical Physics **2010**, 12, 21–31.

Lam, H. K.; Xu, R.; Choczynski, J.; Davies, J. F.; Ham, D.; Song, M.; Zuend, A.; Li, W.; Tse, Y.-L. S.; Chan, M. N. Effects of liquid–liquid phase separation and relative humidity on the heterogeneous OH oxidation of inorganic–organic aerosols: insights from methylglutaric acid and ammonium sulfate particles. Atmospheric Chemistry and Physics **2021**, 21, 2053–2066.

Hua, X.; Bevan, M. A.; Frechette, J. Reversible Partitioning of Nanoparticles at an Oil–Water Interface. Langmuir **2016**, 32, 11341–11352, PMID: 27564252.

Russell, L. M.; Ming, Y. Deliquescence of small particles. The Journal of Chemical Physics **2002**, 116, 311–321.

Zuend, A.; Marcolli, C.; Peter, T.; Seinfeld, J. H. Computation of liquid-liquid equilibria and phase stabilities: implications for RH-dependent

gas/particle partitioning of organic-inorganic aerosols. Atmospheric Chemistry and Physics **2010**, 10, 7795–7820.

Antonov, G. N. Sur la tension superficielle des solutions dans la zone critique. J. Chim. Phys. **1907**, 5, 364–371.

Makkonen, L.; Kurkela, J. Another look at the interfacial interaction parameter. Journal of Colloid and Interface Science **2018**, 529, 243–246.

Winter, A. Antonow's rule 85 years later. Heterogeneous Chemistry Reviews **1995**, 2, 269–308.

Girifalco, L. A.; Good, R. J. A Theory for the Estimation of Surface and Interfacial Energies. I. Derivation and Application to Interfacial Tension. The Journal of Physical Chemistry **1957**, 61, 904–909.

Fowkes, F. M. Determination of interfacial tensions, contact angles, and dispersion forces in surfaces by assuming additivity of intermolecular interactions in surfaces. The Journal of Physical Chemistry **1962**, 66, 382–382.

Fowkes, F. M. Additivity of intermolecular forces at interfaces. I. determination of the contribution to surface and interfacial tensions of dispersion forces in various liquids. The Journal of Physical Chemistry **1963**, 67, 2538–2541.

Freedman, M. A. Liquid–Liquid Phase Separation in Supermicrometer and Submicrometer Aerosol Particles. Accounts of Chemical Research **2020**, 53, 1102–1110.

Ott, E.-J. E.; Freedman, M. A. Inhibition of Phase Separation in Aerosolized Water-Soluble Polymer–Polymer Nanoparticles at Small Sizes and the Effects of Molecular Weight. The Journal of Physical Chemistry B **2020**, 124, 7518–7523, PMID: 32790387.

Ott, E.-J. E.; Kucinski, T. M.; Dawson, J. N.; Freedman, M. A. Use of Transmission Electron Microscopy for Analysis of Aerosol Particles and Strategies for Imaging Fragile Particles. Analytical Chemistry **2021**, 93, 11347–11356.

Amirfazli, A.; Neumann, A. Status of the three-phase line tension: a review. Advances in Colloid and Interface Science **2004**, 110, 121–141.

Gibbs, J. W. Thermodynamics; Longmans, Green and Company, 1906; Vol. 1.

Guggenheim, E. A. The thermodynamics of interfaces in systems of several components. Transactions of the Faraday Society **1940**, 35, 397–412.

Zuend, A.; Marcolli, C.; Luo, B. P.; Peter, T. A thermodynamic model of mixed organic-inorganic aerosols to predict activity coefficients. Atmospheric Chemistry and Physics **2008**, 8, 4559–4593.

Zuend, A.; Marcolli, C.; Booth, A. M.; Lienhard, D. M.; Soonsin, V.; Krieger, U. K.; Topping, D. O.; McFiggans, G.; Peter, T.; Seinfeld, J. H. New and extended parameterization of the thermodynamic model AIOMFAC: calculation of activity coefficients for organic-inorganic mixtures containing carboxyl, hydroxyl, carbonyl, ether, ester, alkenyl, alkyl, and aromatic functional groups. Atmospheric Chemistry and Physics **2011**, 11, 9155–9206.

Yin, H.; Dou, J.; Klein, L.; Krieger, U. K.; Bain, A.; Wallace, B. J.; Preston, T. C.; Zuend, A. Extension of the AIOMFAC model by iodine and carbonate species: applications for aerosol acidity and cloud droplet activation. Atmospheric Chemistry and Physics **2022**, 22, 973–1013.

Bahramian, A.; Danesh, A. Prediction of liquid–vapour surface tension in multi-component systems. Fluid Phase Equilibria **2005**, 236, 156–161.

Bahramian, A.; Danesh, A. Prediction of liquid–liquid interfacial tension in multi-component systems. Fluid Phase Equilibria **2004**, 221, 197–205.

Wang, P.; Anderko, A. Modeling Interfacial Tension in Liquid–Liquid Systems Containing Electrolytes. Industrial & Engineering Chemistry Research **2013**, 52, 6822–6840.

Binyaminov, H.; Abdullah, F.; Zargarzadeh, L.; Elliott, J. A. W. Thermodynamic Investigation of Droplet–Droplet and Bubble–Droplet Equilibrium in an Immiscible Medium. The Journal of Physical Chemistry B **2021**, 125, 8636–8651, PMID: 34310143.

Bahramian, A. Unlocking the Secrets of Liquid–Liquid Interfaces and Phase Equilibria: Exploring the Interplay of Critical Composition, Interfacial Tension, and Mutual Solubility. Langmuir **2024**, 40, 4684–4701, PMID: 38381860.

Aston, M. S.; Herrington, T. M. The effect of added electrolyte on surface pressure/area per molecule isotherms. Journal of Colloid and Interface Science **1991**, 141, 50–59.

Zuend, A.; Seinfeld, J. H. Modeling the gas-particle partitioning of secondary organic aerosol: the importance of liquid-liquid phase separation. Atmos. Chem. Phys. **2012**, 12, 3857–3882.

Zuend, A.; Seinfeld, J. H. A practical method for the calculation of liquid–liquid equilibria in multicomponent organic–water–electrolyte systems using physicochemical constraints. Fluid Phase Equilibria **2013**, 337, 201–213.

Bzdek, B. R.; Power, R. M.; Simpson, S. H.; Reid, J. P.; Royall, C. P. Precise, contactless measurements of the surface tension of picolitre aerosol droplets. Chem. Sci. **2016**, 7, 274–285.

Harkins, W. D.; Humphery, E. C. The Surface-Tension at the Interface Between Two Liquids. Proceedings of the National Academy of Sciences **1915**, 1, 585–590.

Aveyard, R. L.; Saleem, S. M. Interfacial tensions at alkane-aqueous electrolyte interfaces. Journal of the Chemical Society, Faraday Transactions **1976**, 72, 1609–1617.

Pliskin, I.; Treybal, R. E. Interfacial Tensions in Two-Liquid-Phase Ternary Systems. Journal of Chemical and Engineering Data **1966**, 11, 49–52.

Paul, G. W.; De Chazal, L. M. Interfacial tensions in ternary liquid-liquid systems. Journal of Chemical and Engineering Data **1967**, 12, 105–107.

Harris, M. T.; Byers, C. H. An advanced technique for interfacial tension measurement in liquid- liquid systems; 1989.

Rastak, N. et al. Microphysical explanation of the RH-dependent water affinity of biogenic organic aerosol and its importance for climate. Geophysical Research Letters **2017**, 44, 5167–5177.

You, Y.; Smith, M. L.; Song, M.; Martin, S. T.; Bertram, A. K. Liquid–liquid phase separation in atmospherically relevant particles consisting of organic species and inorganic salts. Int. Rev. Phys. Chem. **2014**, 33, 43–77.

4

A Machine Learning Approach for Predicting the Pure–Component Surface Tension of Atmospherically Relevant Organic Compounds

4.1 Preface

In Chapter 3, it was found that the inclusion of interfacial tension between two liquid phases, α and β, acts in competition with the interfacial tension between the underlying bulk phase, l, and the surface phase above it, s. The interfacial tension between α and β reduces the relative humidity at which a particle will phase separate as a function of spherical equivalent diameter. The interfacial tension between l, which may be β or α, and s raises the relative humidity at which a particle will phase separate as a function of spherical equivalent diameter. All of the treatments except for one in chapter 3 rely on estimates of the pure component surface tension of each species in an aerosol particle. Chapter 4 introduces three different machine learning models to estimate the pure component surface tensions of atmospherically relevant organic compounds. This chapter aims to develop a model that can take molecular structure and temperature as inputs and return the surface tension of a pure compound at said temperature.

4.2 Abstract

Atmospheric aerosols are complex mixtures of highly functionalized organic compounds, water, inorganic electrolytes, metals and carbonaceous species. The surface properties of atmospheric aerosol particles can influence many of their properties including aerosol–cloud interactions and heterogeneous chemical reactions. The effects of the various compounds within a particle on its surface tension depend in part on the pure–component surface tensions. Many of the myriad of organic compounds of interest do not have easily accessible pure–component surface tension values. In this work, a compiled database of experimental pure–component surface tension data, covering a wide range of organic compound classes and temperatures, are used to train four different types of machine learning models to predict the temperature-dependent pure–component surface tensions of atmospherically relevant organic compounds. The trained models process input information about the molecular structure of an organic compound, initially in form of a Simplified Molecular Input Line Entry System string, alongside temperature to enable predictions. It was found that extreme gradient-boosted descent along with Molecular ACCess System key descriptors of molecular structure provided the best balance of derived input complexity and model performance. Additionally, a simplified model based only on molar mass, elemental ratios, and temperature as inputs, was developed for use in applications where molecular structure information is incomplete. We demonstrate that including predicted pure–component surface tension values in thermodynamically rigorous bulk–surface partitioning calculations may modify the critical supersaturations necessary for cloud droplet activation.

Introduction

Atmospheric aerosols are suspensions of particles and the gas phase that surrounds them. Atmospheric aerosol particles can modify the global climate both directly by scattering and reflecting incoming and outgoing solar radi-

ation and indirectly through their impacts on clouds by acting as cloud condensation nuclei (CCN) for liquid droplets or ice nucleating particles (INP) in ice and mixed-phase clouds (Aitken, 1881; Twomey, 1974). The activation of aerosol particles into cloud droplets is governed by several factors. The critical supersaturation necessary for cloud droplet activation is given by the global maximum of the following equation (Köhler, 1936):

$$S = a_w \exp\left(\frac{4\sigma M_w}{RT\rho_w D_p}\right). \tag{4.1}$$

Here, S represents the equilibrium saturation ratio, a_w is the activity of water in the particle and M_w and ρ_w are the molar mass and density of water, respectively. R is the gas constant, T is the temperature, D_p is the aerosol particle diameter and σ is the equilibrium droplet surface tension. This equation can be broken up into the Raoult (or solute) effect which is described by a_w and the Kelvin (or surface effect) which is represented by the exponential factor in Eq. (2.1).

Recently, the role of surface properties and corresponding feedbacks on the Raoult effect in the activation of aerosol particles into cloud droplets has come under scrutiny (Sorjamaa et al., 2004; Nozière et al., 2014; Gérard et al., 2016; Petters and Petters, 2016; Ruehl et al., 2016; Ovadnevaite et al., 2017; Kroflič et al., 2018; Malila and Prisle, 2018; Davies et al., 2019; Gérard et al., 2019; Schmedding and Zuend, 2023). Beyond cloud droplet activation, surface tension is crucial in determining the size-dependent surface composition of aqueous aerosol particles (Schmedding and Zuend, 2023). The composition of the surface of aerosol particles may influence multiphase chemical reactions at/near the surface (Sebastiani et al., 2018; Pfrang et al., 2014), ice nucleation capability (Knopf and Forrester, 2011), optical properties (Donaldson and Vaida, 2006), the presence or suppression of liquid–liquid phase separation (Schmedding and Zuend, 2024), the transport of contaminants such as per- and poly-fluoroalkyl substances (PFAS) (Johansson et al., 2019),

and several other surface-influenced processes. For a thorough review of the importance of aerosol surface properties, we refer to Wokosin et al. (2022).

Because of the aforementioned importance of aerosol surface properties, various models have been developed that account for surface tension (σ) modifications as function of aerosol composition and coupled changes in bulk–surface partitioning in aerosol particles (Topping et al., 2007; Vepsäläinen et al., 2023; Kleinheins et al., 2023). Surface tension can be thought of physically as the work per unit surface area required to expand a 2-dimensional phase boundary. On a molecular, chemical level, surface tension can be interpreted as the additional energetic penalty that a molecule at a gas–liquid interface experiences when it is unable to interact with other closely spaced liquid-phase molecules around it in all directions (Berry, 1971).

Many of the models for predicting the effective surface tension of aerosol particles and cloud droplets rely on accurate representations of pure–component surface tension values (σ_i°) at temperatures of interest; hereafter, we use superscript $^\circ$ to denote a pure–component rather than mixture property. Models for the surface tension of multicomponent solutions, which rely on accurate values of pure–component surface tension (σ_i°), range in complexity. The semi-empirical Eberhard model for binary solutions relates the bulk mole fractions of species j and k (x_j and x_k) and their corresponding pure–component surface tensions (σ_j° and σ_k°) to the solution surface tension through a fitted parameter (s_{jk}) as follows (Eberhart, 1966):

$$\sigma = \frac{x_j\sigma_j^\circ + s_{jk}x_k\sigma_k^\circ}{x_j + s_{jk}x_k}. \tag{4.2}$$

A more complex model for binary solutions was derived by Connors and Wright (1989) and later by Shardt and Elliott (2017):

$$\sigma = \sigma_k^\circ - \left(1 - \frac{b(1-x_j)}{1-a(1-x_j)}\right) x_j(\sigma_j^\circ - \sigma_k^\circ), \tag{4.3}$$

where a and b are semi-empirical parameters. This approach was later shown to be applicable to multicomponent solutions by Shardt et al. (2021) and an extension of Eq. (4.2) by Kleinheins et al. (2024). The Sprow–Prausnitz–Butler equation is a thermodynamically rigorous treatment of solution surface tension that also relies on accurate σ_i° values (Sprow and Prausnitz, 1966):

$$\sigma = \sigma_i^\circ + RT \ln\left(\frac{a_i^\mathrm{s}}{a_i^\mathrm{b}}\right). \tag{4.4}$$

In Eq. (4.4), R is the ideal gas constant, T the absolute temperature, a_i^s the (chemical) activity of i in the surface phase, and a_i^b the activity of i in the bulk phase. Beyond predicting the value of σ for solutions, accurate values for σ_i° may also be necessary for predicting interfacial tensions between two liquids, α and β, should liquid–liquid phase separation (LLPS) occur in an aerosol particle. Approaches for interfacial tension estimation include Antonov's rule (Antonov, 1907):

$$\sigma^{\alpha\beta} = \left|\sigma^\alpha - \sigma^\beta\right| \tag{4.5}$$

and the Girifalco–Good equation (Girifalco and Good, 1957):

$$\sigma^{\alpha\beta} = \sigma^\alpha + \sigma^\beta - 2\phi\sqrt{\sigma^\alpha \sigma^\beta}, \tag{4.6}$$

where $\sigma^{\alpha\beta}$ is the interfacial tension between phases α and β, and ϕ is a fitted parameter that is often assumed to be 1.0. The values of σ^α and σ^β may be calculated using one of the above models for solution surface tension or other simplified mixing-rule-based models which depend on σ_i° (Schmedding and Zuend, 2024).

The importance of accurately describing σ_i° is evident. However, because of the high complexity and degree of functionality of many of the myriad of organic aerosol compounds, a rather limited set of measurements for σ_i° of organic species exists (Hyvärinen et al., 2006; Riipinen et al., 2007; Lee et al., 2017; Bzdek et al., 2016; Topping et al., 2007). As such, predictive models

or simplified assumptions about the surface tensions of organic compounds must be employed in many applications.

The simplest treatment of atmospherically relevant organic species is to assume that all have the same value (Davies et al., 2019; Ovadnevaite et al., 2017; Schmedding and Zuend, 2023). The unknown pure–component surface tension of species has also been estimated based on measured values of chemically similar species, or by extrapolating the measured behavior of highly concentrated binary aqueous solutions of organic species toward the pure–component limit (Schmedding and Zuend, 2023, 2024). Shardt and Elliott (2017) estimated σ_i° by fitting a simple linear equation with two parameters ($\theta_{0,i}$ and $\theta_{1,i}$) to include a temperature dependence:

$$\sigma_i^\circ = \theta_{0,i} + \theta_{1,i} T. \tag{4.7}$$

This approach requires detailed temperature-dependent data for σ_i° and was only used for 15 organic compounds in Shardt and Elliott (2017).

Another semi-empirical approach to predicting the surface tension of pure compounds is through the use of the Macleod–Sudgeon parachor, which is defined as follows (Macleod, 1923; Sugden, 1924):

$$\sigma_i^\circ = \left[\mathscr{P}_i(T) \cdot (\rho_i^{\mathrm{l}} - \rho_i^{\mathrm{v}})\right]^4. \tag{4.8}$$

The parachor, $\mathscr{P}_i$, is a semi-empirical term relating the difference between the liquid-state density (ρ_i^{l}) and the vapor-state density(ρ_i^{v}) to the pure–component surface tension at a given temperature (T). Owing to the simplicity of the parachor approach, it has been used extensively in fields outside of atmospheric science to predict the surface tension of organic compounds (Log et al., 2023; Firoozabadi et al., 1988; Escobedo and Mansoori, 1998). The parachor method can also be modified to predict the surface tension of solutions (Weinaug and Katz, 1943; Hugill and Van Welsenes, 1986); however, it has been noted that such modifications perform poorly for solutions

of water and organic compounds (Log et al., 2023). Indeed, the functional form of $\mathscr{P}_i$ is poorly constrained and various methods have been proposed to describe it as a weak function of temperature (Macleod, 1923; Sugden, 1924; Quayle, 1953). Escobedo and Mansoori (1996) related the value of $\mathscr{P}_i$ to a function of the reduced temperature (T_r), $T_r = \frac{T}{T_c}$, through the following equation:

$$\mathscr{P} = \mathscr{P}_\circ (1 - T_r)^{0.37} \cdot T_r \cdot \exp\left(0.30066/T_r + 0.86442\, T_r^9\right). \tag{4.9}$$

$\mathscr{P}_\circ$ was defined in the same work as follows:

$$\mathscr{P}_\circ = 39.643 \left(0.22217 - 2.91042 \times 10^{-3} \frac{\mathscr{R}^\star}{T_{b,r}^2}\right) T_c^{13/12}\, P_c^{5/6}. \tag{4.10}$$

$\mathscr{R}^\star$ is the ratio of the molar refractivity of compound i to the molar refractivity of i in methane. $T_{b,r}$ is the reduced boiling point of i, T_c is the critical temperature, and P_c is the critical pressure of i. Escobedo and Mansoori (1996) found that such equations were able to predict the pure–component surface tension of 94 different compounds to within 2.5% absolute average percent deviation. However, it should be noted that such an approach requires knowledge of numerous physicochemical properties of individual components in order to compute $\mathscr{P}_i$ and by extension σ_i°.

Other approaches to calculate σ_i° include Density Functional Theory (DFT) (Lu et al., 2002; Fu et al., 2001). DFT relates the surface tension of i to the difference of the Grand Potential (Ω) in the surface and in the bulk phase as follows:

$$\sigma_i^\circ = \frac{1}{A}\left(\Omega^{\mathrm{s}} - \Omega^{\mathrm{b}}\right). \tag{4.11}$$

A is the area of the surface in this case. In order to calculate Ω^{s} and Ω^{b}, the Helmholtz energy and the chemical potential of species i must be known (Tang and Gross, 2010). Using density functional theory to predict σ_i° has

several limitations. DFT calculations are computationally expensive and require numerous assumptions about the structure of the surface region. DFT calculations may provide information about the orientation and density of molecules in the surface region, however they are not typically used in applications in the field of aerosol science due to the aforementioned computational limitations.

Another method of predicting σ_i° at a given temperature is the Theory of Corresponding States (Guggenheim, 1945), which relates the reduced surface tension of a compound to the critical pressure and temperature of the compound:

$$\sigma_i^\circ(T) = \sigma_i^{\text{ref}} \left(1 - \frac{T}{T_c}\right)^{n_i}. \tag{4.12}$$

Here, σ_i^{ref} is a constant reference surface tension, n is an empirical (fit) coefficient, equal to $\frac{11}{9}$ in the ideal case but it may range between 1.16 and 1.5 in real systems (Guggenheim, 1945; Lielmezs and Herrick, 1986). T is the absolute temperature of the system in K and T_c is the critical temperature of i in K.

Numerous empirical parameterizations besides the aforementioned method of Escobedo and Mansoori (1996) have been developed based on the critical properties of compounds such as the approach of Brock and Bird (1955):

$$\sigma_i^\circ = P_c^{\frac{2}{3}} T_c^{\frac{1}{3}} Q (1 - T_r)^{\frac{11}{9}}. \tag{4.13}$$

Here, The factor Q can be defined as follows:

$$Q = 0.1196 \left[1 + \frac{T_{b,r} \ln(P_c/101325)}{1 - T_{b,r}}\right] - 0.279. \tag{4.14}$$

In Eq. (4.13) and Eq. (4.14), P_c has units of Pa, T_c, and T_b have units of K, such that σ_i° has units of $\mathrm{J\,m^{-2}}$. Other empirical approaches include additional input parameters, which must be known for predicting σ_i° (Aleem

et al., 2015):

$$\sigma_i^\circ = \varphi \frac{M_i^{1/3}}{6 N_A^{1/3}} \rho_l^{2/3} \left[H_{\text{vap},T_b} + C_{p,l} \cdot (T_b - T) \right]. \tag{4.15}$$

In Eq. (4.15), M_i is the molar mass ($\mathrm{kg\,mol^{-1}}$), N_A denotes Avogadro's number, ρ_l is the liquid-state density ($\mathrm{kg\,m^{-3}}$) at T and P. H_{vap,T_b} is the enthalpy of vaporization at T_b in units of $\mathrm{J\,kg^{-1}}$, $C_{p,l}$ is the liquid-state heat capacity at constant pressure at T in units of $\mathrm{J\,kg^{-1}\,K^{-1}}$ and φ can be defined as follows:

$$\varphi = 1 - 0.0047\, M_i + 6.8 \times 10^{-6}\, M_i^2 \tag{4.16}$$

such that σ_i°, as calculated by Eq. (4.15), has units of $\mathrm{J\,m^{-2}}$. Gharagheizi et al. (2013) proposed another empirical equation which relies on fewer input parameters:

$$\sigma_i^\circ = 8.948226 \times 10^{-4} \left[\frac{A^2}{M_i} \sqrt{\frac{A\,\omega}{M_i}} \right]^{\frac{1}{2}}, \tag{4.17}$$

with A defined as

$$A = T_c - T - \omega, \tag{4.18}$$

where ω denotes the acentric factor of component i. σ_i° carries units of $\mathrm{J\,m^{-2}}$.

We note that many of these empirical equations were not trained or evaluated on diverse classes of input data. For example, Eq. (4.15) was only fitted using alkanes of chain lengths from C_1 to C_{10} and C_{12} and, thus, its utility for functionalized organic compounds may be limited (Aleem et al., 2015). More recent attempts to model the surface tension of functionalized organic species have relied on statistical regression methods (Sanjuán et al., 2020; Randová and Bartovská, 2016) or artificial neural networks (ANN) (Soori et al., 2021; Rafie et al., 2023; Ojaki et al., 2023; Mousavi et al., 2021; Lazzús et al., 2017; Lashkarbolooki and Bayat, 2018; Pierantozzi et al., 2021; G. R. Pazuki and Sahranavard, 2011; Tiejun Xu and Khanghah, 2019).

Artificial neural networks loosely mimic the activity of a brain by con-

taining mathematical representations of neurons grouped into layers. Each artificial neuron contains an activation function that takes inputs and returns the value of said function similar to a biological neuron's action potential in the brain of an animal. Artificial neurons are then grouped into sequences of layers. The artificial neurons in each layer are connected to both the previous and subsequent layers of artificial neurons such that the outputs of the previous layer become the inputs of the current layer, with the final layer producing the output of interest. As the activation functions for each neuron in each layer may return different values, the input values are transformed by passing them through the multiple layers of neurons until an acceptable result is produced. In a regression problem where a single value is desired, in this case, surface tension, a final single neuron is used to generate the output. The number of inner layers and the number of neurons per layer in this type of artificial neural network must be found through a trial and error procedure to avoid underfitting or overfitting of the model. A brief summary of different statistical and machine learning (ML) modeling approaches for estimating the surface tension of organic compounds follows.

Sanjuán et al. (2020) used surface tension values for 87 different alcohols and compared models based on various combinations of temperature, triple point, normal boiling point, and critical temperatures; triple point and critical pressures, critical compressibility factor, critical volume, molar volume, molar mass, radius of gyration, and acentric factor. They found that models that depended on temperature, critical temperature, critical pressure, critical volume, molar volume, and acentric factor had the best correlations with the measurements in question (Sanjuán et al., 2020). Roosta et al. (2012) used an ANN with a single hidden layer and 20 nodes and was able to accurately predict the surface tensions of organic compounds across a broader temperature range than Escobedo and Mansoori (1996), with inputs based on a component's critical pressure, acentric factor, reduced normal and boiling temperature, and specific gravity at the compounds normal boiling

point temperature. Randová and Bartovská (2016) used a group contribution method and Eq. (4.12) to predict the surface tension of straight-chain and branched alkanes.

Lazzús et al. (2017) used 46 different functional groups, the molar mass of the compound, and the absolute temperature to predict the surface tension of different ionic liquid compounds using 1 hidden layer with 30 neurons followed by a gravitational search algorithm to predict σ_i°. Lashkarbolooki and Bayat (2018) specifically examined the surface tension of alkanes and alkenes using an ANN with 1 hidden layer with 27 neurons that took absolute temperature, critical temperature, and number of carbons as inputs. Mousavi et al. (2021) also examined a functional-group-based approach for determining the surface tension of ionic liquids using a combination of a firefly algorithm and the differential evolution method to optimize a radial-basis function model which takes chemical structure and temperature as inputs. Pierantozzi et al. (2021) used a single hidden layer with 41 neurons which took reduced temperature, boiling temperature, and acentric factor for organic acid species to predict their surface tension. Another common application of ANNs is in image recognition and related evaluation of graphical measurement data. For example, Soori et al. (2021) was able to use an ANN to predict the surface tension of binary solutions based on images taken during pendant drop experiments.

Other types of ML-based approaches have been used to predict molecular properties Yee and Wei (2012). A commonly used alternative to ANNs are tree-based models. These models have recently been confirmed to perform better for prediction problems when inputs are tabular as well as having fewer model hyperparameters to tune Uddin and Lu (2024). The simplest tree-based models are decision trees, which utilize a sequence of branching nodes to classify the inputs and predict a value. While individual decision trees are easy to interpret, they are prone to overfitting and may perform poorly for compounds outside of the training data base Chen et al. (2020).

Tree-based ensemble methods have also been developed as a way to create more powerful models. Two such ensemble models are random forests and gradient-boosted trees. Both techniques utilize multiple decision trees in their model architecture to generate more robust predictions. Random forests generate many decision trees, each of which is trained from a small subset of the overall dataset, and takes the average of the predictions as a final result. In comparison, gradient-boosted trees create many decision trees in sequence, where each sequential tree is trained on the residuals of the previous tree's predictions. One of the more popular variants of gradient boosted trees is extreme gradient boosted descent (XGB). XGB has been widely used and generally has been found to perform well for predicting molecular properties Boldini et al. (2023). An additional feature that is unique to an XGB model is that it allows for explicit monotonic constraints on the relationship between input values and model predictions. Such a parameterization allows for XGB models to more easily represent physical behavior in a realistic manner, such as the inverse relationship between T and σ_i° wherein an increase in T leads to a decrease in σ_i°.

While a combination of various ML techniques and functional group-based approaches may have a high degree of flexibility for many quantitative structure–property relationship (QSPR) approaches, such approaches may not be able to adequately represent numerous compounds to a high degree of accuracy. For example, cis–trans isomerism may lead to substantial differences in pure–component surface tension (Cicciarelli et al., 2007). Thus, more thorough methods are desirable to characterize individual molecules from their Simplified Molecular Input Line Entry System (SMILES) notation, which is a method of representing molecules as a single string of characters. One such technique is known as molecular fingerprinting; it involves translating a molecular structure into a series of integer codes that represent the molecule's structure. Two of the more common methods of molecular fingerprinting are Molecular ACCess System (MACCS) keys and so-called

Morgan fingerprints, both of which are widely used in the field of cheminformatics to predict QSPR for different molecular properties (Consonni et al., 2023).

MACCS keys are a set of 166 pre-defined patterns that can be present in a molecule (Durant et al., 2002). Each of these patterns is associated with a corresponding SMARTS (SMiles ARbitrary Target Specification) code. SMARTS allow for the parsing of a given SMILES string to count the matching patterns. Such a defined list of MACCS keys allows for shorter descriptions of molecular features and thus lower computational cost when used as inputs in QSPR models. Because SMARTS are designed to operate on the SMILES, MACCS keys are interpretable by human readers since all that is necessary is a reference table with MACCS key number and the corresponding SMARTS code and molecular pattern. There are some disadvantages to utilizing MACCS keys. For example, due to the limited number of patterns which MACCS keys describe, they may not be able to accurately represent more complex and nuanced patterns in a large, multifunctional molecule. One example of this limitation is MACCS key 44, which is simply labelled as 'other' and describes any feature not captured by the remaining 165 keys.

In comparison, Morgan fingerprints can encode much more information about an individual molecule's structure, albeit in a more abstract way. Morgan fingerprints are in the family of extended-connectivity fingerprints, which numerically encode each atom in a molecule and the local structure around said atom within a given radius of adjacent atoms, typically two (Morgan, 1965). Recently, Orsi and Reymond (2024) developed a novel fingerprinting technique that modifies hashed Morgan fingerprints to include data on the chirality of each atom in a molecule, thus increasing the level of structural detail.

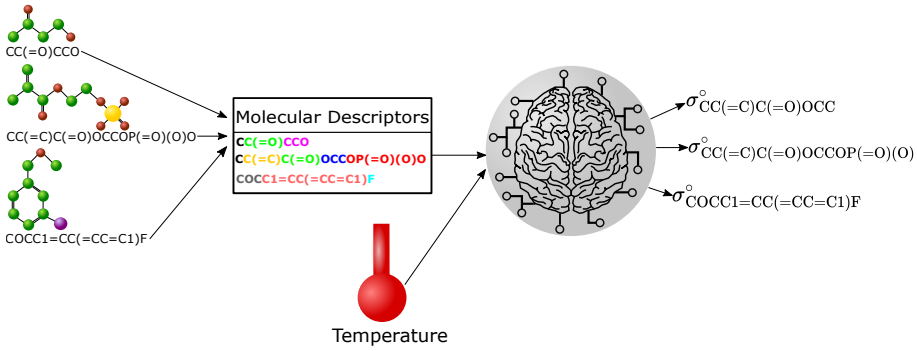

Figure 4.1: A conceptual representation of the model inputs and outputs.

4.3 Methods

4.3.1 Data Collection and Processing

Surface tension data were collected for 1805 unique organic species reported by Jasper (1972). In the aforementioned work, two T-dependent parameters were fit to measured σ_i° values to predict σ_i° within 0.2–0.3 mJ m^{-2} and used to generate additional σ_i° values as a function of T. With the addition of T as a parameter, there were 12446 σ_i° and T data pairs reported by Jasper (1972), which were suitable for use in this work. Stereo-isomers were also counted as two distinct compounds, where measurements were available and sufficiently specific. Compounds with only one σ_i° and T data pair were also included to increase the size of the training data. However, the number of compounds with a surface tension measurements at a single T was low; of the 12446 σ_i° values, only 164 were limited to surface tension data at a single T. Compounds included in the dataset contained the following elements: carbon (1805 distinct compounds), hydrogen (1763 distinct compounds), oxygen (1143 distinct compounds), nitrogen (341 distinct compounds), sulfur (130 distinct compounds), phosphorus (73 distinct compounds), fluorine (78 distinct compounds), chlorine (148 distinct compounds), bromine (58 distinct compounds), and iodine (30 distinct compounds).

Figure 4.2 shows a two-dimensional kernel density estimate of both σ_i° and temperature for all compounds in the training and test databases. Figure C.1 shows the kernel density estimate for groups of compounds with more than three unique SMILES that contain only one type of non-hydrocarbon functional group; for example, compounds only containing carboxyl or amide groups. Figure **??** corresponds to Fig. C.1 but for compounds with multiple non-hydrocarbon functional groups. For example, all compounds that contain a hydroxyl group and any other non-hydrocarbon functional group. Reported T values in the complete set of data ranged from 113 to 523 K and σ_i° ranged from 8.4 to 68.8 $\mathrm{mJ\,m^{-2}}$. For temperatures between 218 K and 318 K, which corresponds to a typical range in the troposphere, there are 5557 σ_i° values, which corresponds to 44.7% of the total dataset. The majority of the remaining data correspond to temperatures above 318 K. From the dataset described in the preceding paragraphs, isomeric SMILES were generated using OEChem v2.3.0 through PubChem release v2021.05.07 (OpenEye Scientific Software, 2024).A link to the complete database of compounds and their SMILES, and σ_i°–T pairs can be found in the Code and Data Availability section at the end of this chapter.

4.3.2 Model Architecture

It is important to note that the overall architecture of a machine-learning model, rather than the individual weights of a model, is itself tunable and impacts model performance. Tunable model features that may constrain model weights and overall performance are known as hyperparameters and also include algorithmic features such as learning rate and batch size. In order to predict temperature-dependent σ_i° values, various models and their hyperparameters were optimized and tested. It is likewise useful to determine which categories of models produce the same or similar results if their hyperparameters and weights are optimized. Thus, an extreme gradient boosted descent (XGB), a decision tree (DT), random forest (RF), and K-nearest neighbors (KNN) regression models were also tested. Prior to training the models, 10%

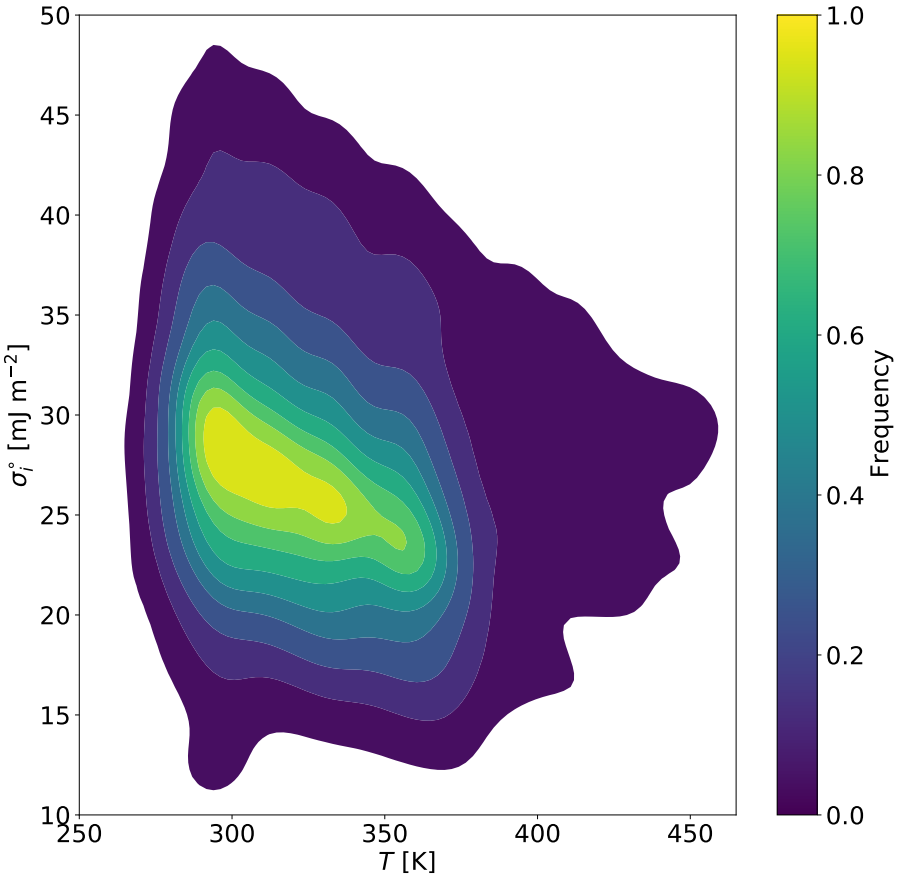

Figure 4.2: A two-dimensional kernel density estimate of σ_i° of all 1805 unique compounds and the corresponding temperatures for which σ_i° values were reported. The median and mean σ_i° values are 26.2 mJ m^{-2} and 27.3 mJ m^{-2}, respectively. The median and mean temperatures are 323 K and 329 K, respectively.

of the σ_i° and T data pairs were randomly selected and set aside for testing following model selection, hyperparameter tuning, and model training. For consistency, the selected test data were kept the same for all of the model types and architectures tested in this work.

A major concern that is often encountered when training ML models is that of an overfitted model, i.e., one that it is only capable of reproducing the training data reliably. In the event that a model is overfit, it may perform poorly when novel inputs (here molecular structures of unseen compounds) are introduced. One method to reduce the likelihood of overfitting a model is through the use of k-fold cross-validation in the training stage. k-fold cross-validation is the process of splitting up a training dataset into k slices, typically five or ten slices (Nti et al., 2021), and then training the model on $k-1$ slices and validating the model performance on the remaining slice. A model performance value is calculated for each slice used as validation data, i.e. all permutations for a slice being the "remaining slice" are run; the mean performance value is used to assess the overall model performance. Typical performance metrics include the root mean square error (RMSE):

$$\text{RMSE} = \sqrt{\frac{1}{n}\sum_{i=1}^{n}(y_i - \hat{y}_i)^2}, \tag{4.19}$$

the mean square error (MSE):

$$\text{MSE} = \frac{1}{n}\sum_{i=1}^{n}(y_i - \hat{y}_i)^2, \tag{4.20}$$

the mean absolute error (MAE):

$$\text{MAE} = \frac{1}{n}\sum_{i=1}^{n}|y_i - \hat{y}_i|, \tag{4.21}$$

the mean absolute percentage error (MAPE):

$$\text{MAPE} = \frac{100\%}{n} \sum_{i=1}^{n} \left| \frac{y_i - \hat{y}_i}{y_i} \right|. \tag{4.22}$$

In Eqs. (4.19), (4.20), (4.21), and (4.22), n is the number of points in the sample, y_i is the original (known) value, and $\hat{y}_i$ is the predicted value from the model. Another model performance metric is the coefficient of determination, R^2:

$$R^2 = 1 - \frac{\sum_{i=1}^{n}(y_i - \hat{y}_i)^2}{\sum_{i=1}^{n}(y_i - \bar{y})^2}. \tag{4.23}$$

In this work, MSE was selected as the primary model performance metric as it is more sensitive to predictions with large errors and thus may lead to a model that performs well for many different inputs.

An additional challenge in ML-based approaches for predicting molecular properties is determining the optimal model parameters for a given model type in order to maximize the model's performance. Past methods for selecting the best combination of model parameters involved grid searches or random searches of parameter combinations. While robust, such approaches can prove computationally expensive to thoroughly explore all possible parameter combinations. Bayesian optimization algorithms have been found to perform quite well in a fraction of the time that traditional grid or random searches require (Victoria and Maragatham, 2021). The hyperparameters for all models in this work were optimized using the Optuna v3.6.1 (Akiba et al., 2019) Bayesian optimization algorithm. All hyperparameter tuning, model training, cross-validation, testing, and plotting were performed using the CryoCloud JupyterBook (Snow et al., 2023).

Because both MACCS keys and Morgan fingerprints can provide useful information about a molecule, a set of the above models was trained using either MACCS keys or Morgan fingerprints along with temperature as inputs. MACCS Keys and Morgan fingerprints were both generated from a com-

ponent's SMILES using RDKit v2024.3.5 (Landrum et al., 2024) in Python v3.11.9. XGB models were developed using the XGBoost v2.1.0 (Chen and Guestrin, 2016) and the RF, DT, and KNN models were generated using SciKit-learn v1.5.1 (Pedregosa et al., 2011).

For situations wherein complete molecular structure information may not be available, a simplified XGB model was also developed which took the following molecular properties as inputs: temperature (T), molar mass (M_i), and the following atomic ratios: O:C, H:C, N:C, S:C, P:C, Cl:C, F:C, I:C, and Br:C. These inputs were selected based on their likely availability from field observations, such as from aerosol mass spectrometer measurements, as well as values that could be easily calculated for surrogate compounds used to represent the various organic aerosol components in chemical transport models.

4.3.3 Model Testing

Given the three models introduced in this work, a comparison to past methods of predicting σ_i° was carried out by utilizing the critical properties found in Yaws (2009) along with Eq. (4.13) and Eq. (4.17) to predict σ_i° for shared compounds between those reported by Yaws (2009) and those reported by Jasper (1972). Eq. (4.13) and Eq. (4.17) were specifically selected because they relied on the fewest inputs among the empirical relationships discussed in the introduction. Matched compounds were specifically selected out of the test dataset that had been previously set aside from the training data to avoid any possible artifacts from model training.

In order to determine if there were additional features that may influence surface tension that were not accounted for by any of the models, the 100 poorest performing σ_i° values were extracted from the best performing model for each of the three types of model inputs. In the case of the simplified inputs, a Student's t-test was performed for each of the model inputs, including temperature, to determine whether there may have been a significant difference between these compounds and the remainder of the test dataset. For

both the MACCS keys and the Morgan fingerprints, a Student's t-test was once again performed for temperature in comparison to the remainder of the test data. However, to better understand any structural artifacts that may not have been captured by the model, Tanimoto similarity values were calculated for all combinations of compounds. Tanimoto similarity ($S_{j,k}$) is a measure of the structural similarity between two compounds,

$$S_{j,k} = \frac{j \cap k}{j \cup k}, \tag{4.24}$$

where j and k are the sets of fingerprints or descriptors that represent molecule j and molecule k, respectively (Michael A Fligner and Blower, 2002). In the case of two identical molecules, the Tanimoto similarity score is equal to 1 and in the case of two molecules that do not share any overlapping features, the Tanimoto score is 0. Following the calculation of Tanimoto scores for all possible pairs of compounds, a similarity matrix can be constructed, which can then be used to construct hierarchical clusters of the poorest-performing compounds.

4.3.4 Model Applications

As mentioned in the introduction, σ_i° is an important parameter for determining the effective solution surface tension for a variety of environmentally relevant systems. One such application is by utilizing the Butler–Sprow–Prausnitz equation (Eq. 4.4) to compute the equilibrium surface compositions and tensions of aerosol particles and cloud droplets, following the approach of Schmedding and Zuend (2023). Such an approach relies on calculating the activity coefficients of each species in a droplet using the Aerosol Inorganic–Organic mixtures Functional groups Activity Coefficients (AIOMFAC) model (Zuend et al., 2008, 2011). Because many aerosols are chemically complex mixtures of secondary compounds formed from the emissions of biogenic precursors, two different systems were tested. The first system is comprised of 21 isoprene-derived organic compounds generated by the Master Chemical

Mechanism (MCM) (Jenkin et al., 2015; Rastak et al., 2017) along with ammonium sulfate (to represent inorganic electrolytes). The second system consisted of 14 α-pinene oxidation products along with ammonium sulfate (Rastak et al., 2017; Jenkin et al., 2012). For a complete list of the oxidation/fragmentation products predicted by the MCM and their SMILES, see Tables 4.2 and 4.3. Both systems were run assuming a water-free (dry) particle diameter of 50 nm. The pure–component surface tension of water at 298 K was set to 71.98 mJ m^{-2} for all systems (Jasper, 1972) and the pure–component surface tension of ammonium sulfate was set to 184.5 mJ m^{-2} following the approach of Dutcher et al. (2010) for inorganic electrolyte systems. Once the effective droplet surface tension is calculated as a function of droplet composition, a Köhler curve can be calculated using Eq. (4.1). The global maximum of S in Eq. (4.1) represents the critical saturation ratio that must be reached or exceeded in the air surrounding that specific aerosol particle for the particle to activate and grow into a much larger cloud droplet.

4.4 Results

Table 4.1 lists the values of the MSE, RMSE, MAE, MAPE, and R^2 generated from the test dataset. This dataset contains 1245 σ_i°–T pairs or 10% of the overall number of σ_i°–T pairs used in this work. Each model (XGB, RF, DT, and KNN) used the three input categories: Simplified inputs (Simp), MACCS keys (MACCS), and Morgan fingerprints (MF). The MACCS-XGB and the MF-XGB models had the largest R^2 values of similar magnitude; hence, they are considered the best predictive models for our application. Overall, the MF-XGB performed slightly better than the MACCS-XGB for predicting σ_i° when considering all compounds. However, we note that the models with MACCS keys inputs use substantially fewer independent (input) variables than the models with Morgan fingerprint inputs, yet they perform slightly better for three model types, and similarly in the case of XGB, as the Morgan fingerprint approach.

Table 4.1: Performance metrics generated form the 1245 test dataset pairs for different input types (SMILES-generated MACCS keys, SMILES-generated Morgan fingerprints, and simplified elemental ratios) and model types tested in this work.

Input type	Model type	MSE	RMSE	MAE	MAPE	R^2
Simplified	Extreme Gradient Boosting (XGB)	3.883	1.970	1.329	5.1%	0.905
	K-Nearest Neighbors (KNN)	21.978	4.68	3.031	10.9%	0.463
	Random Forest (RF)	5.537	2.353	1.640	6.2%	0.865
	Decision Tree (DT)	7.342	2.709	1.883	7.0%	0.821
MACCS key	Extreme Gradient Boosting (XGB)	1.156	1.076	0.660	2.7%	0.972
	K-Nearest Neighbors (KNN)	10.226	3.198	2.028	7.6%	0.750
	Random Forest (RF)	1.872	1.368	0.916	3.7%	0.954
	Decision Tree (DT)	2.725	1.651	2.203	4.7%	0.933
Morgan fingerprint	Extreme Gradient Boosting (XGB)	1.012	1.006	0.633	2.5%	0.975
	K-Nearest Neighbors (KNN)	11.472	3.387	2.195	8.2%	0.720
	Random Forest (RF)	3.126	1.768	1.252	5.0%	0.924
	Decision Tree (DT)	4.080	2.020	1.460	5.6%	0.900

Figure 4.3 shows the predicted σ_i° values from the Simp-XGB, MACCS-XGB, and MF-XGB modelsdescribed in Table 4.1 compared to reported σ_i° values from the test dataset selected from (Jasper, 1972). Also shown in Fig 4.3 are the predictions from the empirical approaches of Gharagheizi et al. (2013) (Eq. 4.17 and Eq. 4.18) and Brock and Bird (1955) (Eq. 4.13 and Eq. 4.14) with critical parameters taken from Yaws (2009). We note that only compounds from the test data with critical parameters included in Yaws (2009) are plotted, reducing the number of points shown to 429 from the test data. a Figure 4.3A shows the Simp-XGB model, Figure 4.3B MACCS-XGB model, and Figure 4.3C shows the MF-XGB approach. In the case of the Simp-XGB, performance was (expectedly) worse than for both the MACCS-XGB and the MF-XGB models, although the model still performed reasonably well with $R^2 = 0.905$,MSE $= 3.883$, and RMSE $= 1.970$ mJ m^{-2}. Both the MACCS-XGB and MF-XGB models generally perform better for compounds with higher σ_i° values than those with lower σ_i°.

The previously described empirical approaches both performed poorly in comparison to all three ML-based approaches shown in Fig. 4.3. The approach of Brock and Bird (1955) (Eq. 4.13 and Eq. 4.14) generally overpredicted σ_i° at higher reported σ_i° values and the approach of Gharagheizi et al. (2013) (Eq. 4.17 and Eq. 4.18) generally underpredicted σ_i° in comparison to the reference values from Jasper (1972),

For comparison to the more complex models, the importance of the various simplified inputs used with the Simp-XGB model are shown in Fig. 4.4A. Here, importance is quantified in terms of the explained variance of the surface tension prediction. In the model with simplified inputs, T was responsible for 15.4% of the explained variance. Of the simplified inputs representing molecular properties, the molar mass, O:C ratio, H:C ratio, and N:C ratio were the most important and explained collectively 56.5% of the model's variance. Because of the ease of interpreting MACCS keys, the top ten MACCS keys that explained the most variance in the MACCS-XGB model were ex-

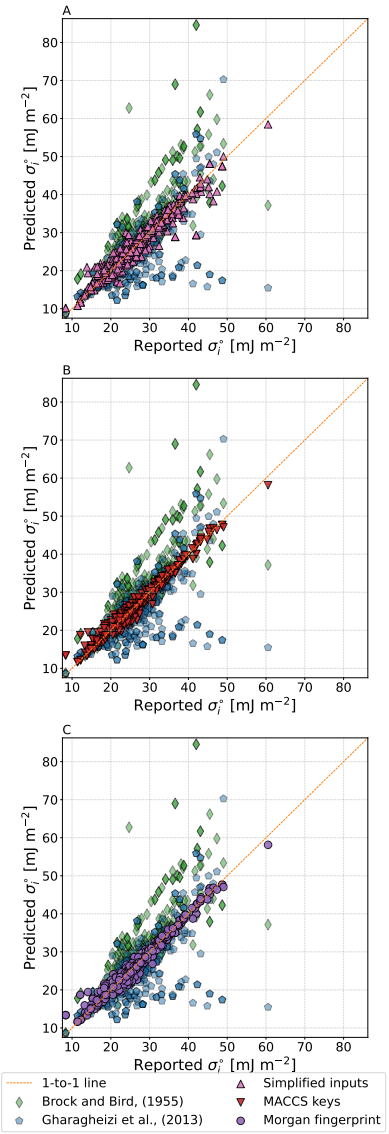

Figure 4.3: The accuracy of the best-performing model (XGB) in comparison to a subset of the test data for each of the input types: (A) simplified inputs, (B) MACCS keys, and (C) Morgan fingerprints. Also shown are estimations by the empirical methods of Brock and Bird (1955) (Eq. 4.13) and Gharagheizi et al. (2013) (Eq. 4.17) for compounds coverd by both the test dataset and the critical properties data available from Yaws (2009).

tracted and are displayed in Fig. 4.4B. The temperature for which the model is run explains the most substantial portion of the variance at 22.7% and the ten most important MACCS keys explain 71.4% of the MACCS-XGB model variance with those inputs. The following ten features were MACCS keys corresponding to the following patterns. The most important individual MACCS key is NAO, which represents a substructure where nitrogen is indirectly connected to an oxygen atom via any intermediate atom. pattern. ACH2O represents a methylene group connected to any atom on one side and to an oxygen atom on the other side. These atoms may be connected by any type of bond. ACH2AACH2A represents a more complex pattern which can be any two atoms between two methylene groups, which themselves are between any other two atoms. In the event that the outer two atoms are the same, this key represents a ring structure containing two methylene groups and two other atoms between them. This key can also represent the same sequence, but if one of the methylene groups is outside of the ring, the substructure becomes one where a methylene group is connected to any atom and then forms a ring structure with another methylene group and two other ring atoms. CH3AACH2A represents a methyl group connected to any two atoms, followed by a methylene group connected to another atom of any type. The bonds between these atoms may be of any type as well. This key can also represent a ring system where a methyl group is connected to a sequence of atoms that includes a methylene group that is part of the same ring. CH3ACH2A represents a methyl group connected by any bond to any atom that is also connected by any bond to a methylene group. This methylene group is further connected by any bond to another atom. N encodes the presence of nitrogen atoms. A!N$A is a pattern that represents a nitrogen atom that is part of a ring but is also connected to another atom outside the ring. A!A$A!A represents a sequence of any four atoms wherein the first and fourth atoms are not a part of a ring system and the second and third atoms are a part of a ring system. N=A is a structure where nitrogen is connected

to any other atom by a double bond. QQ 1 is a structure where any two atoms which are neither carbon nor hydrogen are connected by any type of bond. Cumulatively, these ten MACCS codes along with T explain 94.1% of the variance in the model.

Figure 4.4C shows the SMILES for top ten Morgan fingerprints, the most numerous and complex types of inputs used with the MF-XGB model. For this model, somewhat surprisingly T was responsible for only 0.2% of the explained variance. Oxygen stands out as the most significant non-carbon element, with SMILES containing at least one oxygen atom accounting for 29.7% of the explained variance. Halogen groups come next, contributing 16.1% to the variance. Among them, fluorinated substructures are the most impactful, explaining 9.8% of the variance, followed by iodine (3.1%), chlorine (1.8%), and bromine, which has the smallest impact among the halogens at 1.6%. Nitrogen and sulfur atoms contribute 8.7% and 5.7% of the variance, respectively. Phosphorus-containing substructures play a minimal role, responsible for just 1.2% of the explained variance. For the less abundant elements like bromine and phosphorus, their impact is likely small due to being present in only a small subset of compounds considered.

To further understand the role of temperature in each of the models, σ_i° predictios were generated for humic acid and fulvic acid as a function of temperature. Both humic and fulvic acid are commonly found in aerosols from biogenic sources, including biomass-burning particles, and can therefore experience a broad range of temperatures from very high values near combustion events to much lower temperatures when they are lofted to higher altitudes in the atmosphere. Therefore, the surface tension of these compounds was studied from 200 K to 350 K to include atmospherically relevant temperatures that any aerosol species may experience as well as temperatures that biomass-burning species may experience in a smoke plume. Temperature-dependent surface tensions for humic acid are shown in Fig 4.5A and for fulvic acid are shown in Fig. 4.5B. It is important to note that the Simp-

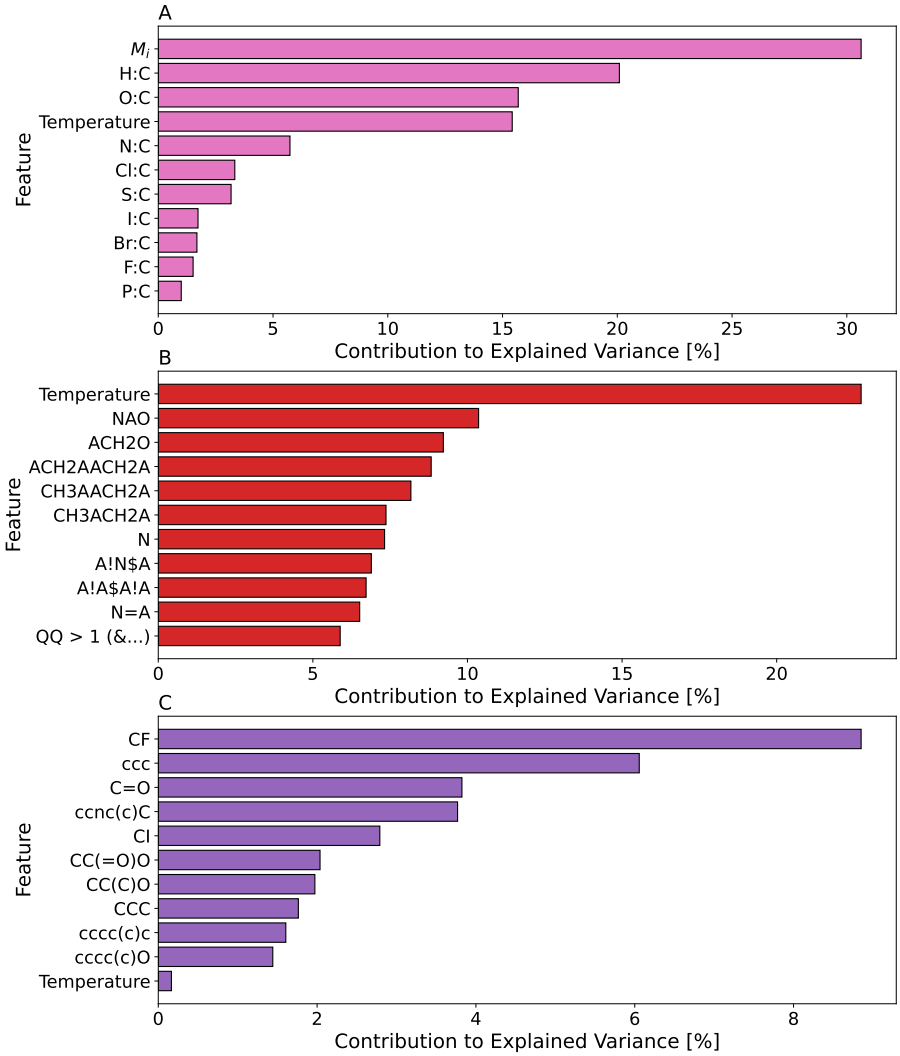

Figure 4.4: Percentage of variance in the XGB models explained by temperature and (A) simplified molecular properties, (B) the ten most important MACCS keys and (C) the SMILES for the substructures corresponding to the ten most important Morgan fingerprint bit vectors. In panel (B), the symbol 'A' represents any element, '!' represents a non-ring bond, '$' represents any bond in a ring system, '=' represents a double bond, and 'Q' represents any element that is neither carbon nor hydrogen.

XGB, MACCS-XGB, and MF-XGB models were constrained during model training in such a way that σ_i° decreased monotonically with respect to T, but not forcing a particular constant slope. σ_i° exhibited an approximately linear dependence on temperature across this range (consistent with typical expectations, e.g., Eq. 4.7). σ_i° decreased by approximately 18 $\mathrm{mJ\,m^{-2}}$ over the shown temperature range (200 K tp 350 K) in the case of the MF-XGB model for both compounds (i.e., a slope of $\sim -0.12\ \mathrm{mJ\,m^{-2}\,K^{-1}}$). For the MACCS-XGB model and the Simp-XGB model, σ_i° decreased by slightly more than 15 $\mathrm{mJ\,m^{-2}}$ for both compounds over the shown temperature range (200 K tp 350 K). In the case of humic acid, all three models predict slightly distinct σ_i° values for the same compound with the MF-XGB yielding the highest value followed by the MACCS-XGB model and then the simplified model. For fulvic acid, the MACCS-XGBmodel and the Simp-XGB predict similar values while the MF-XGB has lower predicted values for σ_i°. Also shown in Fig. 4.5A are measured surface tensions of aqueous humic acid solutions at 295 K Aumann et al. (2010); Klavins and Purmalis (2010). In Fig. 4.5 A, all three models have lower predicted surface tensions than the solution, with MF-XGB most closely replicating the experimental values. Figure 4.5B also shows measured surface tensions of aqueous fulvic acid at 298 K (Aumann et al., 2010). For this case, the MACCS-XGB slightly over predicts $\sigma_{\mathrm{fulvicacid}^\circ}$, with Simp-XGB best replicating the measurements and MF-XGB substantially under predicting $\sigma_{\mathrm{fulvicacid}^\circ}$ by nearly 10 $\mathrm{mJm^{-2}}$. Note that none of the plotted measurements represent pure humic or fulvic acid, respectively; the experimental data were taken from the highest concentrations reported in their respective works. For the aqueous humic acid solution, this concentration was 10.7 $\mathrm{g\,l^{-1}}$ (Aumann et al., 2010) and 1 $\mathrm{g\,l^{-1}}$ (Klavins and Purmalis, 2010). For the aqueous fulvic acid solution, the concentration was 10.7 $\mathrm{g\,l^{-1}}$ as well (Klavins and Purmalis, 2010). Therefore, these values ought to be thought of as upper bounds for $\sigma_{\mathrm{humicacid}^\circ}$ and $\sigma_{\mathrm{fulvicacid}^\circ}$.

The 100 σ°–T data point pairs with the highest error for each of the

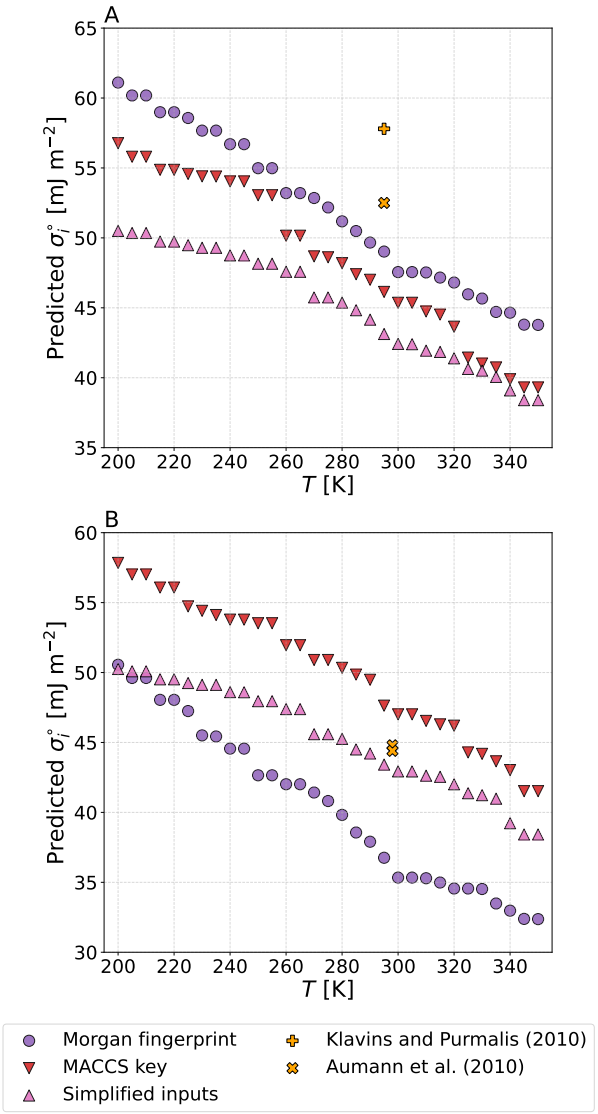

Figure 4.5: Temperature dependence of σ_i° for two biomass burning tracer species not found in the test data: (A) a representative humic acid structure (C1C2C=CC1C(C2C(=O)O)(C(=O)O)[N+](=O)[O-]) and (B) a representative fulvic acid structure (CC1(CC2=C(CO1)C(=O)C3=C(O2)C=C(C(=C3C(=O)O)O)O)O). The temperature range reflects temperatures that may occur within a smoke plume and the troposphere. We note that the reported measurement values were taken from aqueous solutions at the highest concentration of humic or fulvic acid, respectively (Klavins and Purmalis, 2010; Aumann et al., 2010).

Simp-XGB, MACCS-XGB, and MF-XGB models were extracted from the test dataset to determine if there were additional shared features that may have contributed to their poor performance. Figure S3A shows the residuals of these compounds compared to reported σ_i°. We find that all three categories of inputs tend to overpredict σ_i° when the reported σ_i° value is lower than 20 $\mathrm{mJ\,m^{-2}}$. Likewise the models tend to underpredict σ_i° when the reported value is between 20 and 50 $\mathrm{mJ\,m^{-2}}$. Figure S3B shows model error as a function of T, in this case, there does not appear to be a systematic bias in the error of the poorest performing cases. Of these paired data, the mean temperatures were 332.9 K for the Simp-XGB model, 338.0 K for the MACCS-XGB model, and 330.3 K for the MF-XGB model. In the case of the simplified inputs, there was a statistically significant ($p < 0.05$) decrease in the mean molar mass of the poorest performing predictions in comparison to the remainder of the test data. Likewise, there was also a statistically significant decrease in the mean Br:C, I:C, and P:C ratios from the rest of the test data. No other elemental ratio exhibited a significant difference. The average T was slightly higher in the poorest performing data, however, it is important to note that the statistical p-value for this was only weakly significant (0.05958). For a complete list of Student's t-test results for the inputs to the simplified model, please see Table S1. There were no significant differences between the mean T of the poorest performing data and the remainder of the test data in the MACCS-XGB and MF-XGB models.

For the more complex model inputs (MACCS keys and Morgan Fingerprints), similarities between poorly performing compounds were analyzed. Similarity scores between individual pairs of SMILES within the 100 poorest performing compounds were calculated using Eq. (4.24). The distance, or dissimilarity, between two compounds can be computed as $1 - S_{A,B}$. Compounds were then grouped hierarchically based on their distances from one another. Figures S4 and S5 show these hierarchical clusters for the MACCS-XGB model and MF-XGB model. It can be seen that most compounds are

more dissimilar than similar with only a small fraction of the compounds plotted clustered with distances below 0.5, marked by colored branches in those figures. It is also important to note that there are minimal differences between the clustering outputs.

As an example of the utility of the model developed in this work, the effect of using ML-generated surface tension values of organics in a mixture, instead of assuming a single, constant value for all organics, is now explored. A system of 21 surrogates comprised of isoprene-derived multi-generation oxidation and/or fragmentation products was generated based on predictions by the Master Chemical Mechanism (Jenkin et al., 2015; Rastak et al., 2017) and used as input with the models described in this work. The predicted pure–component surface tensions were used as inputs along with the AIOMFAC-based bulk–surface partitioning model of Schmedding and Zuend (2023) to predict the critical supersaturation for mixed organic–inorganic aerosol particles with a water-free (dry) diameter of 50 nm. The particles also contain ammonium sulfate, with the organic dry mass fraction of 0.73. The σ_i° of ammonium sulfate was predicted using the approach of (Dutcher et al., 2010). Figure 4.6A shows the Köhler curves using model-predicted σ_i° values for the isoprene-derived system. Figure 4.6B shows the Köhler curves using model-predicted σ_i° values for an analogous system comprising α-pinene ozonolysis products and ammonium sulfate with a water-free (dry) diameter of 50 nm and the organic dry mass fraction set to 0.8. Figures 4.6A and 4.6B also show case where it is assumed that all organic species have the same surface tension as water and the case where all organic species have a surface tension of 35 mJ m^{-2} (Davies et al., 2019; Ovadnevaite et al., 2017). All inorganic electrolytes use the values reported by Dutcher et al. (2010) in all systems. In the isoprene system, there is more variability between the predicted solution surface tensions shown in Figure 4.6C and, thus, more variation in the estimated critical supersaturations. In the case of the α-pinene system, there is less variability between the predicted solution

surface tensions shown in Figure 4.6D and all three models lead to similar predictions of the critical supersaturation for cloud droplet activation. It is important to note that the equilibrium bulk–surface partitioning framework laid out in Schmedding and Zuend (2023) allows the predicted σ to vary in a range exceeding the highest and lowest σ_i° values, which may occur when the surface exhibits highly non-ideal mixing, e.g. under dilute conditions. This is shown in Fig. 4.6D wherein $\sigma > \sigma_{\mathrm{w}}^\circ$ near the point of cloud droplet activation. Furthermore, interactions between liquid–liquid phase separation, the three dimensional configuration of a particle, such as whether it is of core–shell or partially engulfed morphology, and the selected treatment of interfacial tension may reduce this behavior in the bulk–surface partitioning framework (Schmedding and Zuend, 2023, 2024)

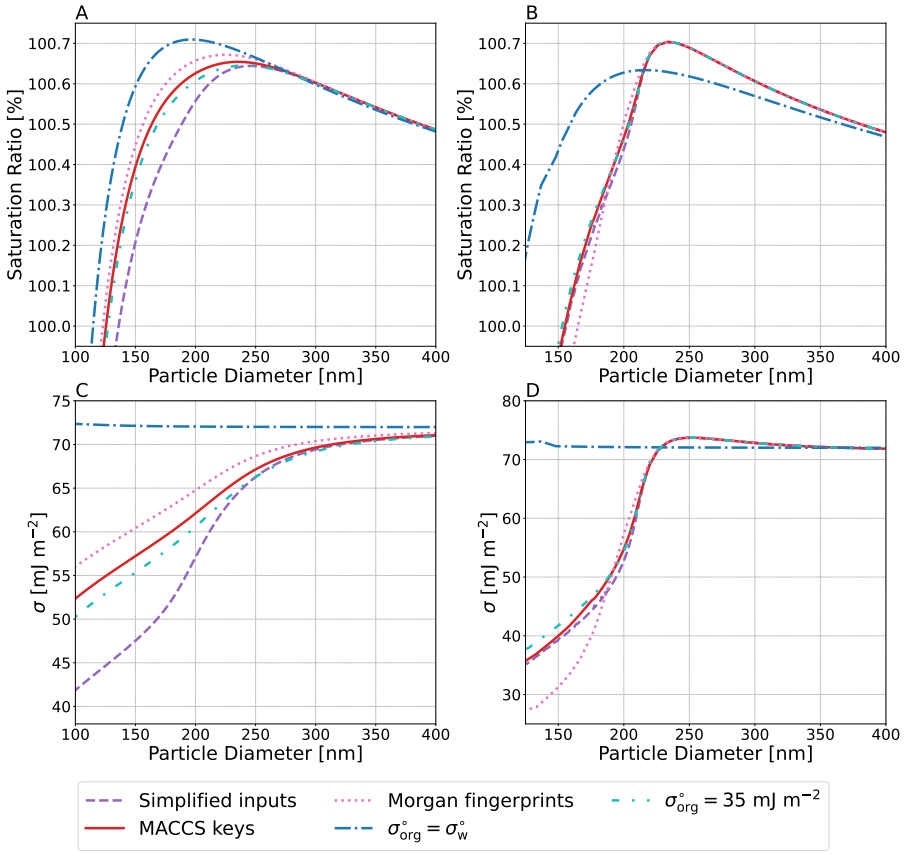

Figure 4.6: Predicted Köhler curves for (A) the isoprene oxidation products system and (B) the α-pinene oxidation products system at 298 K for particles with a dry diameter of 50 nm. The dry mass fraction of organic species is (A) 0.73 and (B) 0.8, with ammonium sulfate as the remainder. Also shown are Köhler curves generated with the assumption that all organic species have the same pure–component surface tension as water ($\sigma^{\circ}_{\mathrm{org}} = \sigma^{\circ}_{\mathrm{w}}$) or the assumption used in other studies that $\sigma^{\circ}_{\mathrm{org}} = 35\ \mathrm{mJ\,m^{-2}}$(Davies et al., 2019; Ovadnevaite et al., 2017). Panels (C) and (D) show the solution surface tension corresponding to panels (A) and (B) as a function of particle size.

Table 4.2: Predicted organic surface tensions for the Isoprene SOA surrogate system as shown in Fig 4.6A at $T = 298$ K. Isoprene SOA species and SMILES were taken from the Master Chemical Mechanism (MCM) (Jenkin et al., 2015; Rastak et al., 2017).

MCM Name	SMILES	Morgan fingerprint σ_i° [mJ m^{-2}]	MACCS keys σ_i° [mJ m^{-2}]	Simplified inputs σ_i° [mJ m^{-2}]
IEB1OOH	OCC(O)C(C)(OO)C=O	22.90	39.92	44.69
IEB2OOH	OOC(C=O)C(C)(O)CO	25.24	38.33	44.69
C59OOH	OCC(=O)C(C)(CO)OO	45.07	36.68	44.69
IEC1OOH	OCC(=O)C(C)(CO)OO	45.07	36.68	44.69
C58OOH	O=CC(O)C(C)(CO)OO	36.78	33.90	44.69
IEPOXA	CC(O)(CO)C1CO1	28.22	36.40	35.22
C57OOH	OCC(O)C(C)(OO)C=O	22.90	39.92	44.69
IEPOXC	CC1(CO1)C(O)CO	35.52	36.40	35.22
HIEB1OOH	OCC(O)C(CO)(OO)C=O	37.78	45.31	44.71
INDOOH	OCC(ON(=O)=O)C(C)(CO)OO	43.45	39.85	44.90
IEACO3H	CC(O)(C1CO1)C(=O)OO	35.47	36.34	46.44
C525OOH	OCC(=O)C(CO)(CO)OO	54.89	44.48	44.71
HIEB2OOH	OOC(C=O)C(O)(CO)CO	34.14	45.79	44.71
IEC2OOH	OCC(=O)C(C)(OO)C=O	43.76	38.42	46.44
INAOOH	OCC(C)(OO)C(O)CON(=O)=O	40.73	39.93	44.90
C510OOH	O=CC(O)C(C)(OO)CON(=O)=O	36.43	38.89	50.10
INB1OOH	OCC(OO)C(C)(CO)ON(=O)=O	33.35	39.85	44.90
IECCO3H	CC1(CO1)C(O)C(=O)OO	33.82	35.94	46.44
INCOOH	OCC(OO)C(C)(O)CON(=O)=O	28.75	39.93	44.90
INB2OOH	OOCC(O)C(C)(CO)ON(=O)=O	37.22	39.97	44.90
Tetrol dimer	CC(O)(CO)C(O)COC(C)(CO)C(O)CO	23.20	37.48	41.55
$(NH_4)_2SO_4$	[NH4+].[NH4+].[O-]S(=O)(=O)[O-]		184.5*	

* Calculated using the approach of Dutcher et al. (2010).

4.5 Discussion

Previous attempts to predict σ_i° have relied on empirical parameterizations, as mentioned in Section 4.2. These equations all rely on various molecular properties, including but not limited to T_c, T_b, P_c, H_{vap}, ρ_l, ρ_v, $\mathscr{R}^\star$, which must be measured or predicted indirectly through application of additional models. This limits the utility of such surface tension models for real-world applications in environmental systems, wherein the pure–component properties of many compounds are poorly constrained due to the complex mechanisms by which they form and the wide variety of multifunctional organic compounds encountered in the atmosphere (Goldstein and Galbally, 2007). Additionally, many of these empirical models are only trained on specific compound classes. This likewise leads to limits on the ability of these models to predict σ_i° for compounds outside of the classes for which they are trained. These limitations are evident in Fig. 4.3, wherein the three types of inputs discussed in this study (simplified inputs, MACCS key, and Morgan fingerprint) all yield more accurate predictions in comparison to the empirical parameterizations. It should be noted that, although the models developed in this study were never trained on the test data, the empirical models that were used for comparison were never trained on these data either. It is therefore possible that these empirical models may show better performance when they are used with the compound classes and datasets for which they were trained.

The models discussed in this study rely on structural properties of molecules along with temperature to predict σ_i°. The most detailed description of molecular structure comes in the form of the Morgan fingerprints, however, such an approach has several drawbacks which limit its utility. The foremost among these is that the most accurate model, MF-XGB, performs only marginally better than the next most detailed series of inputs, MACCS-XGB, despite having over ten times the number of inputs for molecular descriptors (2048 vs 166). Of equal importance, MACCS keys are inherently human

Table 4.3: Predicted organic surface tensions for the α-pinene SOA surrogate system at $T = 298$ K. α-pinene SOA species and SMILES codes were taken from the Master Chemical Mechanism (MCM).

MCM Name	SMILES	Morgan fingerprint σ_i° [mJ m^{-2}]	MACCS keys σ_i° [mJ m^{-2}]	Simplified inputs σ_i° [mJ m^{-2}]
C107OOH	O=CCC1CC(OO)(C(=O)C)C1(C)C	32.61	33.10	40.84
PINONIC	OC(=O)CC1CC(C(=O)C)C1(C)C	32.85	34.90	39.61
C97OOH	OCC1CC(OO)(C(=O)C)C1(C)C	33.33	34.65	40.24
C108OOH	O=CCC(CC(=O)C(=O)C)C(C)(C)OO	22.70	32.43	41.23
C89CO2H	O=CCC1CC(C(=O)O)C1(C)C	30.87	33.98	38.64
PINIC	OC(=O)CC1CC(C(=O)O)C1(C)C	31.22	36.45	39.99
C921OOH	OCC(=O)C1(OO)CC(CO)C1(C)C	49.38	36.66	39.22
C109OOH	OOCC(=O)C1CC(CC=O)C1(C)C	32.83	33.60	40.84
C812OOH	OCC1CC(OO)(C(=O)O)C1(C)C	37.90	36.96	44.96
HOPINONIC	OCC(=O)C1CC(CC(=O)O)C1(C)C	43.59	36.85	40.84
C811OH	OCC1CC(C(=O)O)C1(C)C	31.61	35.33	38.93
C813OOH	OCC(CC(=O)C(=O)O)C(C)(C)OO	30.85	37.20	45.37
ALDOL dimer	CC(=O)C(=O)CC(C(C=O)=CCC1CC(C(O)=O)C1(C)C)C(C)(C)OO	23.48	34.21	39.75
ESTER dimer	CC1(C)C(CC1C(O)=O)CC(=O)OCC(=O)C2CC(CC(O)=O)C2(C)C	31.26	34.09	39.75
$(NH_4)_2SO_4$	[NH4+].[NH4+].[O-]S(=O)(=O)[O-]		184.5*	

* Calculated using the approach of Dutcher et al. (2010).

readable whereas Morgan fingerprints rely on complex descriptions of the relative positions of each atom in a molecule simultaneously. This may make model analysis in terms of the importance of individual substructures mathematically difficult. Thus, it is recommended to use the MACCS-XGB model in the case where SMILES are known and the Simp-XGB model in cases where SMILES are unknown but the elemental ratios and molar weight of a compound are readily available. It is also possible that other types of model inputs may perform well in predicting surface tension. Functional group-based approaches, such as one analogous to that used by AIOMFAC to describe organic compounds, are an additional option. It should be noted that such approaches may not capture the three-dimensional structure and relative orientations of functional groups as well as the MACCS keys or Morgan fingerprints. Likewise, some compounds with more reactive functional groups, such as peroxyacids, may be difficult to isolate in a laboratory setting. Thus accurate surface tension measurements of these compounds are difficult to find.

In terms of specific feature importance from the models discussed in this work for predicting σ_i°, Figure 4.4 indicates that nitrogen-containing and oxygen-containing molecular substructures have a large impact on σ_i° for all three categories of inputs. Despite a substantial reduction in the number of input parameters, the Simp-XGB model was able to perform reasonably well with $R^2 = 0.905$ and RMSE $= 1.970\ \mathrm{mJ\,m^{-2}}$ based on the test dataset described in this work, in comparison the MACCS-XGB model achieved $R^2 = 0.972$ and RMSE $= 1.076\ \mathrm{mJ\,m^{-2}}$, and the MF-XGB model $R^2 = 0.975$ and RMSE $= 1.006\ \mathrm{mJ\,m^{-2}}$. Indeed for applications for which detailed structural information about a species may not be readily available, this model may perform well enough as a first-order approximation. It is also important to note that the simplified model may perform more poorly for compounds containing the elements I, P, or Br, as well as for compounds with lower molar masses. This may be attributed to the fact that there is a small number of

compounds with the aforementioned elements in the training data and that the behavior of smaller, yet still highly functionalized, compounds may not be well captured by a model that only relies on temperature, molar mass, and elemental ratios as inputs.

4.6 Conclusions

In this work, three different approaches for characterizing organic molecules and predicting their temperature-dependent pure–component surface tensions are compared to one another. For each approach to molecular characterization, four different ML approaches were used: extreme gradient boosting, random forests, decision trees, and K-nearest neighbors. We find that the extreme gradient boosting approach results in the highest R^2 in comparison to observations, regardless of which method of molecular characterization for input is used. From each of the three approaches, the most important molecular features were extracted. The molecular properties in the dataset used in this work with the highest importance were functional groups that contained nitrogen and oxygen along with ring structures. More broadly speaking, a combination of M_i, T, O:C ratio, N:C ratio was able to explain 80.1% of the variance in a simplified model which only relied on molecular ratios, M_i, and T as inputs. Such a model is useful in cases wherein the exact structure of an individual chemical species is not readily available. In the case where more detailed structural information is available in the form of SMILES, we find that using MACCS keys as inputs provides the best balance of model performance and input simplicity.

To demonstrate the importance of accurately characterizing temperature-dependent pure–component surface tension values, a Köhler curve was generated for an isoprene SOA surrogate system. It was found that the inclusion of the ML-based approaches for surface tension led to substantial changes of the predicted droplet surface tension evolution during hygroscopic growth compared to the frequently used implicit assumption of $\sigma^{\circ}_{\text{org}} = \sigma^{\circ}_{w}$. The use

of appropriate pure–component values is also shown to impact in the critical supersaturation necessary for cloud droplet activation. It is noted that some atmospherically relevant compounds, such as peroxyacids and peroxyacyl nitrates are not well represented in the dataset used in this work and that further measurements of the pure–component surface tensions of such compounds at atmospherically relevant temperatures may be necessary to improve model performance for these compound classes.

4.7 Code and Data Availability

The training and test data used in this work, the Simp-XGB, MF-XGB, and MACCS-XGB models, and the code used to optimize model hyperparameters and train models can be found at the following Zenodo archive: 10.5281/zenodo.13936980.

Bibliography

Aitken, J. XII.—On Dust, Fogs, and Clouds. Earth and Environmental Science Transactions of The Royal Society of Edinburgh **1881**, 30, 337–368.

Twomey, S. Pollution and the planetary albedo. Atmospheric Environment (1967) **1974**, 8, 1251–1256.

Köhler, H. The nucleus in and the growth of hygroscopic droplets. Transactions of the Faraday Society **1936**, 32, 1152–1161.

Sorjamaa, R.; Svenningsson, B.; Raatikainen, T.; Henning, S.; Bilde, M.; Laaksonen, A. The role of surfactants in Köhler theory reconsidered. Atmos. Chem. Phys. **2004**, 4, 2107–2117.

Nozière, B.; Baduel, C.; Jaffrezo, J.-L. The dynamic surface tension of atmospheric aerosol surfactants reveals new aspects of cloud activation. Nature Communications **2014**, 5, 3335.

Gérard, V.; Nozière, B.; Baduel, C.; Fine, L.; Frossard, A. A.; Cohen, R. C. Anionic, Cationic, and Nonionic Surfactants in Atmospheric Aerosols from the Baltic Coast at Askö, Sweden: Implications for Cloud Droplet Activation. Environmental Science and Technology **2016**, 50, 2974–2982.

Petters, S. S.; Petters, M. D. Surfactant effect on cloud condensation nuclei for two-component internally mixed aerosols. Journal of Geophysical Research: Atmospheres **2016**, 121, 1878–1895.

Ruehl, C. R.; Davies, J. F.; Wilson, K. R. An interfacial mechanism for cloud droplet formation on organic aerosols. Science **2016**, 351, 1447–1450.

Ovadnevaite, J.; Zuend, A.; Laaksonen, A.; Sanchez, K. J.; Roberts, G.; Ceburnis, D.; Decesari, S.; Rinaldi, M.; Hodas, N.; Facchini, M. C.; Seinfeld, J. H.; O' Dowd, C. Surface tension prevails over solute effect in organic-influenced cloud droplet activation. Nature **2017**, 546, 637–641.

Kroflič, A.; Frka, S.; Simmel, M.; Wex, H.; Grgić, I. Size-Resolved Surface-Active Substances of Atmospheric Aerosol: Reconsideration of the Impact on Cloud Droplet Formation. Environmental Science and Technology **2018**, 52, 9179–9187.

Malila, J.; Prisle, N. L. A Monolayer Partitioning Scheme for Droplets of Surfactant Solutions. Journal of advances in modeling earth systems **2018**, 10, 3233–3251.

Davies, J. F.; Zuend, A.; Wilson, K. R. Technical note: The role of evolving surface tension in the formation of cloud droplets. Atmos. Chem. Phys. **2019**, 19, 2933–2946.

Gérard, V.; Noziere, B.; Fine, L.; Ferronato, C.; Singh, D. K.; Frossard, A. A.; Cohen, R. C.; Asmi, E.; Lihavainen, H.; Kivekäs, N.; Aurela, M.; Brus, D.; Frka, S.; Cvitešić Kušan, A. Concentrations and Adsorption Isotherms for Amphiphilic Surfactants in PM1 Aerosols from Different Regions of Europe. Environmental Science and Technology **2019**, 53, 12379–12388.

Schmedding, R.; Zuend, A. A thermodynamic framework for bulk–surface partitioning in finite-volume mixed organic–inorganic aerosol particles and cloud droplets. Atmospheric Chemistry and Physics **2023**, 23, 7741–7765.

Sebastiani, F.; Campbell, R. A.; Rastogi, K.; Pfrang, C. Nighttime oxidation of surfactants at the air–water interface: effects of chain length, head group and saturation. Atmospheric Chemistry and Physics **2018**, 18, 3249–3268.

Pfrang, C.; Sebastiani, F.; Lucas, C. O. M.; King, M. D.; Hoare, I. D.; Chang, D.; Campbell, R. A. Ozonolysis of methyl oleate monolayers at the air–water interface: oxidation kinetics, reaction products and atmospheric implications. Phys. Chem. Chem. Phys. **2014**, 16, 13220–13228.

Knopf, D. A.; Forrester, S. M. Freezing of Water and Aqueous NaCl Droplets Coated by Organic Monolayers as a Function of Surfactant Properties and Water Activity. The Journal of Physical Chemistry A **2011**, 115, 5579–5591, PMID: 21568271.

Donaldson, D. J.; Vaida, V. The Influence of Organic Films at the Air-Aqueous Boundary on Atmospheric Processes. Chemical Reviews **2006**, 106, 1445–1461, PMID: 16608186.

Schmedding, R.; Zuend, A. The role of interfacial tension in the size-dependent phase separation of atmospheric aerosol particles. EGUsphere **2024**, 2024, 1–35.

Johansson, J. H.; Salter, M. E.; Acosta Navarro, J. C.; Leck, C.; Nilsson, E. D.; Cousins, I. T. Global transport of perfluoroalkyl acids via sea spray aerosol. Environ. Sci.: Processes Impacts **2019**, 21, 635–649.

Wokosin, K. A.; Schell, E. L.; Faust, J. A. Emerging investigator series: surfactants, films, and coatings on atmospheric aerosol particles: a review. Environ. Sci.: Atmos. **2022**, 2, 775–828.

Topping, D. O.; McFiggans, G. B.; Kiss, G.; Varga, Z.; Facchini, M. C.; Decesari, S.; Mircea, M. Surface tensions of multi-component mixed inorganic/organic aqueous systems of atmospheric significance: measurements, model predictions and importance for cloud activation predictions. Atmospheric Chemistry and Physics **2007**, 7, 2371–2398.

Vepsäläinen, S.; Calderón, S. M.; Prisle, N. L. Comparison of six approaches

to predicting droplet activation of surface active aerosol – Part 2: strong surfactants. EGUsphere **2023**, 2023, 1–23.

Kleinheins, J.; Shardt, N.; El Haber, M.; Ferronato, C.; Nozière, B.; Peter, T.; Marcolli, C. Surface tension models for binary aqueous solutions: a review and intercomparison. Phys. Chem. Chem. Phys. **2023**, 25, 11055–11074.

Berry, M. V. The molecular mechanism of surface tension. Physics Education **1971**, 6, 79.

Eberhart, J. G. The Surface Tension of Binary Liquid Mixtures1. The Journal of Physical Chemistry **1966**, 70, 1183–1186.

Connors, K. A.; Wright, J. L. Dependence of surface tension on composition of binary aqueous-organic solutions. Analytical Chemistry **1989**, 61, 194–198.

Shardt, N.; Elliott, J. A. W. Model for the Surface Tension of Dilute and Concentrated Binary Aqueous Mixtures as a Function of Composition and Temperature. Langmuir **2017**, 33, 11077–11085, PMID: 28975797.

Shardt, N.; Wang, Y.; Jin, Z.; Elliott, J. A. Surface tension as a function of temperature and composition for a broad range of mixtures. Chemical Engineering Science **2021**, 230, 116095.

Kleinheins, J.; Marcolli, C.; Dutcher, C. S.; Shardt, N. A unified surface tension model for multi-component salt, organic, and surfactant solutions. Phys. Chem. Chem. Phys. **2024**, 26, 17521–17538.

Sprow, F. B.; Prausnitz, J. M. Surface tensions of simple liquid mixtures. Trans. Faraday Soc. **1966**, 62, 1105–1111.

Antonov, G. N. Sur la tension superficielle des solutions dans la zone critique. J. Chim. Phys. **1907**, 5, 364–371.

Girifalco, L. A.; Good, R. J. A Theory for the Estimation of Surface and Interfacial Energies. I. Derivation and Application to Interfacial Tension. The Journal of Physical Chemistry **1957**, 61, 904–909.

Hyvärinen, A.-P.; Lihavainen, H.; Gaman, A.; Vairila, L.; Ojala, H.; Kulmala, M.; Viisanen, Y. Surface Tensions and Densities of Oxalic, Malonic, Succinic, Maleic, Malic, and cis-Pinonic Acids. Journal of Chemical & Engineering Data **2006**, 51, 255–260.

Riipinen, I.; Koponen, I. K.; Frank, G. P.; Hyvärinen, A.-P.; Vanhanen, J.; Lihavainen, H.; Lehtinen, K. E. J.; Bilde, M.; Kulmala, M. Adipic and Malonic Acid Aqueous Solutions: Surface Tensions and Saturation Vapor Pressures. The Journal of Physical Chemistry A **2007**, 111, 12995–13002, PMID: 18044850.

Lee, H. D.; Estillore, A. D.; Morris, H. S.; Ray, K. K.; Alejandro, A.; Grassian, V. H.; Tivanski, A. V. Direct Surface Tension Measurements of Individual Sub-Micrometer Particles Using Atomic Force Microscopy. The Journal of Physical Chemistry A **2017**, 121, 8296–8305, PMID: 28981283.

Bzdek, B. R.; Power, R. M.; Simpson, S. H.; Reid, J. P.; Royall, C. P. Precise, contactless measurements of the surface tension of picolitre aerosol droplets. Chem. Sci. **2016**, 7, 274–285.

Macleod, D. B. On a relation between surface tension and density. Transactions of the Faraday Society **1923**, 19, 38–41.

Sugden, S. CXLI.—The influence of the orientation of surface molecules on the surface tension of pure liquids. J. Chem. Soc., Trans. **1924**, 125, 1167–1177.

Log, A. M.; Diky, V.; Huber, M. L. Assessment of a Parachor Model for the Surface Tension of Binary Mixtures. International Journal of Thermophysics **2023**,

Firoozabadi, A.; Katz, D. L.; Soroosh, H.; Sajjadian, V. A. Surface Tension of Reservoir Crude-Oil/Gas Systems Recognizing the Asphalt in the Heavy Fraction. SPE Reservoir Engineering **1988**, 3, 265–272.

Escobedo, J.; Mansoori, G. A. Surface Tension Prediction for Liquid Mixtures. 1998.

Weinaug, C. F.; Katz, D. L. Surface Tensions of Methane-Propane Mixtures. Industrial & Engineering Chemistry **1943**, 35, 239–246.

Hugill, J.; Van Welsenes, A. Surface tension: a simple correlation for natural gas + conensate systems. Fluid Phase Equilibria **1986**, 29, 383–390.

Quayle, O. R. The Parachors of Organic Compounds. An Interpretation and Catalogue. Chemical Reviews **1953**, 53, 439–589.

Escobedo, J.; Mansoori, G. A. Surface tension prediction for pure fluids. AIChE Journal **1996**, 42, 1425–1433.

Lu, J.-F.; Fu, D.; Liu, J.-C.; Li, Y.-G. Application of density functional theory for predicting the surface tension of pure polar and associating fluids. Fluid Phase Equilibria **2002**, 194-197, 755–769, Proceedings of the Ninth International Conference on Properties and Phase Equilibria for Product and Process Design.

Fu, D.; Lu, J.-F.; Liu, J.-C.; Li, Y.-G. Prediction of surface tension for pure non-polar fluids based on density functional theory. Chemical Engineering Science **2001**, 56, 6989–6996, Festschrift in honour of Professor T.-M. Guo.

Tang, X.; Gross, J. Density functional theory for calculating surface tensions with a simple renormalization formalism for the critical point. Journal of Supercritical Fluids **2010**, 55, 735–742.

Guggenheim, E. A. The Principle of Corresponding States. Journal of Chemical Physics **1945**, 13, 253–261.

Lielmezs, J.; Herrick, T. New surface tension correlation for liquids. The Chemical Engineering Journal **1986**, 32, 165–169.

Brock, J. R.; Bird, R. B. Surface tension and the principle of corresponding states. AIChE Journal **1955**, 1, 174–177.

Aleem, W.; Mellon, S. N.; Sufian, M.; Mutalib, I. A.; Subbarao, D. A Model for the Estimation of Surface Tension of Pure Hydrocarbon Liquids. Petroleum Science and Technology **2015**, 33, 1908–1915.

Gharagheizi, F.; Eslamimanesh, A.; Sattari, M.; Mohammadi, A. H.; Richon, D. Development of corresponding states model for estimation of the surface tension of chemical compounds. AIChE Journal **2013**, 59, 613–621.

Sanjuán, E.; Parra, M.; Pizarro, M. Development of models for surface tension of alcohols through symbolic regression. Journal of Molecular Liquids **2020**, 298, 111971.

Randová, A.; Bartovská, L. Group contribution method: Surface tension of linear and branched alkanes. Fluid Phase Equilibria **2016**, 429, 166–176.

Soori, T.; Rassoulinejad-Mousavi, S. M.; Zhang, L.; Rokoni, A.; Sun, Y. A machine learning approach for estimating surface tension based on pendant drop images. Fluid Phase Equilibria **2021**, 538, 113012.

Rafie, S.; Hajipour, M.; Delijani, E. B. Modeling hydrocarbon surface tension using MLP and RBF neural networks and evolutionary optimization algorithms. Petroleum Science and Technology **2023**, 41, 1622–1640.

Ojaki, H. A.; Lashkarbolooki, M.; Movagharnejad, K. Checking the performance of feed-forward and cascade artificial neural networks for modeling the surface tension of binary hydrocarbon mixtures. Journal of the Iranian Chemical Society **2023**, 20, 655–667.

Mousavi, S.-P.; Atashrouz, S.; Nait Amar, M.; Hadavimoghaddam, F.; Mohammadi, M.-R.; Hemmati-Sarapardeh, A.; Mohaddespour, A. Modeling surface tension of ionic liquids by chemical structure-intelligence based models. Journal of Molecular Liquids **2021**, 342, 116961.

Lazzús, J. A.; Cuturrufo, F.; Pulgar-Villarroel, G.; Salfate, I.; Vega, P. Estimating the Temperature-Dependent Surface Tension of Ionic Liquids Using a Neural Network-Based Group Contribution Method. Industrial & Engineering Chemistry Research **2017**, 56, 6869–6886.

Lashkarbolooki, M.; Bayat, M. Prediction of surface tension of liquid normal alkanes, 1-alkenes and cycloalkane using neural network. Chemical Engineering Research and Design **2018**, 137, 154–163.

Pierantozzi, M.; Mulero, A.; Cachadina, I. Surface tension of liquid organic acids: An artificial neural network model. Molecules **2021**, 26, 1636.

G. R. Pazuki, M. N.; Sahranavard, L. Prediction of Surface Tension of Pure Hydrocarbons by An Artificial Neural Network System. Petroleum Science and Technology **2011**, 29, 2384–2396.

Tiejun Xu, Y. D.; Khanghah, M. A. Toward prediction of surface tension of branched n-alkanes using ANN technique. Petroleum Science and Technology **2019**, 37, 127–134.

Roosta, A.; Setoodeh, P.; Jahanmiri, A. Artificial Neural Network Modeling of Surface Tension for Pure Organic Compounds. Industrial & Engineering Chemistry Research **2012**, 51, 561–566.

Yee, L. C.; Wei, Y. C. Current modeling methods used in QSAR/QSPR. Statistical modelling of molecular descriptors in QSAR/QSPR **2012**, 2, 1–31.

Uddin, S.; Lu, H. Confirming the statistically significant superiority of tree-based machine learning algorithms over their counterparts for tabular data. PLOS ONE **2024**, 19, 1–12.

Chen, C.-H.; Tanaka, K.; Kotera, M.; Funatsu, K. Comparison and improvement of the predictability and interpretability with ensemble learning models in QSPR applications. Journal of Cheminformatics **2020**, 12, 19.

Boldini, D.; Grisoni, F.; Kuhn, D.; Friedrich, L.; Sieber, S. A. Practical guidelines for the use of gradient boosting for molecular property prediction. Journal of Cheminformatics **2023**, 15, 73.

Cicciarelli, B. A.; Hatton, T. A.; Smith, K. A. Dynamic Surface Tension Behavior in a Photoresponsive Surfactant System. Langmuir **2007**, 23, 4753–4764, PMID: 17381140.

Consonni, V.; Ballabio, D.; Todeschini, R. In Cheminformatics, QSAR and Machine Learning Applications for Novel Drug Development; Roy, K., Ed.; Academic Press, 2023; pp 303–327.

Durant, J. L.; Leland, B. A.; Henry, D. R.; Nourse, J. G. Reoptimization of MDL Keys for Use in Drug Discovery. Journal of Chemical Information and Computer Sciences **2002**, 42, 1273–1280, PMID: 12444722.

Morgan, H. L. The Generation of a Unique Machine Description for Chemical Structures-A Technique Developed at Chemical Abstracts Service. Journal of Chemical Documentation **1965**, 5, 107–113.

Orsi, M.; Reymond, J.-L. One chiral fingerprint to find them all. Journal of Cheminformatics **2024**, 16, 53.

Jasper, J. J. The Surface Tension of Pure Liquid Compounds. Journal of Physical and Chemical Reference Data **1972**, 1, 841–1010.

OpenEye Scientific Software, I. OEChem Toolkit, Version 2.3.0. Accessed through PubChem, Release 2021.05.07, 2024; https://pubchem.ncbi.nlm.nih.gov.

Nti, I. K.; Nyarko-Boateng, O.; Aning, J.; others Performance of machine learning algorithms with different K values in K-fold CrossValidation. International Journal of Information Technology and Computer Science **2021**, 13, 61–71.

Victoria, A. H.; Maragatham, G. Automatic tuning of hyperparameters using Bayesian optimization. Evolving Systems **2021**, 12, 217–223.

Akiba, T.; Sano, S.; Yanase, T.; Ohta, T.; Koyama, M. Optuna: A Next-generation Hyperparameter Optimization Framework. Proceedings of the 25th ACM SIGKDD International Conference on Knowledge Discovery and Data Mining. 2019.

Snow, T.; Millstein, J.; Scheick, J.; Sauthoff, W.; Leong, W. J.; Colliander, J.; Pérez, F.; Munroe, J.; Felikson, D.; Sutterley, T.; Siegfried, M. CryoCloud JupyterBook. 2023; https://doi.org/10.5281/zenodo.7576602.

Landrum, G. et al. RDKit: Open-Source Cheminformatics Software. 2024; https://www.rdkit.org/.

Chen, T.; Guestrin, C. XGBoost: A Scalable Tree Boosting System. Proceedings of the 22nd ACM SIGKDD International Conference on Knowledge Discovery and Data Mining. New York, NY, USA, 2016; pp 785–794.

Pedregosa, F. et al. Scikit-learn: Machine Learning in Python. Journal of Machine Learning Research **2011**, 12, 2825–2830.

Yaws, C. L. Yaws' thermophysical properties of chemicals and hydrocarbons, [electronic ed.] ed.; Knovel: Norwich, N.Y., 2009.

Michael A Fligner, J. S. V.; Blower, P. E. A Modification of the Jaccard–Tanimoto Similarity Index for Diverse Selection of Chemical Compounds Using Binary Strings. Technometrics **2002**, 44, 110–119.

Zuend, A.; Marcolli, C.; Luo, B. P.; Peter, T. A thermodynamic model of mixed organic-inorganic aerosols to predict activity coefficients. Atmospheric Chemistry and Physics **2008**, 8, 4559–4593.

Zuend, A.; Marcolli, C.; Booth, A. M.; Lienhard, D. M.; Soonsin, V.; Krieger, U. K.; Topping, D. O.; McFiggans, G.; Peter, T.; Seinfeld, J. H. New and extended parameterization of the thermodynamic model AIOMFAC: calculation of activity coefficients for organic-inorganic mixtures containing carboxyl, hydroxyl, carbonyl, ether, ester, alkenyl, alkyl, and aromatic functional groups. Atmospheric Chemistry and Physics **2011**, 11, 9155–9206.

Jenkin, M. E.; Young, J. C.; Rickard, A. R. The MCM v3.3.1 degradation scheme for isoprene. Atmospheric Chemistry and Physics **2015**, 15, 11433–11459.

Rastak, N. et al. Microphysical explanation of the RH-dependent water affinity of biogenic organic aerosol and its importance for climate. Geophysical Research Letters **2017**, 44, 5167–5177.

Jenkin, M. E.; Wyche, K. P.; Evans, C. J.; Carr, T.; Monks, P. S.; Alfarra, M. R.; Barley, M. H.; McFiggans, G. B.; Young, J. C.; Rickard, A. R. Development and chamber evaluation of the MCM v3.2 degradation scheme for β-caryophyllene. Atmospheric Chemistry and Physics **2012**, 12, 5275–5308.

Dutcher, C. S.; Wexler, A. S.; Clegg, S. L. Surface Tensions of Inorganic Multicomponent Aqueous Electrolyte Solutions and Melts. The Journal of Physical Chemistry A **2010**, 114, 12216–12230.

Aumann, E.; Hildemann, L.; Tabazadeh, A. Measuring and modeling the composition and temperature-dependence of surface tension for organic solutions. Atmospheric Environment **2010**, 44, 329–337.

Klavins, M.; Purmalis, O. Humic substances as surfactants. Environmental Chemistry Letters **2010**, 8, 349–354.

Goldstein, A. H.; Galbally, I. E. Known and unexplored organic constituents in the earth's atmosphere. Environmental science & technology **2007**, 41, 1514–1521.

Part III

Discussion and Conclusions

5

Conclusions and Future Work

5.1 Conclusions

In this work, a rigorous modeling framework for surface and interfacial energies on and inside aerosol particles was developed. In Chapter 2, an initial framework for partitioning between the interior bulk and a three-dimensional surface phase was laid out. It was found that the inclusion of bulk–surface partitioning in a thermodynamically sound manner led to substantial modifications to the internal and surface compositions of the aerosol particle. Such compositional differences were most pronounced in particles with sphere-equivalent diameters below approximately 50 nm. Including bulk–surface partitioning led to reductions in the critical supersaturation for cloud droplet activation for numerous systems compared to traditional assumptions that did not account for bulk–surface partitioning. The bulk–surface partitioning results were sensitive to the selection of reference state surface tensions as

well as the thickness of the surface phase. Tuning these two values allowed for the generation of Köhler curves that agreed well with measured data for several systems.

Chapter 3 compared four different approaches for modeling the interfacial tension that exists between two distinct liquid phases. The interfacial tension between two bulk liquid phases and between a bulk and surface phase was modeled using these four approaches. More extreme models of interfacial tension better matched measured interfacial tensions in bulk systems with very limited miscibility between phases. In systems with higher degrees of miscibility between components, it was found that less extreme models of interfacial tension were able to better replicate measurements. All of the interfacial tension models, except for one, were sensitive to the selection of pure component surface tension values. The inclusion of interfacial tension parameterizations had competing effects: the interfacial tension between two bulk phases led to reductions in the onset relative humidity of liquid–liquid phase separation, while the inclusion of the interfacial tension between a liquid and surface phase raised the onset relative humidity of liquid–liquid phase separation. This effect was most pronounced at particle sphere-equivalent diameters below approximately 100 nm. At particle sizes below approximately 30 nm, the energetic penalty from the liquid–liquid interface became stronger than the liquid–surface interface in the systems studied, suppressing phase separation.

Chapter 4 sought to further understand the role of an individual compound's pure-component surface tension by creating three different machine learning-based models capable of predicting the pure component surface tension of a compound from its molecular structure or properties. The simplest of the three models took elemental ratios and molecular weight as inputs. The second most complex model used MACCS keys derived from SMILES codes as inputs. The most complicated model inputs were Morgan fingerprints generated from SMILES codes. All three models performed better

than past semi-empirical approaches to predicting pure component surface tension. However, the difference in model performance between the MACCS key-based model and the Morgan fingerprint-based model was negligible in comparison to the additional complexity introduced by using more detailed inputs. The models were capable of replicating the monotonic temperature dependence of surface tension across atmospherically relevant temperature ranges. The inclusion of different model inputs led to small differences in the Köhler curves predicted for isoprene degradation products and α-pinene degradation products.

In this work, the bulk–surface partitioning behavior of atmospheric aerosols with a single well-mixed phase was described using a thermodynamically rigorous and consistent approach for the first time. The interactions between liquid–liquid phase separation, bulk–surface partitioning, and gas-particle partitioning were then explored in a novel approach which accounted for all of the liquid–liquid interfaces present in a particle. In order to address uncertainty in these two approaches, a machine learning approach to predicting pure-component surface tensions of organic compounds in the atmosphere was developed. This model, while intended to be used to inform the thermodynamic models laid out in this work, may also have applications in other fields beyond atmospheric science. The inclusion of coupled gas–particle, liquid–liquid, and bulk–surface partitioning with accurate estimates of pure-component surface tensions leads to substantial changes in the water uptake of aerosol particles and the conditions under which they activate into cloud droplets.

5.2 Future Work

While this work represents a step toward a better understanding of surface and interfacial properties in atmospheric aerosols, many unanswered questions remain that may be the subject of future work. As discussed in Chapter 2, there are limited measurements of the surface tension of aerosol particles in the ultrafine regime. Such measurements are inherently difficult, as they must be done in a manner that does not involve the introduction of a new interface or changes to a particle's morphology. For example, impacting a particle on a glass slide would introduce a glass–liquid interface that may change the bulk–surface partitioning behavior of different species. In systems where particle size plays a role in surface tension, additional contactless measurements must be taken to better constrain the bulk–surface partitioning model's behavior. Likewise, the structure of the surface remains an area of ongoing debate as well. Given that the depth of the surface is a highly sensitive parameter in the framework described in Chapter 2, a better understanding of the structure of the surface phase may help to constrain said parameter. Such an understanding would likely result from molecular dynamics simulations, which are capable of resolving the positions of individual molecules in a droplet with a high degree of precision. Unfortunately, these can only be performed for droplets a few nanometers in diameter or the timescale of the simulation becomes prohibitively long. Furthermore, such molecular dynamics simulations depend on the force fields used and correct simulations of the air–liquid interface. The development of more powerful molecular dynamics simulations may lead to better constraints on model parameters relevant to particle structure described in Chapter 2.

Although Chapter 3 attempted to address some questions raised by Chapter 2, namely the interactions between liquid-liquid phase separation and bulk–surface partitioning, it introduced several other unanswered questions that may also be the subject of future work. One implication of the treatment of interfacial tension described in Chapter 3 is that the ratios of surface

tensions for phases α and β, along with the interfacial tension between them, can be used to predict whether a liquid–liquid phase-separated particle is in a core–shell configuration or a partially engulfed configuration. However, such a calculation is complex and will need to be solved iteratively, as changing between core–shell and partially engulfed configurations will change the relative volumes of the bulk and surface for each phase. This will modify the resulting surface tension of each phase and necessitate updating the particle morphology. Likewise, the area of the liquid–liquid interface will be reduced in such a configuration, changing the overall Gibbs energy of the particle at equilibrium. The behaviour of a partially engulfed particle with respect to the Kelvin effect in a Köhler curve may no longer be straightforward, as there would be multiple exposed surfaces with different radii and thus different Kelvin effects for each phase. Another unanswered question that may be of interest is how the inclusion of additional liquid phases will impact the particle mixing state and morphology. A particle with three liquid phases and a surface phase will have one additional interface if it is in a core-shell configuration or possibly multiple additional interfaces if it exists in a more complex morphology that includes combinations of partially engulfing and core-shell morphologies. A framework for determining the structure of such a particle would be useful for modeling more complex systems that have been observed.

Chapter 4 explored one of the key assumptions of Chapters 2 and 3: the values of the reference state surface tensions of organic species in aerosol particles. While the models generated in this chapter were capable of predicting the surface tension of many species well, the training data that was used to fit the models did not contain an even distribution of elements and functional groups. Elements such as P, which have been found in organic aerosol systems, were underrepresented in the training and validation data. Likewise, more complex compounds such as peroxy-acids or peroxy-acyl nitrates were not well represented in the training and validation data either.

Such compounds may be difficult to isolate in a laboratory setting; however, including the effects of these more exotic molecular structures may improve model performance as they are found in many atmospherically relevant organic compounds. Additional measurements of pure component surface tensions at lower, yet still atmospherically relevant, temperatures may also help to better constrain the models developed in Chapter 4.

Bibliography

Kaufman, Y. J.; Tanré, D.; Boucher, O. A satellite view of aerosols in the climate system. Nature **2002**, 419, 215–223.

Gras, J. L. Southern hemisphere tropospheric aerosol microphysics. Journal of Geophysical Research: Atmospheres **1991**, 96, 5345–5356.

Gupta, G.; Ratnam, M. V.; Madhavan, B.; Prasad, P.; Narayanamurthy, C. Vertical and spatial distribution of elevated aerosol layers obtained using long-term ground-based and space-borne lidar observations. Atmospheric Environment **2021**, 246, 118172.

Seinfeld, J. H. et al. Improving our fundamental understanding of the role of aerosol - cloud interactions in the climate system. Proceedings of the National Academy of Sciences **2016**, 113, 5781–5790.

Boucher, O.; Randall, D.; Artaxo, P.; Bretherton, C.; Feingold, G.; Forster, P.; Kerminen, V. M.; Kondo, Y.; Liao, H.; Lohmann, U.; Rasch, P.; Satheesh, S. K.; Sherwood, S.; Stevens, B.; Zhang, X. Y. Clouds and aerosols. Climate Change 2013: The Physical Science Basis. Contribution of Working Group I to the Fifth Assessment Report of the Intergovernmental Panel on Climate Change **2013**, 571–657.

Andreae, M. O.; Gelencsér, A. Black carbon or brown carbon? The nature of light-absorbing carbonaceous aerosols. Atmospheric Chemistry and Physics **2006**, 6, 3131–3148.

Quinn, P.; Bates, T.; Baum, E.; Doubleday, N.; Fiore, A.; Flanner, M.; Fridlind, A.; Garrett, T.; Koch, D.; Menon, S.; others Short-lived pollutants in the Arctic: their climate impact and possible mitigation strategies. Atmospheric Chemistry and Physics **2008**, 8, 1723–1735.

Twomey, S. Pollution and the planetary albedo. Atmospheric Environment (1967) **1974**, 8, 1251–1256.

Albrecht, B. A. Aerosols, Cloud Microphysics, and Fractional Cloudiness. Science **1989**, 245, 1227–1230.

Abraham, F. F.; Zettlemoyer, A. C. Homogeneous Nucleation Theory. Physics Today **1974**, 27, 52–53.

Hinds, W. C. Aerosol technology : properties, behavior, and measurement of airborne particles; J. Wiley: New York, 1982; pp xix, 424 pages : illustrations ; 24 cm.

Andrew Gray, H.; Cass, G. R. Source contributions to atmospheric fine carbon particle concentrations. Atmospheric Environment **1998**, 32, 3805–3825.

Guevara, M. Airborne Particulate Matter: Sources, Atmospheric Processes and Health; The Royal Society of Chemistry, 2016.

Hallquist, M. et al. The formation, properties and impact of secondary organic aerosol: current and emerging issues. Atmospheric Chemistry and Physics **2009**, 9, 5155–5236.

Zhang, Q. et al. Ubiquity and dominance of oxygenated species in organic aerosols in anthropogenically-influenced Northern Hemisphere midlatitudes. Geophysical Research Letters **2007**, 34.

Jimenez, J. L. et al. Evolution of Organic Aerosols in the Atmosphere. Science **2009**, 326, 1525–1529.

Thomas, M. A.; Devasthale, A.; Kahnert, M. Marine aerosol properties over the Southern Ocean in relation to the wintertime meteorological conditions. Atmospheric Chemistry and Physics **2022**, 22, 119–137.

Seinfeld, J. H.; Pandis, S. N. Atmospheric chemistry and physics : from air pollution to climate change, 2nd ed.; J. Wiley: Hoboken, N.J., 2006; pp xxviii, 1203 pages : illustrations ; 26 cm.

Johnston, M. V.; Wexler, A. S. MS of individual aerosol particles. Analytical Chemistry **1995**, 67, 721A–726A.

Nair, A. A.; Yu, F. Quantification of Atmospheric Ammonia Concentrations: A Review of Its Measurement and Modeling. Atmosphere **2020**, 11.

Andreae, M. O.; Ferek, R. J.; Bermond, F.; Byrd, K. P.; Engstrom, R. T.; Hardin, S.; Houmere, P. D.; LeMarrec, F.; Raemdonck, H.; Chatfield, R. B. Dimethyl sulfide in the marine atmosphere. Journal of Geophysical Research: Atmospheres **1985**, 90, 12891–12900.

Weng, H.; Lin, J.; Martin, R.; Millet, D. B.; Jaeglé, L.; Ridley, D.; Keller, C.; Li, C.; Du, M.; Meng, J. Global high-resolution emissions of soil NO_x, sea salt aerosols, and biogenic volatile organic compounds. Scientific Data **2020**, 7, 148.

Xu, H.; Ren, Y.; Zhang, W.; Meng, W.; Yun, X.; Yu, X.; Li, J.; Zhang, Y.; Shen, G.; Ma, J.; Li, B.; Cheng, H.; Wang, X.; Wan, Y.; Tao, S. Updated Global Black Carbon Emissions from 1960 to 2017: Improvements, Trends, and Drivers. Environ. Sci. Technol. **2021**, 55, 7869–7879.

Yin, H.; Dou, J.; Klein, L.; Krieger, U. K.; Bain, A.; Wallace, B. J.; Preston, T. C.; Zuend, A. Extension of the AIOMFAC model by iodine and carbonate species: applications for aerosol acidity and cloud droplet activation. Atmospheric Chemistry and Physics **2022**, 22, 973–1013.

Ariya, P. A.; Amyot, M.; Dastoor, A.; Deeds, D.; Feinberg, A.; Kos, G.; Poulain, A.; Ryjkov, A.; Semeniuk, K.; Subir, M.; Toyota, K. Mercury Physicochemical and Biogeochemical Transformation in the Atmosphere and at Atmospheric Interfaces: A Review and Future Directions. Chemical Reviews **2015**, 115, 3760–3802, PMID: 25928690.

Lund, M. T.; Myhre, G.; Skeie, R. B.; Samset, B. H.; Klimont, Z. Implications of differences between recent anthropogenic aerosol emission inventories for diagnosed AOD and radiative forcing from 1990 to 2019. Atmospheric Chemistry and Physics **2023**, 23, 6647–6662.

Mahrt, F.; Huang, Y.; Zaks, J.; Devi, A.; Peng, L.; Ohno, P. E.; Qin, Y. M.; Martin, S. T.; Ammann, M.; Bertram, A. K. Phase Behavior of Internal Mixtures of Hydrocarbon-like Primary Organic Aerosol and Secondary Aerosol Based on Their Differences in Oxygen-to-Carbon Ratios. Environ. Sci. Technol. **2022**, 56, 3960–3973, Publisher: American Chemical Society.

Chen, Y.; Takeuchi, M.; Nah, T.; Xu, L.; Canagaratna, M. R.; Stark, H.; Baumann, K.; Canonaco, F.; Prévôt, A. S. H.; Huey, L. G.; Weber, R. J.; Ng, N. L. Chemical characterization of secondary organic aerosol at a rural site in the southeastern US: insights from simultaneous high-resolution time-of-flight aerosol mass spectrometer (HR-ToF-AMS) and FIGAERO chemical ionization mass spectrometer (CIMS) measurements. Atmospheric Chemistry and Physics **2020**, 20, 8421–8440.

Zuend, A.; Marcolli, C.; Peter, T.; Seinfeld, J. H. Computation of liquid-liquid equilibria and phase stabilities: implications for RH-dependent gas/particle partitioning of organic-inorganic aerosols. Atmospheric Chemistry and Physics **2010**, 10, 7795–7820.

Song, M.; Marcolli, C.; Krieger, U. K.; Zuend, A.; Peter, T. Liquid-liquid phase separation and morphology of internally mixed dicarboxylic

acids/ammonium sulfate/water particles. Atmospheric Chemistry and Physics **2012**, 12, 2691–2712.

Reid, J. P.; Dennis-Smither, B. J.; Kwamena, N.-O. A.; Miles, R. E. H.; Hanford, K. L.; Homer, C. J. The morphology of aerosol particles consisting of hydrophobic and hydrophilic phases: hydrocarbons, alcohols and fatty acids as the hydrophobic component. Physical Chemistry Chemical Physics **2011**, 13, 15559–15572.

Kwamena, N. O. A.; Buajarern, J.; Reid, J. P. Equilibrium Morphology of Mixed Organic/Inorganic/Aqueous Aerosol Droplets: Investigating the Effect of Relative Humidity and Surfactants. The Journal of Physical Chemistry A **2010**, 114, 5787–5795.

Ciobanu, V. G.; Marcolli, C.; Krieger, U. K.; Weers, U.; Peter, T. Liquidâ^'Liquid Phase Separation in Mixed Organic/Inorganic Aerosol Particles. The Journal of Physical Chemistry A **2009**, 113, 10966–10978, PMID: 19775109.

Song, M.; Marcolli, C.; Krieger, U. K.; Lienhard, D. M.; Peter, T. Morphologies of mixed organic/inorganic/aqueous aerosol droplets. Faraday Discuss. **2013**, 165, 289–316.

Shiraiwa, M.; Zuend, A.; Bertram, A. K.; Seinfeld, J. H. Gas-particle particle partitioning of atmospheric aerosols: interplay of physical state, non-ideal mixing and morphology. Phys. Chem. Chem. Phys. **2013**, 15, 11441–11453.

Gorkowski, K.; Donahue, N. M.; Sullivan, R. C. Aerosol Optical Tweezers Constrain the Morphology Evolution of Liquid-Liquid Phase-Separated Atmospheric Particles. Chem **2020**, 6, 204–220.

Kucinski, T. M.; Dawson, J. N.; Freedman, M. A. Size-Dependent Liquid–Liquid Phase Separation in Atmospherically Relevant Complex Systems. The Journal of Physical Chemistry Letters **2019**, 10, 6915–6920.

Huang, Y.; Mahrt, F.; Xu, S.; Shiraiwa, M.; Zuend, A.; Bertram, A. K. Coexistence of three liquid phases in individual atmospheric aerosol particles. Proceedings of the National Academy of Sciences **2021**, 118, e2102512118.

Lilek, J.; Zuend, A. A predictive viscosity model for aqueous electrolytes and mixed organic–inorganic aerosol phases. Atmospheric Chemistry and Physics **2022**, 22, 3203–3233.

Gervasi, N. R.; Topping, D. O.; Zuend, A. A predictive group-contribution model for the viscosity of aqueous organic aerosol. Atmospheric Chemistry and Physics **2020**, 20, 2987–3008.

Slade, J. H. et al. Bouncier Particles at Night: Biogenic Secondary Organic Aerosol Chemistry and Sulfate Drive Diel Variations in the Aerosol Phase in a Mixed Forest. Environmental Science & Technology **2019**, 53, 4977–4987, PMID: 31002496.

Reid, J. P.; Bertram, A. K.; Topping, D. O.; Laskin, A.; Martin, S. T.; Petters, M. D.; Pope, F. D.; Rovelli, G. The viscosity of atmospherically relevant organic particles. Nature Communications **2018**, 9, 956.

Schmedding, R.; Ma, M.; Zhang, Y.; Farrell, S.; Pye, H. O. T.; Chen, Y.; Wang, C.-t.; Rasool, Q. Z.; Budisulistiorini, S. H.; Ault, A. P.; Surratt, J. D.; Vizuete, W. alpha-Pinene-Derived organic coatings on acidic sulfate aerosol impacts secondary organic aerosol formation from isoprene in a box model. Atmospheric Environment **2019**, 213, 456–462.

Schmedding, R.; Rasool, Q. Z.; Zhang, Y.; Pye, H. O. T.; Zhang, H.; Chen, Y.; Surratt, J. D.; Lopez-Hilfiker, F. D.; Thornton, J. A.; Goldstein, A. H.; Vizuete, W. Predicting secondary organic aerosol phase state and viscosity and its effect on multiphase chemistry in a regional-scale air quality model. Atmos. Chem. Phys. **2020**, 20, 8201–8225.

Wagner, R.; Möhler, O.; Saathoff, H.; Schnaiter, M.; Skrotzki, J.; Leisner, T.; Wilson, T. W.; Malkin, T. L.; Murray, B. J. Ice cloud processing of ultra-viscous/glassy aerosol particles leads to enhanced ice nucleation ability. Atmospheric Chemistry and Physics **2012**, 12, 8589–8610.

Wilson, T. W.; Murray, B. J.; Wagner, R.; Möhler, O.; Saathoff, H.; Schnaiter, M.; Skrotzki, J.; Price, H. C.; Malkin, T. L.; Dobbie, S.; Al-Jumur, S. M. R. K. Glassy aerosols with a range of compositions nucleate ice heterogeneously at cirrus temperatures. Atmospheric Chemistry and Physics **2012**, 12, 8611–8632.

Schill, G. P.; Tolbert, M. A. Heterogeneous ice nucleation on phase-separated organic-sulfate particles: effect of liquid vs. glassy coatings. Atmospheric Chemistry and Physics **2013**, 13, 4681–4695.

Lang-Yona, N.; Abo-Riziq, A.; Erlick, C.; Segre, E.; Trainic, M.; Rudich, Y. Interaction of internally mixed aerosols with light. Physical Chemistry Chemical Physics **2010**, 12, 21–31.

Fard, M. M.; Krieger, U. K.; Peter, T. Shortwave radiative impact of liquid–liquid phase separation in brown carbon aerosols. Atmospheric Chemistry and Physics **2018**, 18, 13511–13530.

Köhler, H. The nucleus in and the growth of hygroscopic droplets. Transactions of the Faraday Society **1936**, 32, 1152–1161.

Zhang, Q.-N.; Zhao, L.-J.; Chen, S.-H.; Guo, X.; Luan, Y.-M.; Zhang, Y.-H. Hygroscopic property of inorganic salts in atmospheric aerosols measured with physisorption analyzer. Atmospheric Environment **2021**, 247, 118171.

Pöhlker, M. L. et al. Global organic and inorganic aerosol hygroscopicity and its effect on radiative forcing. Nature Communications **2023**, 14, 6139.

Davies, J. F.; Zuend, A.; Wilson, K. R. Technical note: The role of evolving surface tension in the formation of cloud droplets. Atmos. Chem. Phys. **2019**, 19, 2933–2946.

Petters, M. D.; Kreidenweis, S. M. A single parameter representation of hygroscopic growth and cloud condensation nucleus activity. Atmospheric Chemistry and Physics **2007**, 7, 1961–1971.

Topping, D.; Barley, M.; Bane, M. K.; Higham, N.; Aumont, B.; Dingle, N.; McFiggans, G. UManSysProp v1.0: an online and open-source facility for molecular property prediction and atmospheric aerosol calculations. Geoscientific Model Development **2016**, 9, 899–914.

Kanji, Z. A.; Ladino, L. A.; Wex, H.; Boose, Y.; Burkert-Kohn, M.; Cziczo, D. J.; Krämer, M. Overview of Ice Nucleating Particles. Meteorological Monographs **2017**, 58, 1.1 – 1.33.

Matsumoto, M.; Saito, S.; Ohmine, I. Molecular dynamics simulation of the ice nucleation and growth process leading to water freezing. Nature **2002**, 416, 409–413.

Li, J.; Carlson, B. E.; Yung, Y. L.; Lv, D.; Hansen, J.; Penner, J. E.; Liao, H.; Ramaswamy, V.; Kahn, R. A.; Zhang, P.; Dubovik, O.; Ding, A.; Lacis, A. A.; Zhang, L.; Dong, Y. Scattering and absorbing aerosols in the climate system. Nature Reviews Earth & Environment **2022**, 3, 363–379.

Fredenslund, A.; Jones, R. L.; Prausnitz, J. M. Group-contribution estimation of activity coefficients in nonideal liquid mixtures. AIChE Journal **1975**, 21, 1086–1099.

Hansen, H. K.; Rasmussen, P.; Fredenslund, A.; Schiller, M.; Gmehling, J. Vapor-liquid equilibria by UNIFAC group contribution. 5. Revision and extension. Industrial & Engineering Chemistry Research **1991**, 30, 2352–2355.

Dutcher, C. S.; Ge, X.; Wexler, A. S.; Clegg, S. L. Statistical Mechanics of Multilayer Sorption: Extension of the Brunauer–Emmett–Teller (BET) and Guggenheim–Anderson–de Boer (GAB) Adsorption Isotherms. The Journal of Physical Chemistry C **2011**, 115, 16474–16487.

Wexler, A. S.; Clegg, S. L. Atmospheric aerosol models for systems including the ions H+, NH4, Na, SO42, NO3, Cl, Br, and H2O. Journal of Geophysical Research: Atmospheres **2002**, 107, ACH 14–1–ACH 14–14.

Erdakos, G. B.; Asher, W. E.; Seinfeld, J. H.; Pankow, J. F. Prediction of activity coefficients in liquid aerosol particles containing organic compounds, dissolved inorganic salts, and water—Part 1: Organic compounds and water by consideration of short- and long-range effects using X-UNIFAC.1. Atmospheric Environment **2006**, 40, 6410–6421.

Yan, W.; Topphoff, M.; Rose, C.; Gmehling, J. Prediction of vapor–liquid equilibria in mixed-solvent electrolyte systems using the group contribution concept. Fluid Phase Equilibria **1999**, 162, 97–113.

Zuend, A.; Marcolli, C.; Luo, B. P.; Peter, T. A thermodynamic model of mixed organic-inorganic aerosols to predict activity coefficients. Atmospheric Chemistry and Physics **2008**, 8, 4559–4593.

Zuend, A.; Marcolli, C.; Booth, A. M.; Lienhard, D. M.; Soonsin, V.; Krieger, U. K.; Topping, D. O.; McFiggans, G.; Peter, T.; Seinfeld, J. H. New and extended parameterization of the thermodynamic model AIOMFAC: calculation of activity coefficients for organic-inorganic mixtures containing carboxyl, hydroxyl, carbonyl, ether, ester, alkenyl, alkyl, and aromatic functional groups. Atmospheric Chemistry and Physics **2011**, 11, 9155–9206.

Ganbavale, G.; Zuend, A.; Marcolli, C.; Peter, T. Improved AIOMFAC model parameterisation of the temperature dependence of activity coefficients for

aqueous organic mixtures. Atmospheric Chemistry and Physics **2015**, 15, 447–493.

Matthews, M. A. A to Z of Thermodynamics By Pierre Perrot (Université des sciences et technologies de Lille). Oxford University Press: Oxford, New York, and Tokyo. 1998. vi + 329 pp. $65.00. ISBN 0-19-856556-9 (Hardback). Journal of the American Chemical Society **2000**, 122, 3799–3800, 3799.

Amirfazli, A.; Neumann, A. Status of the three-phase line tension: a review. Advances in Colloid and Interface Science **2004**, 110, 121–141.

Ovadnevaite, J.; Zuend, A.; Laaksonen, A.; Sanchez, K. J.; Roberts, G.; Ceburnis, D.; Decesari, S.; Rinaldi, M.; Hodas, N.; Facchini, M. C.; Seinfeld, J. H.; O' Dowd, C. Surface tension prevails over solute effect in organic-influenced cloud droplet activation. Nature **2017**, 546, 637–641.

Ruehl, C. R.; Davies, J. F.; Wilson, K. R. An interfacial mechanism for cloud droplet formation on organic aerosols. Science **2016**, 351, 1447–1450.

Malila, J.; Prisle, N. L. A Monolayer Partitioning Scheme for Droplets of Surfactant Solutions. Journal of advances in modeling earth systems **2018**, 10, 3233–3251.

Sorjamaa, R.; Svenningsson, B.; Raatikainen, T.; Henning, S.; Bilde, M.; Laaksonen, A. The role of surfactants in Köhler theory reconsidered. Atmos. Chem. Phys. **2004**, 4, 2107–2117.

Nozière, B.; Baduel, C.; Jaffrezo, J.-L. The dynamic surface tension of atmospheric aerosol surfactants reveals new aspects of cloud activation. Nature Communications **2014**, 5, 3335.

Gérard, V.; Nozière, B.; Baduel, C.; Fine, L.; Frossard, A. A.; Cohen, R. C. Anionic, Cationic, and Nonionic Surfactants in Atmospheric Aerosols from

the Baltic Coast at Askö, Sweden: Implications for Cloud Droplet Activation. Environmental Science and Technology **2016**, 50, 2974–2982.

Petters, S. S.; Petters, M. D. Surfactant effect on cloud condensation nuclei for two-component internally mixed aerosols. Journal of Geophysical Research: Atmospheres **2016**, 121, 1878–1895.

Kroflič, A.; Frka, S.; Simmel, M.; Wex, H.; Grgić, I. Size-Resolved Surface-Active Substances of Atmospheric Aerosol: Reconsideration of the Impact on Cloud Droplet Formation. Environmental Science and Technology **2018**, 52, 9179–9187.

Gérard, V.; Noziere, B.; Fine, L.; Ferronato, C.; Singh, D. K.; Frossard, A. A.; Cohen, R. C.; Asmi, E.; Lihavainen, H.; Kivekäs, N.; Aurela, M.; Brus, D.; Frka, S.; Cvitešić Kušan, A. Concentrations and Adsorption Isotherms for Amphiphilic Surfactants in PM1 Aerosols from Different Regions of Europe. Environmental Science and Technology **2019**, 53, 12379–12388.

Kleinheins, J.; Shardt, N.; El Haber, M.; Ferronato, C.; Nozière, B.; Peter, T.; Marcolli, C. Surface tension models for binary aqueous solutions: a review and intercomparison. Phys. Chem. Chem. Phys. **2023**, 25, 11055–11074.

Kleinheins, J.; Marcolli, C.; Dutcher, C. S.; Shardt, N. A unified surface tension model for multi-component salt, organic, and surfactant solutions. Phys. Chem. Chem. Phys. **2024**, 26, 17521–17538.

Binyaminov, H.; Abdullah, F.; Zargarzadeh, L.; Elliott, J. A. W. Thermodynamic Investigation of Droplet–Droplet and Bubble–Droplet Equilibrium in an Immiscible Medium. The Journal of Physical Chemistry B **2021**, 125, 8636–8651, PMID: 34310143.

Facchini, M. C.; Mircea, M.; Fuzzi, S.; Charlson, R. J. Cloud albedo enhancement by surface-active organic solutes in growing droplets. Nature **1999**, 401, 257–259.

Facchini, M. C.; Decesari, S.; Mircea, M.; Fuzzi, S.; Loglio, G. Surface tension of atmospheric wet aerosol and cloud/fog droplets in relation to their organic carbon content and chemical composition. Atmospheric Environment **2000**, 34, 4853–4857.

Topping, D. O.; McFiggans, G. B.; Kiss, G.; Varga, Z.; Facchini, M. C.; Decesari, S.; Mircea, M. Surface tensions of multi-component mixed inorganic/organic aqueous systems of atmospheric significance: measurements, model predictions and importance for cloud activation predictions. Atmospheric Chemistry and Physics **2007**, 7, 2371–2398.

Prisle, N. L.; Raatikainen, T.; Laaksonen, A.; Bilde, M. Surfactants in cloud droplet activation: mixed organic-inorganic particles. Atmos. Chem. Phys. **2010**, 10, 5663–5683.

Prisle, N. L.; Raatikainen, T.; Sorjamaa, R.; Svenningsson, B.; Laaksonen, A.; Bilde, M. Surfactant partitioning in cloud droplet activation: a study of C8, C10, C12 and C14 normal fatty acid sodium salts. Tellus B **2008**, 60, 416–431.

Prisle, N. L.; Dal Maso, M.; Kokkola, H. A simple representation of surface active organic aerosol in cloud droplet formation. Atmospheric Chemistry and Physics **2011**, 11, 4073–4083.

Gibbs, J. W. On the Equilibrium of Heterogeneous Substances. **1874**,

Szyszkowski, B. V. Experimentelle Studien über kapillare Eigenschaften der wässerigen Lösungen von Fettsäuren. **1908**,

Jura, G.; Harkins, W. D. Surfaces of Solids. XIV. A Unitary Thermodynamic Theory of the Adsorption of Vapors on Solids and of Insoluble Films on Liquid Subphases. Journal of the American Chemical Society **1946**, 68, 1941–1952.

You, Y.; Smith, M. L.; Song, M.; Martin, S. T.; Bertram, A. K. Liquid–liquid phase separation in atmospherically relevant particles consisting of organic species and inorganic salts. Int. Rev. Phys. Chem. **2014**, 33, 43–77.

Hua, X.; Bevan, M. A.; Frechette, J. Reversible Partitioning of Nanoparticles at an Oil–Water Interface. Langmuir **2016**, 32, 11341–11352, PMID: 27564252.

Russell, L. M.; Ming, Y. Deliquescence of small particles. The Journal of Chemical Physics **2002**, 116, 311–321.

Ohno, P. E.; Brandão, L.; Rainone, E. M.; Aruffo, E.; Wang, J.; Qin, Y.; Martin, S. T. Size Dependence of Liquid–Liquid Phase Separation by in Situ Study of Flowing Submicron Aerosol Particles. The Journal of Physical Chemistry A **2023**, 127, 2967–2974, PMID: 36947002.

Ott, E.-J. E.; Kucinski, T. M.; Dawson, J. N.; Freedman, M. A. Use of Transmission Electron Microscopy for Analysis of Aerosol Particles and Strategies for Imaging Fragile Particles. Analytical Chemistry **2021**, 93, 11347–11356.

Antonov, G. N. Sur la tension superficielle des solutions dans la zone critique. J. Chim. Phys. **1907**, 5, 364–371.

Makkonen, L.; Kurkela, J. Another look at the interfacial interaction parameter. Journal of Colloid and Interface Science **2018**, 529, 243–246.

Winter, A. Antonow's rule 85 years later. Heterogeneous Chemistry Reviews **1995**, 2, 269–308.

Girifalco, L. A.; Good, R. J. A Theory for the Estimation of Surface and Interfacial Energies. I. Derivation and Application to Interfacial Tension. The Journal of Physical Chemistry **1957**, 61, 904–909.

Fowkes, F. M. Determination of interfacial tensions, contact angles, and dispersion forces in surfaces by assuming additivity of intermolecular interactions in surfaces. The Journal of Physical Chemistry **1962**, 66, 382–382.

Fowkes, F. M. Additivity of intermolecular forces at interfaces. I. determination of the contribution to surface and interfacial tensions of dispersion forces in various liquids. The Journal of Physical Chemistry **1963**, 67, 2538–2541.

Freedman, M. A. Liquid–Liquid Phase Separation in Supermicrometer and Submicrometer Aerosol Particles. Accounts of Chemical Research **2020**, 53, 1102–1110.

Ott, E.-J. E.; Freedman, M. A. Inhibition of Phase Separation in Aerosolized Water-Soluble Polymer–Polymer Nanoparticles at Small Sizes and the Effects of Molecular Weight. The Journal of Physical Chemistry B **2020**, 124, 7518–7523, PMID: 32790387.

Dutcher, C. S.; Wexler, A. S.; Clegg, S. L. Surface Tensions of Inorganic Multicomponent Aqueous Electrolyte Solutions and Melts. The Journal of Physical Chemistry A **2010**, 114, 12216–12230.

Wexler, A. S.; Dutcher, C. S. Statistical Mechanics of Multilayer Sorption: Surface Tension. The Journal of Physical Chemistry Letters **2013**, 4, 1723–1726, PMID: 26282984.

Yee, L. C.; Wei, Y. C. Current modeling methods used in QSAR/QSPR. Statistical modelling of molecular descriptors in QSAR/QSPR **2012**, 2, 1–31.

Chen, C.-H.; Tanaka, K.; Kotera, M.; Funatsu, K. Comparison and improvement of the predictability and interpretability with ensemble learning models in QSPR applications. Journal of Cheminformatics **2020**, 12, 19.

Consonni, V.; Ballabio, D.; Todeschini, R. In Cheminformatics, QSAR and Machine Learning Applications for Novel Drug Development; Roy, K., Ed.; Academic Press, 2023; pp 303–327.

Durant, J. L.; Leland, B. A.; Henry, D. R.; Nourse, J. G. Reoptimization of MDL Keys for Use in Drug Discovery. Journal of Chemical Information and Computer Sciences **2002**, 42, 1273–1280, PMID: 12444722.

Kuwahara, H.; Gao, X. Analysis of the effects of related fingerprints on molecular similarity using an eigenvalue entropy approach. Journal of Cheminformatics **2021**, 13, 27.

Morgan, H. L. The Generation of a Unique Machine Description for Chemical Structures-A Technique Developed at Chemical Abstracts Service. Journal of Chemical Documentation **1965**, 5, 107–113.

Sanjuán, E.; Parra, M.; Pizarro, M. Development of models for surface tension of alcohols through symbolic regression. Journal of Molecular Liquids **2020**, 298, 111971.

Randová, A.; Bartovská, L. Group contribution method: Surface tension of linear and branched alkanes. Fluid Phase Equilibria **2016**, 429, 166–176.

Soori, T.; Rassoulinejad-Mousavi, S. M.; Zhang, L.; Rokoni, A.; Sun, Y. A machine learning approach for estimating surface tension based on pendant drop images. Fluid Phase Equilibria **2021**, 538, 113012.

Rafie, S.; Hajipour, M.; Delijani, E. B. Modeling hydrocarbon surface tension using MLP and RBF neural networks and evolutionary optimization algorithms. Petroleum Science and Technology **2023**, 41, 1622–1640.

Ojaki, H. A.; Lashkarbolooki, M.; Movagharnejad, K. Checking the performance of feed-forward and cascade artificial neural networks for modeling the surface tension of binary hydrocarbon mixtures. Journal of the Iranian Chemical Society **2023**, 20, 655–667.

Mousavi, S.-P.; Atashrouz, S.; Nait Amar, M.; Hadavimoghaddam, F.; Mohammadi, M.-R.; Hemmati-Sarapardeh, A.; Mohaddespour, A. Modeling surface tension of ionic liquids by chemical structure-intelligence based models. Journal of Molecular Liquids **2021**, 342, 116961.

Lazzús, J. A.; Cuturrufo, F.; Pulgar-Villarroel, G.; Salfate, I.; Vega, P. Estimating the Temperature-Dependent Surface Tension of Ionic Liquids Using a Neural Network-Based Group Contribution Method. Industrial & Engineering Chemistry Research **2017**, 56, 6869–6886.

Lashkarbolooki, M.; Bayat, M. Prediction of surface tension of liquid normal alkanes, 1-alkenes and cycloalkane using neural network. Chemical Engineering Research and Design **2018**, 137, 154–163.

Pierantozzi, M.; Mulero, A.; Cachadina, I. Surface tension of liquid organic acids: An artificial neural network model. Molecules **2021**, 26, 1636.

G. R. Pazuki, M. N.; Sahranavard, L. Prediction of Surface Tension of Pure Hydrocarbons by An Artificial Neural Network System. Petroleum Science and Technology **2011**, 29, 2384–2396.

Tiejun Xu, Y. D.; Khanghah, M. A. Toward prediction of surface tension of branched n-alkanes using ANN technique. Petroleum Science and Technology **2019**, 37, 127–134.

Roosta, A.; Setoodeh, P.; Jahanmiri, A. Artificial Neural Network Modeling of Surface Tension for Pure Organic Compounds. Industrial & Engineering Chemistry Research **2012**, 51, 561–566.

Cicciarelli, B. A.; Hatton, T. A.; Smith, K. A. Dynamic Surface Tension Behavior in a Photoresponsive Surfactant System. Langmuir **2007**, 23, 4753–4764, PMID: 17381140.

Hyvärinen, A.-P.; Lihavainen, H.; Gaman, A.; Vairila, L.; Ojala, H.; Kulmala, M.; Viisanen, Y. Surface Tensions and Densities of Oxalic, Malonic,

Succinic, Maleic, Malic, and cis-Pinonic Acids. Journal of Chemical & Engineering Data **2006**, 51, 255–260.

Booth, A. M.; Topping, D. O.; McFiggans, G.; Percival, C. J. Surface tension of mixed inorganic and dicarboxylic acid aqueous solutions at 298.15 K and their importance for cloud activation predictions. Phys. Chem. Chem. Phys. **2009**, 11, 8021–8028.

Ernst, R. C.; Watkins, C. H.; Ruwe, H. The Physical Properties of the Ternary System Ethyl Alcohol–Glycerin–Water. The Journal of Physical Chemistry **1935**, 40, 627–635.

Jenkin, M. E.; Saunders, S. M.; Pilling, M. J. The tropospheric degradation of volatile organic compounds: a protocol for mechanism development. Atmospheric Environment **1997**, 31, 81–104.

Jenkin, M. E.; Wyche, K. P.; Evans, C. J.; Carr, T.; Monks, P. S.; Alfarra, M. R.; Barley, M. H.; McFiggans, G. B.; Young, J. C.; Rickard, A. R. Development and chamber evaluation of the MCM v3.2 degradation scheme for β-caryophyllene. Atmospheric Chemistry and Physics **2012**, 12, 5275–5308.

Jenkin, M. E.; Young, J. C.; Rickard, A. R. The MCM v3.3.1 degradation scheme for isoprene. Atmospheric Chemistry and Physics **2015**, 15, 11433–11459.

Rastak, N. et al. Microphysical explanation of the RH-dependent water affinity of biogenic organic aerosol and its importance for climate. Geophysical Research Letters **2017**, 44, 5167–5177.

Vargaftik, N. B.; Volkov, B. N.; Voljak, L. D. International Tables of the Surface Tension of Water. Journal of Physical and Chemical Reference Data **1983**, 12, 817–820.

Sequeira, M. C.; Pereira, M. F.; Avelino, H. M.; Caetano, F. J.; Fareleira, J. M. Viscosity measurements of poly(ethyleneglycol) 400 [PEG 400] at temperatures from 293 K to 348 K and at pressures up to 50 MPa using the vibrating wire technique. Fluid Phase Equilibria **2019**, 496, 7–16.

Součková, M.; Klomfar, J.; Pátek, J. Standard reference data for the air–liquid and vapor–liquid surface tension of benzene. Fluid Phase Equilibria **2013**, 356, 329–337.

Koller, T. M.; Klein, T.; Giraudet, C.; Chen, J.; Kalantar, A.; van der Laan, G. P.; Rausch, M. H.; Fröba, A. P. Liquid Viscosity and Surface Tension of n-Dodecane, n-Octacosane, Their Mixtures, and a Wax between 323 and 573 K by Surface Light Scattering. Journal of Chemical & Engineering Data **2017**, 62, 3319–3333.

Jasper, J. J. The Surface Tension of Pure Liquid Compounds. Journal of Physical and Chemical Reference Data **1972**, 1, 841–1010.

Ai, J.; Li, F.; Zhang, J.; Wu, Z. Density, viscosity, surface tension, and spectral analysis of polyethylene glycol 300 + 1,2-Propylenediamine binary liquid mixture. Journal of Molecular Liquids **2022**, 361, 119579.

Sigma-Aldrich Technical Bulletin AL-128; 2006.

Tuckermann, R.; Cammenga, H. K. The surface tension of aqueous solutions of some atmospheric water-soluble organic compounds. Atmospheric Environment **2004**, 38, 6135–6138.

Riipinen, I.; Koponen, I. K.; Frank, G. P.; Hyvärinen, A.-P.; Vanhanen, J.; Lihavainen, H.; Lehtinen, K. E. J.; Bilde, M.; Kulmala, M. Adipic and Malonic Acid Aqueous Solutions: Surface Tensions and Saturation Vapor Pressures. The Journal of Physical Chemistry A **2007**, 111, 12995–13002, PMID: 18044850.

Varga, Z.; Kiss, G.; Hansson, H.-C. Modelling the cloud condensation nucleus activity of organic acids on the basis of surface tension and osmolality measurements. Atmospheric Chemistry and Physics **2007**, 7, 4601–4611.

A

Supplement to Chapter 2 - A thermodynamic framework for bulk–surface partitioning in finite-volume mixed organic–inorganic aerosol particles and cloud droplets

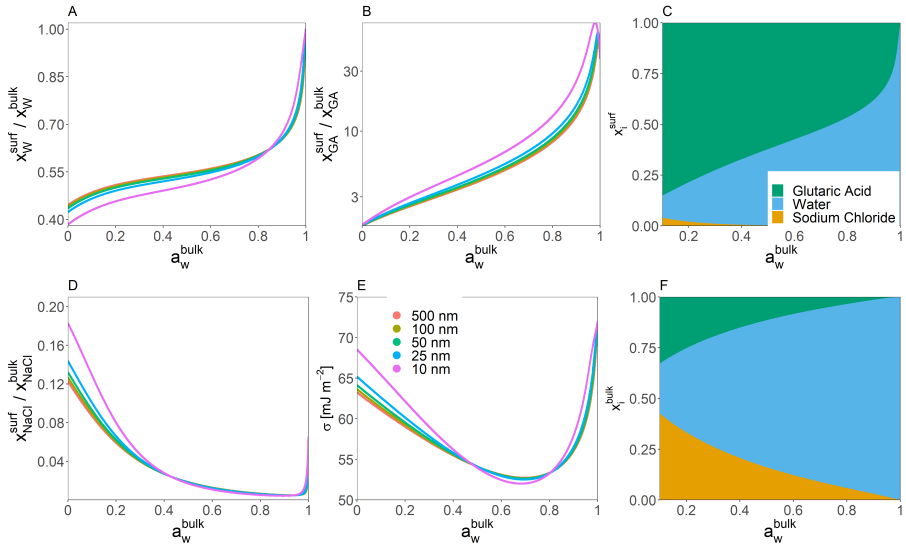

Figure A.1: Predicted bulk–surface partitioning coefficient ($\frac{x_i^{\mathrm{surf}}}{x_i^{\mathrm{bulk}}}$) of (A) water, (B) glutaric acid, and (D) sodium chloride present in a forced single-bulk-phase particle at $T = 298$ K as a function of a_w^{bulk}. Right column (composition bar graphs): shown are the mole fractions of each species in the surface and the bulk phase (α) for the particle of 25 nm dry diameter.

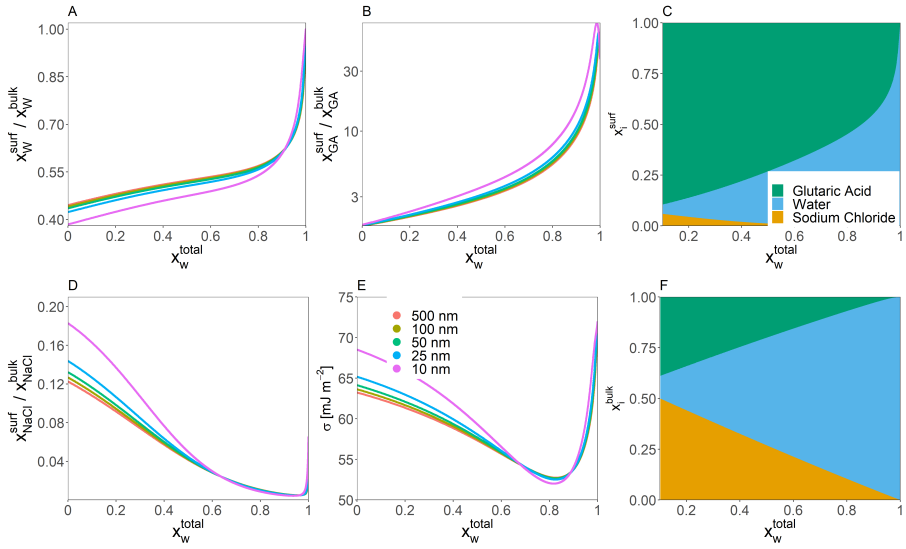

Figure A.2: Predicted bulk–surface partitioning coefficient ($\frac{x_i^{\mathrm{surf}}}{x_i^{\mathrm{bulk}}}$) of (A) water, (B) glutaric acid, and (D) sodium chloride present in a forced single-bulk-phase particle at $T = 298$ K as a function of x_w^{total}. Right column (composition bar graphs): shown are the mole fractions of each species in the surface and the bulk phase (α) for the particle of 25 nm dry diameter.

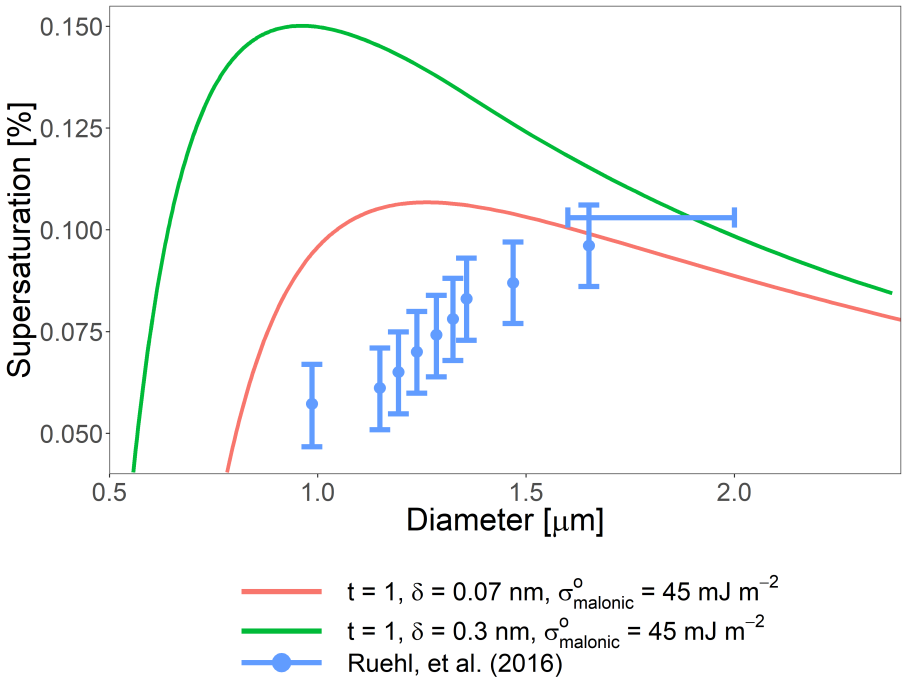

Figure A.3: Predicted saturation ratio for a ternary water–malonic-acid–ammonium-sulfate system corresponding to a 50 nm diameter ammonium sulfate core coated to a total diameter of 150 nm with malonic acid, corresponding to measurements by Ruehl et al.. In order to better match the experimental data better, δ was set to 0.07 nm. No combination of t and modifications to $\sigma^{\circ}_{\text{malonic}}$ were able to capture both the points leading up to the critical supersaturation and the critical supersaturation itself. Also shown is a prediction using the more standard assumptions that $t = 1$, $\delta = 0.3$ nm, and $\sigma^{\circ}_{\text{malonic}} = 45.0\ \text{mJ}\,\text{m}^{-2}$ (Hyvärinen et al., 2006) The horizontal bar represents the critical supersaturation for cloud activation (Ruehl et al., 2016).

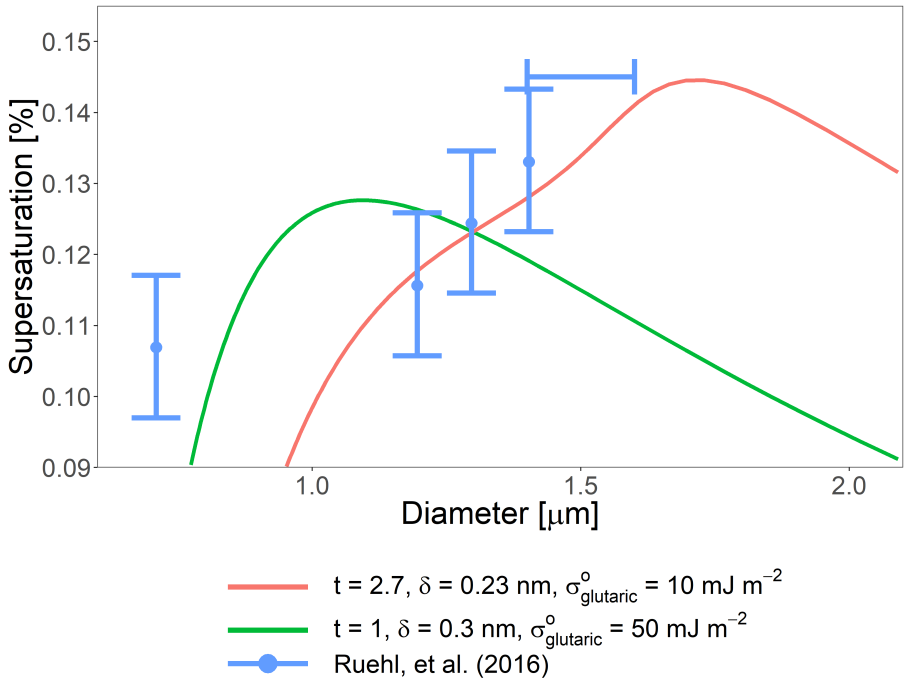

Figure A.4: Predicted saturation ratio for a ternary water–glutaric-acid–ammonium-sulfate system corresponding to a 50 nm diameter ammonium sulfate core coated to a total diameter of 150 nm with glutaric acid, corresponding to measurements by Ruehl et al.. In order to better match the experimental data better, δ was set to 0.23 nm. t was set to 2.7 and $\sigma^{\circ}_{\text{glutaric}}$ was set to 10 mJ m^{-2}. Also shown is a prediction using the more standard assumptions that $t = 1$, $\delta = 0.3$ nm, and $\sigma_{\text{glutaric}} = 50$ mJ m^{-2} (Ruehl et al., 2016; Hyvärinen et al., 2006; Booth et al., 2009) The horizontal bar represents the critical supersaturation for cloud activation Ruehl et al..

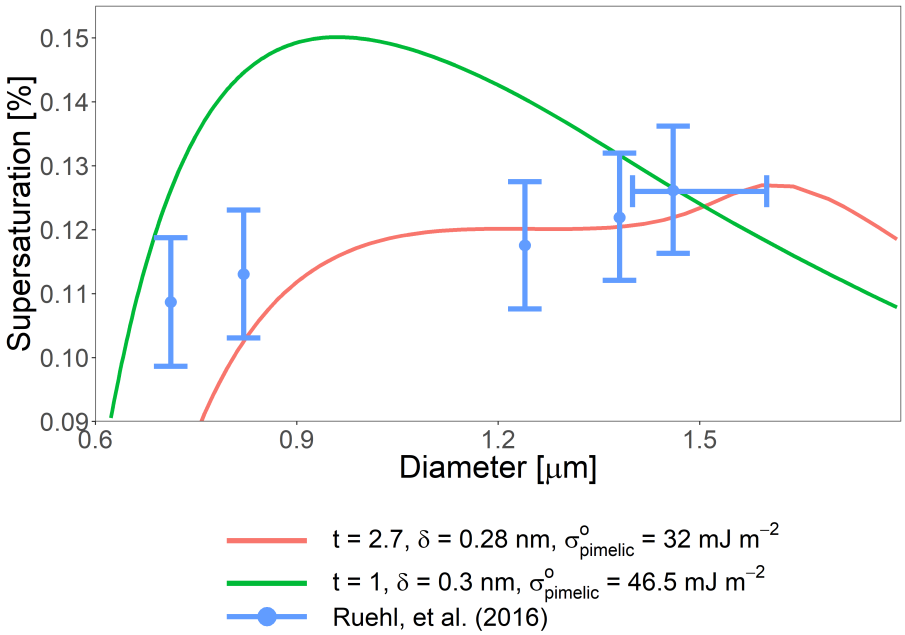

Figure A.5: Predicted saturation ratio for a ternary water–pimelic-acid–ammonium-sulfate system corresponding to a 50 nm diameter ammonium sulfate core coated to a total diameter of 150 nm with succinic acid, corresponding to measurements by Ruehl et al.. In order to better match the experimental data better, δ was set to 0.28 nm, t was set to 2.7 and σ_{pimelic} was set to 32 mJ m^{-2} Also shown is a prediction using the more standard assumptions that $t = 1$, $\delta = 0.3$ nm, and $\sigma_{\text{pimelic}} = 46.5$ mJ m^{-2} based on similartiy to other surface tensions of similar dicarboxylic acids reported by Hyvärinen et al.. The horizontal bar represents the critical supersaturation for cloud activationRuehl et al..

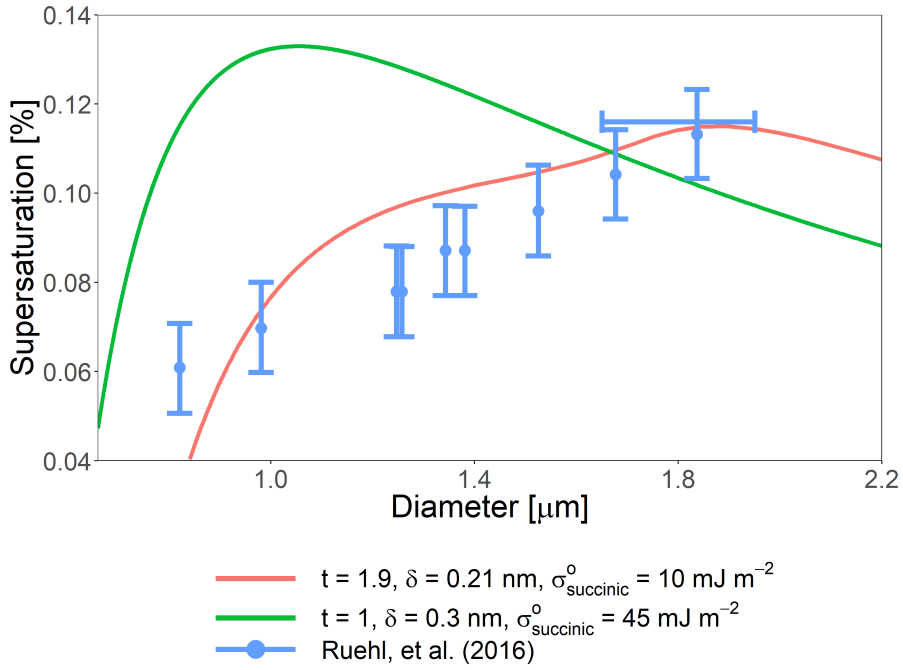

Figure A.6: Predicted saturation ratio for a ternary water–succinic-acid–ammonium-sulfate system corresponding to a 50 nm diameter ammonium sulfate core coated to a total diameter of 150 nm with succinic acid, corresponding to measurements by Ruehl et al.. In order to better match the experimental data better, $\sigma^{\circ}_{\text{succinic}}$ was set to 10 mJ m^{-2}, δ was set to 0.21 nm, the value of t was set to 1.9. Also shown is a prediction using the more standard assumptions that $t = 1$, $\delta = 0.3$ nm, and $\sigma^{\circ}_{\text{succinic}} = 45.0$ mJ m^{-2} (Hyvärinen et al., 2006) The horizontal bar represents the critical supersaturation for cloud activation Ruehl et al..

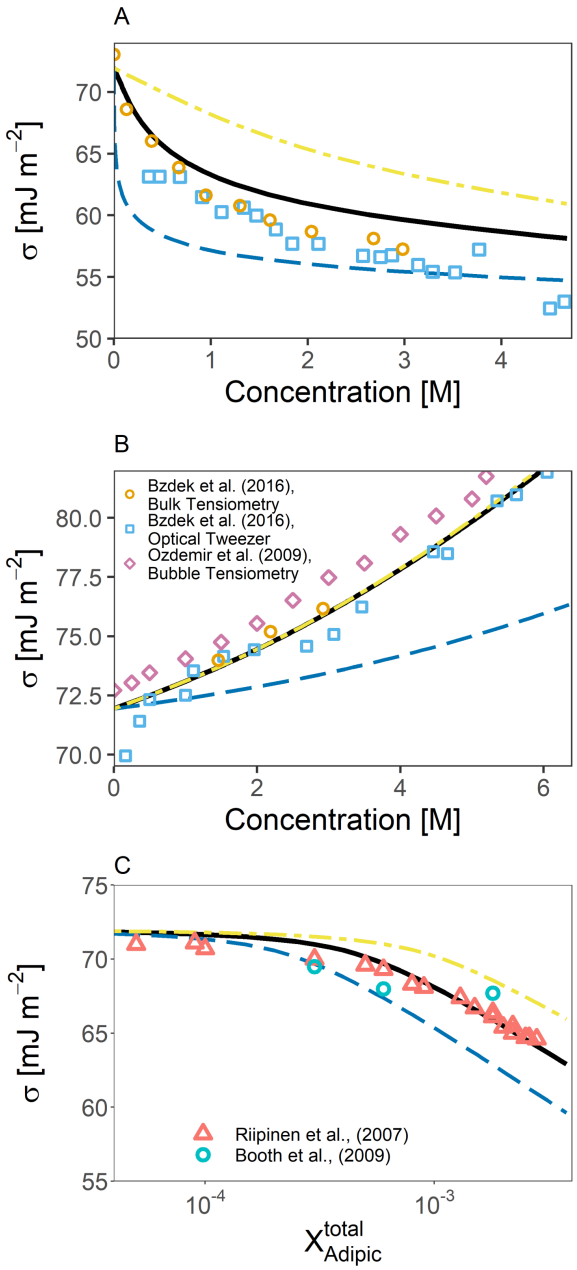

Figure A.7: Predicted solution surface tensions assuming a 10% reduction or increase in σ°_{solute} (blue and yellow curves respectively) for the systems shown in (A) Figure 1A, (B) Figure 1B, and (C) Figure 3. All systems had a starting particle size of 5 μm and $\delta = 0.3$ nm

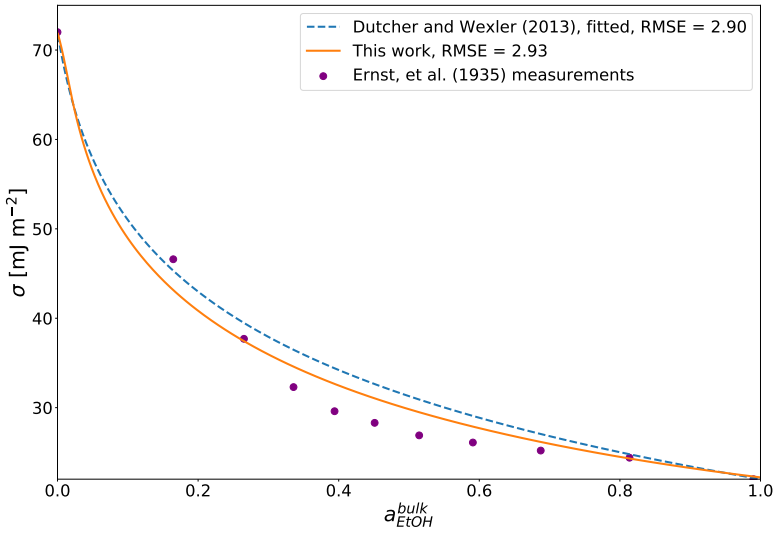

Figure A.8: Surface tension of a binary water-ethanol droplet with a dry diameter of 50 μm as predicted by Eq (24) and the simplified statistical mechanics model from Wexler and Dutcher. Measurements of the solution surface tension as a function of the AIOMFAC-predicted bulk ethanol activity are also shown from Ernst et al. (1935).

Table A.1: Surrogate component concentrations for isoprene-derived SOA based on a simulation by the Master Chemical Mechanism (Jenkin et al., 1997, 2012, 2015). The listed concentrations are total amounts (gas plus particle phase) per unit volume of air for the co-condensation scenario, as well as condensed phase concentrations only for the calculations without co-condensation of organic species. For more details, see the supplementary material of Rastak et al. and Gervasi et al..

		Input Concentration $[\mathrm{mol\,m^{-3}}]$	
Name (MCM)	**M** $[\mathrm{g\,mol^{-1}}]$	**Co-condensation Enabled**	**Co-condensation Disabled**
IEB1OOH	150.11	3.76459×10^{-8}	2.38011×10^{-8}
IEB2OOH	150.11	6.75043×10^{-9}	1.83810×10^{-9}
C59OOH	150.09	3.92509×10^{-8}	3.11576×10^{-8}
IEC1OOH	150.09	1.37006×10^{-8}	1.08756×10^{-8}
C58OOH	150.11	3.91125×10^{-9}	2.47284×10^{-9}
IEPOXA	118.13	2.56541×10^{-15}	8.11516×10^{-19}
C57OOH	150.11	3.17789×10^{-9}	2.00918×10^{-9}
IEPOXC	118.13	1.99219×10^{-14}	2.61410×10^{-17}
HIEB1OOH	166.11	1.92764×10^{-9}	1.92561×10^{-9}
INDOOH	197.14	1.41401×10^{-9}	1.40886×10^{-9}
IEACO3H	148.10	1.08728×10^{-13}	4.00883×10^{-16}
C525OOH	166.09	1.44713×10^{-9}	1.44655×10^{-9}
HIEB2OOH	166.11	9.55507×10^{-10}	9.48692×10^{-10}
IEC2OOH	148.06	7.53565×10^{-13}	1.56989×10^{-14}
INAOOH	197.14	7.93083×10^{-10}	7.82336×10^{-10}
C510OOH	195.10	7.27167×10^{-11}	2.37637×10^{-11}
INB1OOH	197.14	4.04138×10^{-10}	4.02731×10^{-10}
IECCO3H	148.11	4.87375×10^{-13}	5.69206×10^{-15}
INCOOH	197.14	1.82889×10^{-10}	1.72834×10^{-10}
INB2OOH	197.14	1.98863×10^{-10}	1.96461×10^{-10}
Tetrol Dimer	254.28	3.15073×10^{-8}	3.15073×10^{-8}

Table A.2: List of abbreviations used in chapter 2 and their meanings.

Abbreviation	**Meaning**
VOC	Volatile Organic Compound
SVOC	Semi-Volatile Organic Compound
IVOC	Intermediate Volatility Organic Compound
LVOC	Low Volatility Organic Compound
POA	Primary Organic Aerosol
SOA	Secondary Organic Aerosol
LLPS	Liquid–Liquid Phase Separation
CCN	Cloud Condensation Nucleus
RH	Relative Humidity
LLE	Liquid–Liquid Equilibrium
AIOMFAC	Aerosol Inorganic–Organic Mixtures Functional groups Activity Coefficients
PM	Particulate matter

Table A.3: List of mathematical symbols used in chapter 2 and their meanings.

Category	Symbol	Meaning	Units
Mathematical Variables	A	area of the surface	m^2
	$\mathscr{A}_i$	partial molar area of i	$\mathrm{m}^2\,\mathrm{mol}^{-1}$
	a_i	chemical activity (mole-fraction- or molality-based) of i	$-$
	A^{SL}	Szyszkowski–Langmuir fit parameter	$\mathrm{J\,m}^{-2}$
	B^{SL}	Szyszkowski–Langmuir fit parameters	molm^{-3}
	C^{SL}	bulk concentration in Szyszkowski–Langmuir model	concentration
	$A_\circ^{CF}$	maximum surface adsorbtion in the compressed film model	$\mathrm{mol\,m}^{-2}$
	A^{CF}	current surface adsorption in compressed film model	$\mathrm{mol\,m}^{-2}$
	D	diameter	m
	G	Gibbs energy	J
	f_i	volume fraction of i	$-$
	M_i	molar mass of i	$\mathrm{kg\,mol}^{-1}$
	n_i	number of moles	mol
	P	pressure	Pa
	R	universal gas constant	$\mathrm{J\,mol}^{-1}\,\mathrm{K}^{-1}$
	S	entropy or saturation ratio (depending on context)	$\mathrm{J\,K}^{-1}$ or $-$
	SS	supersaturation	%
	T	temperature	K
	t	exponential scaling factor for surface activity coefficients	$-$
	U	internal energy	J
	V	system volume	m^3

	$\mathscr{V}_i$	molar volume of i	$\mathrm{m^3\,mol^{-1}}$
	x_i	mole fraction of i	–
Greek Letter Variables	Γ	Gibbs surface excess	$\mathrm{mol\,m^{-2}}$
	γ_i	activity coefficient of i	–
	δ	thickness of Guggenheim surface phase	m
	ϵ	machine precision	–
	ε_i	fraction of the total particle amount of species $i$partitioned to the surface phase (surface fraction)	–
	ζ_i	fraction of i in between the maximum and minimum possible volumes it can occupy in the surface	–
	κ	hygroscopicity parameter	–
	μ_i	chemical potential of i	$\mathrm{J\,mol^{-1}}$
	ξ_i	intrinsic chemical potential of the surface phase of i	$\mathrm{J\,mol^{-1}}$
	ρ_i	density of i	$\mathrm{kg\,m^{-3}}$
	σ_i	surface tension of i	$\mathrm{J\,m^{-2}}$
Superscripts and Subscripts	b	bulk phase	–
	c	thermodynamic critical point	–
	CF	compressed film model	–
	$calc$	calculated value	–
	$crit$	CCN critical activation property	–
	dry	particle under dry conditions (water-free condensed phase, RH ¡ 1 %)	–
	$guess$	initial guess	–
	i	chemical component or species index	–
	max	maximum	–
	min	minimum	–
	np	non-partitioning case	–

pm	particle phase	–
SL	Szyszkowski–Langmuir	–
s	surface phase	–
rg	range	–
tot	total	–
w	water	–
wet	particle under wet conditions (water present in condensed phase, RH ¿ 1 %)	–
α	inorganics-rich phase	–
β	organics-rich phase	–
ϕ	phase index	–
$\star$	unnormalized	–
$\circ$	standard or reference state	–

B

Supplement to Chapter 3 - The role of interfacial tension in the size-dependent phase separation of atmospheric aerosol particles

Table B.1: List of abbreviations used in chapter 3 and their meanings.

Abbreviation	**Meaning**
AIOMFAC	Aerosol Inorganic–Organic Mixtures Functional groups Activity Coefficients
CCN	Cloud Condensation Nucleus
CSOA	Complex Secondary Organic Aerosol mixture
IFE	Interfacial Energy
LLE	Liquid–Liquid Equilibrium
LL	Liquid–Liquid
LLPS	Liquid–Liquid Phase Separation
OIR	Organic-to-Inorganic dry mass Ratio
PM	Particulate Matter
RH	Relative Humidity
SOA	Secondary Organic Aerosol
SRH	Separation Relative Humidity

Table B.2: List of mathematical symbols used in chapter 3 and their meanings.

Category	Symbol	Meaning	Units
Mathematical Variables	A	area of the surface	m^2
	$\mathscr{A}$	partial molar area	$\mathrm{m}^2\,\mathrm{mol}^{-1}$
	D	diameter	m
	d	distance	m
	G	Gibbs energy	J
	M	molar mass	$\mathrm{kg}\,\mathrm{mol}^{-1}$
	n	number of moles	mol
	P	pressure	Pa
	R	universal gas constant	$\mathrm{J}\,\mathrm{mol}^{-1}\,\mathrm{K}^{-1}$
	r	radius	m
	S	entropy or saturation ratio (depending on context)	$\mathrm{J}\,\mathrm{K}^{-1}$ or $-$
	T	temperature	K
	U	internal energy	J
	V	system volume	m^3
	$\mathscr{V}$	molar volume	$\mathrm{m}^3\,\mathrm{mol}^{-1}$
	x	mole fraction	$-$
Greek Letter Variables	η	exponential scaling factor for interfacial composition	-
	γ	activity coefficient	-
	δ	thickness of Guggenheim surface phase	m
	ι	length of a three-phase boundary line	m
	μ	chemical potential	$\mathrm{J}\,\mathrm{mol}^{-1}$
	ρ	density	$\mathrm{kg}\,\mathrm{m}^{-3}$
	σ	surface or interfacial tension	$\mathrm{J}\,\mathrm{m}^{-2}$
	τ	line energy at a three-phase boundary	$\mathrm{J}\,\mathrm{m}^{-1}$
	ε	fraction of the total particle amount of species partitioned to the surface phase (surface fraction)	-
Superscripts and Subscripts	α	inorganics-rich phase	$-$
	β	organics-rich phase	$-$
	b	bulk phase	$-$
	disp	dispersion force based calculation	$-$
	el	inorganic electrolyte species	$-$
	G	Gas-phase property	$-$
	i	chemical component or species index	$-$
	$\circ$	standard or reference state	$-$
	ϕ	phase index or semi-empirical Girifalco–Good equation parameter (depending on context)	$-$
	ls	Liquid–Surface	$-$
	p	particle	$-$
	$\prime$	liquid–liquid-interface-corrected property	$-$
	s	surface phase	$-$
	sat	saturation	$-$
	suppr	suppression limit	$-$
	tot	total	$-$
	vf	volume-fraction-based	$-$
	w	water	$-$
	$\star$	measurable	$-$

Table B.3: Reference pure-component liquid-state surface tension values at 298 K (σ_i°) and dry particle mass fractions for the systems discussed in chapter 3. Organic compounds of unknown σ_i° due to lack of experimental data were assigned $\sigma_i^\circ = 35\ \mathrm{mJ\,m^{-2}}$. $\sigma_w^\circ = 71.98\ \mathrm{mJ\,m^{-2}}$ at 298 K (Vargaftik et al., 1983).

Compound	**Figure**	**Molar Mass** [kg mol^{-1}]	**Dry Mass Frac** [–]	σ_i° [mJ m^{-2}]	**Reference**
Glutaric acid	3.2A	0.132115	1.00[1]	45.0	Booth et al. (2009)
NaCl	2B	0.058443	1.00[1]	174.0	Dutcher et al. (2010)
PEG-400 n7	3.3, 3.4A, 3.6,	0.3704376	0.155	44.5	Sequeira et al. (2019)
PEG-400 n8	3.8A, B.1A,	0.4144904	0.345	44.5	Sequeira et al. (2019)
$(NH_4)_2SO_4$	B.2, B.3	0.132139	0.500	184.5	Dutcher et al. (2010)
Benzene	3.4B,	0.078108	0.57-0.9999[2]	28.75	Součková et al. (2013)
NaCl	B.1B	0.058443	0.0001-0.43[2]	174.5	Dutcher et al. (2010)
Dodecane	3.4C,	0.148152	0.67-0.9999 [2]	25.0	Koller et al. (2017)
KCl	B.1C	0.074551	0.0001-0.33[2]	155.4	Dutcher et al. (2010)
Benzene	3.4D,	0.078108	0.55-0.9999[2]	28.75	Součková et al. (2013)
Methanol	B.1D	0.032042	0.0001-0.45[2]	22.5	Jasper (1972)
Suberic acid	3.5	0.174156	0.537	45.0	Hyvärinen et al. (2006)
$(NH_4)_2SO_4$		0.132139	0.463	184.5	Dutcher et al. (2010)
PEG-300 n5	3.7A, 3.8A,	0.282332	0.181	43.6	Ai et al. (2022)
PEG-300 n6	B.4A, B.5A	0.326384	0.168	43.6	Ai et al. (2022)
$(NH_4)_2SO_4$		0.132139	0.651	184.5	Dutcher et al. (2010)
1,2,6-Hexanetriol	3.7B, 3.8B, 3.9,	0.134172	0.504	48.5	Sigma-Aldrich (2006)
$(NH_4)_2SO_4$	B.4B, B.5B	0.132139	0.496	184.5	Dutcher et al. (2010)
1,2,5,8-Octanetetrol	3.7C, 3.8C, B.4C, B.5C	0.178224	0.0505	35.0	–
2-Methylglutaric acid		0.146104	0.0504	50.0	Hyvärinen et al. (2006)[3]
3,5-Dihydroxybenzoic acid		0.142054	0.0464	70.5	Tuckermann and Cammenga (2004)[4]
3-Hydroxybenzoic acid		0.138082	0.0252	70.5	Tuckermann and Cammenga (2004)
3-Methyladipic acid		0.160130	0.0504	35.0	Riipinen et al. (2007)[5]
Levoglucosan		0.162122	0.0504	22.7	Topping et al. (2007)
Malic acid		0.134052	0.0504	50.0	Hyvärinen et al. (2006)
Pinolic acid		0.186226	0.0067	35.0	–
Pinonic acid		0.196176	0.0140	66.1	Varga et al. (2007)
Succinic acid		0.118052	0.0504	47.5	Hyvärinen et al. (2006)
$(NH_4)_2SO_4$		0.132139	0.605	184.5	Dutcher et al. (2010)
C107OOH (MCM name)	3.7D, 3.8D, B.4D, B.5D	0.200166	8.92×10^{-4}	35.0	–
Pinonic acid		0.184166	4.64×10^{-4}	66.1	Varga et al. (2007)
C97OOH (MCM name)		0.188174	9.65×10^{-3}	35.0	–
C108OOH (MCM name)		0.21613	0.37	35.0	–
Pinalic acid		0.170166	6.97×10^{-5}	35.0	–
Pinic acid		0.186166	3.05×10^{-2}	23.8	Topping et al. (2007)
C921OOH (MCM name)		0.204182	3.83×10^{-2}	35.0	–
C109OOH (MCM name)		0.200174	6.46×10^{-5}	35.0	–
C812OOH (MCM name)		0.158174	3.27×10^{-2}	35.0	–
10-Hydroxypinonic acid		0.206138	9.49×10^{-3}	66.1	Varga et al. (2007)[6]
C811OH (MCM name)		0.158174	2.88×10^{-4}	35.0	–
C813OOH (MCM name)		0.206138	1.39×10^{-2}	35.0	–
Aldol dimer		0.368298	4.50×10^{-3}	35.0	–
Ester dimer		0.368306	1.80×10^{-2}	35.0	–
$(NH_4)_2SO_4$		0.132139	0.471	184.5	Dutcher et al. (2010)

[1] binary systems were run assuming the dry composition case is pure solute.

[2] the system was run at variable dry composition at fixed RH to replicate measurements.

[3] estimated from structural similarity to glutaric acid.

[4] estimated from structural similarity to hydroxybenzoic acid.

[5] estimated from structural similarity to adipic acid.

[6] estimated from structural similarity to pinonic acid.

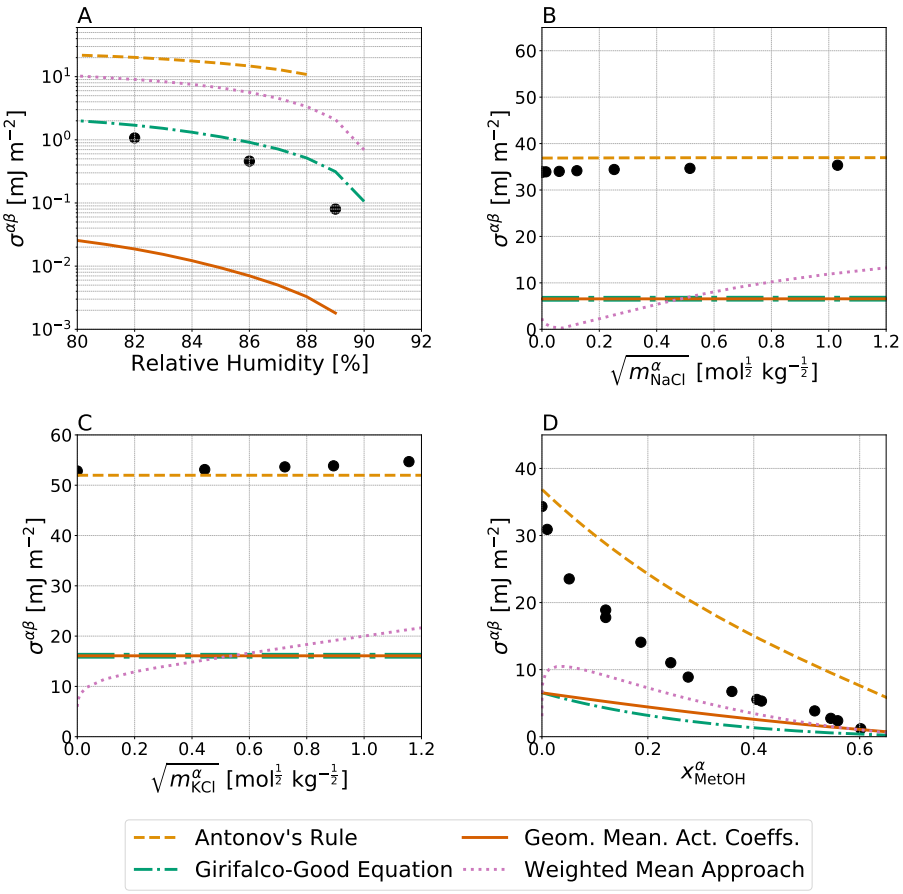

Figure B.1: Predicted $\sigma^{\alpha\beta}$ with adjustments to $\sigma^{\circ}_{\mathrm{org}}$ and $\sigma^{\circ}_{\mathrm{el}} = \sigma^{\circ}_{\mathrm{w}}$. $\sigma^{\circ}_{\mathrm{PEG-400}}$, $\sigma^{\circ}_{\mathrm{benzene}}$, and $\sigma^{\circ}_{\mathrm{MetOH}} = 35$ mJ m^{-2} in subplots A, C, and D. In subplot D, $\sigma^{\circ}_{\mathrm{dodecane}} = 20$ mJ m^{-2}. These values were selected to better fit Antonov's rule to the measured data for the systems shown in subplots B and C and to explore the sensitivity of the more miscible systems shown in subplots A and D to changes in $\sigma^{\circ}_{\mathrm{org}}$ and $\sigma^{\circ}_{\mathrm{el}}$.

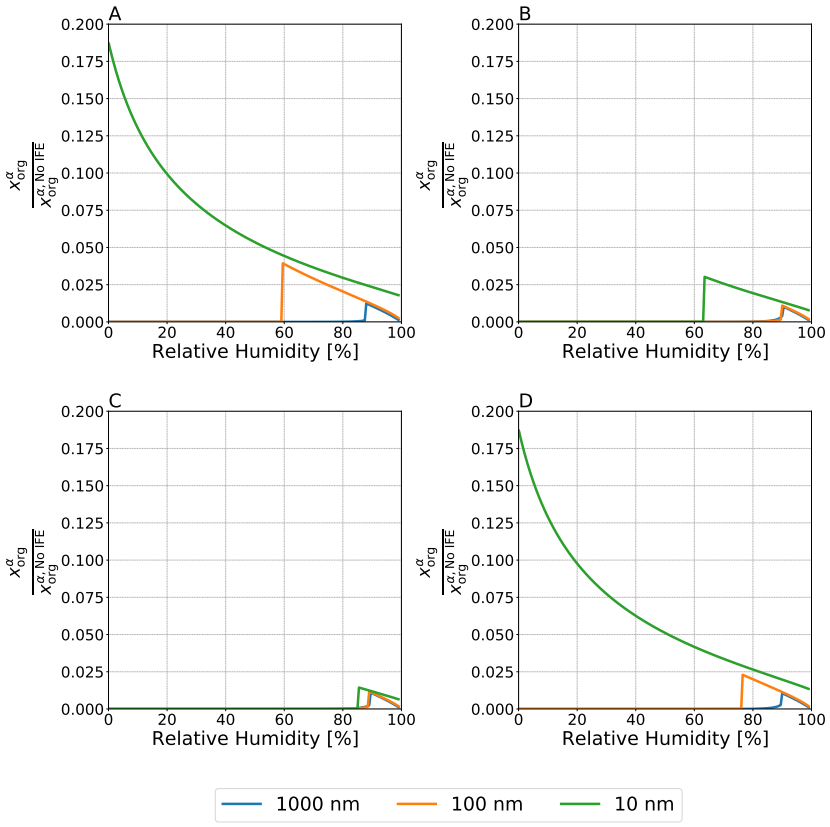

Figure B.2: Normalized mole fraction of PEG-400 in the aqueous phase for water, PEG-400, and ammonium sulfate particles with dry diameters ranging from 10 nm to 1000 nm for (A) Antonov's rule, (B) the Girifalco–Good equation, (C) Butler equation with modified activity coefficients, and (D) the weighted mean interfacial composition approach.

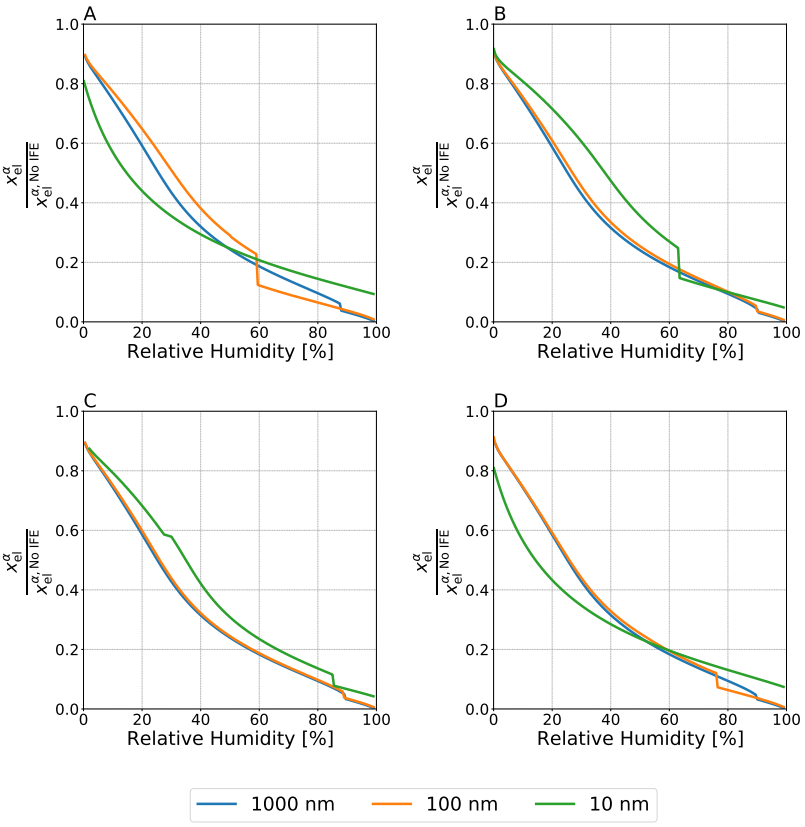

Figure B.3: Normalized mole fraction of ammonium sulfate in the aqueous phase for water, PEG-400, and ammonium sulfate particles with dry diameters ranging from 10 nm to 1000 nm for (A) Antonov's rule, (B) the Girifalco–Good equation, (C) Butler equation with modified activity coefficients, and (D) the weighted mean interfacial composition approach.

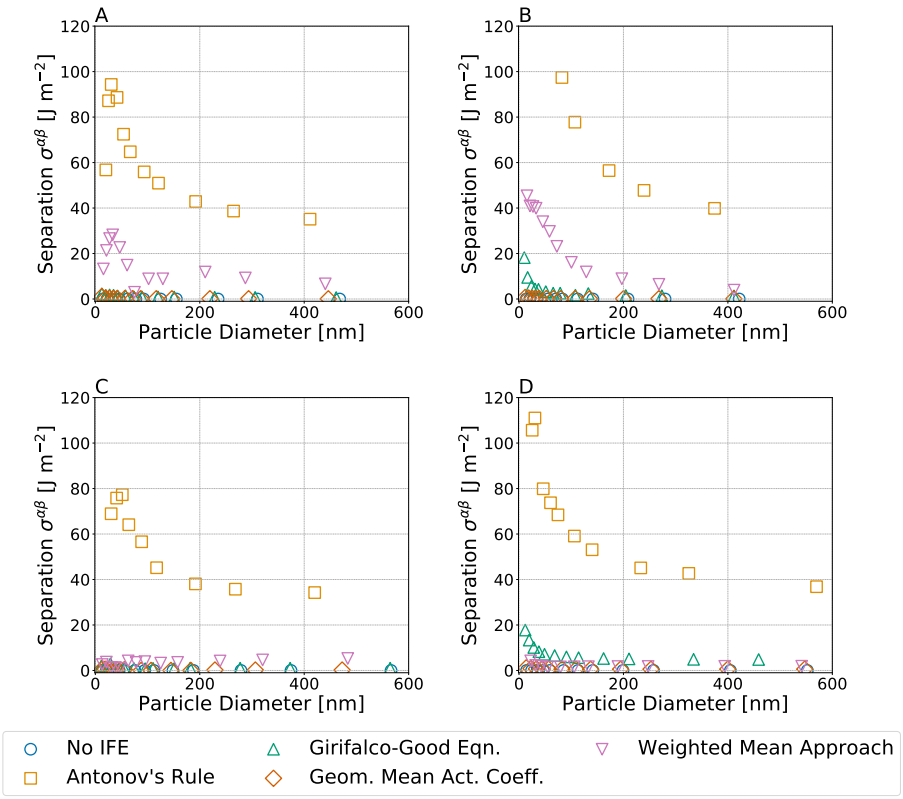

Figure B.4: Predicted $\sigma^{\alpha\beta}$ at the onset of LLPS upon dehumidification, shown for a range of particle (wet) diameters at $T = 298$ K. The systems shown are: (A) Water–PEG-300–ammonium sulfate, (B) water–1,2,6-hexanetriol–ammonium-sulfate, (C) water, a CSOA mixture with succinic acid and ammonium sulfate, and (D) water, α-pinene SOA surrogates, and ammonium sulfate. Distinct symbols refer to different approaches used for the LL interfacial tension estimations; see legend. For particles with stronger size-dependent onset of LLPS, there is less agreement among the predicted $\sigma^{\alpha\beta}$ at the onset of phase separation. At these sizes, complete partitioning of one species into the aqueous, organic, or surface phase leads to greater differences in the internal composition of the particle.

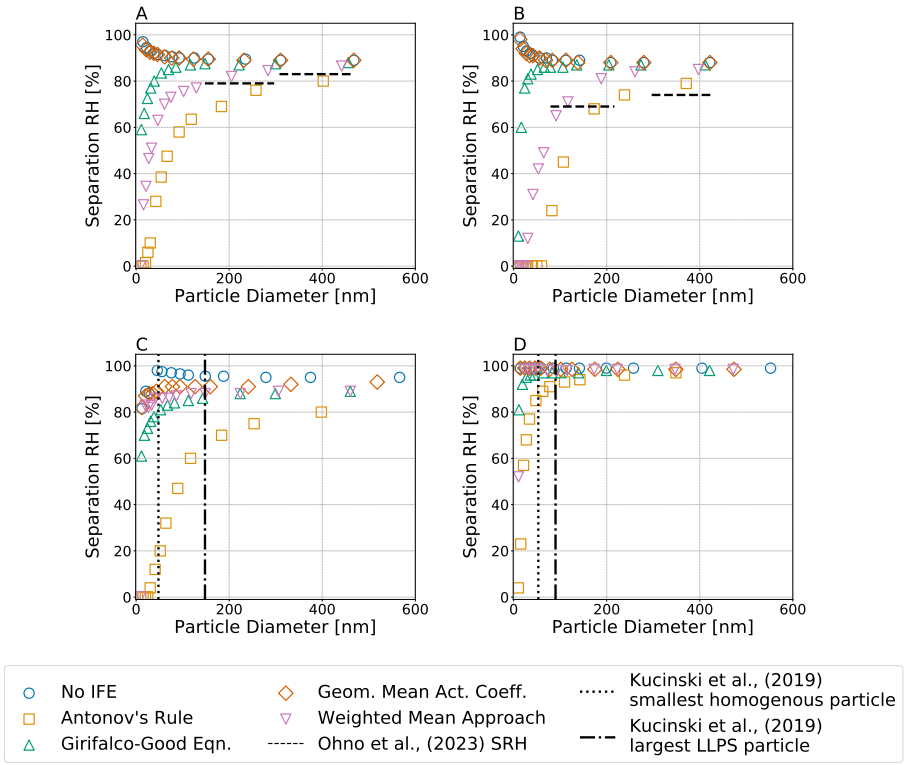

Figure B.5: Predicted equilibrium separation RH versus particle wet diameter for particles of the same dry composition but different choices of interfacial tension treatment; see legend. In this case it is assumed that $\sigma^{\mathrm{ls}} = 0$ and therefore $\sigma^{\mathrm{s}\star} = \sigma^{\mathrm{s}}$. Systems shown are: (A) water–PEG-300–ammonium-sulfate; (B) water–1,2,6-hexanetriol–ammonium-sulfate; (C) water–CSOA-with-succinic-acid–ammonium-sulfate; (D) water–α-pinene-SOA–ammonium-sulfate. Shown by dashed horizontal lines in (A, B) are measured equilibrium separation RH values by Ohno et al. (2023). Shown in (C, D) by vertical lines are the observed largest homogenous and smallest phases-separated particles as determined by Kucinski et al. (2019). All calculations were performed at 298 K.

C

Supplement to Chapter 4 - A Machine Learning Approach for Predicting the Pure Component Surface Tension of Atmospherically Relevant Organic Compounds

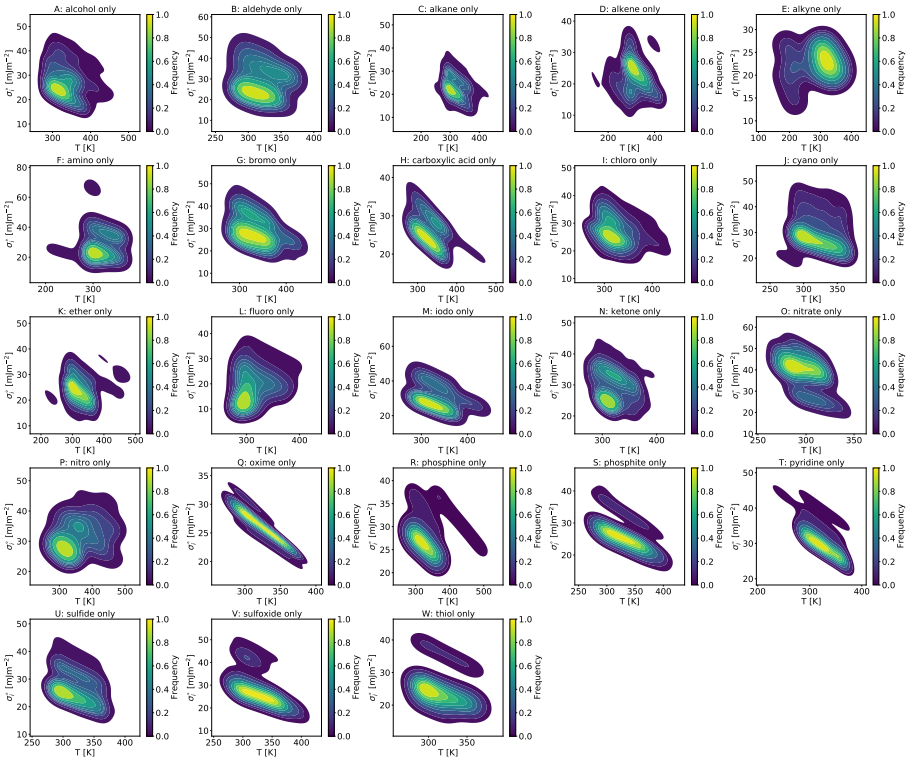

Figure C.1: Two dimensional kernel density estimates for compound classes with 5 or more unique SMILES codes and a single unique non-hydrocarbon functional group class.

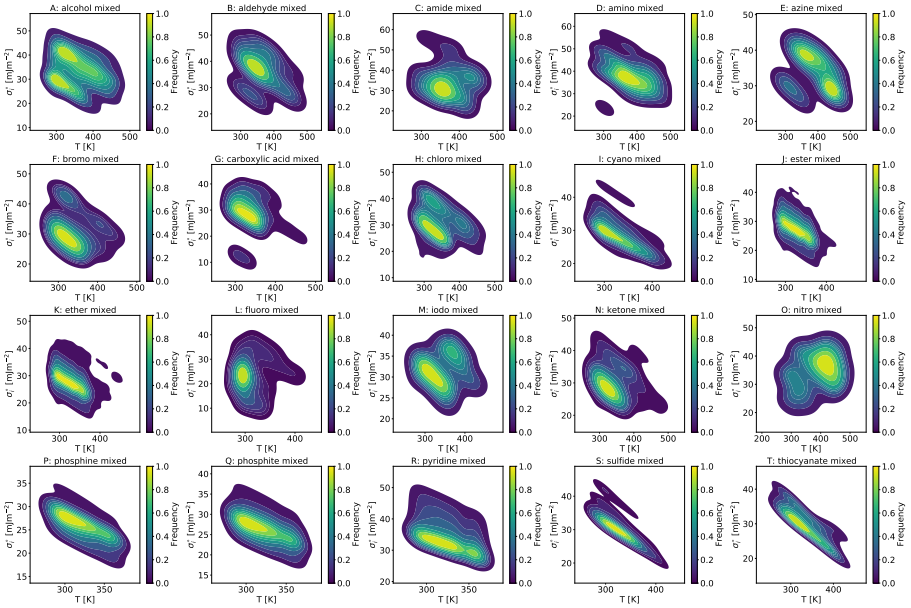

Figure C.2: Two dimensional kernel density estimates for compound classes that contain the same non-hydrocarbon functional group and any other non-hydrocarbon functional group.

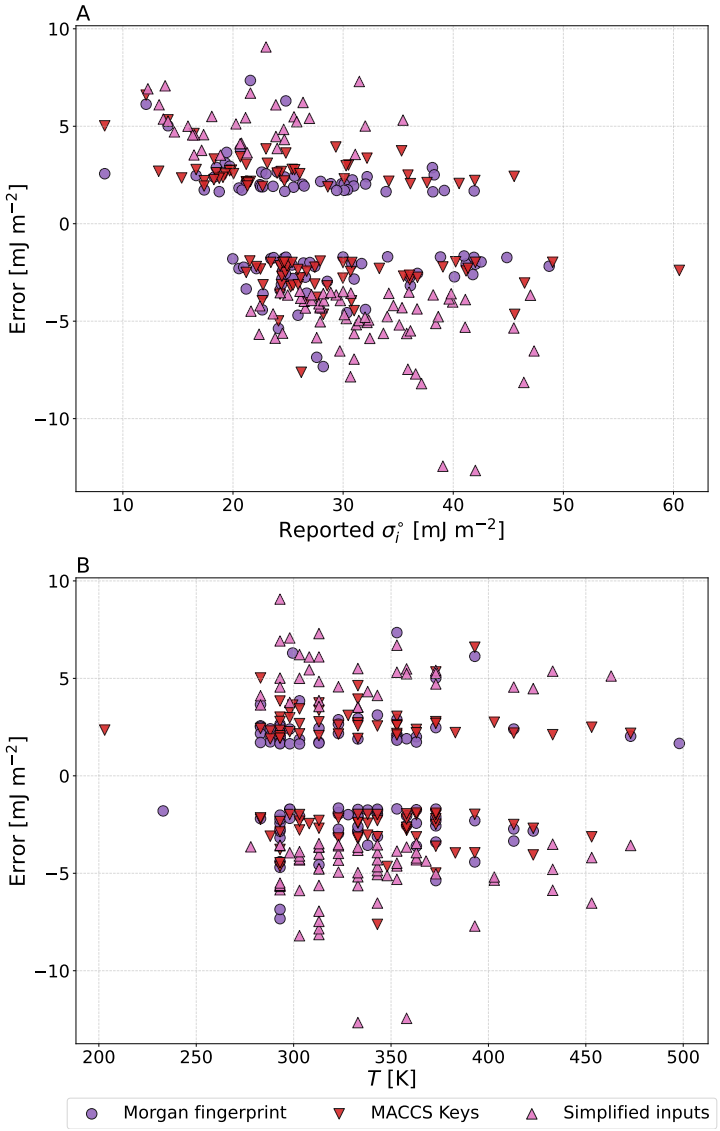

Figure C.3: Residuals from the XGBoost models for the 100 worst performing model inputs in the validation dataset.

Table C.1: t-test results for the 100-worst performing values of the simplified model inputs.

Input	t statistic	p value
Molar Weight	-3.54	0.00060
O:C ratio	1.03	0.30
H:C ratio	-0.68	0.50
N:C ratio	0.94	0.35
S:C ratio	-0.014	0.99
P:C ratio	3.45	0.00058
F:C ratio	0.84	0.40
Cl:C ratio	-0.52	0.60
Br:C ratio	-3.15	0.0017
I:C ratio	-3.43	0.00064
Temperature	1.90	0.060

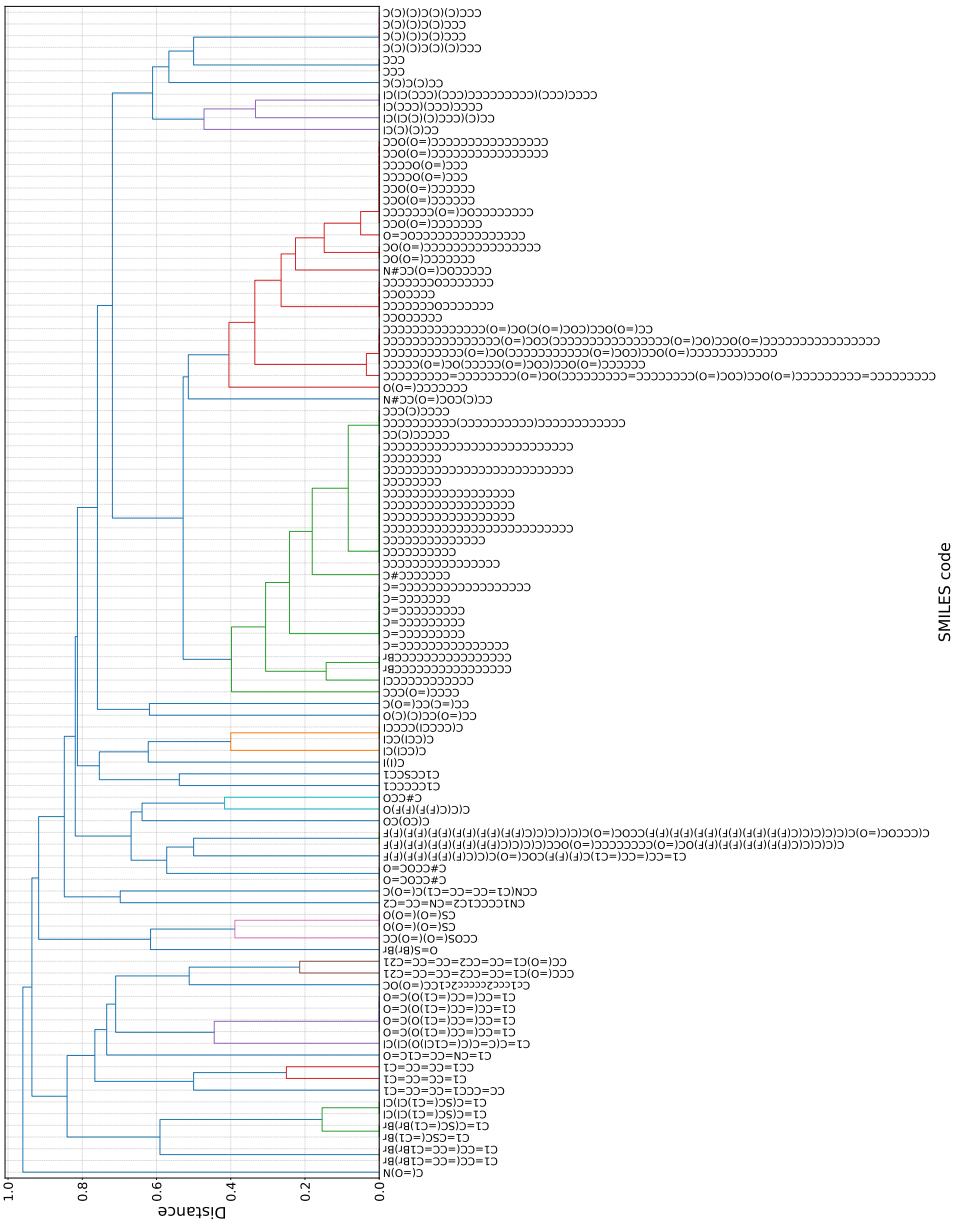

Figure C.4: Hierarchical similarities between compounds from the 100 most poorly performing MACCS keys based compounds. Colored branches denote clusters with distance values less than 0.5.

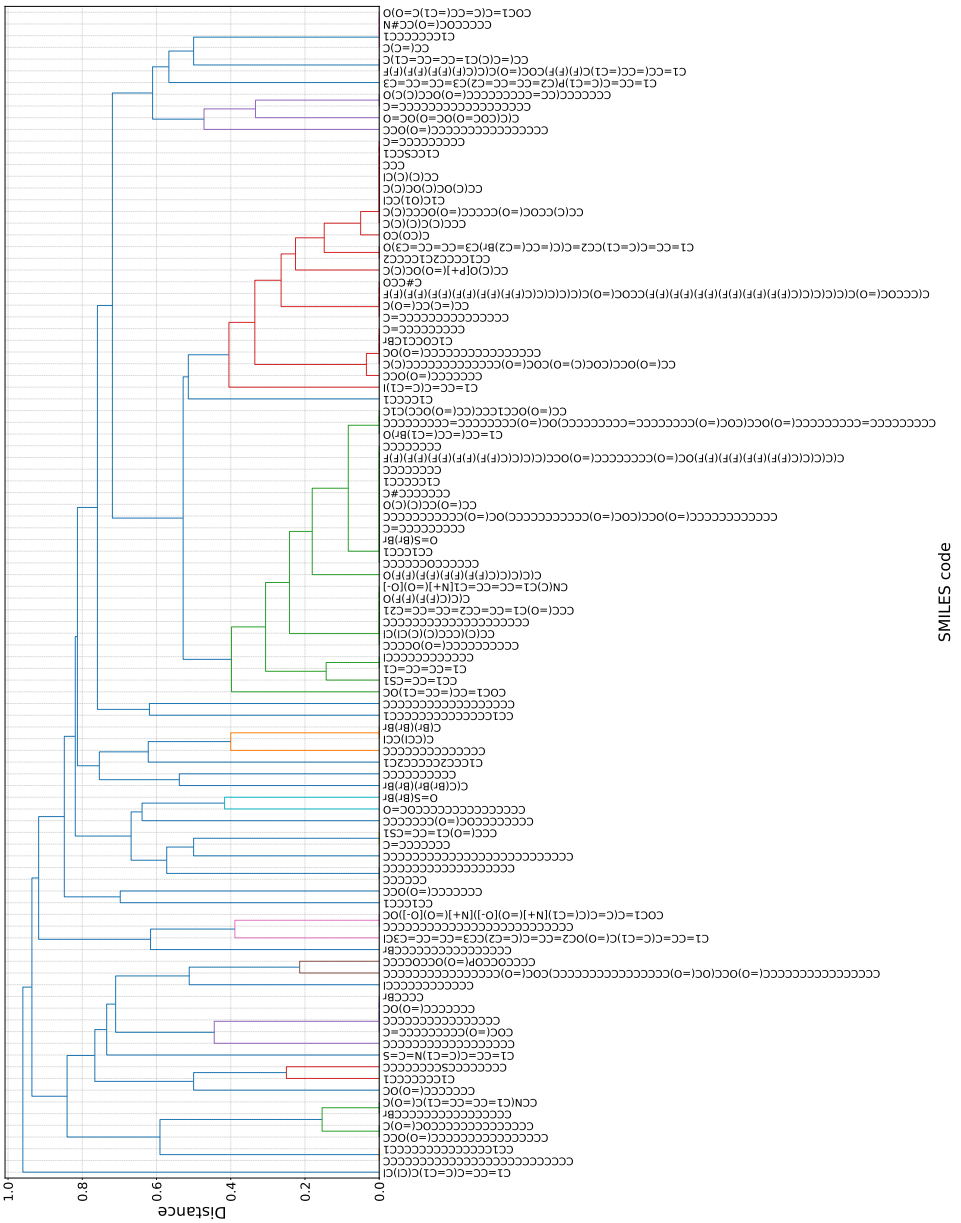

Figure C.5: Hierarchical similarities between compounds from the 100 most poorly performing Morgan fingerprints compounds. Colored branches denote clusters with distance values less than 0.5.